Fabrication, Microstructure and Properties of New Chalcogenide Thin Films and Characterization of Functional Compounds

Tayebeh Mousavi

Balliol College

A thesis submitted for the degree of Doctor of Philosophy in the University of Oxford

Supervised by Prof. C. R. M. Grovenor, Dr S. C. Speller

Michaelmas Term 2015

ABSTRACT

Fabrication, Microstructure and Properties of New Chalcogenide Thin Films and Characterization of Functional Compounds

Tayebeh Mousavi
Balliol College

A thesis submitted for the degree of Doctor of Philosophy in the University of Oxford
Michaelmas Term 2015

Fe-chalcogenides are of great interest because they have the simplest structure in the Fe-based superconductors, and show low anisotropies, high critical fields and high current densities all of which make these compounds useful for understanding Fe-based superconductors, a new class of superconductors with unusual properties, both for fundamental physics and potential high-field applications. The main part of this thesis concentrates on the fabrication and characterization of $Fe_ySe_{1-x}Te_x$ (Fe-11) thin films in order to link superconductivity and microstructure in this system. Since sputtering has been rarely used for the deposition of Fe(Se,Te) films, we used sputtering to study the feasibility of this technique for this purpose and to optimize the processing conditions. Phase evolution and texture development as a function of processing conditions are studied, and the optimum conditions for the best quality film are found. Crystallization temperature of the 11-phase was found to be 250°C, and texture is shown to be dependent on substrate, substrate temperature and film thickness which strongly control in-plane alignment. The best texture is obtained at 315°C for films thinner than 50nm on the MgO. Texture of the films becomes poorer on the substrates in the order MgO>LAO>STO>CaF_2>LiF>LSAT, and the relationship between texture and substrate is shown to be more related to the growth mechanism rather than lattice misfit. 2D layer-by-layer growth is found for the LSAT, while the films on the LAO and MgO show 3D island growth, and a combination of both growths is found for the film on the STO.

The films grown by in-situ sputtering are shown to have better quality than those grown by the ex-situ. A sharp T_C of about 10.2K is obtained for a single crystal $Fe_{1.01}Se_{0.56}Te_{0.44.}$film with a thickness of 58nm. Most of the deposited films are Fe-rich (y>1) due to compositional variation in the target and the volatility of Se and Te. Extra Fe is the main detrimental parameter for the suppression of superconductivity in these films showing the necessity of using multiple sources in sputtering. Nano-scale inhomogeneities are also observed in the majority of the films possibly as a result of different Se/Te ratios and Fe_3O_4 impurity. Substitution of 2% Mn for Fe in the $Fe_ySe_{1-x}Te_x$ structure leads to the stabilization of tetragonal 11 phase and improvement of crystallographic texture. Mn atoms are shown to occupy interstitial Fe sites in the tetragonal unit cell.

I also applied TEM technique to functional materials from external collaborators including Bi_2Te_3 and $CaFe_2As_2$. Studies of Mn-doped Bi_2Te_3 single crystals reveal that at doping concentrations, Mn incorporates with the Bi_2Te_3 structure differently. At low doping concentrations (9%Mn), Mn atoms are randomly substituted onto the Bi sites resulting in the variation in both composition and lattice parameter. At high doping concentrations (15%Mn), supersaturation occurs and the extra Mn atoms occupy the interstitial sites in addition to forming nano-scale Mn-rich precipitates.

$CaFe_2As_2$ single crystals grown by the FeAs-flux method are unstable FeAs-supersaturated crystals containing a high concentration of stacking faults. Annealing at high temperature (700°C) causes the extra FeAs to form needle-shaped precipitates perpendicular to the c-axis by Ca diffusion, and the matrix develops dislocations. Annealing at lower temperature (400°C) results in a number of stacking faults and similar precipitates with low Ca. As a result, the microstructure of the $CaFe_2As_2$ single crystals, especially the amount of strain, can be controlled by the annealing temperature resulting in similar effects to applying external pressure.

ACKNOWLEDGEMENTS

During the course of my DPhil I have received invaluable help and assistance from many people and I would like to take this opportunity to thank them.

My supervisor **Prof. Chris Grovenor** for giving me the opportunity to study for my DPhil and for his excellent supervision, guidance and support. Being his DPhil student will always be an honour in my educational life.

My supervisor **Dr Susie Speller** for her invaluable advice, supervision and support and for always being encouraging.

Prof. George Smith for his unforgettable support to start my DPhil.

Dr Marina Galano for giving me the opportunity of being involved in the characterization module.

Clarendon Fund Scholarship during my DPhil, and some other financial supports from the Materials Department and Balliol College.

Ron Doole for giving me expert advice and guidance on low temperature TEM experiments, Dr Gareth Hughes and Steve Lett for their help on TEM sample preparation, Dr Neil Young for training and good advice on TEM, and Dr Prabhakaran for his help and advice on transport and SQUID measurements.

Dr Rebecca Nicholls for helping me with EELS experiments.

The current and past members of the superconductivity and NanoSIMS groups especially Katie Moore for always being helpful.

The IOP, IOM^3, Armourers&Brasiers for providing me conference grants for two conference trips to USA and Turkey.

My parents, my sister and my brother for their endless support, and my parents-in-law for their warm encouragement.

And finally special thanks must go to my husband, Jamshid, whose love and support made this all possible.

PREFACE

The work described in this thesis was carried out by the author in the Department of Materials, University of Oxford, between January 2011 and July 2014, under the supervision of Prof. C.R.M. Grovenor and Dr S.C. Speller.

Financial support of this work was provided by Clarendon Scholarship. No part of this thesis has been previously submitted for a degree at this or any other university. The work of other authors has been freely drawn upon and duly acknowledged in the text. A list of references has been given at the end of each chapter. There are approximately 40,000 words in this thesis. Some of the work described in this thesis has been published in the following journals and has been presented at conferences listed below:

- "Characterization of Superconducting $Fe_y(Se_{1-x}Te_x)$ Thin Films Deposited on MgO Substrates by Sputtering", T. Mousavi, C.R.M. Grovenor, S.C. Speller, *Journal of Materials Science*, 20 (2015) 6970-6978.

- "Effects of Processing Condition on the Properties of Fe(Se,Te) Thin Films Grown by Sputtering", T. Mousavi, C.R.M. Grovenor, S.C. Speller, *IEEE Transactions on Applied Superconductivity*, 25(3) (2015) 1-4.

- "Structural Parameters Affecting Superconductivity in iron-chalcogenides"
  T. Mousavi, C.R.M. Grovenor, S.C. Speller, *Materials Science and Technology*, 30(15) (2014) 1929-1943.

- "Study of the Structural, Electric and Magnetic Properties of Mn-doped Bi_2Te_3 Single Crystals", M.D. Watson, L.J. Collins-McIntyre, L.R. Shelford, A.I. Coldea, D. Prabhakaran, S.C. Speller, T. Mousavi, C.R.M Grovenor, Z. Salman, S.R Giblin, G. van der Laan, T. Hesjedal, *New Journal of Physics*, 15 (2013) 103016.

- "A Review of Influential Microstructural Parameters on the Superconductivity in iron-chalcogenides", Oral Presentation, IOM^3 Materials Literature Review Prize Competition, *Institute of Materials, Minerals and Mining*, London, UK, March 2012.

- "Epitaxial Growth of $Fe_y(Se_{1-x}Te_x)$ Thin Films by Sputtering", Oral Presentation, 4th *International Conference on Superconductivity and Magnetism (ICSM2014),* Antalya, Turkey, 2014.

- "The Effects of Substrate Temperature on Microstructure of Fe(Se,Te) Thin Films on MgO", Oral Presentation, *Applied Superconductivity Conference*, Charlotte, USA, 2014.

- "The Effect of Mn Substitution on the Properties of 11-Phase Thin Films", *Proceedings of the 3rd International Conference on Superconductivity and Magnetism (ICSM2012),* Istanbul, Turkey, 2012.

- "Microstructure of the Deposited Fe-chalcogenide Thin Films on MgO Substrate", Poster presentation, *11th European Conference on Applied Superconductivity,* Genova, Italy, 2013.

- "Texture Development of $FeSe_{1-x}Te_x$ Thin Films on Different Substrates by Sputtering", Poster presentation, *IOP Superconductivity meeting*, London, 2013.

- "Microstructural Characterization of iron Chalcogenide Thin Films Grown in Different Thicknesses by Sputtering", Poster presentation, *Oxford Symposium on Quantum Materials*, Oxford, 2013.

Glossary

AFM	Atomic Force Microscopy
BE image	Backscattered Electron image
CVD	Chemical Vapor Deposition
EDX	Energy Dispersive X-ray
EELS	Electron Energy Loss Spectroscopy
FFT	Fast Fourier Transform
FWHM	Full Width at Half Maximum
H_C	Critical Field
J_C	Critical current density
LAO	$LaAlO_3$
LSAT	$(LaAlO_3)_{0.3}$ $(Sr_2AlTaO_6)_{0.7}$
PVD	Physical Vapor Deposition
SAD	Selected Area Diffraction
SE image	Secondary Electron image
SEM	Scanning Electron Microscopy
SQUID	Superconducting Quantum Interference Device
STO	$SrTiO_3$
T_C	Transition Temperature
TEM	Transmission Electron Microscopy
XRD	X-Ray Diffraction

CONTENTS

Chapter 3: Experimental methods

Chapter 4: Fabrication and characterization of FeySe1-xTex thin films

Chapter 6: TEM investigation of $CaFe_2As_2$ single crystals

Chapter 1: Introduction

1. Introduction

Iron chalcogenides are of great interest for both basic physics and high-field applications. Although their superconducting transition temperatures (T_C) are typically lower than those of iron pnictides, iron chalcogenides exhibit lower anisotropies and very high upper critical field values near the superconducting transition temperature. They also have the simplest structures among the iron-based superconductors. Iron chalcogenide thin films are even more interesting because higher T_Cs have been found in thin films than in bulk iron chalcogenides. Most of the iron chalcogenide thin films in the literature have been made by pulsed laser deposition and a few by molecular beam epitaxy. But they have not been yet fabricated by sputtering and relatively little is known about the relation between microstructure and superconductivity in these films. The main aim of this thesis is to explore the feasibility of sputtering for the fabrication of superconducting $Fe_ySe_{1-x}Te_x$ thin films, to optimize the processing conditions and to correlate microstructure, superconducting properties and processing conditions. In the next chapter, a literature review of iron chalcogenide thin films including the properties, influential parameters for the superconductivity and the studies carried out on this subject will be present. Chapter 3 gives the experimental methods and chapter 4 presents the results of fabrication and characterization of Fe(Se,Te) thin films followed by conclusion and future work.

In addition to the above-mentioned work, I did characterization, mostly TEM analysis, on a number of single crystal samples of functional compounds received from collaborators. These samples include Bi_2Te_3 and $MnBi_2Te_3$ and $CaFe_2As_2$. The rest of this thesis deals with results from these compounds. Chapter 5 reports microstructural analysis of undoped Bi_2Te_3 and

Mn-doped Bi_2Te_3 single crystals received from the Clarendon Laboratory of the University of Oxford. An introduction to Mn-doped Bi_2Te_3, sample preparation, results, conclusions and future work will be presented in this chapter.

Chapter 6 concerns TEM analysis of $CaFe_2As_2$ single crystals grown by the FeAs flux method and different post-annealing processes by collaborators at the Ames Laboratory in Iowa State University. In this chapter, following an introduction and a review of microstructural studies of $CaFe_2As_2$ in the literature, sample preparation and results will be presented followed by conclusions and suggestions for future work.

Finally, a summary of the important findings and conclusions from all of the chapters are presented in Chapter 7 along with suggestions for further work.

Chapter 2: Literature review

2.1 Introduction to superconductivity[1]

Superconductors are materials which exhibit zero electrical resistance when cooled below a specific T_C value. This property can be exploited in a wide range of applications, from transmission lines to electronic devices, and in particular, in applications where large current densities and small losses are desirable such as the large electromagnets used for magnetic resonance spectroscopy and magnetic levitation trains, and electrical power transmission and distribution, all of which are large scale industrial applications. Studies show that despite the high refrigeration costs, superconductors are competitive with the conventional technologies for power transmission. Therefore, they have been of great interest since their discovery [1, 2]. There are three critical parameters below which a material becomes a superconductor, critical temperature (T_C), critical field (H_C) and critical current density (J_C). If a magnetic field ($H<H_C$) is applied to a material in the superconducting state, currents are induced within a surface layer to a depth known as penetration depth (λ). The magnetic field created by these currents cancels the applied magnetic field resulting in the exclusion of flux from the bulk of the superconductor. Within the surface layer, the flux is not completely cancelled but at the depths greater than λ there is zero field. If a magnetic field ($H<H_C$) is applied when $T> T_C$ and then the material is cooled into its superconducting state, the flux originally penetrating the material is expelled. This phenomenon is called the Meissner Effect [2-3].

In the description of superconductors, one of the characteristic lengths is called the coherence length (ξ) which is the minimum spatial extent of a transition layer between a normal and superconducting region in a material. In fact, superconducting electron density can not change quickly, and there is a minimum length over which a given change can be made at the normal/superconductor interface. This distance is sensitive to the presence of alloying

[1] A substantial part of this chapter has been published as a review paper: "Structural parameters affecting superconductivity in iron-chalcogenides", T. Mousavi, C.R.M. Grovenor, S.C. Speller, *Materials Science and Technology*, 30(15) (2014) 1929-1943.

elements, and in alloyed materials, ξ is shorter than the intrinsic coherence length for the pure material [4].

Superconductors can be classified into two types (type I and type II) depending on the type of transition to the normal state when a magnetic field is applied. As shown in Figure 2.1, type I superconductors exhibit complete flux expulsion below H_C and the material displays perfect diamagnetism. Above H_C, magnetic flux penetrates and superconductivity is destroyed.

In type II superconductors, there are two critical fields H_{Cl} and H_{C2}. This type of superconductor exhibits perfect diamagnetism up to H_{Cl} at which point the flux partly penetrates the material and the material enters the "vortex state" composing of non-superconducting cores surrounded by superconducting regions. At the upper critical field H_{C2} the flux penetrates completely and the superconducting state is destroyed. Pure metals tend to be type I superconductors while alloys and the high temperature ceramic superconductors are type II [2,4].

As the critical fields for type I superconductors are generally low and not useful for many applications, type II superconductors are of more significance for practical applications. However in order for a type II superconductor to remain superconducting above H_{C1} (operating field), pinning sites are required to prevent the migration of the flux lines. The pinning sites need to be in similar size to the diameter of the flux lines, which are on the same scale as the coherence lengths. Pinning sites are typically microstructural features such as dislocations, secondary phases, grain boundaries and voids which interact with the flux lines and restrict their movement. In conventional superconductors, i.e. alloys and intermediate compounds, with relatively large coherence lengths (ξ~100nm), secondary phases, grain boundaries and regions of high dislocation densities can act as pinning sites although particular emphasis has been placed on the role of the grain boundaries [1-3].

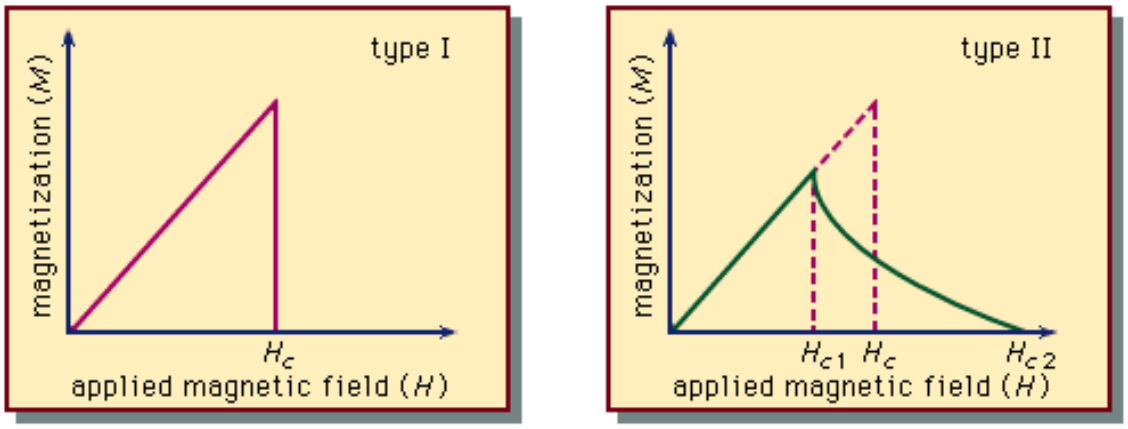

Figure 2.1: Magnetisation versus applied magnetic field for type I and II superconductors [2].

2.2 A brief history of superconductivity

Superconductivity was first discovered in mercury in 1911 by Kamerlingh Onnes [3]. Since then, it has been found that many elements, alloys and ceramics show superconducting properties below well-defined critical temperatures (T_C) [1, 4]. Figure 2.2 shows the timeline of the discovery of important superconductors, with their T_C values. One of the most remarkable discoveries in these superconductor families is the copper oxide-based superconductors as they operate at higher temperatures than conventional metallic superconductors, and thus may be operated with lower cooling costs [5]. Comprehensive details on the properties and mechanisms of superconductivity can be found in Lee's book entitled "Engineering Superconductivity"[1] and Schrieffer's book entitled "Theory of Superconductivity"[4].

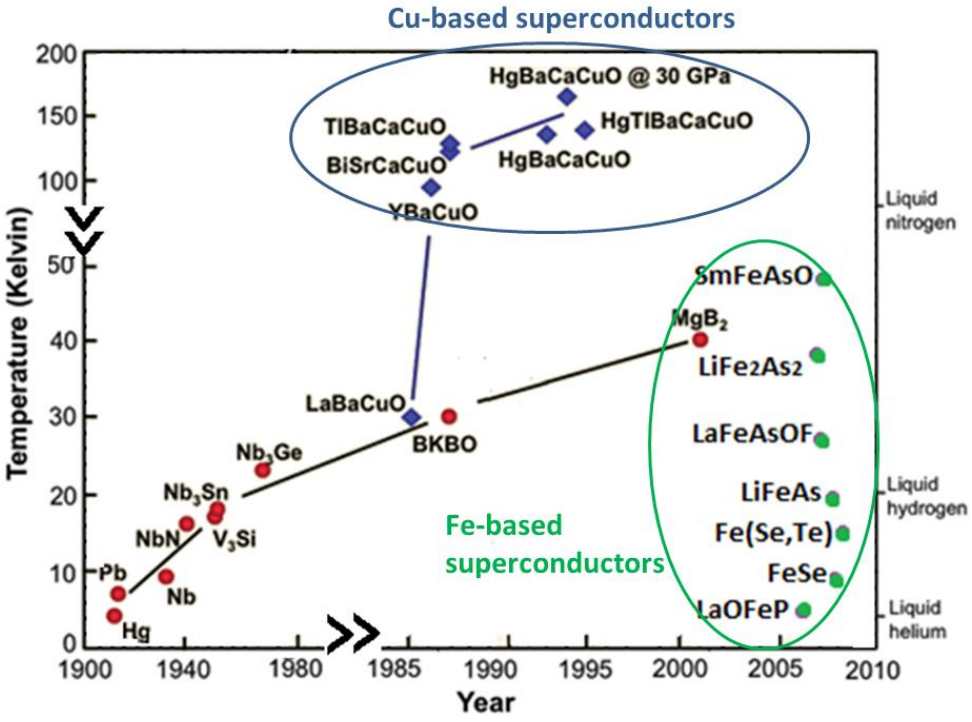

Figure 2.2: The timeline of the discovery of superconducting families.

2.3 Fe-based superconductors

Since the discovery of high T_C values in layered Cu-based oxides, there have been extensive efforts to explore new compounds containing transition metal ions other than copper, with the hope of achieving higher T_C, because the high T_C values of the copper oxides are believed to be related to the strong electron correlation associated with transition metal ions. Moreover, researchers have mostly focused on layered structures due to the freedom they offer in controlling the carrier density in the transition metal oxide layers [5-7]. These efforts have led to the discovery of several novel superconductors, such as Sr_2RuO_4 [8], KOs_2O_6 [9], $Na_xCoO_2/1.3H_2O$ [10] and $LnFe_4P_{12}$ (Ln=Y,La) [11, 12]. But the most surprising discovery was the family of Fe-based superconductors in 2008 because they contradicted conventional thinking that a magnetic material could never coexist with a superconductor. This unknown phenomenon was a sign of a new mechanism of superconductivity which is believed to be different from that in the Cu-based superconductors, and offers the hope of achieving new

superconducting properties[13]. In addition, these new materials also have very high values of upper critical field (H_{C2}) compared to other superconductors, which makes them attractive for high-field applications such as magnetic energy storage [14]. Figure 2.3 shows T_C, H_{C2}, and J_C values plotted for different families of superconducting materials. Although Cu-based superconductors can have higher values of all three of these parameters, they also show high anisotropy and brittle mechanical properties which have limited their application. Fe-based superconductors have high upper critical fields, high irreversibility fields, low anisotropy with $H_{C2}(0)$ approaching 50 T [15], and better mechanical properties, which are all important for high-field applications [13, 16].

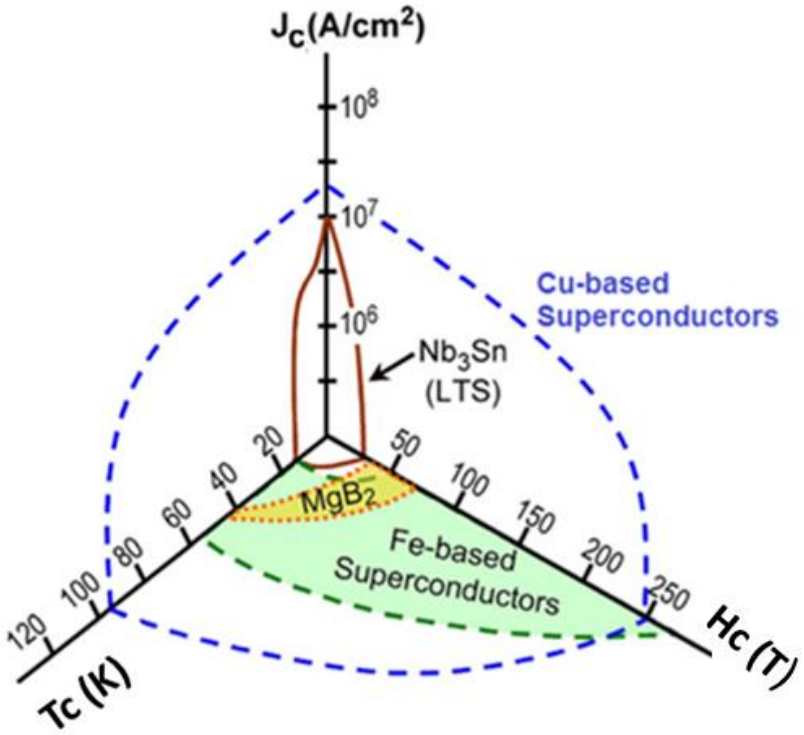

Figure 2.3: Critical parameters, T_C, H_C and J_C of Fe-based superconductors compared to other well-known superconductors [14].

2.4 Classification of Fe-based superconductors

Fe-based superconductors are classified into two families (see Figure 2.4), Fe-pnictides, compounds containing iron and a pnictogen (an element from group-V of the periodic table,

especially phosphorus and arsenic), and Fe-chalcogenides, compounds containing iron and a chalcogen (an element from group-VI, especially Se and Te).

The earliest discovered members of the Fe-pnictides, iron-oxypnictides, have alternating layers of iron-pnictides and rare earth oxides. They have the general formula of ReOFePn, where Re denotes a rare earth element and Pn a pnictogen [17], [18-20]. Known as the "1111" phase owing to the stoichiometry of the four components, this group also has a high non-cuprate T_C value for $Sm[O_{1-x}F_x]FeAs$, (T_C=55K) [18]. Subsequently, two other families of iron pnictides with no oxygen in their structure, $AeFe_2Pn_2$ (Ae=alkaline-earth metal) known as "122" [21] and AFePn (A=Li, Na) known as "111" [22] were discovered. The most recently discovered compounds of this family are Fe-chalcogenides, known as the "11" phase. In addition to Fe, they contain at least one chalcogen. Although all of the group 6 elements are defined as chalcogens, the term is more commonly reserved for suphides (FeS), Selenides (FeSe), and tellurides (FeTe), rather than oxides [23],[24]. All of these three Fe-chalcognides have the anti-PbO-type crystal structure. With decreasing ionic radius of the chalcogen, the PbO structure tends to become unstable. Thus, among these three compounds, FeTe is the most stable phase and can easily be synthesized by conventional solid-state reaction methods.

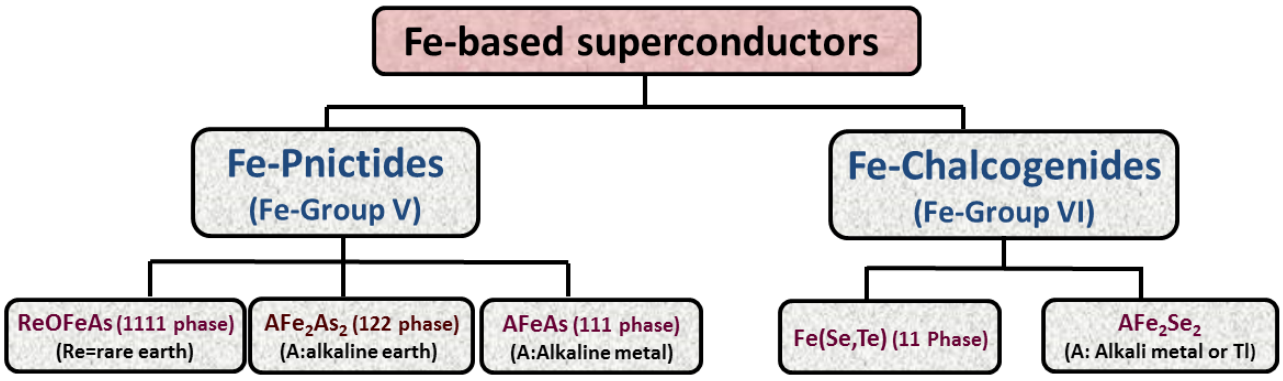

Figure 2.4: Classifications of Fe-based superconductors.

2.5 Advantages of iron chalcogenides (11-phase)

Iron selenide, FeSe, was discovered as a superconductor by Hsu et al. in 2008 with a T_C of 8K [24]. The crystal structure of FeSe is the anti-PbO-type structure (space group: P4/nmm) composed of stacked Fe_2Se_2 layers which are responsible for superconductivity. The Fe_2Se_2 layers are tetrahedrally co-ordinated and are analogous to the Fe_2As_2 layers in iron pnictide and oxypnictide superconductors. In fact, Fe-based superconductors share a common layered structure and two-dimensional physical properties (as can be seen in Figure 2.5), but FeSe has the advantage of being the simplest structure among all of these compounds with no atoms occupying the van der Waals gap [25]. By growing monolayer FeSe on $SrTiO_3$(001) surface, the highest T_C of Fe-based superconductors (T_C=~65-70K) has been recently obtained [26].

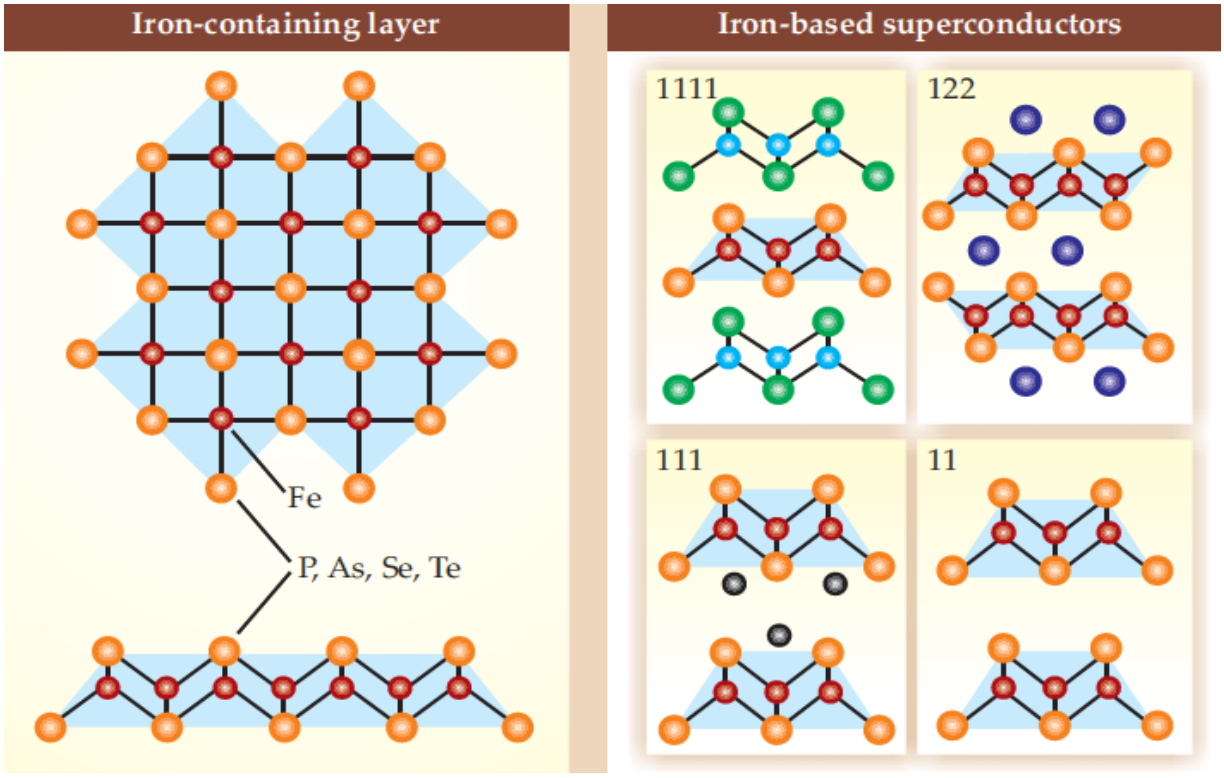

Figure 2.5: The layered structure of ReOFePn (refered as 1111), AFe_2Pn_2 (122), AFePn (111) and FeSe (11) superconductors [27].

Furthermore, theoretical studies show that there are similarities in the electronic states of Fe-chalcogenides (FeS, FeSe and FeTe) and the Fe-pnictides [28, 29]. Therefore the study of FeSe can be useful to understand the fundamental physics underlying superconductivity in Fe-based superconductors with more complicated structures including interleaved ions or insulating layers between the FeSe slabs which may affect electronic and structural properties.

Besides their complex crystal structures, Fe-pnictides suffer from inherent difficulty in synthesis of the superconducting phase, especially the loss of volatile elements during high temperature processing [30-32]. Moreover, they are problematic due to the toxicity of arsenic which usually constitutes the pnictogen part of the structure. To overcome these limitations, FeSe is of great interest because it has simple structure and can be easily processed [24, 25].

It is also notable that the characteristic layered structure and superconductivity induced by carrier doping in FeSe are similar to the key features of superconductivity in the Cu-based materials with Cu-O superconducting layers. Therefore, comparing the physical properties of Fe-based superconductors with those of Cu-based superconductors might provide a suitable alternative to study the mysteries of high-T_C superconductivity in the Cu-based materials.

Because of these interesting and unique features, FeSe is an attractive material to elucidate the key parameters controlling superconducting properties in these families of layered superconductors.

2.6 Phase diagrams

The binary phase diagram of Fe–Se (Figure 2.6) shows several equilibrium phases of different compositions and temperatures. These include [33]:

(i) a PbO-type tetragonal β-phase with a narrow stability range (from $Fe_{1.01}Se$ to $Fe_{1.04}Se$) which appears below 450°C.

(ii) NiAs type hexagonal δ-phase which is stable at high temperature.

(iii) a NiAs type hexagonal phase (Fe_7Se_8) with a wider existence range which transforms to a tetragonal phase at about 150°C.

(iv) a $FeSe_2$ phase with the orthorhombic marcasite structure.

Among all of these, only the β-phase with just below 50 at.% Se (45 to 49.4 at.% Se or $Fe_{1.01}Se$-$Fe_{1.04}Se$) exhibits superconductivity. The first experiments on β-$Fe_{1+\delta}Se$ indicated a T_C of 8K [24] and attributed superconductivity to a selenium-deficient phase. McQueen et al. found that the superconducting properties strongly depend on small variations in Fe content, with the highest T_C of 9 K for the compound $Fe_{1.01}Se$. Increasing the Fe content leads to a drastic decrease of T_C which falls to 5 K for β-$Fe_{1.02}Se$, and superconductivity is completely suppressed for β-$Fe_{1.03}Se$ [25].

Figure 2.7 shows this extreme dependency of T_C on stoichiometry. Therefore a small Se deficiency is necessary for the occurrence of superconductivity. A change from Se vacancies at low Fe excess to Fe interstitials at high Fe excess has been reported [34]. Moreover, fabrication of pure β-FeSe using high temperature methods has been found to be difficult because δ-FeSe appears as an impurity phase if the processing temperature exceeds about 400°C [24].

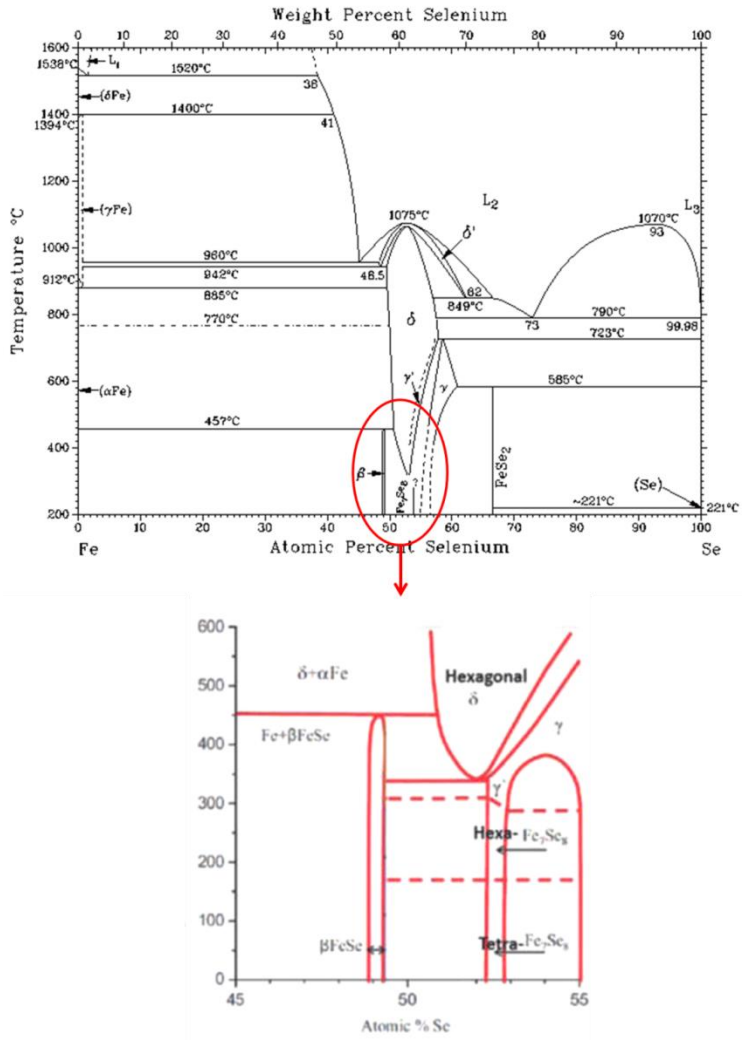

Figure 2.6: Fe-Se binary phase diagram[33].

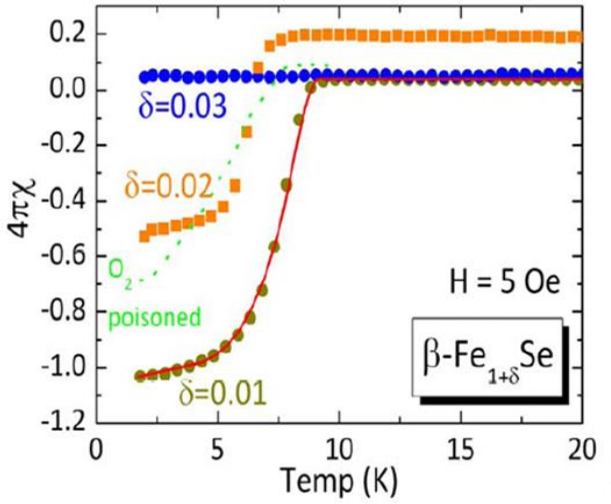

Figure 2.7: Low field susceptibility of β-$Fe_{1+\delta}Se$ in different stoichiometries showing the high sensitivity of T_C to composition. The highest T_C of 8.5 K is found in $Fe_{1.01}Se$ [25].

2.7 Chemical substitution in FeSe

Iron-chalcogenides have shown a large value of the pressure derivative of T_C, (dT_C/dP=9.1 K/GPa [35]) which will be explained later. This strong pressure-dependence of T_C is a good indication that higher T_C values might be achieved by chemical means, via doping of smaller atom sizes and different valences. The optimum doped level is suggested to correspond to the density of states at the maximum T_C under high pressure [36][13, 18]. However, it is not clear how separate the effects of external pressure and chemical substitution are because in chemical substitution in addition to altering the lattice parameters, the atoms are also different leading unavoidably to changes in the electronic band structure and density of states at the Fermi level through the addition of holes or electrons. If a proper concentration of a suitable element is chosen, chemical substitution can modify the electronic band structure and the density of states at the Fermi level through both carrier concentration changes and changes to the lattice parameters [37].

Chemical substitutions in FeSe can be on both the Se and Fe sites, and many systems in which either Fe or Se are partially substituted by other elements have been studied. The literature shows that the substitution for Fe is generally disadvantageous for superconductivity, or at least shows a complicated dependence, while isoelectronic substitution for Se can increase T_C values.

2.7.1 Substitution on the Fe site

Since Fe plays a significant role in the occurrence of superconductivity in Fe-chalcogenides, it is interesting to study doping other elements on this site. Fe has been substituted by nonmagnetic 3^+ ions (Al, Ga and In), nonmagnetic 2^+ ions (Ba), transition metals (Ti, V, Cr, Mn, Co, Ni and Cu) and magnetic rare-earths (Sm). Transition metals, especially those with unpaired 3d electrons such as Co, Mn, Cu and Ni, can be of more interest due to the potential to study the interplay between magnetism and superconductivity which might also lead to better

insight into the origin of superconductivity in this family of materials. For substitution by group III elements, the results show that the change in T_C depends on the size of the substituting ions. T_C is lower for smaller ions such as Al and Ga, while 10% substitution by larger Sm and Ba ions slightly increases $T_{C(onset)}$ compared to undoped FeSe. Further Sm substitution decreases T_C. These results together suggest that superconductivity in FeSe is strongly related to the structural deformation of the unit cell rather than the magnetism of the substituted ions [38]. Substitution by Ti, V, and Cr completely suppresses superconductivity, while Mn substitution does not affect the superconducting properties but slightly increases the normal state resistivity.

2.7.2 Te substitution for Se ($FeSe_{1-x}Te_x$)

In 2008, soon after the discovery of FeSe as a superconductor, it was shown that T_C increases remarkably if Se is substituted by Te [39]. Yeh et al studied superconductivity in $FeSe_{1-x}Te_x$ (where x=0-1) and obtained a maximum T_C of 15.2K at 50% Te substitution [39]. The T_C increases without any change in carrier concentration when Se^{2-} is replaced by Te^{2-} [40]. This T_C enhancement is correlated with the structural deformation resulting from Te doping. Te substitution for Se also substantially increases the upper critical field [41]. When FeSe is 70% Te-doped, $H_{C2}(0)$ increases from 16.3T (for FeSe) to 96.9T [24].

Another effect of Te substitution is the stabilization of the crystalline structure (PbO-tetragonal) which is crucial for the occurrence of superconductivity in this system. For example, tetragonal $Fe_{1+y}Te$ is stabilized over a composition range y=0.06–0.17 [42], whereas the tetragonal structure in $Fe_{1+x}Se$ is stabilized over a much narrower composition range of x=0.01–0.025, and is extremely sensitive to the synthesis conditions as discussed above [25]. A solid solution of tetragonal $FeTe_{1-x}Se_x$ can be formed over $0 \leq x \leq 0.5$ with a maximum T_C(~15 K)[43, 44].

2.8 Thin films of superconducting Fe(Se,Te)

Fe-chalcogenide superconductors are advantageous for the fabrication of both thin films and superconducting wires compared to other high temperature superconductors because they are alloys with a relatively simple chemistry. Superconducting thin films are promising for use in electronic and power electric applications as well as for the fundamental study of superconducting properties [45]. For the 11-phase, in particular, thin films are of interest because they exhibit significantly higher superconducting transition temperatures than those of bulk polycrystalline samples and single crystals over the entire doping regime [46-50].

Thin films of 11-phase have been widely studied in the literature in an attempt to understand how superconductivity is linked with other parameters such as stoichiometry, structural parameters and strain. Many of these studies, however, found different results and, in some cases the effects of these parameters and the optimum values for the highest T_C are contradictory. A review of these studies is presented in the following section. One of the main aims of this thesis is to study influential parameters for superconductivity in 11-phase thin films with more emphasis on the microstructural parameters.

2.9 Effective parameters controlling superconductivity in 11-phase thin films

Superconducting properties of Fe(Se,Te) thin films are, in general, controlled by two main parameters; (i) chemistry and structural parameters which influence intrinsic properties such as T_C, (ii) microstructure (such as grain boundaries and impurities) which control extrinsic properties such as J_C. In order to improve superconducting properties, both the chemistry and microstructure have to be well controlled.

T_C of the 11-phase has been correlated with a structural transition at low temperature (~70-80K) [38, 39, 51-53]. This transition is from the tetragonal structure to one of the monoclinic,

triclinic or orthorhombic structures depending on the composition, form of sample (thin film or single crystal) and strain. In the cases where monoclinic or triclinic structures have been observed at low temperature, T_C is related to the monoclinic/triclinic angle [38, 39, 51-53]. Any parameter influencing this low temperature structural transition is important for superconductivity in Fe(Se,Te). These parameters are as follows.

2.9.1 Structural parameters

Lattice parameters (bond lengths and angles) are strongly linked with superconductivity of the 11-phase. β-FeSe has the PbO-tetragonal crystal structure shown in Figure 2.8. The four Se atoms are located above and below the Fe plane at a height of $h=zc$, and form a tetrahedron characterized by an Fe-Se bond length of $(\frac{a^2}{4} + z^2c^2)^{1/2}$, an Se-Fe-Se bond angle of $\alpha = 2tan^{-1}(\frac{a}{2zc})$, an Se-Se interlayer separation in the c direction of $c_{Se-Se} = c(1-2z)$, and an Se-Se distance of $d_{Se-Se} = (\frac{a^2}{2} + c_{Se-Se}^2)^{1/2}$ [54].

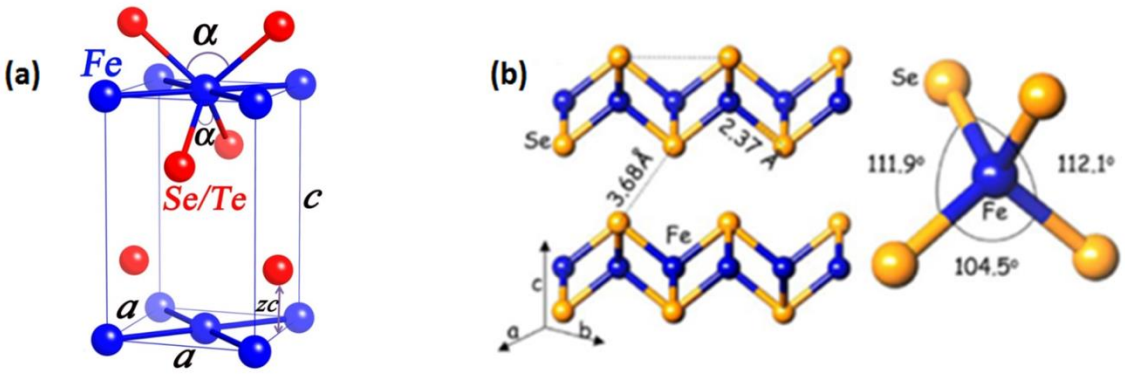

Figure 2.8: (a) Structure of FeSe with lattice parameters *a* and *c*, Se position or anion height from the Fe layer *zc* and bond angle *α* [54], (b) The values of these parameters in standard conditions [55].

A link between the *c/a* ratio and T_C was first reported by Mizuguchi et al, with the highest T_C for a *c/a* ratio just above 1.464 [56]. However, soon after it was shown by both theoretical and

experimental studies that the anion height above the Fe layer (*zc* in Figure 2.8), which correlates with Se-Fe-Se bond angle, is the main parameter affecting the T_C value [57]. Figure 2.9 shows the anion height dependence of T_C for a range of Fe-based superconductors, showing a symmetric curve with a peak around 1.38 Å. Surprisingly, the data points for binary FeSe follow this unique curve under high pressure indicating that T_C can be increased by the application of pressures above 2Gpa [52].

From the concept that the T_C of the Fe-based superconductor strongly depends on the anion height, disorder at the anion site which usually happens in substitution on the Se sites should strongly affect the superconducting properties. One of the obvious differences between the structures of FeSe and $Fe(Se_{1-x}Te_x)$ is disorder at the anion site when Te is substituted for Se, since the anion height of Te is significantly different from the anion height of Se. High-resolution x-ray single crystal diffraction for $FeTe_{0.56}Se_{0.44}$ indicates chalcogen heights of 1.478 Å and 1.718 Å for Se and Te respectively. As a result, the Fe-Se bond is shorter by 0.154Å than the Fe-Te bonds, and three independent (Te,Se)-Fe-(Te,Se) bond angles occur [58]. This disorder lowers the local symmetry of the iron atoms by splitting the Fe-Ch bond lengths in Fe(Se,Te) compounds and strongly affects the superconducting properties.

This inhomogeneity in the Te distribution has been shown by microstructural analysis of Fe(Se,Te) single crystals. These crystals exhibit significant chemical and structural inhomogeneity, specially in the Te-rich end of the phase diagram where superconductivity and magnetic order are found to co-exist [59]. Figure 2.10 shows local structural variations in $Fe_ySe_{0.25}Te_{0.75}$ single crystals with different Fe contents using the high resolution electron backscatter diffraction (HR-EBSD) technique. Local variation in unit cell and anisotropy across these samples can be clearly seen [59].

The fact that T_C increases up to 14K for 50% Te substitution despite the significant Se/Te disorder shows the potential of this group of superconductors to achieve higher T_C value.

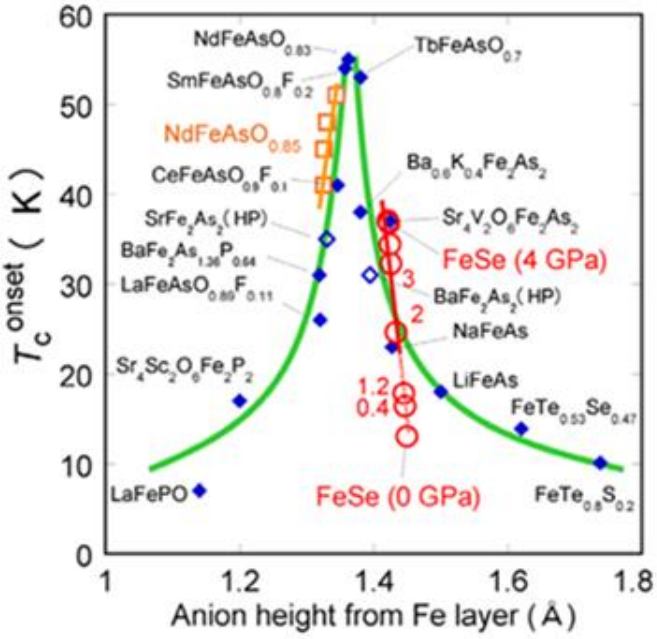

Figure 2.9: The relation between anion height and T_C for Fe-based superconductors [56].

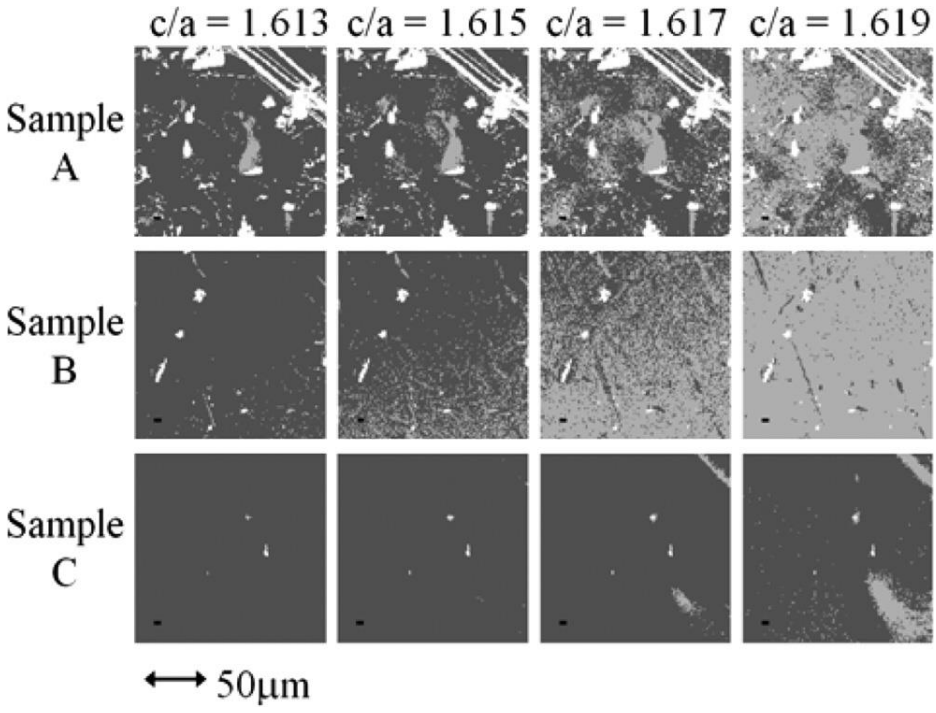

Figure 2.10: HR-EBSD maps of $Fe_ySe_{0.25}Te_{0.75}$ single crystals; A (y=0.95), sample B (y=1.03) and sample C (y=1.07). Light grey indicates regions with c/a ratio below the threshold value for superconductivity and dark grey indicates regions with c/a ratio above the threshold [59].

2.9.2 Chemical composition

Chemical composition is one of the most significant parameters for the occurrence of superconductivity in iron chalcogenides. As was shown earlier, a small Se deficiency is needed for $Fe_y(Se_{1-x}Te_x)$ to be a superconductor. In $Fe_y(Se_{1-x}Te_x)$ in addition to the stoichiometry of Fe (y) which is crucial for the occurrence of superconductivity, the ratio of Se/Te is also important to increase the value of T_C [43, 56]. Figure 2.11 shows how Te content changes the value of T_C by changing the structural parameters.

This relation has been reported differently in some reports of thin films compared to results from single crystals. For example Sales et al [44] found that the c/a ratio decreases monotonically with increasing Te and Fe content, while in thin films grown by sputtering [48] this trend has not been observed. Clearly, the strain induced in thin films can change this dependency of structural parameters on composition.

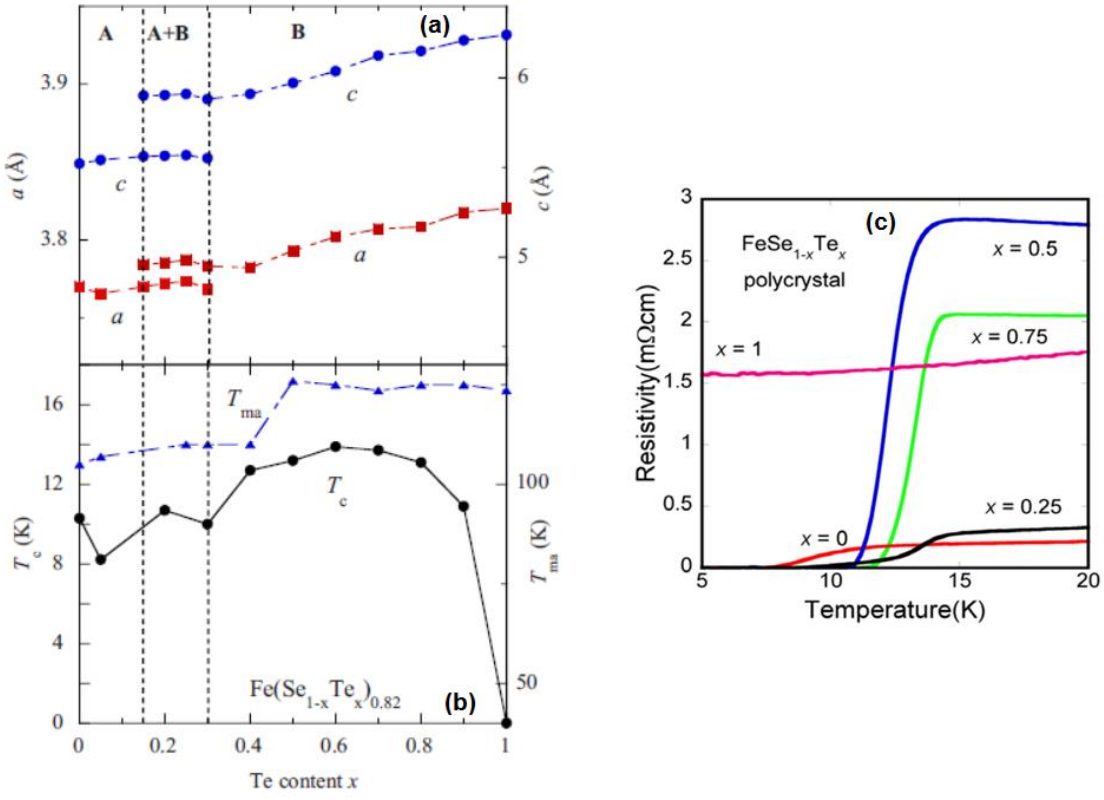

Figure 2.11: The effect of Te content on (a) lattice parameters [43], (b) magnetic anomaly temperature T_{ma}, and T_C [43] (c) resistivity of $Fe_y(Se_{1-x}Te_x)$ [56].

Similar to FeSe, $FeSe_{1-x}Te_x$ shows a structural transition from tetragonal (P4/nmm) to orthorhombic (Cmma) space groups. This structural transition is suppressed with increasing Te concentration [60]. Mizuguchi et al. have established a phase diagram for mixed phase $Fe_{1+d}Te_{1-x}Se_x$ by combining both experimental results and theoretical data. The highest T_C appears in the tetragonal phase near x=0.5. When the Te content is increased, the tetragonal-orthorhombic structural transition is suppressed, the T_C decreases and antiferromagnetic ordering accompanying the tetragonal-monoclinic distortion appears [56].

2.9.3 Pressure

A strong pressure dependence of T_C has been seen in iron-based superconductor bulks. Applying pressure initially enhances T_C to an optimum value and then decreases it with further pressure [55, 61]. The 11-phase shows the most significant pressure dependence of T_C among the Fe chalcogenides. The $T_{C(onset)}$ of FeSe at ambient pressure is 13K whilst it dramatically increases to 27K at 1.48 GPa (see Figure 2.12). With applying further hydrostatic pressure up to 4 GPa, T_C reaches 37K [62] then decreases to 6 K at 14 GPa [55].

The reason for achieving higher T_C under pressure has been reported to be the stabilization of the low-temperature orthorhombic structure at high pressures [63]. Moreover, it is clear that pressure alters the lattice constants through bond lengths and angles (as shown in Figure 2.13) that inevitably affect the electronic and magnetic correlations and the carrier density of states [37]. It was soon noted that this pressure sensitivity was direction dependent [64].

When Se is substituted by Te, T_C becomes even more pressure-dependent. The pressure sensitivity in $Fe(Se_{0.5}Te_{0.5})$ has been reported to be ten times greater than that in FeSe [39]. For $FeTe_{1-x}Se_x$, the data point at ambient pressure is located near the anion height curve (Figure 2.9), but in contrast to FeSe, the anion height does not follow the master curve at high pressure [56].

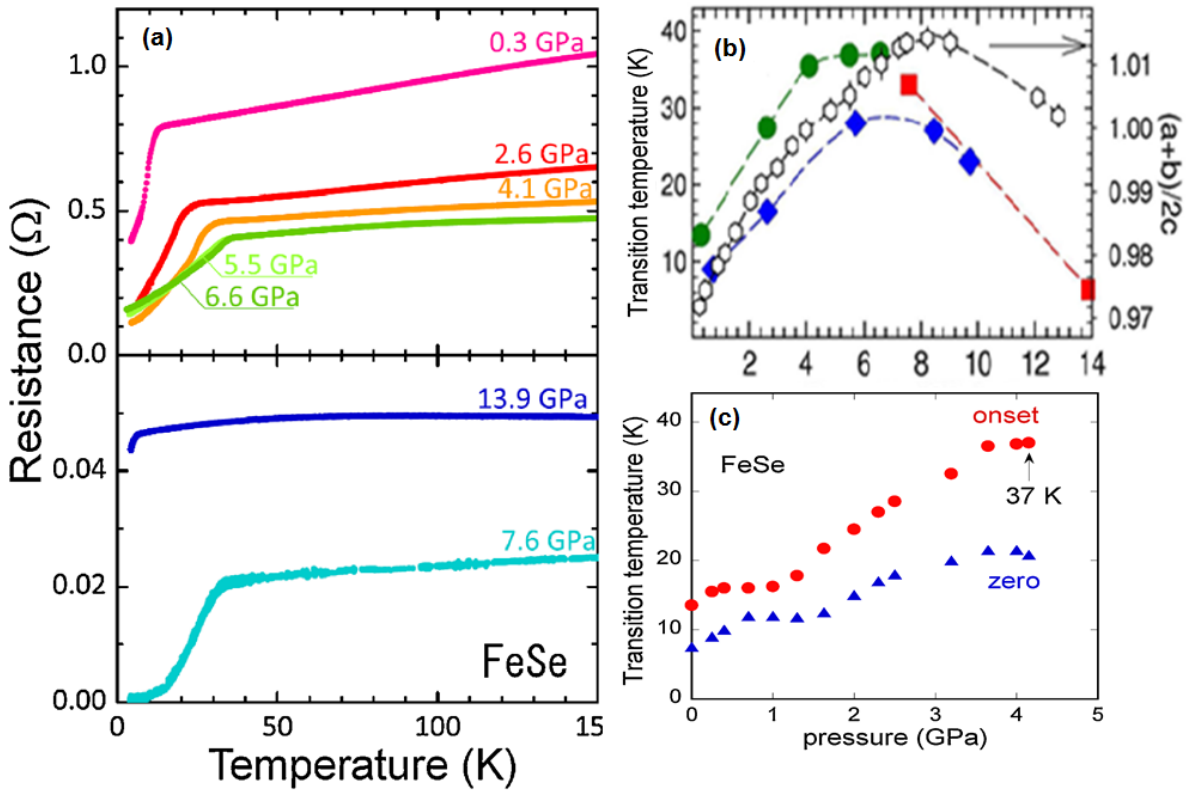

Figure 2.12: (a) Pressure dependence of T_C for FeSe compound (b) The dome-shaped pressure dependence of T_C in FeSe [55] (c) The increase of T_C to 37K at 4 GPa [56].

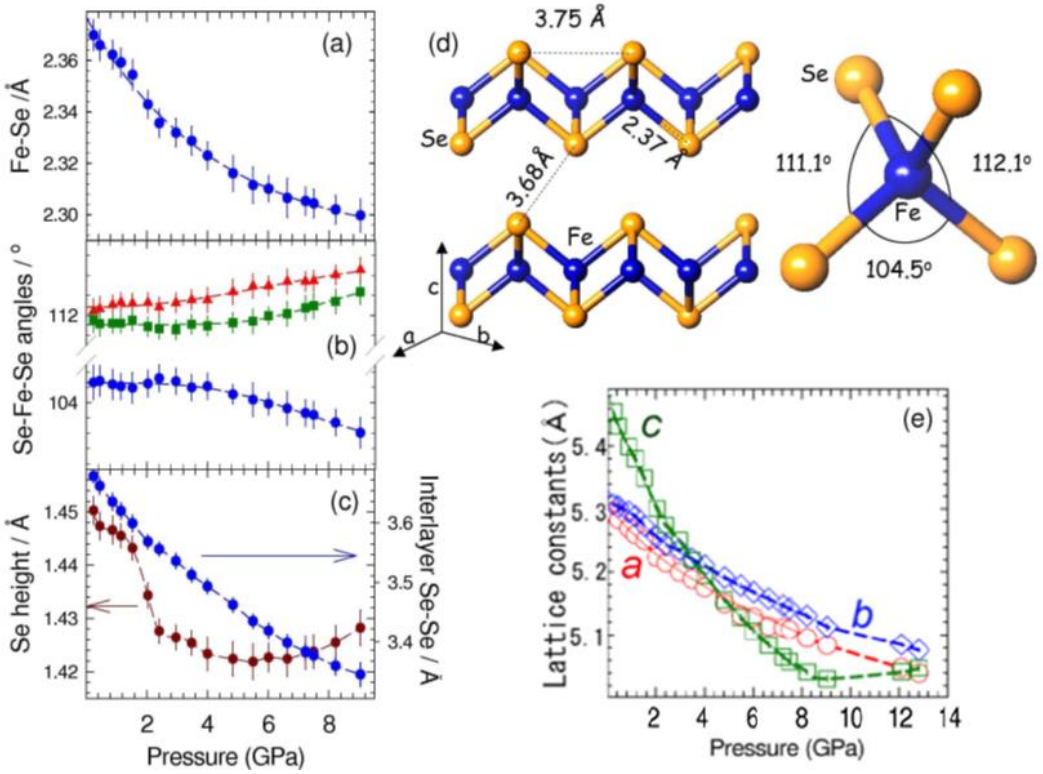

Figure 2.13: Structural parameters of FeSe under high pressure: (a) Fe-Se distance, (b) Se-Fe-Se angle, (c) Se height from Fe layer, (d) schematic diagram of atoms under 0.25 GPa, (e) lattice parameters *a*, *b* and *c* [55].

2.9.4 Strain

Strain, either compressive or tensile, changes the lattice structure and hence affects superconducting properties. The effect of compressive strain is similar to the case when the material is subjected to hydrostatic pressure and, as discussed above, increases the T_C value [65-67]. Thin films of the 11-phase are of great interest because this compressive strain can be achieved by the epitaxial growth of thin films [68]. In this case, in-plane tensile stain usually leads to a decrease/compressive strain in the c-axis. The strain in the film is affected by processing temperature, growth mechanism, film thickness and lattice mismatch with the substrate [69].

FeSe films under tensile strain in the c-axis have not shown superconductivity down to 5K, which implies that tensile strain suppresses superconductivity [65]. In contrast, epitaxial FeSe films grown on CaF_2 are compressed along the a-axis and show a T_C of 11.4K [70]. A high value of T_C=21K, significantly larger than the bulk value, has been obtained in the epitaxial $FeSe_{0.5}Te_{0.5}$ thin films which are compressed along the c-axis [68].

2.9.5 Substrate choice

In order to grow high quality superconducting thin films, a suitable single crystal substrate with a uniform and flat surface has to be chosen that is compatible with the thin film material in lattice parameter, thermal expansion coefficient and chemical reaction [71]. Lack of any of these can lead to structural defects or grain boundaries which are likely to be detrimental for superconductivity.

The most common substrates which have been used for deposition of superconducting $Fe_y(Se_xTe_{1-x})$ films are $SrTiO_3$, $LaAlO_3$, LSAT (which is a mixed-perovskite of $LaAlO_3$ and Sr_2AlTaO_6), Al_2O_3, MgO and CaF_2. Imai et al. have investigated the crystal structure and superconducting properties of $FeSe_{0.5}Te_{0.5}$ thin films grown on eight different substrates by pulsed laser deposition [49]. They found that the $FeSe_{1-x}Te_x$ films intrinsically favour two-

dimensional growth as a strong c-axis orientation was observed even in the films prepared on the (0001) plane of hexagonal Al_2O_3 [49] where there is no structural match with the tetragonal superconducting phase. It has been also shown that thin films on different substrates have different in-plane alignment regardless of lattice matching [48, 49]. The study by Yeh et al, where epitaxial thin films were used to measure the effects of biaxial stress on the superconducting properties [39] (along with many others [72],[29],[73]) also show that this superconducting phase is not strongly affected by lattice mismatch with the substrate. The presence of an amorphous-like layer between the substrate and films has been observed in some cases (LSAO and YSZ substrates) as shown in Figure 2.14 [49],[74, 75]. The nature of this interface layer is not known yet and needs more study.

Different structural defects and critical current density values are also observed in $Fe_y(Se_xTe_{1-x})$ films grown on different substrates. Baccini et al reported the presence of defects looking like lattice disorder at a very small scale (5-20 nm) and a high critical current density value in Fe(Se,Te) films grown on CaF_2 [76], while in films grown on $SrTiO_3$ columnar defects parallel to the c-axis were observed (see Figure 2.15).

An oxygen penetration from the substrate into the film has been observed for films grown on some oxide substrates [74]. Due to suppression of superconductivity in the presence of oxygen, Tsukada et al reported CaF_2 substrate as a good choice compared to oxide substrates for growing Fe(Se,Te) films [77]. Moreover, using suitable buffer layers between the substrate and the film can also prevent undesirable reactions between the superconductor and the substrate, and lead to an improvement in the superconducting performance of the films [46, 47]. Iida et al obtained a T_C value of 17K by using Fe-buffered MgO substrates [46], and Si et al found high critical current density up to $10^5 Acm^{-2}$ in $FeSe_{0.5}Te_{0.5}$ thin films grown on CeO_2 buffer layers [47]. All of these reports indicate the significant role of substrate for growing high quality Fe(Se,Te) thin films with improved superconducting properties.

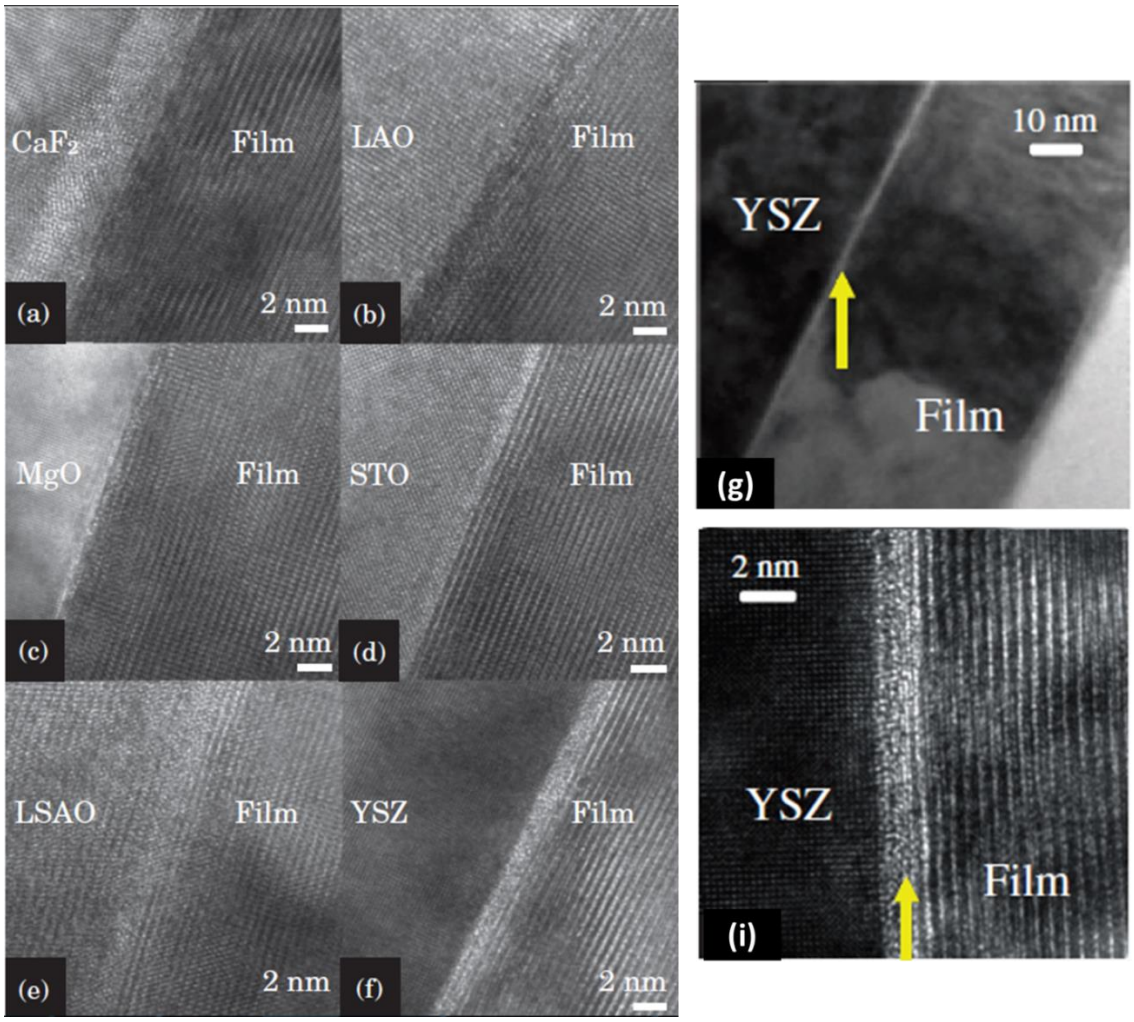

Figure 2.14: High-magnification TEM cross-sectional images of Fe(Se,Te) thin films growth on (a) CaF_2 (100), (b)LAO (100), (c) MgO (100), (d)STO (100), (e)LSAO (001) [74], (f-h) YSZ (100) [49].

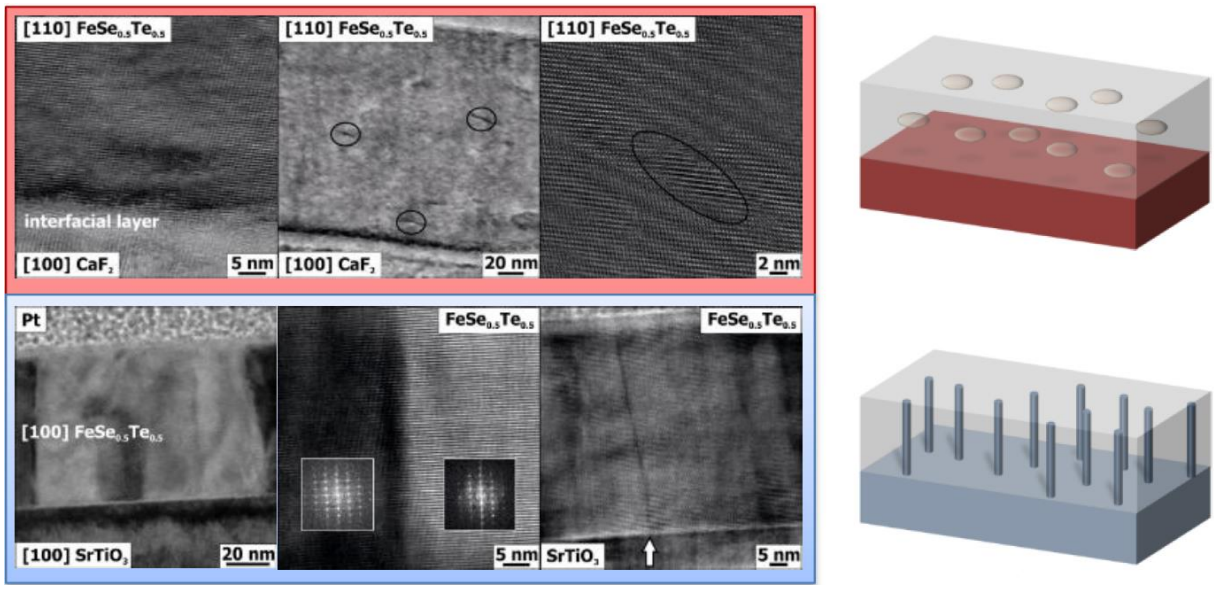

Figure 2.15: Fe(Se,Te) thin films grown on (a) CaF_2 and (b) $SrTiO_3$ with different types of defects. The sketches of the defect are observed on the right side. It is point defects for the film grown on CaF_2 and nanorods parallel to the c-axis for the film grown on $SrTiO_3$ [76].

2.9.6 Substrate temperature

The substrate temperature is important for the growth of the 11-phase thin films because the epitaxy of the film is known to be strongly controlled by temperature [54]. It appears that the most successful films have been grown at 350-550°C. Huang et al. reported differences in electrical properties between films grown above and below 400°C [54]. Above 400°C, non-superconducting hexagonal δ-FeSe phase has been detected as impurity [78]. Examination of the films using x-ray diffraction shows that their crystallinity is poor at 300°C and below which gives a lower limit for in-situ film processing [54]. However, the effect of temperature on the crystallographical alignment of the film has not been studied. This is one of the issues which will be investigated in this thesis.

There is also another limit for the substrate temperature in sputtering which is related to the tellurium yield (the ratio between the average at.% of an element in the film compared to the target) [48]. The yield of Te has been found to decrease with increasing substrate temperatures above 300–325°C in the thin film growth of V_2VI_3 compounds such as Bi_2Te_3 [79],[80]. This trend has also been observed in the growth of Fe(Se,Te) thin films by sputtering [48]. The decrease in Te content is attributed to the strongly temperature dependent sticking factor of Te atoms arriving on the substrate surface and preferential re-sputtering [81],[79],[80].

2.9.7 Thickness of the films

As mentioned earlier, the 11-phase exhibits higher T_C under pressure, which can be applied both by chemical substitution and epitaxial compressive strains in films grown on the substrates with different lattice parameters. One of the important parameter controlling strain induced in the epitaxial films is thickness [68][53, 82]. Bellingeri et al. grew different thicknesses of $Fe(Se_{0.5}Te_{0.5})$ films to study the effect of epitaxial strain on the superconductivity [68]. They found that the films grew by a Volmer–Weber growth mechanism where a large tensile strain may be induced at the film/substrate interface. At the beginning of the growth, isolated islands

of $Fe(Se_{0.5}Te_{0.5})$ are nucleated and at a thickness of about 30 nm they start to coalesce and show the onset of the superconducting transition as shown in Figure 2.16. With further deposition, the tensile strain decreases and may even become compressive [68]. Finally, a uniform film is obtained in which the strain induced by the epitaxial growth acts as an external pressure leading a significant T_C enhancement up to 21K [68].

Regarding the effect of film thickness on T_C, Wang et al. prepared FeSe thin films on MgO substrates at 320ºC with several different thicknesses [53]. They observed a (00l) preferred orientation with strong lattice strain in the deposited films. They reported that the $T_{C(onset)}$ increases with increasing thickness, and the appearance of superconductivity seems to require film thicknesses above 140 nm [53].

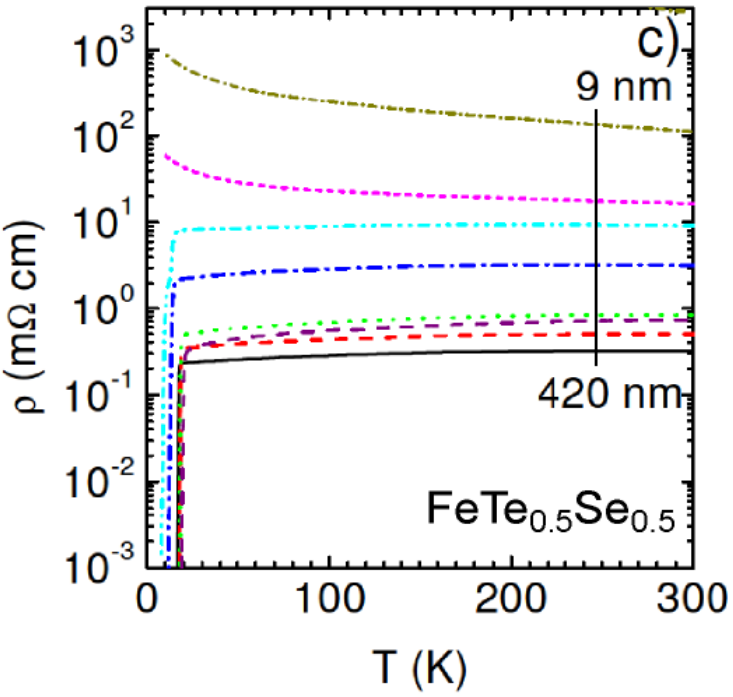

Figure 2.16: Temperature dependence of resistivity for $FeTe_{0.5}Se_{0.5}$ films with several different thicknesses [68].

2.10 Fabrication of Fe(Se,Te) thin films

The techniques for the deposition of thin films can be divided into two categories according to the method of material transport from the source to the substrate; physical vapour deposition techniques (PVD) and chemical vapour deposition techniques (CVD). In physical deposition such as laser ablation, sputtering and electron beam evaporation the target is vaporised and the vapour species transferred to the substrate. In the chemical deposition, e.g. spray pyrolysis and metal-organic CVD, metal ions are transferred to the substrate in the form of a solution or vaporised volatile compounds containing the desired ions. Reactions occur at the substrate surface in the presence of other gases to form a solid thin film on the substrate. The main advantages and disadvantages of different PVD techniques are listed in Table 2.1.

Thin films of 11-phase have been extensively grown by pulsed laser deposition [45-47],[49],[53-54]. A small number of Fe(Se,Te) films have been also deposited by molecular beam epitaxy [83] and sputtering [48]. One of the main aims of this thesis is to explore the feasibility of the sputtering technique to fabricate high quality superconducting Fe(Se,Te) thin films.

Table 2.1: Advantages and disadvantages of the main PVD deposition techniques [71].

Technique	Advantages	Disadvantages
Pulsed Laser deposition	High deposition rate Stoichiometry	Uniformity over only small areas
Sputtering	Good uniformity Inexpensive	Difficult to control the stoichiometry of the film
E-beam evaporation	Precise control on stoichiometry High deposition rate	High vacuum is needed Complex adjustment and calibration

2.11 Sputtering

Sputtering is a physical vapor deposition (PVD) method to deposit thin film by ejecting material from a target that is a source onto a substrate in the presence of a noble gas (usually Ar). Due to the electric field applied between the electrodes (target and substrate), Ar^+ ions are

formed and accelerated towards the cathode and electrons to the anode. The Ar^+ ions bombard the cathode (target) causing sputtering of the target atoms [84]. The incident particles need to be of sufficient mass for momentum transfer. Inert gases, specifically argon, are usually employed as the sputtering gas because they tend not to react with the target material or combine with any process gases and because they produce higher deposition rates due to their high molecular weight. The ejected atoms from the target move to the substrate and may then stick to the surface, and depending on the substrate temperature form a crystalline or amorphous thin film [84-87].

Depending on the conductivity of the targets, the ions are formed by applying a high DC voltage for conductive targets, or radio frequency (RF) electric field for nonconductive targets in low pressure argon [69]. DC sputtering cannot be used for insulator deposition, because when the ions strike the surface, their charge will remain localized and over time the charge will build up, making it impossible to further bombard the surface. In order to prevent this, RF sputtering with an alternating current is used for insulator targets. Since electrons cannot travel through an insulator they will cause negative charging on the target, which would result in self bias. In fact this self bias is used to attract and accelerate positive ions towards the target and cause sputtering of the target. A high frequency is usually used so that the heavy ions cannot follow the switching fast enough and only electrons hit the surface to neutralize charge.

In DC sputtering high pressure is required to achieve the plasma, and this can degrade film quality. However, RF sputtering can operate at lower pressures while still sustaining the plasma [84]. In RF sputtering, plasma tends to fill the chamber as opposed to DC plasma which is confined to the cathode. As a result, plasma efficiency in RF sputtering is better since free electrons are oscillated back and forth and make more collisions. While any type of film can be RF sputtered, deposition rates are still low. Moreover, applying RF power is not so simple, and power supplies are expensive and additional circuitry is needed [69,84].

In the case of planar magnetron as shown in Figure 2.17, a magnetic field is imposed in such a way that the electrons are trapped above the target causing them to accelerate in a circle, colliding with other gas atoms. The collisions in turn cause the ionisation of further gas atoms resulting in higher ionization efficiency. This means that a lower gas pressure is needed to maintain the sputtering process.

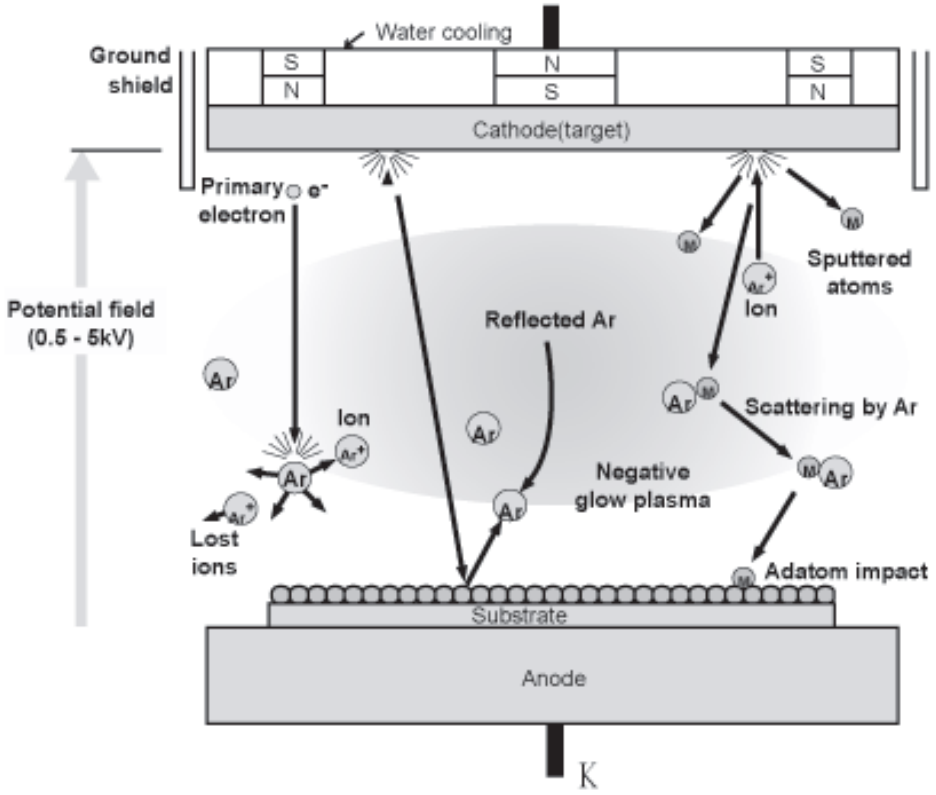

Figure 2.17: A schematic of a magnetron sputtering setup [69].

The main advantage of sputtering over the other deposition techniques is deposition of films containing elements with highly different melting points and also over a large area of the order of 50cm^2. However, the main disadvantage is the lack of stoichiometric transfer from target to substrate. This lack of stoichiometric transfer is due to re-sputtering of atoms from the substrate, evaporation from a heated substrate and different sputtering yields for different elements. Re-sputtering is re-emission of the deposited material during the deposition process

by ion or atom bombardment. A more detailed discussion on the sputtering process can be found in [69, 84].

2.11.1 Sputtering yield

The sputtering yield for element A is defined as the ratio between the average atomic percent of A in the film compared to the target:

$$\text{Sputtering yield of element A} = \frac{\text{atomic\% of A in film}}{\text{atomic\% of A in target}}$$

The sputter yield is influenced by the type of target atoms, binding energy of target atoms, relative mass of ions and atoms, incident ion energy, angle of incidence of ions and vapour pressure of the components. Therefore different elements have different sputtering yields, as listed in Table 2.2. If using a single target made up of several elements, the difference in sputtering yields of components must be carefully considered in order to achieve thin films within the desired stoichiometry. At high substrate temperatures, the vapour pressure of the components has to be also considered as another important parameter affecting the stoichiometry of the films due to re-evaporation of the atoms from the substrate surface.

Table 2.2: Sputtering yield of different elements relative to gold (assuming gold to be 1) [69].

Au	Gold	1.0	Mo	Molybdenum	0.3
Ag	Silver	1.2	Ni	Nickel	0.5
Co	Cobolt	0.5	Pd	Palladium	0.85
Cr	Chromium	0.5	Pt	Platinum	0.6
Cu	Copper	0.7	Ta	Tantalum	0.2
Fe	Iron	0.5	W	Tungsten	0.2

2.11.2 Important parameters in sputtering

The structure and properties of the deposited films are significantly changed by variations of processing parameters. In the sputtering process, these parameters include type of gas used for

the bombardment of the target, the pressure of the gas, substrate temperature, DC/AC power, position of the substrate, i.e. where the substrate is placed with respect to the target surface which might be off-axis or on-axis, using single or multiple targets, deposition of the film via an in-situ (deposition of the film onto the heated substrates) or ex-situ growth process and post annealing [69, 88]. The availability of many parameters that control sputter deposition make it a complex process, but also allow experts a large degree of control over the growth and microstructure of the film. Detailed information about the effect of these parameters on the properties of deposited films can be found in the "Handbook of Sputter Deposition Technology" [88].

2.12 Thin film growth process

In any deposition technique, formation of a thin film takes place via nucleation and growth processes. Depending on these two steps, there are different growth modes by which the microstructure of the deposited film can be controlled.

2.12.1 Nucleation

The unit species, on impacting the substrate, lose their velocity component normal to the substrate (provided the incident energy is not too high) and are physically adsorbed on the substrate surface. The adsorbed species are not in thermal equilibrium with the substrate initially and move over the substrate surface. In this process they interact among themselves, forming bigger clusters. The clusters or the nuclei are thermodynamically unstable and may tend to desorb in time depending on the deposition parameters. If the deposition parameters are such that a cluster collides with other adsorbed species before getting desorbed, it starts growing in size. After reaching a certain critical size, the cluster becomes thermodynamically stable and the nucleation barrier is said to have been overcome. This step is called the nucleation stage.

2.12.2 Growth process

The critical nuclei grow in number as well as in size until a saturation nucleation density is reached. The nucleation density and the average nucleus size depend on a number of parameters such as the energy of the impinging species, the rate of impingement, the activation energies of adsorption, desorption, thermal diffusion, the temperature, topography, and chemical nature of the substrate. A nucleus can grow both parallel to the substrate by surface diffusion of the adsorbed species, as well as perpendicular to it by direct impingement of the incident species. In general, however, the rate of lateral growth at this stage is much higher than the perpendicular growth. The growing nuclei are called islands.

The next stage in the process of film formation is the coalescence stage, in which the small islands start coalescing with each other in an attempt to reduce the surface area. This tendency to form bigger islands is termed agglomeration and is enhanced by increasing the surface mobility of the adsorbed species by, for example, increasing the substrate temperature. Larger islands grow together, leaving channels and holes of uncovered substrate. The structure of the films at this stage changes from discontinuous island type to porous network type. A completely continuous film is formed by filling of the channels and holes.

Depending on the thermodynamic parameters of the deposit and the substrate surface including relative energies of the film free surface (γ_f), the substrate free surface (γ_s) and the interface (γ_i), contact angle (shown in Figure 2.18) of the growing nuclei and subsequently the initial nucleation and growth stages will be different. There are three basic modes of film growth schematically illustrated in Figure 2.19 [84],[71].

(i) Volmer-Weber (island growth mode); in this growth mode, the bonding between the deposit atoms is stronger than the bonding of the deposit atoms with the substrate

leading to a finite contact angle, three dimensional growth of the nuclei and formation of the islands. The islands grow until they impinge.

(ii) Frank-van der Merwe (layer-by-layer growth mode); in this growth mode, the atoms arriving at the substrate surface preferentially bond to the substrate atoms rather than the other deposit atoms leading to a contact angle of zero and lateral growth (two dimensions) of the nuclei until a layer of single atom thickness is formed. Further growth results in the formation of successive layers.

(iii) Stranski-Krastanov (a mixed of both island growth and layer-by-layer mode); this growth mode occurs when the contact angle between the film and the substrate is zero and the deposit is elastically stressed from its bulk lattice parameters. Therefore the deposition starts with the two dimensional mode up to some critical thickness. As the thickness is increased further, 2-D growth becomes unstable and three dimensional island growth occurs.

Texture development in the deposited films depends on the growth mode and processing conditions. Except under special conditions, the crystallographic orientations of different islands are randomly distributed, so that when they touch each other during growth, grain boundaries and various point and line defects are incorporated into the film. The lateral grain size (or the crystallite size) of a film is primarily determined by the initial nucleation density. If, however, recrystallization takes place during the coalescence stage, the lateral grain size is larger than the average separation of the initial nuclei, and the average number of grains per unit area of the film is less than the initial nucleation density.

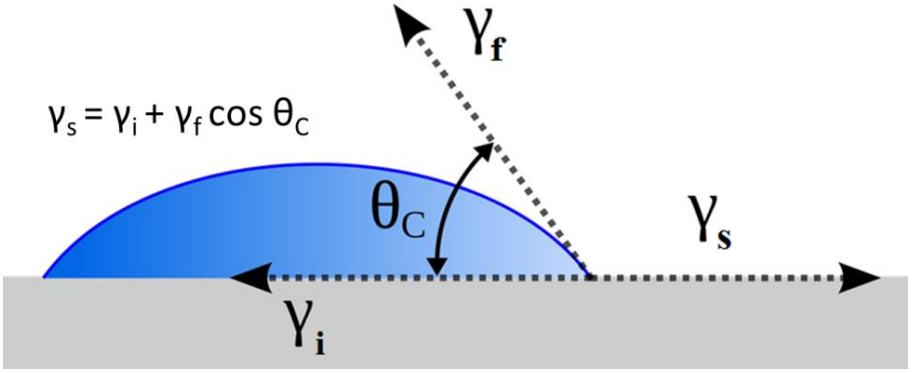

Figure 2.18: The schematic of an island growing on the surface with the contact angle (θ_C) and interfacial energies (γ_s: surface energy of the substrate, γ_f: surface energy of the island, γ_i: interface energy).

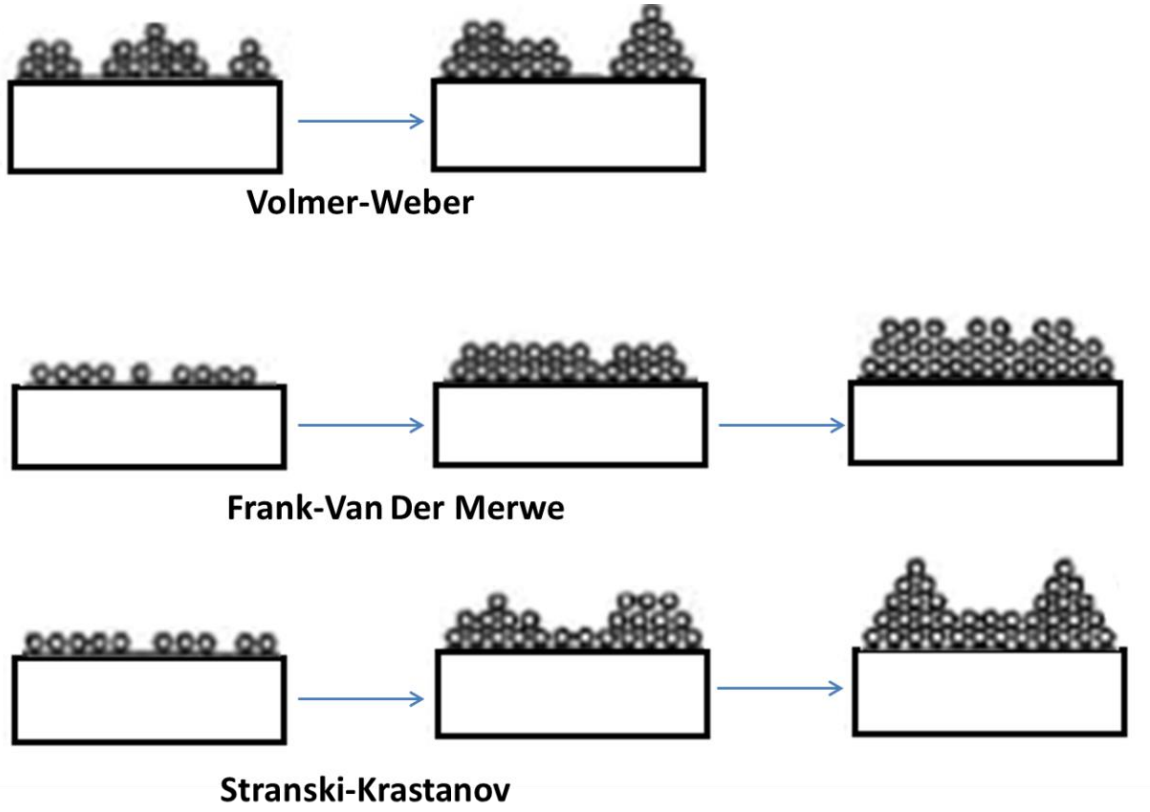

Figure 2.19: Schematic diagram of the three film growth modes [71].

2.13 The objectives of studying Fe(Se,Te) thin films

The main part of my thesis (chapter 4) concentrates on the fabrication and characterization of Fe-chalcogenides. As the literature review in this chapter showed, almost all of the Fe(Se,Te)

thin films have been grown by the pulsed laser deposition and molecular beam epitaxy. The first objective of my work is to fabricate Fe(Se,Te) thin films by sputtering and investigate the capability of sputtering for the fabrication of high-quality superconducting Fe(Se,Te) thin films.

The second objective is to discover the effects of fabrication parameters on the growth process and the relation between growth/microstructure and electrical properties. As a new and different class of superconductors, relatively a little is known about the effect of microstructure on the superconducting properties of iron chalcognide thin films. As has been reviewed, the effects of some microstructural parameters have not yet been investigated or at least their effects are not completely understood, and in some cases contradictory results have been reported for the key parameters controlling superconductivity of this compound.

Besides the investigation of the relationships between processing parameters, microstructure and electrical properties, the optimization of the processing conditions is also another objective of my work.

2.14 References

1. P.J. Lee, *Engineering superconductivity*, 2001, New York, Chichester, Wiley-Interscience.
2. R. Waldram, *Superconductivity of Metals and Cuprates*, 1996, lOP Publishing Ltd.
3. H.K. Onnes, *The superconductivity of mercury*, Commun. Phys. Lab. Univ. Leiden, 1911, V8:122.
4. J.R. Schrieffer, *Theory of superconductivity*, 1999, Perseus Books.
5. J.G. Bednorz, *Possible High T_c Superconductivity in the Ba-La-Cu-O System.* J. Phys.: Condensed Matter, 1986, B64: p. 189.
6. M.K. Wu, C. Torng, P.H. Hor, R.L. Meng, L. Gao, Z.J. Huang, Y.Q. Wang, W. Chu,, *Superconductivity at 93 K in a new mixed-phase Y-Ba-Cu-O compound system at ambient pressure*, Phys. Rev. Lett., 1987, 58(9): p. 908.
7. H. Maeda, M. Fukutomi,T. Asano, *A New High-T_c Oxide Superconductor without a Rare Earth Element.* Jpn. J. Appl. Phys., 1988, 27(2): p. L209.
8. Y. Maeno, H.H., K. Yoshida, S. Nishizaki, T. Fujita, J.G. Bednorz, F. Lichtenberg, *Superconductivity in a layered perovskite without copper*, Nature, 1994. 372: p. 532.
9. Z. Hiroi, Y. Muraoka,, *Unprecedented Superconductivity in β-Pyrochlore Osmate KOs_2O_6.* J. Phys. Soc. Jpn., 2004, 73: p. 1651.
10. K. Takada, E. Takayama-Muromachi, F. Izumi, R.A. Dilanian, T. Sasaki, *Superconductivity in two-dimensional CoO_2 layers.* Nature, 2003, 422: p. 53.

11. I. Shirotani, K. Kihou, C. Sekine, N. Takeda, M. Ishikawa, T. Yagi, *Superconductivity of new filled skutterudite YFe_4P_{12} prepared at high pressure*, J. Phys.: Condens. Matter, 2003, 15(28): p. S2201.
12. G.P. Meisner, *Superconductivity and magnetic order in ternary rare earth transition metal phosphides*, Phys. B, 1981, 108B: p. 763.
13. G. Crabtree, L. Greene, P. Johnson, *Celebrating 100 years of superconductivity: special issue on the iron-based superconductors* Reports on Progress in Physics, 2011, 74(12): P. 123.
14. D. Larbalestier, A. Gurevich, D. M. Feldmann, A. Polyanski, *High-T_c superconducting materials for electric power applications*, Nature, 2001, 414: P. 368.
15. D. Braithwaite, W. Knafo, I. Sheikin, *Evidence for Anisotropic Vortex Dynamics and Pauli Limitation in the Upper Critical Field of $FeSe_{1-x}Te_x$*, J. Phys. Soc. Jpn., 2010, 79: p. 0537703.
16. Y. Takano, *Focus on superconducting properties of iron chalcogenides*, Science and Technology of Advanced Materials, 2012, 13(5): P.32.
17. Y. Kamihara, *Iron-Based Layered Superconductor: LaOFeP*, Journal of the American Chemical Society, 2006, 128: p. 10012.
18. R. Zhi-An, *Superconductivity at 55 K in Iron-Based F-Doped Layered Quaternary Compound $Sm[O_{1-x}F_x]$ FeAs.* Chinese Physics Letters, 2008, 2: p. 25.
19. G.F. Chen, et al., *Superconductivity at 41 K and Its Competition with Spin- Density-Wave Instability in Layered $CeO_{l-x}F_xFeAs$.* Europhysics Letters, 2008, 34: p. 109.
20. Z.A. Ren, J. Yang, W. Lu, *Superconductivity at 52 K in iron based F doped layered quaternary compound $Pr[O_{l-x}F_x]FeAs$.* Materials Research Innovations, 2008, 12: p. 105.
21. M. Rotter, I. Schellenberg, W. Hermes, R. Pottgen, D. Johrendt, *Spin Density Wave Anomaly at 140 K in the Ternary Arsenide $BaFe_2As_2$,* Phys. Rev. B, 2008, 78: p. 020503.
22. X.C.Wang, Y.X. Lv, W.B. Gao, L.X. Yang, R.C. Yu, F.Y. Li, C.Q. Jin, *The superconductivity at 18 K in LiFeAs system,* Solid State Commun., 2008. 148: p. 538.
23. A.R. Lennie, P.F. Schofield, D.J. Vaughan, *Synthesis and Rietveld refinement of mackinawite, tetragonal FeS*, Mineralogical Magazine, 1995, 59: p. 677
24. F.C. Hsu, K.W. Yeh, *Superconductivity in the PbO-type structure a-FeSe.* Proceedings of the National Academy of Sciences, 2008, 105: P.543.
25. T.M. McQueen, et al., *Extreme sensitivity of superconductivity to stoichiometry in FeSe.* Physical review B, 2009, B79: p. 014522.
26. Q.Y. Wang et al, *Interface-Induced High-Temperature Superconductivity in Single Unit-Cell FeSe Films on $SrTiO_3$*, Chin. Phys. Lett., 2012, 29(3): p. 037402.
27. K. Ishida, H. Hosono, *To What Extent Iron-Pnictide New Superconductors Have Been Clarified: A Progress Report.* Journal of the Physical Society of Japan, 2009, 78(6): p. 062001.
28. A. Subedi, D.J. Singh, M.H. Du, *Density functional study of FeS, FeSe, and FeTe: Electronic structure, magnetism, phonons, and superconductivity*, Phys. Rev. B., 2008. 78: p. 134514.
29. W. Si, Q. Jie, W.G. Yin, J. Zhou, G. Gu, P.D. Johnson, *Enhanced superconducting transition temperature in $FeSe_{0.5}Te_{0.5}$ thin films,* Appl. Phys. Lett., 2009 95(5): p. 2504.
30. A.S. Sefat, M.A. McGuire, *Superconductivity in Co-doped LaFeAsO*, Phys. Rev. B 2008. 78(10): p. 4505.
31. M. Putti, E. Bellingeri, *New Fe-based superconductors: relevant for applications,* Superconductor Science and Technology, 2010, 34: p. 23.
32. G. Cao, C.W., Z.i Zhu, S. Jiang, Y. Luo, S. Chi, Z. Ren, Q. Tao, Y. Wang, Z. Xu, *Superconductivity induced by cobalt doping in iron-based*, Physical Review B, 2009, 79: p. 054521.
33. H. Okamoto, *The fese (ironselenium) system.* J. Phase Equilib., 1991, 12: p. 383.
34. R. Viennoisa, D. van der Marela, R. Cerny, *Effect of Fe excess on structural, magnetic and superconducting properties of single-crystalline $Fe_{1+x}Te_{1-y}Se_y$*, Journal of Solid State Chemistry, 2010, 183(4): p. 769–775.
35. V. Awana, et al., *Superconductivity in $SmFe_{1-x}Co_xAsO$ (x=0-0.30)*, Journal of Applied Physics, 2010, 107(9): P.432.
36. H. Takahashi, H.O., K. Igawa, Y. Kamihara, M. Hirano, H. Hosono, K. Matsubayashi, Y. Uwatoko, *High-Pressure Studies on Superconductivity in $LaFeAsO_{1-x}F_x$ and $SmFeAsO_{1-x}F_x$.* Journal of Superconductivity and Novel Magnetism, 2009, 22(6): p. 595.

37. A.S. Sefat, *Pressure effects on two superconducting iron-based families,* Reports on Progress in Physics, 2011, 74(12): p. 124502.
38. M.K. Wu, et al., *The development of the superconducting PbO-type β-FeSe and related compounds,* Physica C, 2009. 469: p. 340.
39. K.W. Yeh, Y. Huang *Tellurium substitution effect on superconductivity of the alpha-phase iron selenide,* Europhysics Letters, 2008, 84(3): p. 14.
40. K. Horigane, H.H., K. Ohayama, *Relationship between Structure and Superconductivity in $FeSe_{1-x}Te_x$.* Journal of the Physical Society of Japan, 2009, 78(7): p. 074718.
41. H. Lei, R. Hu, R. Hyejin, M. Abeykoon, S. Bozin, C. Petrovic, *Iron chalcogenide superconductors at high magnetic fields,* Sci. Technol. Adv. Mater., 2012, 13(05): p. 4305.
42. H. Okamoto, L.E.T., *The Mn-Zn (Manganese-Zinc) system.* Bull. Alloy Phase Diagr., 1990 11 (4): p. 377.
43. M.H. Fang, B. Qian, T.J. Liu, E.K. Vehstedt, Y. Liu, L. Spinu, Z.Q. Mao, *Superconductivity Close to Magnetic Instability in $Fe(Se_{1-x}Te_x)_{0.82}$.* Phys. Rev. B., 2008, 78: p. 224503.
44. B.C. Sales, M.A. McGuire, R.Y. Jin, D. Mandrus, Y. Mozharivskyj, *Bulk superconductivity at 14 K in single crystals of $Fe_{1+y}Te_xSe_{1-x}$.* Phys. Rev. B., 2009, 79(9): p. 4521.
45. Q. Li, I.K. Dimitrov, *Films of iron chalcogenide superconductors.* Rep. Prog. Phys., 2011, 74: p. 124510.
46. K. Iida, et al., *Generic Fe buffer layers for Fe-based superconductors: Epitaxial $FeSe_{1-x}Te_x$ thin films.* Applied Physics Letters, 2011. 99(20): P. 53.
47. W.D. Si, et al., *High current superconductivity in $FeSe_{0.5}Te_{0.5}$-coated conductors at 30 tesla,* Nature Communications, 2013. 4: P. 345.
48. S.C. Speller, C. Aksoy, M. Saydam, H. Taylor, G. Burnell, A.T. Boothroyd, C.R.M. Grovener *Analysis of $FeySe_{1-x}Te_x$ thin films grown by radio frequency sputtering,* Supercond. Sci. Technol., 2011, 24: p. 075023.
49. I. Imai, M. Hanawa, I. Tsukada, A. Ichinose, A. Maeda, T. Hikage, T. Kawaguchi, H. kuta, *Systematic Comparison of Eight Substrates in Growth of $FeSe_{0.5}Te_{0.5}$ Superconducting Thin Films.* applied physics express, 2010, 3: p. 043102.
50. L. Malavasi, *Structure–properties correlations in Fe chalcogenide superconductors.* Chem Soc Rev, 2012, 41: p. 3897.
51. K. W. Yeh, T. W. Huang, P. M. Wu, Y.L. Huang, T.K. Chen, J.Y. Luo, M.K. Wu, *Se and Te Doping Study of the FeSe Superconductors.* J. Phys. Soc. Jpn., 2008, 77, Supplement C, P. 19.
52. S. Margadonna, M.T. McDonald, K. Kasperkiewicz, Y. Mizuguchi, Y. Takano, A.N. Fitch, E. Suard, K. Prassides, *Crystal structure of the new FeSe superconductor.* Chem. Commun., 2008, 43: p. 5607.
53. M.J. Wang, T.W. Huang, H.H. Chang, T.K. Chen, F.C. Hsu, C.T. Wu, P.M. Wu, A.M. Chang, M.K. Wu, *Crystal orientation and thickness dependence of the superconducting transition temperature of tetragonal $FeSe_{1-x}$ thin films,* Phys. Rev. Lett., 2009, 103(11): p. 7002.
54. S.X. Huang, V. Thampy, C. Broholm, *Control of tetrahedral coordination and superconductivity in $FeSe_{0.5}Te_{0.5}$ thin films,* Phys. Rev. Lett., 2010, 104: p. 217002.
55. S. Margadonna, Y. Ohishi, Y. Mizuguchi, Y. Takano, T. Kagayama, T. Nakagawa, M. Takata, K. Prassides, *Pressure evolution of the low-temperature crystal structure and bonding of the superconductor FeSe (T_c=37K),* Phys. Rev. B, 2009, 80(6): p. 4506.
56. Y. Mizuguchi, *A review of Fe-chalcogenide superconductors: the simplest Fe-based superconductor,* J. Phys. Soc. Jpn., 2010, 79: p. 102001.
57. K. Kuroki, S. Onari, R, Arita, H. Aoki, *Pnictogen height as a possible swtich between high T_c nodeless and low T_c nodal pairings in the iron based superconductors,* Phys. Rev. B., 2009. 79: p. 224511.
58. M. Tegel, D. Johrendt, *The crystal structure of $FeSe_{0.44}Te_{0.56}$.* Solid State Commun., 2010, 150: p. 383.
59. Speller, S.C., et al., *Analysis of local chemical and structural inhomogeneities in $Fe_ySe_{1-x}Te_x$ single crystals.* Applied Physics Letters, 2011, 99(19).
60. N.C. Gresty, A. Y. Ganin, T. McDonald, B. Claridge, D.Giap, Y. Mizuguchi, Y. Takano,T. Kagayama, Y. Ohishi, M. Takata, M. J. Rosseinsky, S. Margadonna, K. Prassides, *Structural*

Phase Transitions and Superconductivity in $Fe_{1+\delta}Se_{0.57}Te_{0.43}$ at Ambient and Elevated Pressures. J. Am. Chem. Soc, 2009, 131: p. 16944.

61. T. Imai, F. L. Ning, T. M. McQueen, R. J. Cava, *Why Does Undoped FeSe Become a High-Tc Superconductor under Pressure?* Phys. Rev.Lett., 2009, 102: p. 177005.
62. Y. Mizuguchi, S. Tsuda, *Superconductivity at 27 K in tetragonal FeSe under high pressure.* Appl Phys Lett, 2008, 93.
63. G. Garbarino, P. Lejay, A. Sulpice, P. Toulemonde, W. Crichton, M. Mezouar, and M. Nunez, Regueiro, *High temperature superconductivity (T_c onset at 34K) in the high pressure orthorhombic phase of FeSe* EPL, 2009, 86: p. 27001.
64. S. Medvedev, I. A. Troyan, T. Palasyuk, M. I. Eremets, R. J. Cava, S. Naghavi, F. Casper, V. Ksenofontov, G. Wortmann, C. Felser, *Electronic and magnetic phase diagram of β-$Fe_{1.01}Se$ with superconductivity at 36.7 K under pressure.* Nature Materials, 2009, 8: p. 630.
65. Y.F. Nie, J.I.Budnick, W.A. Hines, M. Jain, B.O. Wells, *Suppression of superconductivity in FeSe films under tensile strain,* Applied Physics Letters, 2009, 94(24): p. 2505.
66. M. Jourdan, *Preparation, characterization, and upper critical field of epitaxial FeSe thin films.* J. Appl. Phys., 2010, 108: p. 023913.
67. S.Y. Tan, et al., *Interface-induced superconductivity and strain-dependent spin density waves in FeSe/$SrTiO_3$ thin films,* Nature Materials, 2013, 12(7): p. 634.
68. E. Bellingeri, I.P., R. Buzio, A. Gerbi, D. Marre, M.R. Cimberle, M. Tropeano, M. Putti, A. Palenzona, C.Ferdeghini, *T_C =21K in epitaxial $FeSe_{0.5}Te_{0.5}$ thin films with biaxial compressive strain,* Applied Physics Letters, 2010, 96(10): p. 2512.
69. K. Wasa, M. Kitabatake, H. Adachi, *Thin film materials technology: sputtering of compound materials,* 2004, Norwich, NY, Heidelberg, Springer.
70. F. Nabeshima, et al., *Enhancement of the superconducting transition temperature in FeSe epitaxial thin films by anisotropic compression,* Applied Physics Letters, 2013, 103(17): p. 34.
71. S.C. Speller, *Microstructural development and control in $Ti_2Ba_2CaCu_2O_8$,* DPhil thesis, *Materials Department,* 2004, Oxford University.
72. Y. Han, L.X. Cao, S. Zhang, B. Xu, B.R. Zhao, *Preparation and superconductivity of iron selenide thin films.* J. Phys. Condens. Matter, 2009, 21(23): p. 5702.
73. T.G. Kumary, J. Janaki, A. Mani, A.T. Satya, R.M. Sarguna, P.K. Ajikumar, A.K. Tyagi, A. Bharathi, *Superconducting $Fe_{1+\delta}Se_{1-x}Te_x$ thin films: growth, characterization and properties.* Supercond. Sci. Technol., 2009, 22 (9): p. 5018.
74. M. Hanawa, et al., *Empirical Selection Rule of Substrate Materials for Iron Chalcogenide Superconducting Thin Films,* Japanese Journal of Applied Physics, 2012, 51(1): p. 986.
75. M. Hanawa, et al., *Substrate dependence of structural and transport properties in $FeSe_{0.5}Te_{0.5}$ thin films,* Japanese Journal of Applied Physics, 2011, 50: p. 053101.
76. V. Braccini, et al., *Highly effective and isotropic pinning in epitaxial Fe(Se,Te) thin films grown on CaF_2 substrates,* Applied Physics Letters, 2013, 103(17): p. 75.
77. I. Tsukada, T. Akike,Y. Imai, A. Ichine, S. Komia, T. Hikage, H.I. Kawaghi, A. Maeda, *Epitaxial Growth of $FeSe_{0.5}Te_{0.5}$ Thin Films on CaF_2 Substrates with High Critical Current Density,* Applied Physics Express, 2011. 4: p. 053101.
78. H. Hiramatsu, et al., *Water-induced superconductivity in $SrFe_2As_2$.* Physical Review B, 2009, 80(5): p. 964.
79. J. George, B.P., *Preparation and properties of co-evaporated Bismuth Telluride Bi_2Te_3 thin films.* Solid State Communications, 1985 56(1): p. 117.
80. E. Charles, A.M. Boyer, A. Campbell, F.J. Blunt, J.D. Johnson, P.A. Freeman, *Structural and electrical properties of Bismuth Telluride films grown by the molecular beam technique,* J. Appl. Phys., 1988, 73: p. 1252.
81. M. Stolzer, V.B., J. Meusel, *Deposition of $(Bi,Sb)_2Te_3$ films by magnetron co-sputtering from two targets.* 15th Int. Conf. on Thermoelectrics, 1996, p. 422.
82. M.A. Brown, A.J. Rosakis, X. Feng, Y. Huang, E. Ustundag, *Thin film/substrate systems featuring arbitrary film thickness and misfit strain distributions. Part II: Experimental validation of the non-local stress/curvature relations,* International Journal of Solids and Structures, 2007, 44 (6): p. 1755.

83. S. Agatsuma, *MBE growth of FeSe and $Sr_{1-x}K_xFe_2As_2$,* Physica C: Superconductivity, 2010, 470(20): p. 1468.
84. M. Ohring, *Materials Science of Thin films, Deposition & Structure,* 2002: New York, Academic press.
85. J. Sarkar, *Sputtering Materials for VLSI and Thin Film Devices,* 2013, William Andrew.
86. D. Depla, *Magnetrons, reactive gases and sputtering,* First edition, 2013, Diederik Depla.
87. B. Rainer, *Sputtering by Particle Bombardment,* 2007,Wolfgang.
88. K. Wasa, *Handbook of Sputter Deposition: Technology, Fundamentals and Applications for Functional Thin Films,* 2nd ed, 2008, Spriger.

Chapter 3: Experimental methods

This chapter describes the experimental techniques used in this work in two major categories: the fabrication of $Fe_y(Se_{1-x}Te_x)$ thin films and the characterization of microstructure and physical properties. In the section on characterization, in addition to the techniques used for $Fe_y(Se_{1-x}Te_x)$ thin films, some other techniques are described which have been used for the characterization of single crystal samples of functional compounds received from collaborators. These samples include Bi_2Te_3 and $MnBi_2Te_3$ and $CaFe_2As_2$.

3.1.Fabrication of $Fe_y(Se_{1-x}Te_x)$ thin films

Magnetron sputtering [1, 2] was used to fabricate $Fe_y(Se_{1-x}Te_x)$ thin films using a variety of deposition conditions. Optimising these conditions has been a major part of this work. In the sputtering process, the overall quality of films is affected by many parameters including target stoichiometry, substrate, relative position of the substrate to the target, pressure, sputtering power, choice of substrate, substrate temperature and the length of sputtering. In my work, the pressure and the sputtering power were kept the same for all of the films fabricated. Other parameters were changed to investigate their effects on the structure and properties of the films. In addition, post-deposition annealing heat treatments have been investigated.

3.1.1. Target preparation

Sputtering targets were made by ball milling for 24 hrs a mixture of high purity iron (99.99%, 80 mesh), selenium (99.99%, 100 mesh), tellurium (99.997%, 30 mesh) and manganese (99.99%, 60-70 mesh) powders in the chosen stoichiometry. After sieving, the milled powders were pressed at room temperature (at a pressure of 8MPa for 20-30 minutes) into a two-inch disc with a thickness of about 5mm. Fortunately, the cold-pressed target was mechanically strong enough without sintering to be mounted inside the sputtering chamber. This is important because sintering at high temperatures may lead to change the composition of the target especially due to a large difference in the vapour pressure of Se, Te and Fe. This issue will be explained in detail in the next chapter.

Due to the lack of stoichiometric transfer from the target to the substrate in sputtering [1, 2], the ratio of Fe, Se and Te in the target must be carefully calculated in order to produce thin films with the correct stoichiometry. Using chemical analysis of each batch of films, the composition required for the next target was calculated with consideration of the sputtering yield for each element (as will be explained in chapter 4).

Three targets with different nominal compositions of $(Fe_{0.98}Mn_{0.02})_{1.05}(Se_{0.33}Te_{0.67})$, $Fe_{0.95}Se_{0.2}Te_{0.8}$ and $Fe_{0.4}Se_{0.2}Te_{0.8}$ were used in this work in order to deposit $(Fe,Mn)_y(Se_{1-x}Te_x)$ thin films. A small amount of Mn was added to one of the targets to study the effect of Mn-doping on the properties of $Fe_y(Se_{1-x}Te_x)$ films since Mn has been reported as a potential stabilizer for the 11-phase [3].

3.1.2. Sputtering

Radio frequency (rf) magnetron sputtering was carried out in an Oxford Applied Research DS500 sputter kit with a combined rotary and turbo pumping system. Before sputtering the chamber was evacuated to 10^{-6} mbar to minimize any contamination from the air. Just before sputtering, the turbo pump was switched off and argon allowed into the chamber. When the gas pressure was 10^{-1} mbar, sputtering was started and then the Ar pressure decreased to 2×10^{-2} mbar and kept steady until the end of sputtering. The substrates are held directly in front of the target, i.e. on-axis geometry, on a copper block which may be heated by means of a resistive element. A wide range of samples were grown by this method on various substrates, temperatures and lengths of sputtering time.

The films were grown in two different ways; by the in-situ and ex-situ process. In the in-situ process films are grown directly onto the substrates heated to temperatures in the range 150-400°C for various lengths of time (30, 60, 90, 120, 150 and 180 minutes). In the ex-situ process, thin films are deposited onto the cold substrates followed by a post-annealing heat treatment since in cold sputtering there is not enough motion of deposit atoms for the formation of the desired phase. The post-annealing was carried out at 400°C either in the sputtering chamber immediately after sputtering (in Ar) or in a separate furnace by sealing the precursor films in evacuated quartz tubes and heating in a furnace.

3.1.3. Substrates

The crystallography and surface preparation of the substrate is of primary importance in determining the growth mechanism and microstructure of the films [1, 4]. An appropriate substrate for epitaxial growth of a thin film has some basic requirements, such as lattice matching with the desired phase, phase stability at the processing temperature, uniform and high quality surface, chemical compatibility and thermal expansion coefficient match. If, for example, the lattice mismatch is large, elastic strain will lead to the formation of misfit dislocations and microcracks in the film [1, 2, 4]. A close match of thermal expansion coefficients will also prevent the generation of strain at the interface, which may otherwise lead to microcracks and other defects [1, 2]. As it is not possible to find a single substrate which perfectly fulfils all the given criteria, a wide range of substrates, listed in Table 3.1, were investigated in this work.

The substrates have to be clean before growing the film. Any contamination on the surface can affect the growth mechanism, migration of deposited atoms on the surface, and so the microstructure and purity of the films. It is essential to thoroughly cleanse the substrate surface to remove any contamination such as grease and dust before growing the film. In this study, all the substrates were cleaned just before sputtering by ultrasonic cleaning firstly in acetone and then in methanol. Finally the surface was dried with a compressed nitrogen duster until no methanol remains.

Table 3.1: The properties of the substrates used in this work for growing $Fe_y(Se_{1-x}Te_x)$ thin films.

	MgO (100)	LiF (100)	$SrTiO_3$ (STO)	$LaAlO_3$ (LAO)	$(LaAlO_3)_{0.3}(Sr_2AlTaO_6)_{0.7}$ (LSAT) (100)	CaF_2 (100)
Lattice parameter (Å)	a=4.2170	a=4.020	a=3.905	a=3.789	a = 3.868	$a/\sqrt{2}$=3.862
Thermal expansion coefficient (K^{-1})	8×10^{-6}	37×10^{-6}	9×10^{-6}	1.0×10^{-5}	8.2×10^{-6}	24.0×10^{-6}
Thermal conductivity at 300k ($W \cdot m^{-1} \cdot K^{-1}$)	45–60	11.3	11.2	11.6	5.1	9.71
Unit cell	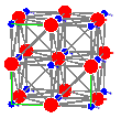	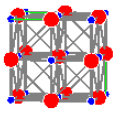	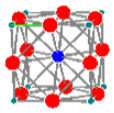	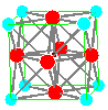	–	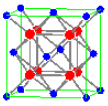

3.2. Characterization

A variety of techniques have been used for the characterization of sputtered thin films, including θ-2θ X-ray diffraction (XRD), X-ray diffraction texture analysis, scanning electron microscopy (SEM), transmission electron microscopy (TEM), atomic force microscopy (AFM), electrical-magnetic property measurements (SQUID and transport resistivity measurements). As the superconducting properties of $Fe_y(Se_{1-x}Te_x)$ samples can be easily affected by exposure to air [5], it was important to measure electrical properties immediately after the fabrication of the films, and the samples were stored in a vacuum desiccator at all times.

3.2.1. X-ray diffraction (θ-2θ)

X-ray diffraction (XRD) experiments were carried out using a Philips PW179 X-ray generator for phase identification. Cu-Kα X-rays were produced at accelerating voltage of 35kV and a current of 50mA. The sample is rotated (by the θ angle) with respect to a fixed beam of x-rays and the resulting reflections are collected by a detector which moves simultaneously by 2θ.

Each crystalline phase produces characteristic peaks in θ-2θ pattern when the Bragg condition (Equation 3.1) is satisfied.

$$\lambda=2d_{(hkl)}\sin\theta \qquad \text{Equation 3.1}$$

Where λ is the wavelength of Cu-Kα X-rays and $d_{(hkl)}$ is the interplanar spacing of (hkl) planes in the sample.

In my project, each sample was scanned two or three times with slight rotation and readjustment in an attempt to minimise any height errors especially when lattice parameters were calculated from the XRD patterns. The position of the peaks corresponds to the interplanar spacing for a set of planes (hkl) and can be used for the calculation of the unit cell parameters. Any parameter such as uniform strain and chemical substitution by atoms with different radii can alter the position of the peaks.

The intensity of each peak is controlled primarily by the scattering intensity of each atom and their arrangement in the unit cell for a polycrystalline sample with random orientation [6]. Since in this scan geometry, only planes which are parallel to the surface produce peaks, in an orientated epitaxial sample or one containing a few large grains, the relative intensity of the peaks will change. For a polycrystalline sample, all the possible diffracting planes will produce an individual peak, and we may have a large number of peaks in an XRD pattern, while in a textured sample only the peaks corresponding to the planes parallel to the surface are detected.

The width of each peak can give information on crystallite size and non-uniform lattice strain [6]. If the strain is not uniform throughout the sample, peak broadening happens as the Bragg condition is satisfied over a range of angles.

3.2.1.1. Lattice parameter calculation

Lattice parameters are calculated from XRD patterns using the Bragg equation if the crystal structure is known, and the peaks are indexed according to the crystal planes. In this method, for each *(hkl)* XRD peak, lattice spacing of the *(hkl)* planes can be calculated by $d_{(hkl)} = \frac{\lambda}{2\sin(\theta)}$ where θ is obtained from the XRD pattern. However, since any error in measuring the exact value of θ produces errors in $\sin\theta$ and subsequently in the calculated lattice parameter, it is important to choose the peaks which minimize this error. As shown in Figure 3.1, for the function of $\sin\theta$, the error in $\sin\theta$ would be the minimum if θ is close to 90°. Therefore, it is more accurate to use peaks near θ=90° to minimize the errors in $\sin\theta$. However, we cannot measure an XRD peak at θ=90° because the source and detector cannot be in the same place, so the lattice parameters are calculated by extrapolating the data from all the peaks in the pattern against a selected function of θ. There are different functions of θ which can be used to account for different errors based on the optical set up of the diffractometer and the structure of the material. So for precise measurements, it is important to use the correct function to minimize the above error in each XRD machine. It is worth mentioning that without any extrapolation, simply by selection of the parameter calculated for the highest-angle line on the pattern, a precision of 0.01Å (about 0.3 percent for most compounds) can be obtained. With good experimental technique, and the use of a proper extrapolation function, this precision can be increased to 0.001Å (0.03 percent) [6].

In this work, $Fe_y(Se_{1-x}Te_x)$ thin films are mostly grown with c-axis texture perpendicular to the surface. Therefore, only the {*00l*} peaks are observed in XRD patterns, so only the c-axis parameter can be calculated. The values of θ were obtained by the X'Pert Software. Different functions of θ were applied to the data (Figure 3.2) and the lattice parameter obtained from the function with the best extrapolated value. In most samples $\cos^2\theta/\sin\theta+\cos^2\theta/\theta$ gave the best extrapolation, as expected for the type of diffractometer used.

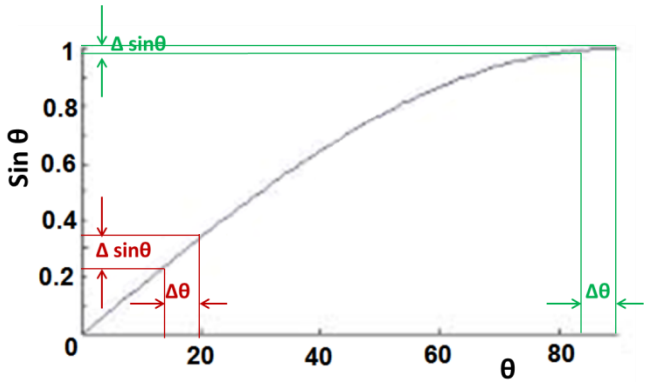

Figure 3.1. The errors in Sinθ for the same error in θ (the same Δθ) in different values of θ, the error in sinθ is the minimum when θ is near 90.

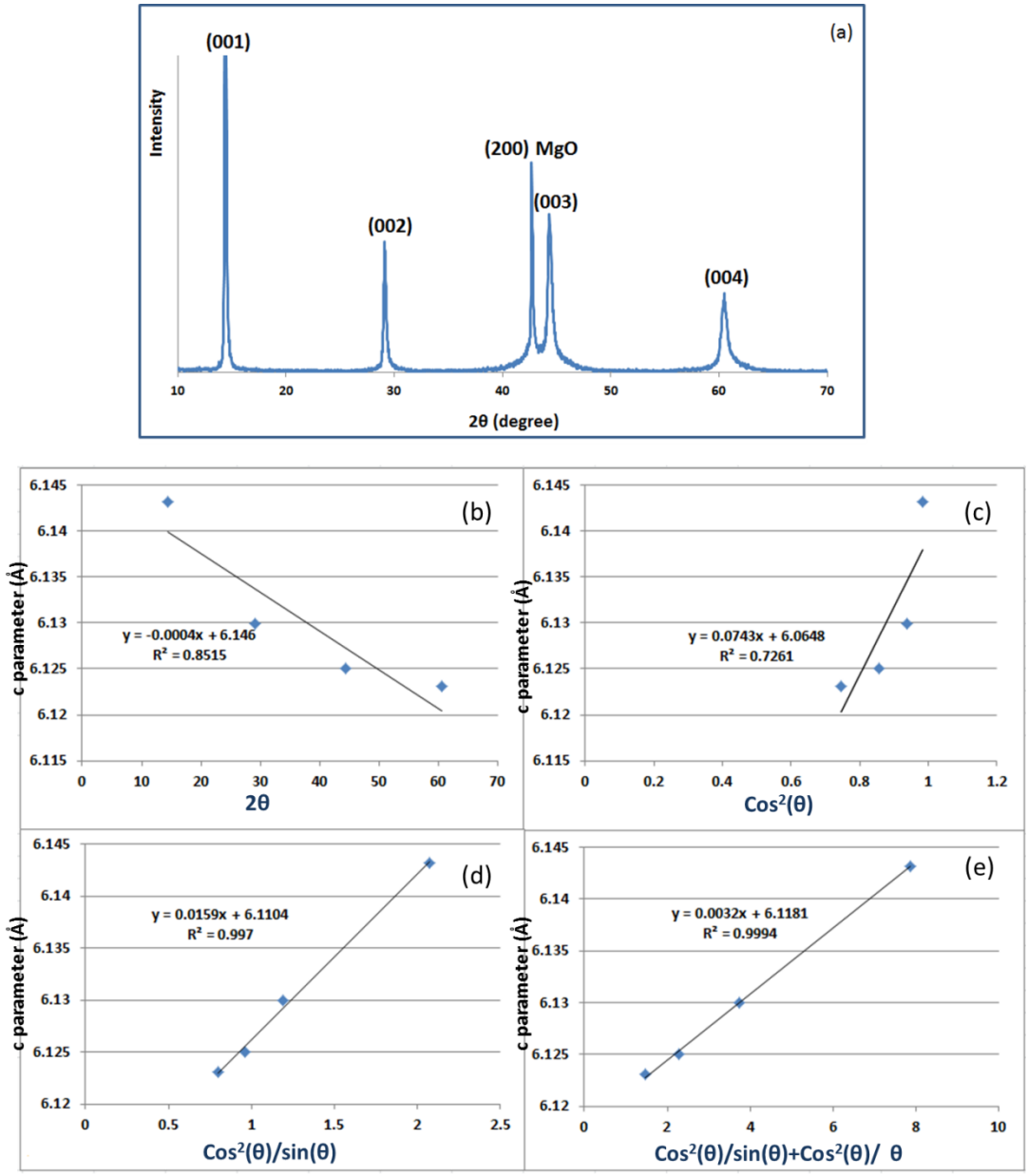

Figure 3.2: (a) A typical XRD pattern of an $Fe_y(Se_{1-x}Te_x)$ film grown on MgO, (b-e) Calculation of c-axis parameter by extrapolation of different functions. The last two functions are the most accurate.

3.2.2. Texture analysis

In order to examine the texture of thin films fabricated by sputtering, XRD texture measurements were carried out using a Philips X'Pert MRD system. Cu-Kα radiation was generated at 40kV and 50 mA. In this technique, the goniometer allows the sample to rotate around three axes φ, ψ and ω (see Figure 3.3a below). Depending on how the instrument is set up in these angles, different types of scans are possible giving different texture information about the sample.

To examine **out-of-plane texture**, an ω scan, known as a rocking curve is used. In this scan ψ=0, φ is constant and the source and detector are kept fixed at a 2θ angle which satisfies the Bragg condition for a particular $(00l)_{11\text{-phase}}$ plane. The scan is done while the sample is tilting around the ω axis (usually the scan range is ±3°).

To examine **in-plane texture**, a φ scan is used. In this scan, the sample is rotating around the φ axis while the ω, 2θ and ψ angles are set up to satisfy the Bragg condition for a particular {hkl} plane.

The planes which are selected for these two types of scan should be strongly diffracting with no interference with a peak from the single crystal substrate. For c-axis aligned $Fe_y(Se_{1-x}Te_x)$ thin films, the $(001)_{11\text{-phase}}$ peak at about 2θ =15° and the $(101)_{11\text{-phase}}$ peak at about 2θ=28° were used for out-of-plane and in-plane measurements respectively. For in-plane measurements, the sample was tilted to ~57° (ψ: the angle between the $(101)_{11\text{-phase}}$ and the $(001)_{11\text{-phase}}$ planes). The full-width at half maximum intensity (FWHM) of the ω and φ peaks characterises the degree of out-of-plane and in-plane alignment respectively, with lower FWHM values for a sharper texture.

The FWHM can be directly determined using the X'Pert Software. In some cases where the software does not fit a proper curve to the peak, the FWHM was calculated from a Gaussian curve fitted to the experimental data using the method of least squares.

To examine the relative orientation of the film to the substrate, φ scan measurements were run for a set of (hkl) planes of the substrate. Since this set of planes should be strongly diffracting with no overlaps with the thin films, different planes and subsequently ψ values were selected for various substrates. However for most of them e.g MgO, $SrTiO_3$ and LiF, the $(111)_{11\text{-phase}}$ plane at ψ=54.2 was used for the φ scans.

The distribution of crystallographic orientations of a sample can be represented in two-dimensions in a pole figure. A pole figure is obtained by carrying out a 360° φ scan for ψ steps of 2° (from 0-88°) when the ω and 2θ are set to satisfy the Bragg condition for a particular {hkl} plane. Figure 3.3b schematically shows how a pole figure is constructed. As can be seen, the radial position of a point in the pole figure is related to the ψ angle by following equation:

$$\frac{r}{R} = \tan(\frac{\psi}{2}) \qquad \text{Equation 3.2}$$

For $Fe_y(Se_{1-x}Te_x)$ specimens, the $(101)_{11\text{-phase}}$ pole figure was obtained by setting 2θ=28°. Four regions of high intensity appear in the pole figure when the sample is single crystalline, while if it is c-axis aligned with random in-plane orientation, a ring would be observed. The ψ value in these pole figures is the angle between the $(001)_{11\text{-phase}}$ and $(101)_{11\text{-phase}}$ planes. Therefore tan(ψ) is equal to the c/a ratio in the $Fe_y(Se_{1-x}Te_x)$ tetragonal structure. If the accurate value of ψ is calculated from the pole figure, it is possible to calculate c/a. As the c-axis parameter can be calculated from the θ-2θ XRD pattern (as explained earlier), knowing the c/a ratio gives the value of a-axis parameter. In a c-axis aligned sample, the a-axis parameter cannot be measured by general XRD as none of these diffract in the θ-2θ geometry.

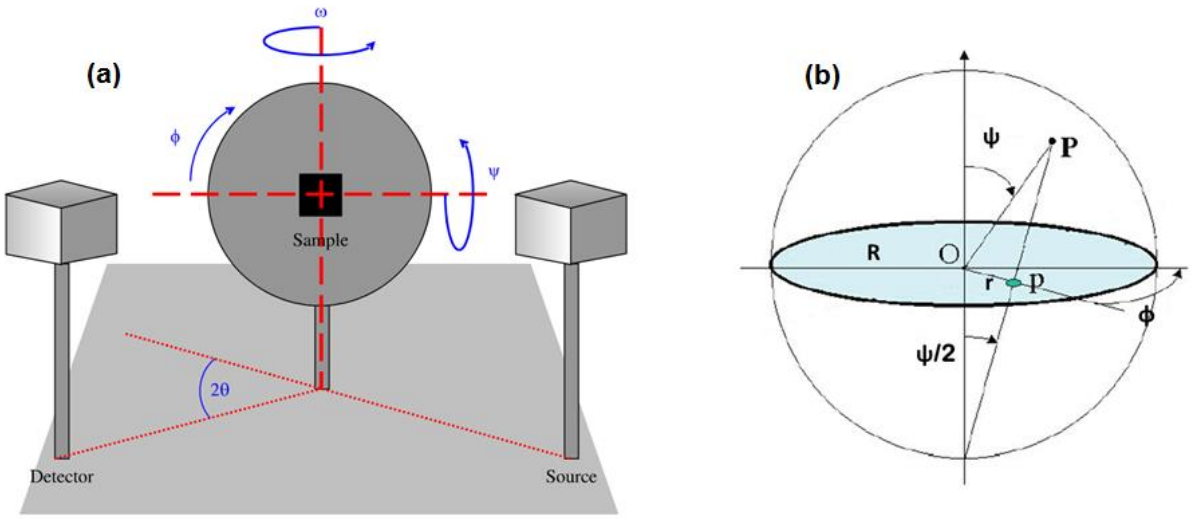

Figure 3.3: Schematic diagram of (a) a goniometer (b) the construction of a pole figure. φ, θ, ψ and ω axes can be seen in these images [7].

3.2.3. Scanning electron microscopy

Scanning electron microscopy (SEM) has been used to study film microstructure, morphology and porosity through both secondary electron (SE) and back-scattered electron (BE) imaging modes. SEM micrographs in this thesis were taken on JEOL 6300, 5510 and 840A instruments. SE imaging is mostly used to study surface morphology, while the BE detector measures the electrons elastically scattered and primarily gives contrast based on variations in the average atomic number, sometimes called z-contrast. In conjunction with imaging, the SEMs were also used to study variations in chemical composition using Energy Dispersive X-ray analysis (EDX). The electron beam in SEM excites some electrons from the ground state; the resulting holes are filled by electrons of higher energy, emitting the excess energy in the form of either X-rays (as used in EDX) or Auger electrons. The energy of emitted X-ray corresponds to energy difference between electron orbitals in an atom. The X-ray energy distribution is therefore characteristic of an element and can be used for qualitative analysis. However for quantitative analysis, calibration is needed as different atoms emit x-rays in different efficiencies [8].

The minimum incident electron energy should typically be twice the X-ray energy of interest. However, higher incident energy creates a larger interaction volume which for thin film samples can excite the elements from the substrate as well. In this work, $Fe_y(Se_{1-x}Te_x)$ thin films were grown onto a variety of substrates. Figure 3.4 shows a typical EDX spectra of a $(Fe_{1-d}Mn_d)_y(Se_{1-x}Te_x)$ film on a LiF substrate. EDX was used in this work to provide qualitative information about the composition of the films and to study variations in chemical composition. Most of EDX experiments were done at accelerating voltage of 20kV in order to detect the K line of Se which appears at about 11eV.

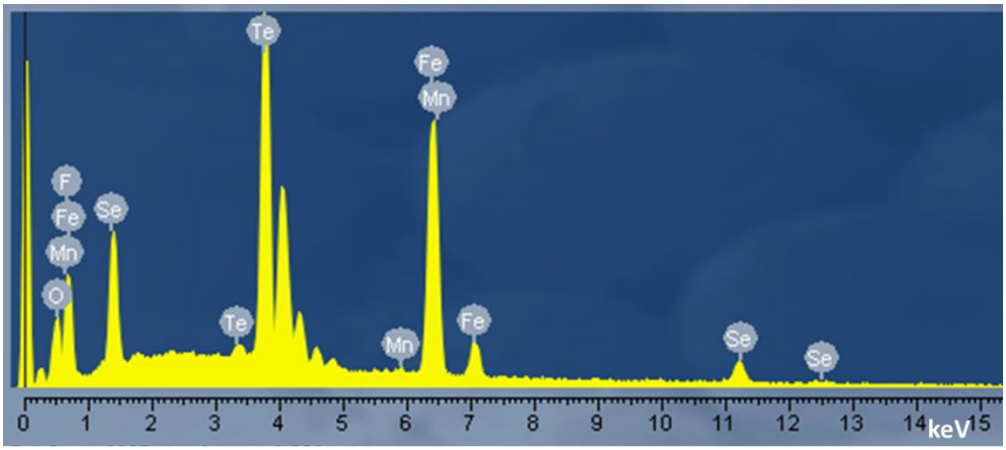

Figure 3.4: A typical EDX spectrum of $(Fe_{1-d}Mn_d)_y(Se_{1-x}Te_x)$ thin film on a LiF substrate.

3.2.4. Transmission electron microscopy

Transmission electron microscopy (TEM) was used to study the microstructure of $Fe_y(Se_{1-x}Te_x)$ thin films as well as other samples received from my collaborators. In TEM, a focused beam of electrons are transmitted through a very thin sample. The image is formed from the interaction (either elastic or inelastic) of these electrons with atoms in the sample. TEM analysis includes many different techniques and experimental procedures that allow different kinds of information to be obtained from the same sample. In this thesis, bright-field and dark-field imaging, diffraction patterns, EDX compositional analysis and EDX mapping were used. To understand how these techniques work the reader is referred to standard references like [9-

11]. The TEMs used most regularly in this work include a Philips CM20, JEOL 2000FX and JEOL 3000EX. Software packages like CrystalMaker and SingleCrystal Limit were used to help indexing diffraction patterns from single crystal samples. In addition to these microscopes, I occasionally used microscopes with special capabilities. For example, beam-sensitive $MnBi_2Te_3$ samples were analysed in JEOL2010 and JEOL2200 instruments which can be operated at 80kV.

3.2.4.1. Lattice parameter calculation and camera length calibration

The lattice parameters of a unit cell can be calculated from TEM diffraction patterns using the following equation derived from Bragg's law with the small angle approximation.

$$\lambda L = d_{hkl} R \qquad \text{Equation 3.3}$$

where λ is the wavelength of the electron beam (which depends on accelerating voltage), L is camera length, d_{hkl} is the (hkl) plane spacing and R is the either ring radius in the diffraction pattern from a polycrystalline sample or the distance between spots from a single crystal sample. To identify an accurate lattice spacing from TEM diffraction patterns, calibrating the camera length is essential. Since the exact values of λ and L are difficult to measure, the product λL, which is called the camera constant, can be acquired for each camera length by precise measurement of R for a calibration sample with a known value of d_{hkl}. In this work, wherever a lattice parameter is reported using this method, calibration was done just before the TEM investigation on a gold standard sample in order to avoid any errors from changing microscope conditions. Figure 3.5 shows a typical diffraction pattern from a single crystal Au sample and a table of camera constants for the JEOL 2000FX TEM operating at 200kV. It is worth mentioning that for measuring the distance between spots, as many spots as possible were considered by the software in different directions and the average value for the lattice parameter was calculated.

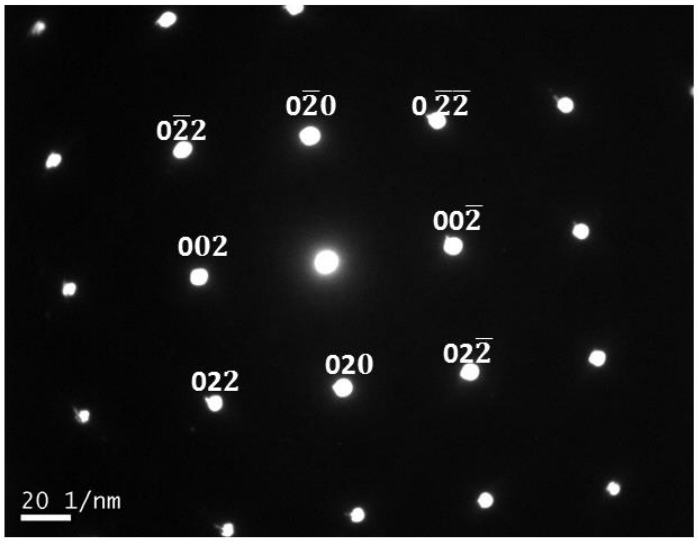

Camera length (cm)	λL (mm.Å)
100	27.439
150	30.192
200	39.525
250	61.223

Figure 3.5: [100]-zone diffraction pattern of Au standard sample used for camera length calibration and the calculated camera constants for the JEOL 2000FX operating at 200kV.

3.2.4.2. Image/diffraction pattern rotation calibration

The image/diffraction pattern rotation calibration is usually used to identify the orientation of the crystal lattice relative to features in the images. This calibration is done by taking double exposure of the image and diffraction pattern from a calibration sample at each magnification and each camera length for every accelerating voltage. The calibration sample must have distinct features with a known crystallographic orientation. For a MoO_3 single crystal, which was used in this work, the (001) reflection corresponds to the long edge of the crystal, as shown in Figure 3.6.

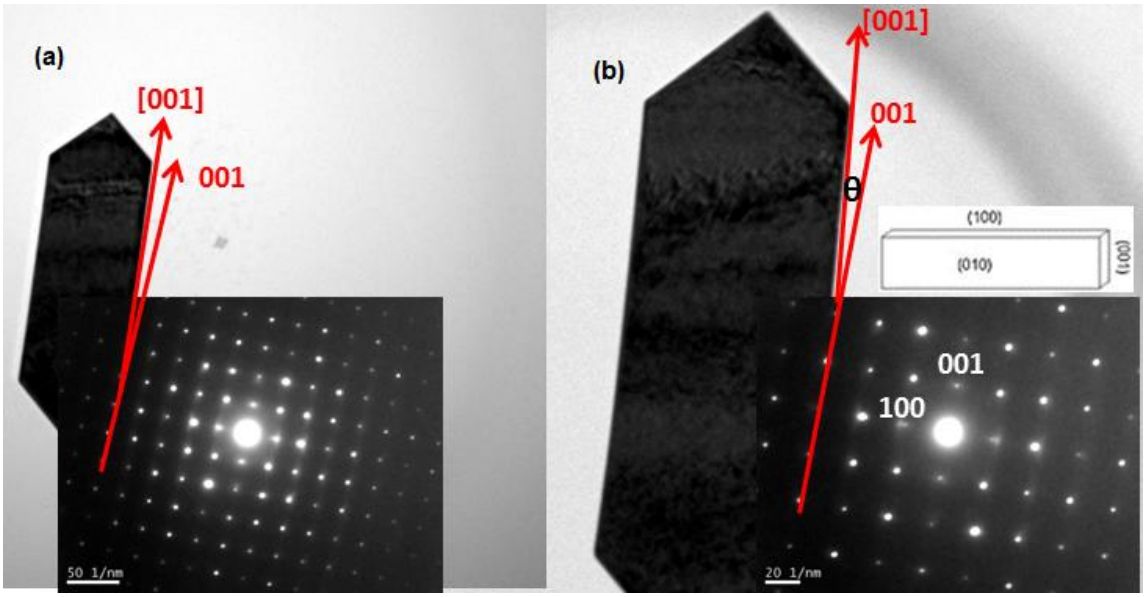

Figure 3.6: TEM images and diffraction patterns of a MoO_3 single crystal taken in the JEOL 2000FX at 200kV for rotation calibration; (a) magnification:20k, camera length: 120cm, (b) magnification:40k, camera length:250cm. The red lines show the [001] direction in the image and diffraction pattern and the angle of these lines is the rotation angle for a specific set of magnification and camera length.

3.2.5. Electron energy loss spectroscopy

Electron energy loss spectroscopy (EELS) is a TEM analytical technique that measures the change in kinetic energy of electrons after they have interacted with a specimen. The energy loss can be interpreted in terms of specific mechanisms of interaction and give both structural and chemical information with a spatial resolution down to the atomic level [12]. The energy resolution is typically 1eV but can approach 0.1eV if an electron-beam monochromator is used. More detailed information about EELS can be found in [12]. In this work, a 300 kV TEM (JEOL 3000EX) with an EELS detector (Gatan, GIF 2002) was used to investigate chemical interaction between $Fe_y(Se_{1-x}Te_x)$ thin films and substrate materials.

3.2.6. TEM sample preparation

The basic requirement for specimens for TEM is that electrons can be transmitted through the material. Therefore, the thickness of the specimen must be less than approximately 200 nm, depending on the scattering efficiency of the sample, which strongly depends on the average

atomic mass. As mentioned earlier, this thesis deals with two groups of samples; $Fe_y(Se_{1-x}Te_x)$ thin films and different single crystals including $MnBi_2Te_3$ and $CaFe_2As_2$. For both categories, focused ion beam (FIB) milling was used to prepare cross-sectional TEM samples as will be explained in the following section. For $MnBi_2Te_3$, in addition to FIB sample preparation, the exfoliation was also used to prepare plan-view TEM samples. The layered structure of $MnBi_2Te_3$ with a weak van der Waals interplane bonding allows thin sheets to be easily isolated by sticky tape [13]. The exfoliation method will be explained in chapter 5.

3.2.7. Focused ion beam (FIB)

FEI FIB 200 milling (lift-out method) was used for the preparation of cross-sectional TEM samples. Focused ion beam microscopes operate in a similar way to an SEM, but instead of electrons it uses a beam of focussed gallium ions. This allows the FIB to image (in low current mode) and selectively mill the sample (in high current mode) to create micron-sized structures, for example site-specific foils for the TEM. The first stage of fabricating a cross-sectional TEM specimen by FIB is to deposit a protective layer (Pt layer) onto the top surface of the sample (shown in Figure 3.7). The area around the Pt is then milled from both sides until the specimen is about 0.5 μm thick. Then the stage is tilted by 45° and a cut is made along the bottom and one side of the specimen to allow it to be separated from the bulk sample at a later stage. The specimen is then further thinned to approximately 100 nm. Finally, the other edge of the specimen is cut, freeing the membrane completely from the bulk sample. The sample is then taken out of the FIB chamber, and using a very fine glass needle the free specimen is plucked from the trench and deposited on to a carbon-coated copper TEM grid for inspection in the microscope. As the materials used in this thesis were quite different in terms of physical and mechanical properties, different milling parameters had to be established for each sample. For example, low voltage, low current and low angle of incident beam were used for $MnBi_2Te_3$

as a soft material, while for $Fe_y(Se_{1-x}Te_x)$ films on a hard substrate such as MgO higher values of these parameters could be used.

Similar to other TEM sample preparation techniques, this method may induce changes to the specimen such as impurities (Ga penetration into the sample) and disruption of the structure (forming an amorphous thin layer around the sample), especially at in the high voltage mode. These effects can be minimized by using a low voltage (5 kV) with a low angle of incidence (2°) for final thinning. It is also important that the amount of imaging of the area is kept minimum in this single beam FIB at all stages of the process, because the sample is being slowly milled during imaging.

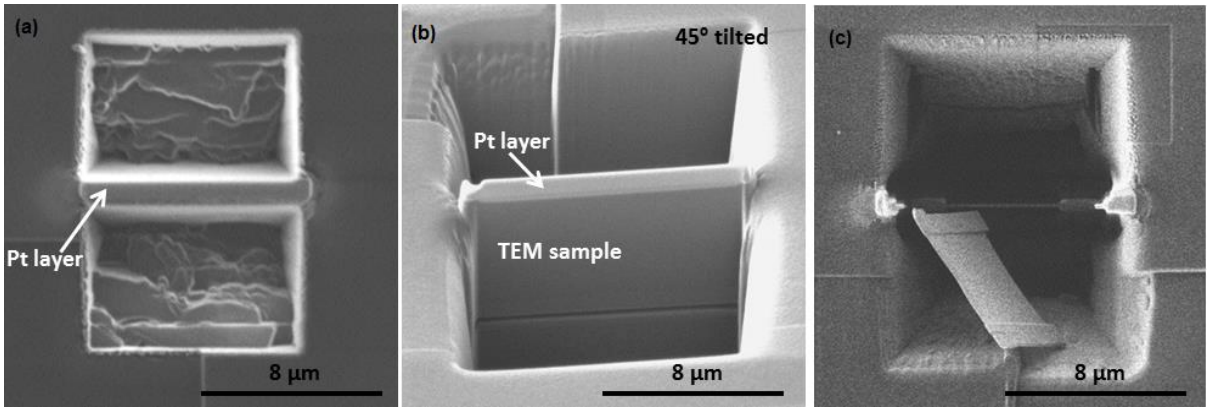

Figure 3.7: The procedure of cross sectional TEM sample preparation by FIB. (a) Depositing Pt protective layer and milling both sides of Pt layer to a depth of 8µm, (b) partly cutting around the sample (c) final thinning and completely cutting out the sample.

3.2.8. Atomic Force Microscopy

Atomic force microscopy (AFM) provides a nanoscale 3D profile of the surface by measuring forces between a sharp probe (<10 nm), supported on a flexible cantilever, and surface at very short distance (0.2-10nm). Depending on the measured parameter and relative position of the probe and surface, there are three different AFM modes; contact mode (<0.5 nm probe-surface distance), intermittent contact or tapping mode (0.5-2nm probe-surface distance) and non-contact mode (0.1-10 nm probe-surface distance). More information can be found in [14]. In

this work, contact mode in a JEOL JSTM 4200D AFM was used to investigate the surface topography of freshly prepared thin films. The AFM was calibrated using a standard sample having steps with specific height and the data was analysed using WSXM 5.0 software.

3.2.9. Electrical properties

Electrical properties of $Fe_y(Se_{1-x}Te_x)$ samples at low temperature were investigated using both magnetization measurements and transport resistivity measurements. In the superconducting state below T_C, the electrical resistance becomes zero and the characteristic diamagnetic behaviour appears.

3.2.9.1. Magnetic measurements

Magnetic susceptibility measurements presented in this thesis were performed using a Quantum Design MPMS-XL SQUID magnetometer (MPMS90). The MPMS system includes an integrated SQUID (which is a very sensitive magnetometer for the measurement of extremely subtle magnetic fields), cryostat (1.8-400 K), 7T superconducting magnet, and sample transport, together with a data acquisition system. It provides the means to measure the magnetic moment of a sample in a function of temperature and field.

The sample was mounted into a plastic straw, the diamagnetic moment of which is very small, and inserted coaxially inside the detection coils. A magnetic field is applied parallel to the c-direction of $Fe_y(Se_{1-x}Te_x)$ compound which is perpendicular to the substrate surface because the deposited films are mostly c-axis aligned. To obtain the correct value of the magnetic susceptibility the sample must be placed in the correct position relative to the detection coils inside the magnetometer (see Figure 3.8a). This was adjusted by applying a magnetic field (200Oe) to induce sufficient magnetic moments to the sample. The coils detect the magnetic

signals while the sample is moving through the detection coils. Using a graph (magnetic moment vs position), the best position for the sample was determined.

Two forms of susceptibility measurements zero field cooled (ZFC) and field cooled (FC) were used. For a ZFC measurement the sample is cooled from room temperature in as close to zero field as the apparatus allows. The data is recorded while the sample is warming through a series of temperatures. In FC measurements, the magnetic field is applied to the sample at a temperature above T_C and then the sample is cooled in that field. The data can be collected either on warming or cooling.

3.2.9.2. Resistivity measurements

A Physical Property Measurement System (PPMS) was used to examine the resistivity of the samples at low temperature. PPMS is a multifunctional probe with a series of different sample platforms. It can measure a variety of materials property measurements as a function of field (up to 14 T) and temperature (0.4 K-400 K). These include heat capacity, thermal transport, DC and AC magnetometry, resistivity and AC transport. For the experiments presented here the four-contact resistivity option was used. In this experiment, samples were mounted on standard PPMS sample holder (see Figure 3.8b) which has four contacts, one positive and one negative contact for current and voltage for each sample. Up to three samples may be mounted on this sample holder at one time. In a four-wire resistance measurement, current is passed through the sample via two current leads (usually terminals 1 and 4), and two separate voltage leads (terminals 2 and 3) measure the potential difference across the sample. Thus resistivity is calculated by Ohm's law.

To minimize the resistance between the leads and the contact surface, high conductivity silver paint was used to connect silver wires to the electrical contacts. Pre-measurement was carried out at room temperature to test the contacts. The contact resistance were measured as a function of temperature in a Cryodyne closed cycle He cryostat during the cooling procedure.

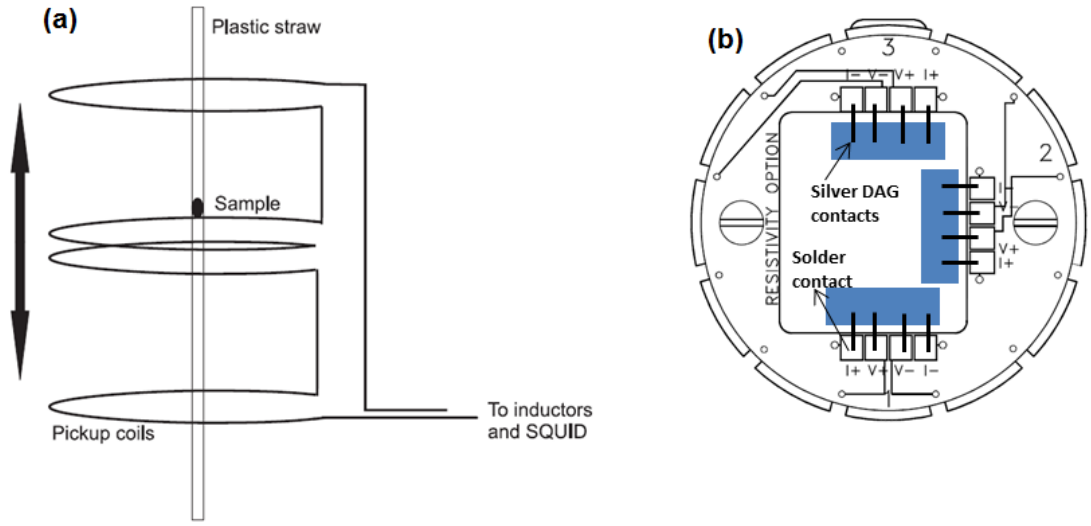

Figure 3.8: Schematic diagram showing (a) the relative positions of the sample and three coils inside SQUID (b) the PPMS sample holder.

3.3. References

1. K. Wasa, M. Kitabatake, H. Adachi, *Thin film materials technology: sputtering of compound materials*, 2004, Norwich, NY, Heidelberg: Springer.
2. J. Sarkar, *Sputtering Materials for VLSI and Thin Film Devices*, 2013, William Andrew.
3. A. Gunther, C. Kant, H.A. Krugvon Nidda, V. Tsurkan, A. Loidl, *Improvement of superconducting properties of $FeSe_{0.5}Te_{0.5}$ single crystals by Mn substitution* Supercond. Sci. Technol., 2011, 24: p. 045009.
4. B. Rainer, *Sputtering by Particle Bombardment*, 2007, Wolfgang.
5. Y. Mizuguchi, Y. Takano, *Review of Fe Chalcogenides as the Simplest Fe-Based Superconductor*, Journal of the Physical Society of Japan, 2010, 79 (10): p. 102001.
6. B.D. Cullity, *Elements of X-Ray Diffraction*: Addison-Welsey Publishing company.
7. S.C. Speller, *Microstructural development and control in $Ti_2Ba_2CaCu_2O_8$*, DPhil Thesis, Materials Department, 2004, Oxford University.
8. D. Harris, *Quantitative chemical analysis*. 6th ed, 2002, W. H. Freeman.
9. D.B. Williams, *Transmission Electron Microscopy, A Textbook for Materials Science*, 1996, New York: Springer.
10. B. Fultz, *Transmission Electron Microscopy and Diffractometry of Materials*. 3rd ed, 2007, New York: Springer.
11. P.B. Hirsch, *Electron Microscopy of Thin Crystals*, 1967, Krieger Publishing Company.
12. R.F. Egerton, *Electron Energy-Loss Spectroscopy in the Electron Microscope*. 3rd ed, 2011, springer.
13. R. Mas-Balleste, et al., *2D materials: to graphene and beyond.* Nanoscale, 2011. 3(1): p. 20.
14. P. Jonathan, *Atomic Force Microscopy*, 2010, OUP Oxford.

Chapter 4: Fabrication and characterization of $Fe_ySe_{1-x}Te_x$ thin films

This chapter deals with the fabrication of $Fe_ySe_{1-x}Te_x$ thin films by sputtering and characterization of the deposited films by a wide range of techniques. An introduction on the significance of $Fe_ySe_{1-x}Te_x$ thin films, their properties and the objectives of this chapter was given in chapter 2. The experimental methods used were also explained in detail in chapter 3. Here the results will be described in different sections as follows. Compositional analysis will be first presented since it is the major issue to be controlled, and then the results on phase analysis, texture development, microstructural TEM analysis, surface morphology and superconducting properties will be discussed respectively, followed by conclusions and suggestions for future work.

4.1 Substrate position relative to target

In the sputtering process, the position of substrate relative to target is very important and properties of the deposited films can be varied by even a small change in the substrate position [1, 2]. To explore how significant this issue is in my sputtering system, four MgO substrates were loaded onto the holder in different positions as shown in Figure 4.1a, and Fe(Se,Te) films were simultaneously deposited on all four substrates at 300°C for 30 mins from a target with nominal composition of $Fe(Se_{0.4}Te_{0.6})$. XRD patterns along with chemical compositions of these four films are reported in Figure 4.1b and c. As can be seen, the films grown on positions 2 and 3 are very similar in terms of both phase and composition. However, in positions 1 and 4, the XRD peaks corresponding to the films are weaker suggesting that there is lower amount of transferred atoms in these positions, i.e. the films are thinner. This was also confirmed by the EDX data where higher Mg/Fe ratios were obtained for positions 2 and 3 compared to those of position 1 and 4 (146 versus 99). We can explain this by the sputtered particles having an angular distribution above target resulting in a smaller number of sputtered atoms reaching the substrates further from the centre [3-5]. The substrates further from the centre also show a

lower Te content according to the EDX data in Figure 4.1c. This may be due to the considerable difference between the mean free paths[1] of Te and Se/Fe. Te has the shortest mean free path (will be shown later) leading to less Te content on the outer substrates. However, no obvious change is observed in films grown on the middle positions (2 and 3). Therefore all the samples fabricated later on in this work were loaded in these two positions.

It can be also noted that in all of these films, the contribution of MgO substrate in XRD pattern is extremely high indicating that these films, grown with a 30 minute sputtering time, are very thin. The thickness of these films measured by cross-sectional TEM was found to be only 25-30 nm. Later films were deposited for longer times to produce thick enough films for microstructural characterization.

4.2 Compositional analysis of deposited films

In any sputtering process, as described in chapter 2, the composition of the sputtered films depends on sputtering conditions and usually will be different from that of the target because of different sputter yields for various elements, re-sputtering of atoms from the substrate and differential evaporation from a heated substrate. Therefore it is necessary to consider these parameters to determine the precise target composition needed to grow films with exactly the desired composition. Figure 4.2 shows the nominal compositions of three targets made in this work as well as the measured compositions of the films grown from these targets. For calculating the composition of the films, the ratio of elements was considered to minimize the error of measurement. For example, for the formula $Fe_y(Se_{1-x}Te_x)$, the value of y is calculated by $\frac{Fe}{(Se+Te)}$, and the value of x is calculated by $\frac{Te}{(Se+Te)}$. The level of uncertainty for x and y is about 0.02-0.04. According to the literature, films of $Fe_{1.01}(Se_{0.5}Te_{0.5})$ with slightly deficient

[1] The average distance travelled by the sputtered atoms in the sputtering chamber.

chalcogen stoichiometry and substitution of 50at.% Se by Te show the highest transition temperature [6-8]. This stoichiometry is indicated by the green spot in Figure 4.2. The red spots in these diagrams correspond to the target compositions and each black spot is the average composition of a particular film. As can be seen, the films grown from the first target show tendency towards the Fe corner of the diagram (i.e. they have less Se and Te compared to the target composition).

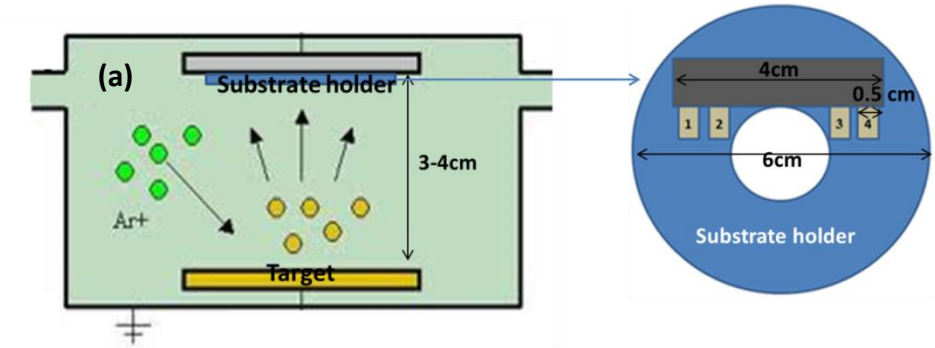

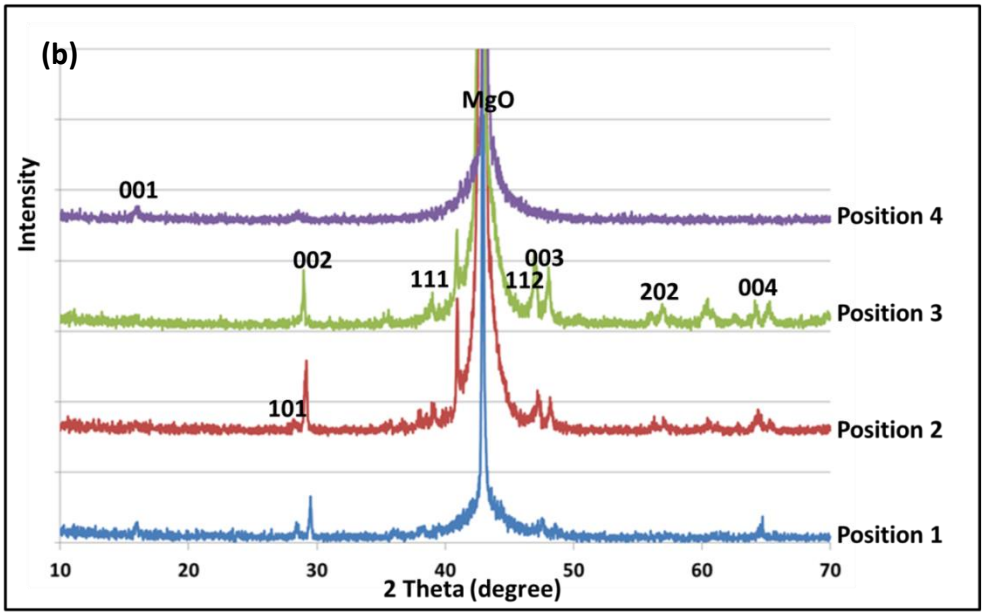

(c)	Position 1	Position 2	Position 3	Position 4
Composition	$Fe_{0.95}(Se_{0.8}Te_{0.2})$	$Fe_{0.85}(Se_{0.6}Te_{0.4})$	$Fe_{0.87}(Se_{0.6}Te_{0.4})$	$Fe(Se_{0.8}Te_{0.2})$

Figure 4.1: (a) Schematic diagram of the position of MgO substrates relative to the target, (b) XRD patterns of the films grown at 300°C for 30 mins in different positions, (c) compositions of these four films normalized to a stoichiometry of $Fe_y(Se_{1-x}Te_x)_1$. Normalization has been done according to this stoichiometry because the Fe/(Se+Te) ratio is an important parameter for superconductivity in this compound.

Using this analysis, the second and third targets were made with more Se and Te compared to target 1 to achieve the right composition in the films. The films grown from the second target still contain too high an Fe content, but when fabricated from target three, the films seem to be very close to the desired composition. However, the data still shows a large scatter in comparison. Possible reasons for obtaining these big chemical variations from film to film are presented in the next section.

It was also found by careful EDX analysis that the Fe content increases with Te. Figure 4.3 shows the variation of Fe content (y) in the deposited films as a function of Te content (x) according to the $Fe_y(Se_{1-x}Te_x)$ formula. It is seen that the Fe content clearly increases with increasing Te. As Te atoms are larger than Se atoms, substitution of Se by Te leads to an expansion in the unit cell allowing more Fe into the structure. It has been reported that excess Fe in Fe(Se,Te) occupies the interstitial site (showed in the inset in Figure 4.3) [9]. In this structure, if more Te atoms are substituted for smaller Se atoms, the unit cell will be expanded making more spacious interstitial sites for extra excess Fe. A similar relationship between Fe and Te content has also been observed in other work [10] and explained by reference to the equilibrium phase diagrams of Fe-Te and Fe-Se where the stable composition range for β- FeSe is narrow, ($1.02<y<1.04$), whereas β-FeTe is stable over a wider range ($1.08<y<1.17$) [10].

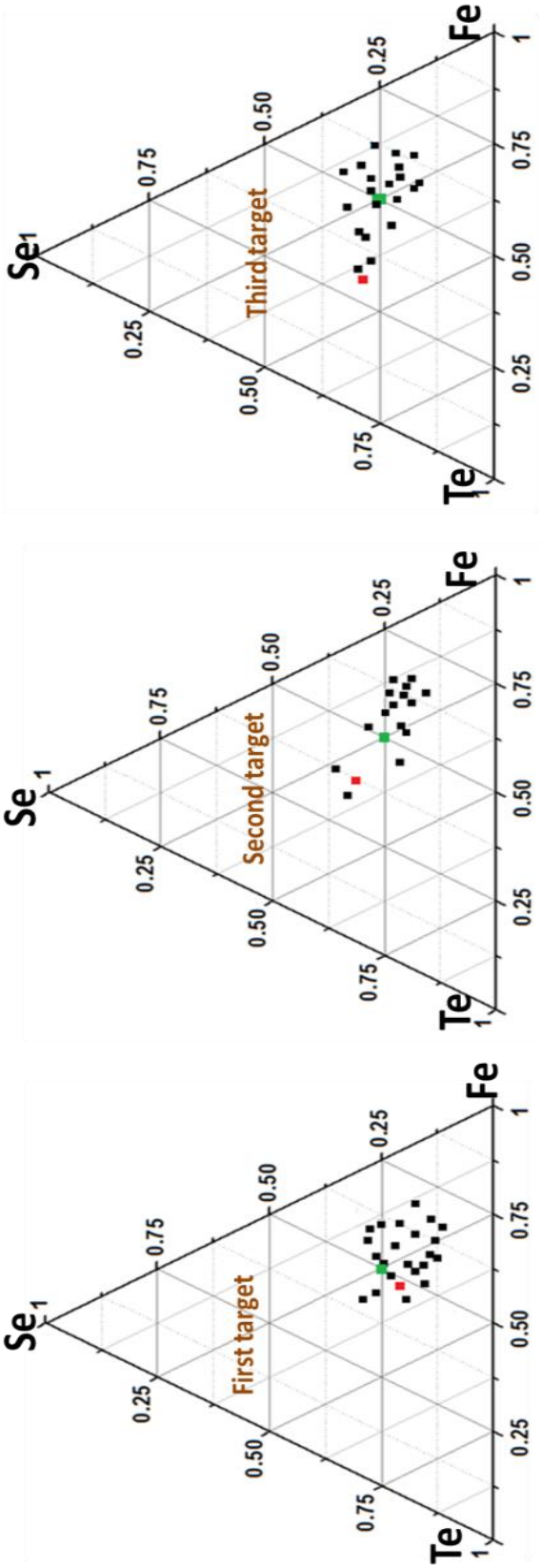

Figure 4.2: Chemical composition of the films grown from three different targets. The red spot indicates the target composition based on the weighted powder mixture, the green spot indicates the desired composition for the films and each black spot is the average composition of each deposited film measured by doing SEM/EDX over 5 large regions (100μm×100μm) and reporting the average value. The level of uncertainty in these measured compositions is ~0.02-0.04. Compositional variation from film to film is larger than the error bar for each film.

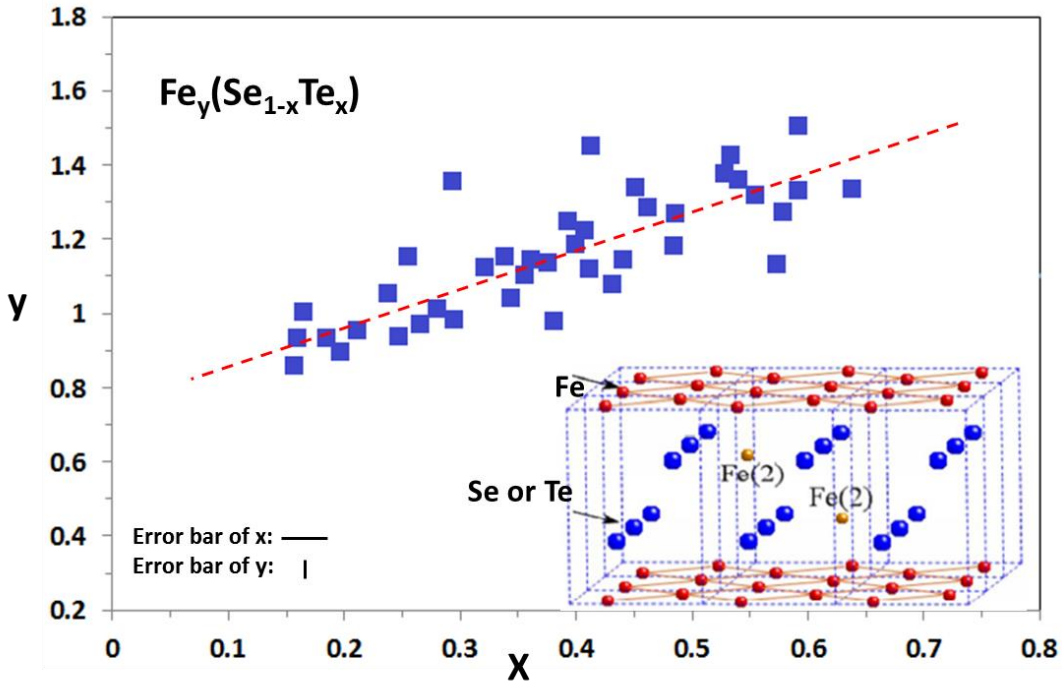

Figure 4.3: Fe content (y) as a function of Te content (x) according to $Fe_y(Se_{1-x}Te_x)$ formula, (inset: Interstitial sites for excess iron in the tetragonal β-phase Fe(Se,Te) structure).

4.2.1 Chalcogen deficiency

The compositional variation between the films and the target from which they are deposited is due to different transfer rates for different elements. The transfer rate was calculated for Fe, Se and Te using the following equation.

$$\text{Transfer rate of element A} = \frac{\text{atomic\% of A in film}}{\text{atomic\% of A in target}} \qquad \text{Equation 4.1}$$

As Figure 4.4a shows, when films are grown onto unheated substrates (in this case the substrate temperature during sputtering was measured to be 60°C) under the standard power and gas pressure conditions used in this work, Te has the lowest transfer rate (0.84) and Fe has the highest transfer rate (1.15), probably due to differences in their atomic mass as Te is the heaviest (127.6 g.mol^{-1}) and Fe is lightest (55.8 g.mol^{-1}). In sputtering processes, the heavier atoms generally have lower sputtering rates as they need more energy to be removed from the target and moreover the scattered heavy atoms have lower mean free paths inside the chamber

[2]. Therefore, the difference in atomic mass is one reason for the fabrication of Fe-rich thin films by this method.

(a)	Fe	Se	Te
Transfer rate at 60°C	1.15	1.05	0.84
Transfer rate at 305°C	1.16	0.98	0.43
Transfer rate at 310°C	1.24	0.88	0.31
Transfer rate at 320°C	1.24	0.85	0.15

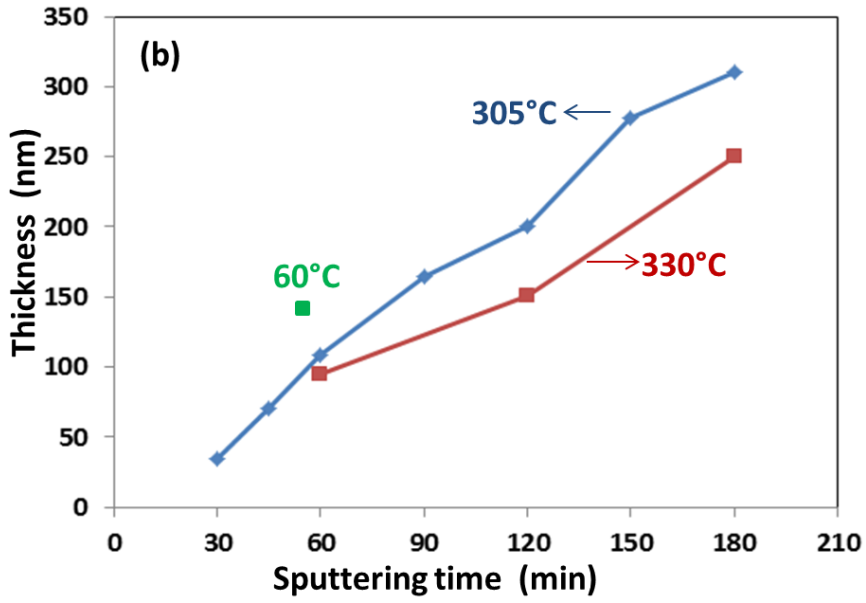

Figure 4.4: (a) Measured transfer rates of Fe, Se and Te at different temperatures, (b) Thickness of the deposited film (measured from cross-sectional TEM images) as a function of sputtering time.

Other mechanisms are involved when films are grown onto the heated substrates at higher temperatures. The transfer rate of both Se and Te decreases remarkably (as shown in Figure 4.4a) due to the large difference between the vapour pressures of Se and Te and that of Fe. This also results in significantly thinner films at higher substrate temperatures as the graph of thickness against sputtering time (Figure 4.4b) shows. The deposition rate at 305°C is 1.7 nm/min (the slope of the graph), while it decreases to 1.4 nm/min at 330°C because re-evaporation of the deposited atoms is higher, especially for the high vapour pressure elements (Te and Se). The vapour pressures of these three elements as a function of temperature are

plotted in Figure 4.5. Te and Se clearly show much higher equilibrium vapour pressures. All the films in this work were grown at 2×10^{-2} mbar Ar. According to the graph the vapour pressures of Se and Te exceed this value when the substrate temperature is higher than ~227°C (for Se) and ~327°C (for Te). It means that above these temperatures, Se and Te are likely to evaporate from the surface of the substrate resulting in the films containing even higher Fe concentrations. This issue is a major restriction for growing Fe(Se,Te) films at high temperatures in spite of achieving much better crystallinity and more uniform composition (see below). High-temperature grown films were found to be more uniform in chemical composition due to the higher mobility of atoms on the substrate surface at higher temperatures.

In the literature, deposition of films with a different composition from that of target by sputtering has been reported in other compounds containing elements with different vapour pressures [3, 11, 12]. However, sputtering has been still reported as a suitable way of producing thin films of these compounds, as other methods of thin film processing are performed at even higher temperatures [3].

It should be noted that in my sputtering system, a systematic relationship between composition and temperature cannot be determined and intentionally controlled due to the alteration of target composition during sputtering as discussed below.

4.2.2 Compositional change of target surface

As mentioned in the experimental methods chapter, targets were made by ball milling followed by cold pressing. Figure 4.6 shows an XRD pattern and SEM images of one of the fabricated targets. In the XRD pattern, only peaks corresponding to elemental Te, Se and Fe can be seen. There is no sign of impurities or other compounds indicating that no reaction happens during target processing and then these elements exist in their elemental forms or dilute solid solutions.

In the backscattered image, these individual elements appear in two obvious contrasts with the bright regions corresponding to heavy Te.

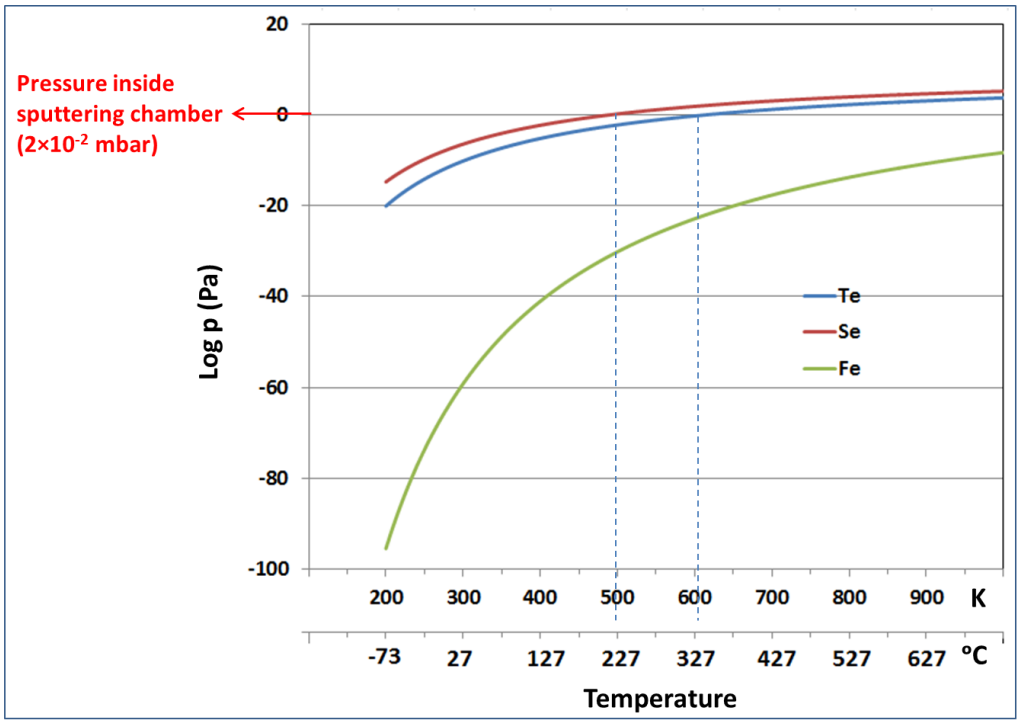

Figure 4.5: Equilibrium vapour pressure of Fe, Te and Se versus temperature. This graph is drawn according following equations: Log P_{Te}=9.72-5960/T [13], Log P_{Se}=10.21-4989/T [13], Log P_{Fe}=12.01-21723/T [14].

In an attempt to understand the reasons for the large data scatter in the composition of the grown films, it was thought that the composition of target might change during sputtering. To investigate this, three thin films were grown in a sequence under the same sputtering conditions from a fresh target and then the target was taken out from sputtering chamber for compositional analysis. As it can be seen in Figure 4.7, after 6 hrs sputtering (2hrs for each film), the target surface composition was found to be notably different from the initial composition, especially in that the Se and Te contents remarkably decrease compared to the Fe content due to their high vapour pressure and target heating. In general, target heating happens during sputtering because of the bombardment of the target by high energy Ar ions. Most of the power input to the system also appears as target heating. This temperature increase in the target can lead to damage of the

target, including compositional alteration. Enhancement of the target temperature has been reported in several works [12, 15, 16], and for example an excessive local high temperature of 400°C has been found by Kelly et al [16].

The compositional change of the target can also occur due to the different ejection rates of the components from the target, and targets are usually enriched with heavier atoms. For example, Pt enrichment in a target surface containing Pt and Si has been observed due to the higher ejection for lighter Si [17]. Therefore, the difference in both vapour pressure and ejection rate results in an alteration of the target surface composition, but the former mechanism seems to be much more dominant in my sputtering targets leading to Fe-enrichment of the target during sputtering similar to other reports where the effects of ejection rate variations are smaller compared to those of vapour pressure variations [2].

This alteration in target composition causes film-to-film compositional variations even for films deposited under the same processing conditions, and makes it impossible to intentionally control the composition of deposited films over an extended set of experiments.

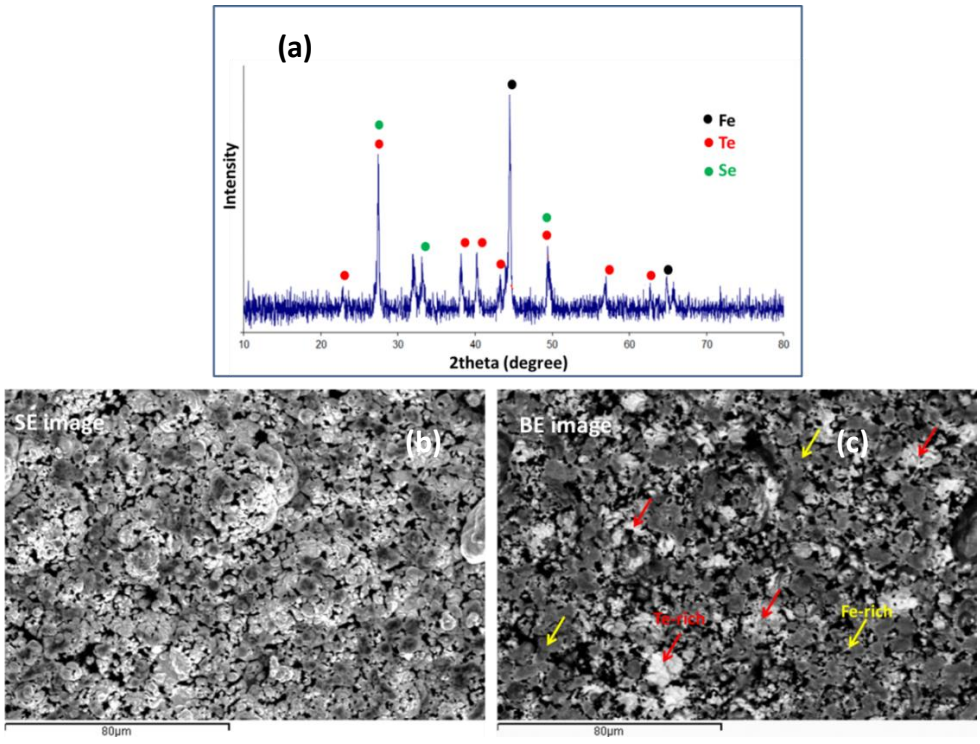

Figure 4.6: (a) XRD pattern of a typical fabricated target, (b) secondary electron and (c) backscattered-electron SEM images of the target surface.

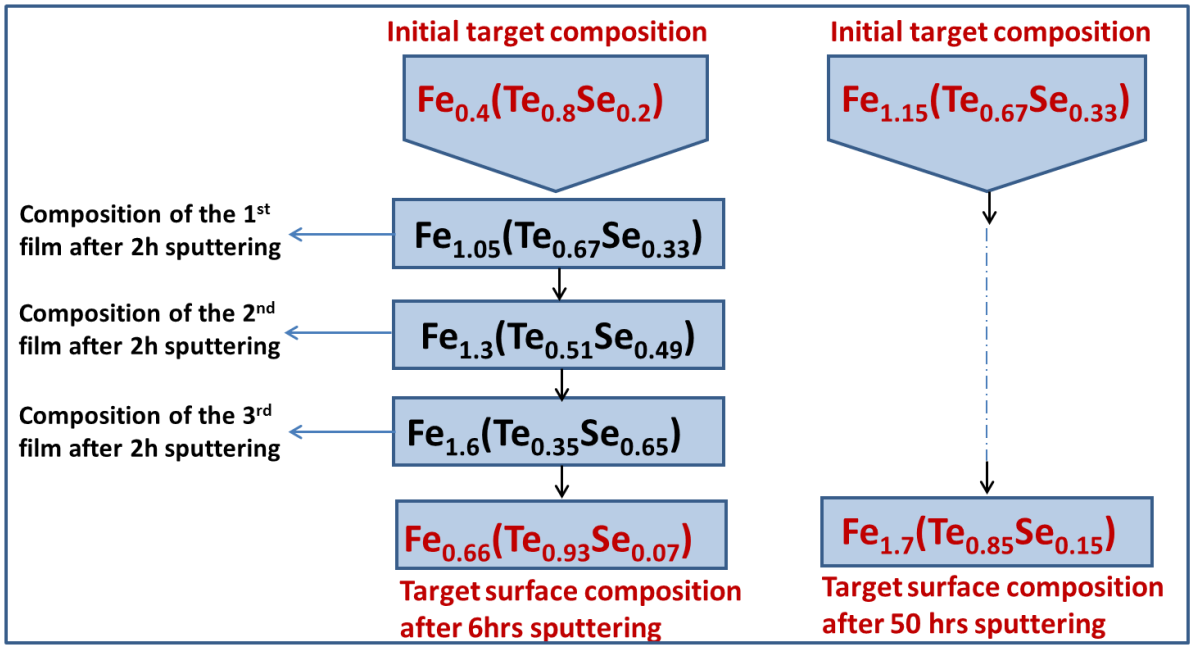

Figure 4.7: The composition of the films grown on a LiF substrate at 310°C for 2 hrs, and the change of target surface composition after 6hrs and more than 50 hrs sputtering.

4.3 Phase analysis of the deposited films

In sputtering deposition, phase development in the films depends strongly on the substrate temperature. In order to investigate how crystallinity develops in different temperatures in sputtered Fe(Se,Te) films, a large number of films were deposited for 90 minutes at various substrate temperatures in the range 150-400°C. XRD patterns of these films are shown in Figure 4.8. It can be seen that films grown at 150°C and 200°C are not Fe(Se,Te) phase and only MgO peaks are observed in their XRD patterns. The crystalline peaks corresponding to the tetragonal PbO-structure of the 11-phase appear in films grown at temperatures above 250°C. At this temperature, the film is not perfectly epitaxial with the single crystal substrate as a number of (*hkl*) peaks are observed indicating that the sample is polycrystalline. However, c-axis alignment seems to be more dominant because the intensity ratios of the (*00l*) peaks to the other peaks are higher than expected from the powder diffraction data [18]. By increasing the temperature up to 300°C, more (*00l)* peaks with higher relative intensity are observed showing

that the sample develops a stronger c-axis alignment. This can be also seen by comparing the relative intensity of MgO substrate peaks to the film ($(200)_{MgO}/(001)_{Fe(Se,Te)}$). Above 300°C, only the (*00l*) reflections are observed, implying that the films are pure phase and preferentially oriented along the *c*-axis, although the intensity and sharpness of the peaks reduces with further increase in temperature. Moreover, at high temperatures (330°C), traces of the (101) peak can be seen as a result of growing a number of small off-axis grains at high temperatures. This suggests that the sample is no longer perfectly c-axis aligned at these temperatures.

According to these XRD patterns, it can be suggested that the crystallization temperature for these films is about 250°C. In the range of 250-300°C the film is polycrystalline with high tendency to align along c-axis. In the range of 300-320°C, only c-axis aligned films are grown and above 330°C, again off-axis grains appear.

It can be also seen that a considerable (*00l*) peak shift to higher angles occurs with increasing temperature which means that the *c*-axis length of tetragonal structure decreases at high temperatures. Two reasons might be responsible for the smaller c-axis at higher temperatures. First, the presence of less Te (which is larger than Se) in the tetragonal structure at higher temperatures confirmed by EDX data, and second by a uniform compressive strain along the c-axis induced by epitaxial growth of Fe(Se,Te) on the MgO substrate. In this case, compressive strain along the c-axis is expected because Fe(Se,Te) (a=3.78Å) has smaller a-axis parameter compared to that of the MgO substrate (a=4.21Å) resulting in in-plane tensile strain and uniform compressive strain along the c-axis if the films is epitaxially grown on the MgO substrate. However, a low content of Te seems to be more dominant reason for the XRD peak shift because at higher temperatures the texture becomes poor as seen in Figure 4.8 and strain is likely to be relieved.

Furthermore, it was found that if the films are deposited at much higher temperatures (e.g. at 400°C), hexagonal δ-FeSe appears in the XRD pattern as shown in Figure 4.8. According to the

Fe-Se phase diagram, β-FeSe is a low-temperature phase and hexagonal δ-FeSe is formed at high temperature. Hexagonal δ-FeSe has been detected at high temperatures in other works as well [19]. However, since hexagonal FeSe is non-superconducting, the aim is to avoid formation of this phase. Therefore, it is suggested that the optimum range of temperature for growing pure tetragonal β-Fe(Se,Te) is 250-400°C.

Comparing this range of temperatures with the literature, the potential of sputtering can be noted for the fabrication of pure β-Fe(Se,Te) phase without high-temperature impurities (e.g. hexagonal phase) and in a fairly high degree of crystalline alignment. In the literature, a large number of articles have found it challenging to fabricate pure β-Fe(Se,Te) phase in both single crystals and thin films grown by pulsed laser deposition [20-23], and reported that the hexagonal phase appears as an impurity if the processing temperature exceeds about 400°C [21], and they found it difficult to achieve a high degree of crystallographic alignment below 400°C. However, as my thin films show, sputtering allows me to fabricate the β-Fe(Se,Te) phase with a high degree of crystallinity at a relatively a wide range of low temperatures. In the following section, the texture development of the films grown in this range of temperature is discussed.

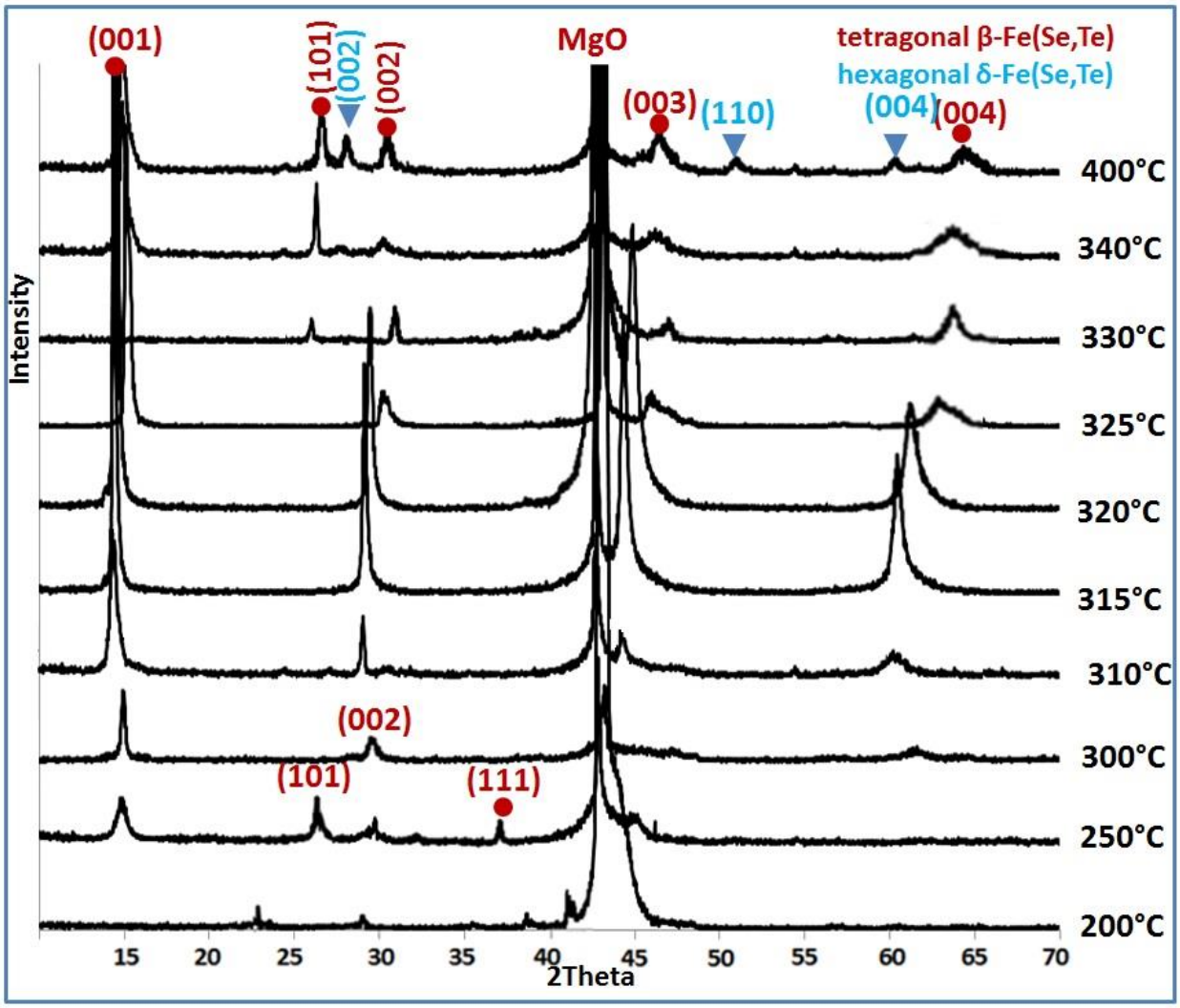

Figure 4.8: XRD patterns of the films deposited on MgO substrates at different temperatures for 90 minutes sputtering. The peaks indexed by (●) correspond to the tetragonal β-Fe(Se,Te) phase and the peaks indexed by (▼) correspond to the hexagonal δ-Fe(Se,Te) phase..

4.4 Texture development

In high-temperature superconductors, grain boundaries reduce J_C, however the effects of grain boundaries on J_C is not clear for the low-temperature superconductors, and it seems that in some cases, depending on the properties of the grain boundaries, they can act as pinning sites and lead to an increase in J_C. Therefore the presence of grain boundaries in the films (or crystallographic texture) is significant. In order to investigate how crystallographic texture develops in the deposited films under various processing conditions, texture of the films was

studied, and it was found that substrate temperature, film thickness and choice of substrate are highly influential in the texture development of the Fe(Se,Te) films.

4.4.1 Temperature dependence

(101) pole figures of the grown films were obtained by texture XRD to study in-plane mis-orientation in films deposited at various temperatures. As can be seen in Figure 4.9, in-plane alignment improves by increasing the substrate temperature from 305°C to 315°C. At 320°C two sets of in-plane alignment within 45° are observed, and finally at 330°C the films are no longer in-plane aligned. This trend can be also seen in Figure 4.9b where full width at half maximum (FWHM) of the (001) peak in rocking curves and the (101) peak in the φ scan are plotted as a function of temperature for comparison. It can be suggested that the window of temperatures for obtaining epitaxial thin films is 305-320°C. It is worth mentioning that the epitaxial temperature also depends on deposition rate and increases with increasing deposition rate. However, this parameter was kept the same in this work by deposition of films at a specific Ar pressure (2×10^{-2} mbar) and power.

It is found from Figure 4.9 that the in-plane orientation is more temperature-dependent compared to the out-of-plane orientation. The c-axis orientation is usually observed in most of these deposited films. This indicates that the films obey the empirical Bravais' law which says crystal faces are most likely to develop along those planes with the highest atomic density [24]. In the tetragonal Fe(Se,Te) structure, the (00l) plane has the highest atomic density, and so if the temperature is high enough to provide sufficient mobility for the adatoms on the surface of the substrate, the initial islands are formed by the adatoms arranged in the (00l) plane resulting in c-axis aligned films. This c-axis orientation in Fe(Se,Te) thin films has been reported in other work [20, 23, 25-30].

In-plane alignment is drastically influenced by temperature, and from Figure 4.9 it seems that the optimum temperature for the highest degree of alignment is 315°C. The reason for reduction of crystallinity at high temperatures was found to be the formation a thin layer between the substrate and the film.

Figure 4.10 shows cross-sectional TEM micrographs of thin films deposited at different temperatures. At 310°C the interface between the film and the substrate is smooth and the film grows immediately on the substrate. In contrast, at 320°C, a thin reaction layer exists between the film and substrate. By increasing the temperature to 330°C, the thickness of this layer increases. The nature of this layer is unclear but presumably it is an amorphous layer possibly formed due to the mutual diffusion between thin films and the substrate. The presence of this layer at the interface interferes with texture development in the film and leads to in-plane mis-orientaion. Lowering the substrate temperature reduces this interaction allowing the absorbed atoms to follow the atomic orientation of the substrate.

In the literature, among many Fe(Se,Te) thin films grown by pulsed laser deposition, most of them have been reported to grow directly on the substrate with no interface layer, but, an amorphous-like layer has been detected in [26, 31, 32] and suggested to be a result of oxygen penetration from the substrate to the film [31]. These authors only found this layer on yttria-stablized zirconia substrate (YSZ) [26] and LSAO substrates [32] while in both works MgO substrates were also used. The fact that this layer is absent on MgO substrates in other work, but it is present in my samples can be due to the different processing methods. In sputtering, in contrast to pulsed laser deposition, the substrate is bombarded by high energy particles which can result in a damaged layer formation at the top surface of the substrate. The mutual diffusion/reaction between this damaged surface and the film would be more considerable especially when the temperature is high. Therefore, the formation of this layer in sputtering process is more likely.

In addition to the higher mobility of the atoms and the formation of the interface layer between the film and substrate at higher temperatures, the different stoichiometry of the films at high substrate temperatures can be another reason for loss of the texture. As it has been shown above, the high-temperature deposited films are Fe-rich, and this excess Fe content in the film can destroy the epitaxial growth of the Fe(Se,Te) structure.

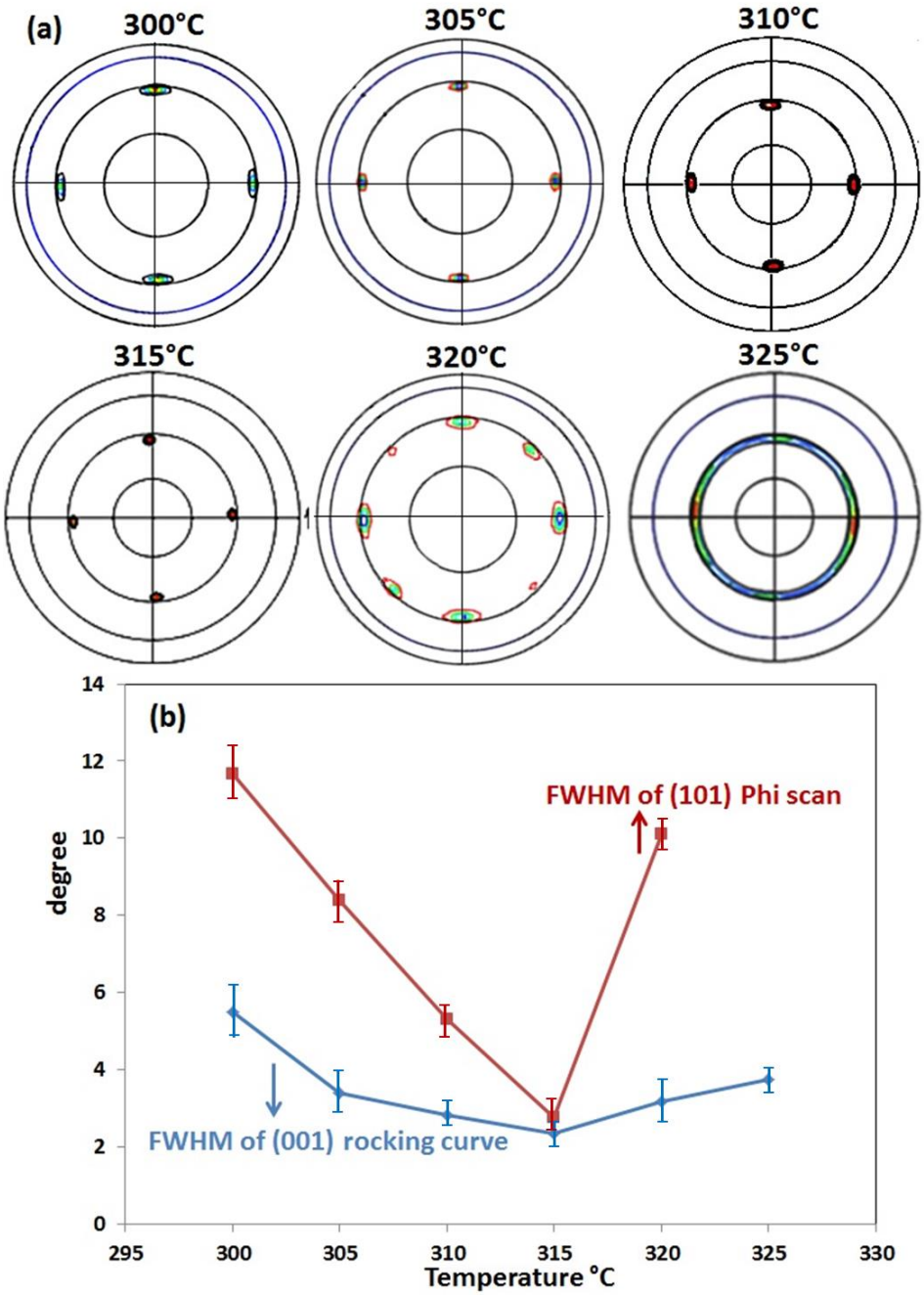

Figure 4.9: (a) (101) pole figures obtained from texture XRD analysis of the films grown on MgO substrates at different temperatures, (b) FWHM of (001) peak in the rocking curve and FWHM of (101) peak in the φ scan as a function of temperature.

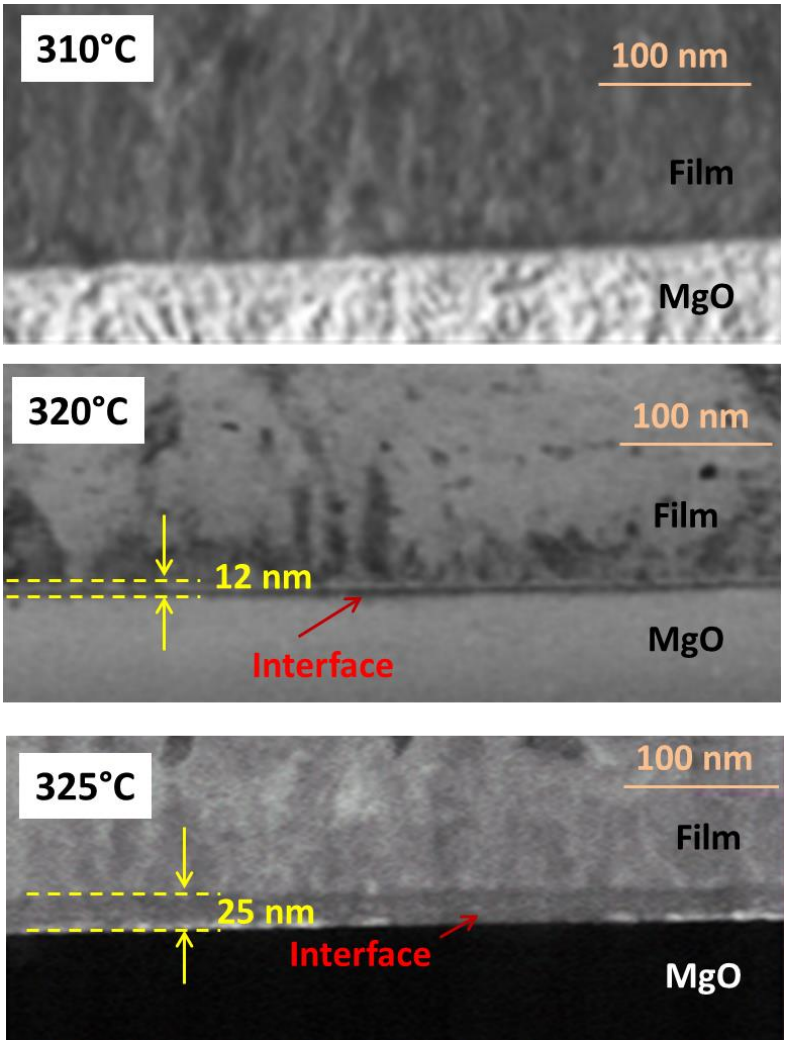

Figure 4.10: Cross-sectional TEM micrographs of Fe(Se,Te) films grown on MgO substrates at different temperatures showing the formation of an interface layer (red arrows) between the substrate and the film at high temperatures. At low temperature, there is no extra layer in the substrate/film interface, however; at higher temperatures, a layer is formed in the substrate/film interface and the thickness of this layer increases at higher temperatures. The dark regions observed in the films in these images are possibly due to the variation in either chemical composition (different Se/Te ratio or different oxygen level as a result of diffusion form the substrate to the film confirmed later) or crystallographic orientation.

4.4.2 Thickness dependence

In addition to temperature, thickness was found to be influential on the texture of the deposited films. To study the effect of thickness, three films were grown on MgO substrate at the same substrate temperature (315°C) but for different sputtering times. Figure 4.11 shows TEM cross-sectional images of these films along with their (101) pole figures. Sputtering for 45 mins

results in a uniform single crystal film with a thickness of 70 nm. Sputtering for 90 mins leads to a 155nm-thick film with two in-plane orientations. In the TEM micrograph of this sample, two different columnar regions with sharp boundaries parallel to the c-axis can be seen in different contrasts. These regions represent the two in-plane orientations detected by XRD texture in this sample. Finally at a thickness of 310 nm, no indication of in-plane alignment is observed and the film is randomly in-plane aligned, but the majority of the grains are still parallel to the c-axis. The TEM micrograph of this sample shows more random features in different contrasts indicating that more mis-oriented grains exist. Moreover, micro-cracks are formed along the c-axis in this sample at a distance of ~157 nm from the film/substrate interface and extend to the surface of the film. It can be suggested that the critical thickness (t_C) for epitaxial growth of Fe(Se,Te) thin films on MgO substrate is about 75nm. As long as the film thickness (t) is smaller than t_C, the film will keep its coherence with MgO substrate and maintain a fully strained layer. When $t > t_C$, lattice distortion and shear strain originating from the epitaxial growth increases and will be partially relaxed by the appearance of in-plane grain boundaries. When $t >> t_C$, a complete relaxation occurs by the formation of more grain boundaries, microcracks and holes along the c-axis.

To my knowledge the relation between the thickness of Fe(Se,Te) and texture has not been studied previously for MgO substrate. Bellingeri et al studied the relation between epitaxial strain and film thickness for Fe(Se,Te) films grown on LAO substrates in different thicknesses (9-420nm) and found different values for epitaxial strain and transition temperature in different thicknesses [28]. However, texture development with thickness is not clear in their thin films.

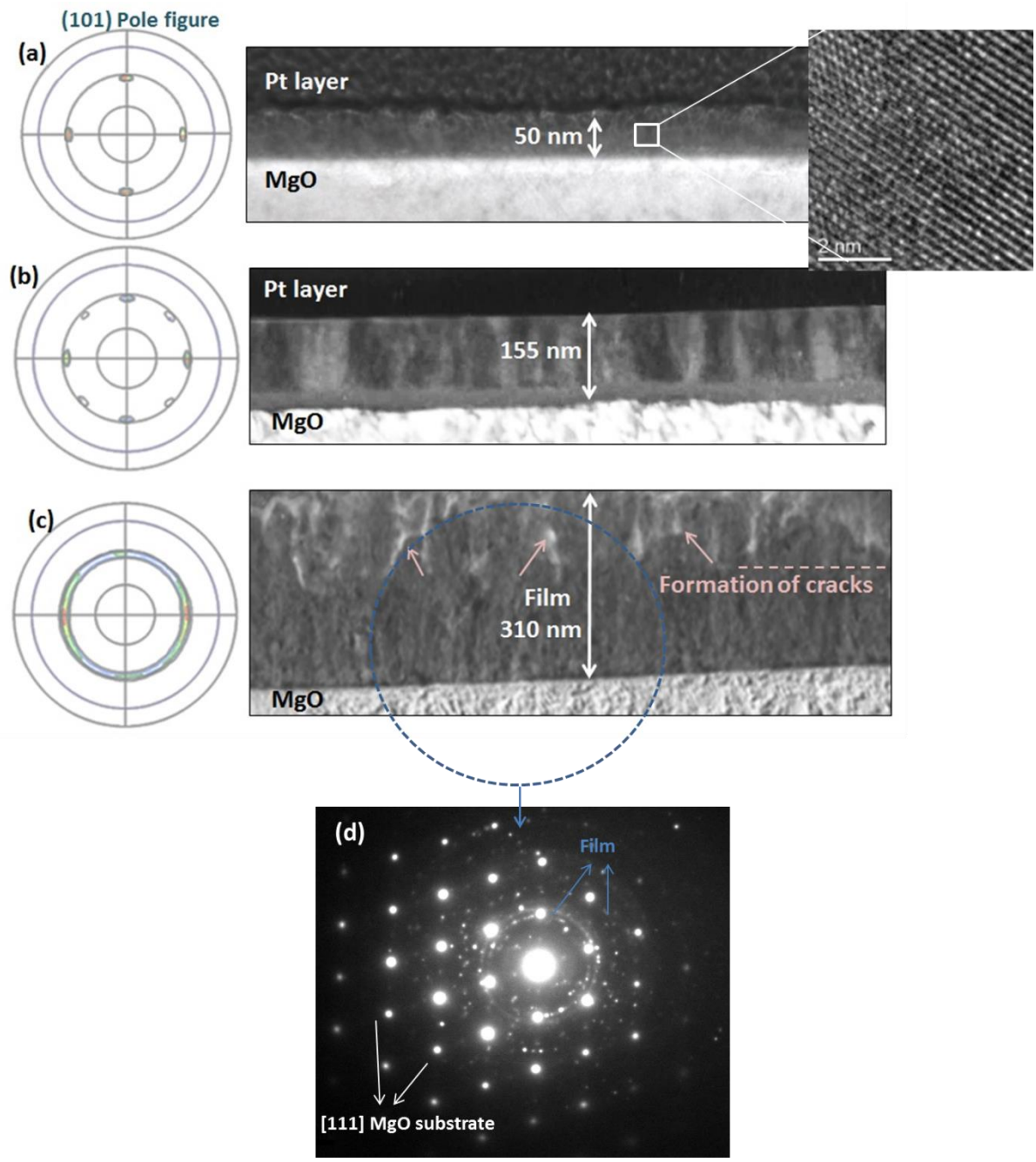

Figure 4.11: TEM micrographs and (101) pole figure of the films deposited on MgO substrates at 315°C for different sputtering times, (a) 45mins, (b) 90mins, (c) 180 mins showing that with increasing sputtering time (film thickness), crystallographic orientation of the films decreases. (d) diffraction pattern of the indicated region covering both substrate and film showing that the film is polycrystalline after 180 minutes of sputtering.

The detailed studies of Fe(Se,Te) thin film growth on MgO substrate are summarized in Figure 4.12. It can be suggested that the crystallization temperature for growing polycrystalline Fe(Se,Te) is 250°C, and temperature window for epitaxy is 305-320°C. The optimum

temperature and thickness for having the best crystallinity are about 315°C and 70nm respectively. In most cases the growth of Fe(Se,Te) films does obey Bravais' empirical law and show a c-axis orientation. Other parameters such as deposition rate and gas pressure also affect the texture development of these films and can be considered as good areas for future work.

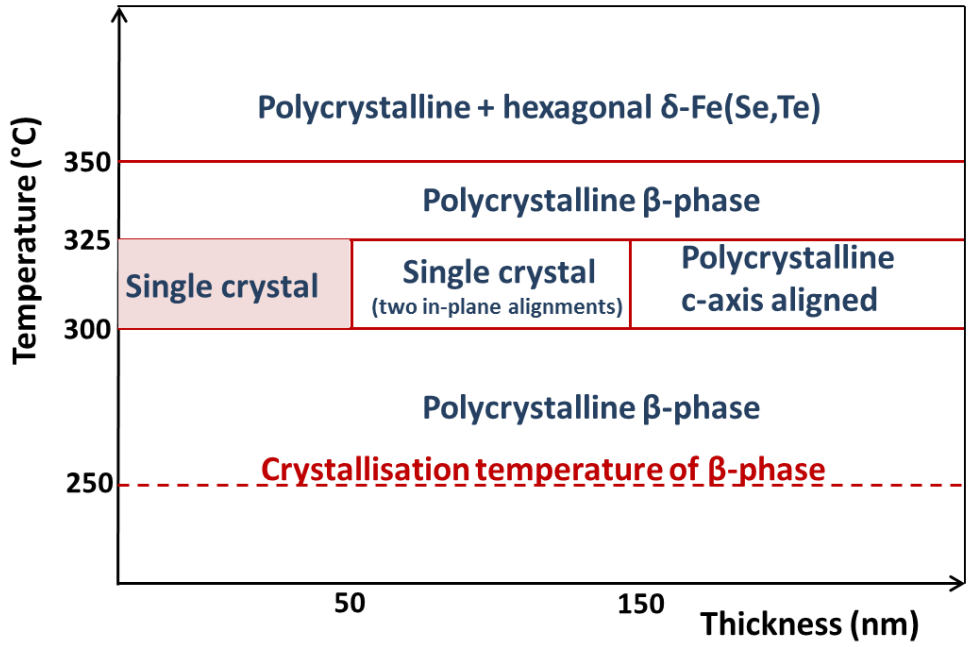

Figure 4.12: Evolution of the tetragonal β-Fe(Se,Te) phase in thin films deposited on MgO substrates as a function of processing conditions (temperature and thickness).

4.4.3 Substrate

The crystal orientation of the epitaxial Fe(Se,Te) thin film is also dependent on the substrate. Once the optimum conditions (temperature and thickness) for the best crystallinity of the films on MgO substrates were determined (T:315°C and sputtering time:90mins), Fe(Se,Te) thin films were grown at these optimum processing conditions on other substrates, including LiF, CaF_2, LAO, $SrTiO_3$ and LSAT, to study the effects of substrate on the orientation of the deposited films.

Figure 4.13 shows Phi scans of the (101) peak for films deposited on these substrates. The films on MgO, LAO and CaF_2 have a four-fold in-plane orientation indicating epitaxial growth,

although the peak intensity for the film on CaF_2 is not strong, the peaks are wider and the pattern is not as perfect as that for the other two films. In the film grown on $SrTiO_3$, there are two sets of four-fold symmetries within 45°. The film on LiF shows a weak in-plane alignment, and for the film on LSAT there is no clear evidence of in-plane alignment.

The lattice misfit between substrate and film was calculated using $(a_{sub}-a_0)/a_{sub}\times100$, where a_0=3.794Å (bulk value for the 11-phase) [33] and a_{sub} is the lattice parameter of the substrate. It can be seen in Figure 4.13 that there is no systematic correlation between lattice misfit and texture development. The extreme examples of this are MgO with the largest lattice misfit, but very strong epitaxy in the film, and LSAT with rather small lattice misfit but very poor texture, both in-plane and out-of-plane. The reason why the film on the LSAT substrate does not show strong crystallinity was found to be chemical interaction with the substrate with no distinct and sharp interface between film and substrate. This will be explained in more detail in the TEM observation section. LSAT has the lowest thermal conductivity among these substrates (k_{LSAT}=5.1 $W.m^{-1}.K^{-1}$ vs k_{MgO}=45-60 $W.m^{-1}.K^{-1}$), therefore it is possible that the temperature of the surface of the LSAT substrate is lower than the set temperature of 315°C.

The presence of c-axis orientation in almost all of these films deposited on substrates with a wide range of lattice misfit once again shows that Fe(Se,Te) films intrinsically favour growth along the c-axis. c-axis alignment has been also reported in most of the Fe(Se,Te) films deposited in the literature [20, 26, 27, 30-32] even on the (0001) plane of hexagonal Al_2O_3 [26]. However, in-plane alignment seems to be too complicated to be linked with sample parameters such as lattice misfit. A large variety of in-plane alignments has been reported in the literature, with no clear correlation with other parameters [20, 26, 27, 30, 31]. In cross-sectional TEM observations (next section), it will be shown that the interface is affected by the growth conditions, type of substrate and even composition of the film and, hence, causes different growth morphologies. It can be suggested that texture development in Fe(Se,Te) thin films is

more dependent on the growth mechanism and processing conditions rather than lattice misfit between film and substrate.

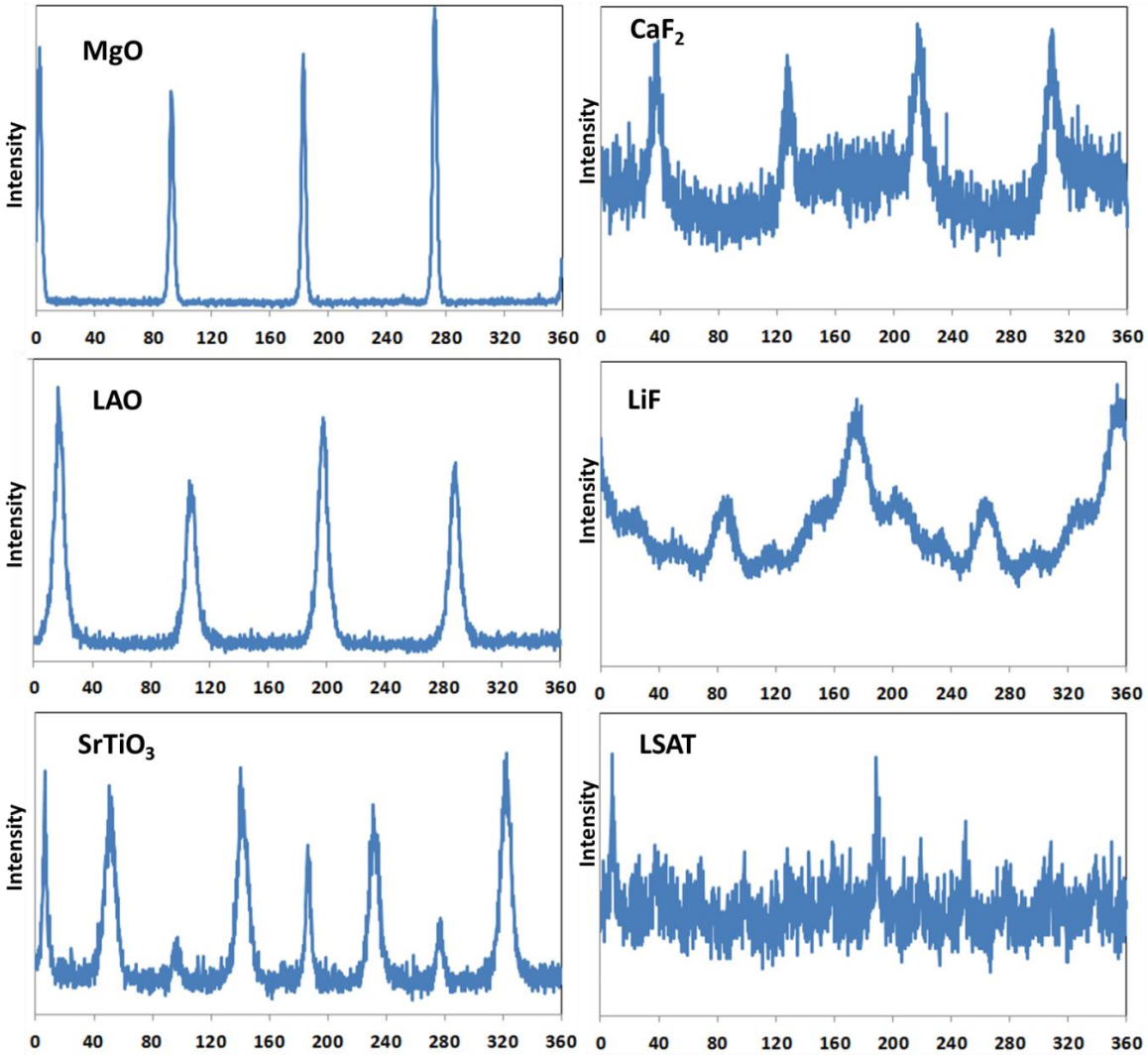

(b)	MgO	LSAT	LAO	LiF	CaF_2	STO
Lattice Mismatch (%)	9.9	1.9	-0.12	5.7	1.6	2.8
FWHM (001) (°)	1.6	4.8	2.2	3.7	2.3	1.8

Figure 4.13: XRD in-plane patterns (Phi scan) of the (101) peak of Fe(Se,Te) thin films on different substrates, (b) Lattice mismatch of film/substrate and FWHM of (001) peak for the films grown on different substrates showing that there is no direct link between lattice mismatch and texture development in the Fe(Se,Te) films grown on different substrates.

4.5 Lattice parameters and strain

A remarkable feature of Fe-based superconductors, especially the Fe(S,Te) phase, is the strong correlation between structural parameters and superconductivity [34]. In order to find out how structural parameters change with processing conditions in this work, lattice parameters were calculated. The c-axis parameter was calculated as explained in the experimental chapter, and the a-axis parameter was calculated using the equation of $\tan(\psi) = \frac{c}{a}$ where ψ is the angle between (001) and (101) plane and can be obtained from texture XRD measurements. Figure 4.14 shows the calculated c-axis and a-axis parameters as a function of Te content. As a reference, the black line has been added to the graph showing lattice constants for $FeTe_{1-x}Se_x$ according to Vegard law and the lattice constants of pure β-FeSe and FeTe. According to Vegard law a linear relation exists between the lattice parameters of a compound and the concentration of the components [35]. This law has been considered useful for $FeTe_{1-x}Se_x$ single crystals as well [36]. The lattice parameter and unit cell volume increase almost linearly with Te concentration in powder and bulk samples as the Te atoms are larger than Se atoms [37]. However, in my samples as Figure 4.14 shows that both a-axis and c-axis parameters deviate from the Vegard line, which might be due to the presence of strain and non-stoichiomtry of Fe content.

It can be assumed that tensile strain along the c-axis leads to the c-axis parameter values above the line and, in contrast, compressive strain leads to the c-axis parameter below the line. In epitaxial growth of Fe(Se,Te) on MgO substrates, compressive strain along the c-axis is expected because of the larger lattice parameter of MgO compared to that of Fe(Se,Te) which induces in-plane tensile strain and compressive strain along the c-axis. Moreover, thermal strain might be also present since the thermal expansion coefficient of Fe(Se,Te) is higher than that of the MgO substrate [27]. Tensile thermal stress is expected to be introduced during cooling and it would be larger when the substrate temperature is high. Therefore, there are three

reasons for deviation of the data from the line: non-stoichiometry in Fe content, thermal tensile strain and compressive epitaxial strain.

As these samples were grown in a temperature range of 280-350°C, it can be assumed that all of them experience a similar amount of thermal tensile strain. In $FeSe_{0.5}Te_{0.5}$ thin films deposited on MgO substrates by PLD, this tensile strain has been found to be insignificant when the substrate temperature is above 350°C [27].

In Te-rich samples, more excess Fe exists in the sample due to relationship between Fe-content and Te content (shown earlier), and because excess Fe atoms occupy the interstitial sites in the Fe(Se,Te) phase [9], the c-axis parameter expands above the line. In Se-rich samples, it seems that compressive strain takes over and the c-axis parameters are below the line. Looking at the graph in Figure 4.14, a number of samples have c-axis values corresponding to the Vegard line indicating that in these samples, there is no strain or at least this strain is not considerable. Characterizing these samples in detail revealed that these samples are either polycrystalline with no epitaxial strain or they have an interlayer between the film and substrate. The presence of this amorphous-like layer leads to a loss of the direct correlation between lattice parameters and orientation of the films and those of the substrate. Similar independence of the film on the substrate due to the presence of interface layer has been also found in [26].

The calculated a-axis parameter shows less variation with Te content, and all the data are above the Vegard law line indicating that tensile in-plane strain exists in all samples. This tensile strain is a combination of epitaxial strain and thermal strain. The deviation from the line is much smaller than that for c-axis parameter indicating that strain along the c-axis is greater than that along the a-axis in epitaxial Fe(Se,Te) films. This is in agreement with anisotropic elastic properties reported for the 11 phase which shows the c-axis is the soft elastic direction and it is easier to accumulate strain in this direction [38]. Moreover, the c-axis strain is more dependent on the processing conditions. One reason for this observation is the nature of

Fe(Se,Te) structure in which Te content affects the c-axis most strongly, and another reason might be the lower degree of in-plane alignment, reported in the texture section, in these samples which shows the presence of in-plane grain boundaries releasing a-axis strain.

This independence in variation of a and c parameter is an advantage of epitaxial Fe(Se,Te) thin films over single crystals, since it allows exploration of regions of lattice parameters for a specific composition [23, 28-32, 39]. This also distinguishes thin films from samples under external pressure where c generally scales with a [40-42].

4.6 TEM analysis of the deposited films

To evaluate the microstructure of the deposited films, an extensive cross-sectional TEM analysis was carried out on films grown under different processing conditions. TEM micrographs for the majority of the deposited films show that the films are continuous with no large cracks or gap through the film. The thickness distribution of the sputtered films is uniform indicating that sputtering has been well set up in terms of gas pressure, relative position and size of the substrate and target, angular distribution of sputtered particles and power. However, deposited films develop various microstructures according to their growth process. In majority of the films, nano-scale regions are present in different contrast which can be an indication of nano-scale phase separation. Locally different Te/Se ratios can create nano-scale phase separation as previously reported [43, 44]. In fact, Te substitution in FeSe may create disorder on the anion site and nano-scale local variations in Te/Se ratio. High-resolution TEM can be considered for future work to analyse the nature of these nano-scale secondary phase.

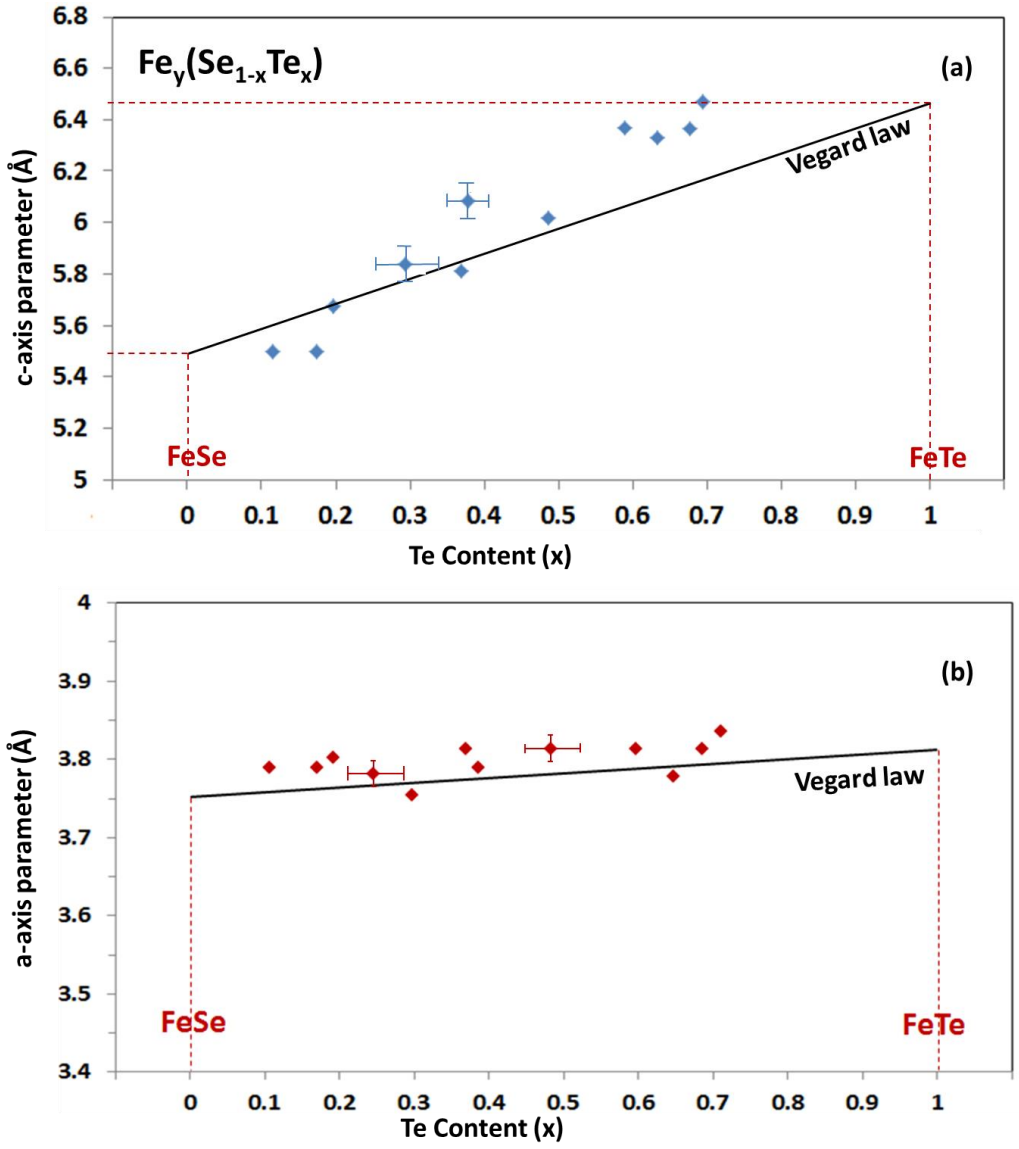

Figure 4.14: (a) c-axis parameter and (b) a-axis parameter variation as a function of Te content (x). The black line shows the linear relation between lattice parameters and Te content in Fe($Se_{1-x}Te_x$) according to the Vegard law and any deviation from the line shows the presence of strain in the deposited films.

4.6.1 Films on MgO

Figure 4.15 shows TEM micrographs of Fe(Se,Te) thin films grown on MgO substrates at 310°C. As shown earlier, when the substrate temperature is above 320°C, an interlayer is formed between MgO and the film. At lower temperatures, the interface is sharp and the film is directly grown on the substrate. At a thickness of about 150nm, microcracks appear in the film and extend up to the film surface. Furthermore, there are nano-scale regions with different

shapes and unrelated orientations in different contrast which might be either nano-grains in different orientations from that of the matrix or secondary phases with different compositions, especially the different Se/Te ratios discussed earlier. As it is seen in both TEM and SEM images in Figure 4.15, the surface of the grown film is not smooth, and the root mean square (rms) value obtained from AFM measurement is about 287nm. The surface roughness is due to columnar growth of the film and, in particular, micro-cracks close to the surface. The rough surface of the film provides preferential places for the precipitation of Te rich regions on the surface after sputtering. These regions can be clearly seen in the SEM image presented in Figure 4.15, and the EDX spectra of these features and matrix show that these features are Te-rich. The reason for the formation of these regions will be explained in the section on surface morphology. It can be suggested that the surface of the film was even rougher before the holes on the surface are filled by Se and Te atoms.

Figure 4.16 shows TEM micrographs of Fe(Se,Te) thin films grown on MgO substrates at a higher temperature (320°C). The microstructure of the film seems to vary significantly with temperature. In addition to the presence of the interlayer, the film consists of two distinct regions, columnar grains close to the interface and the rest of film which is in brighter contrast and contains fewer features. A number of dark nanoparticles are distributed over the sample as shown by the red arrows in the image. A possibility for these nanoparticles is Fe_3O_4 or another Fe oxide as this film contains large amount of excess iron ($Fe_{1.34}Se_{0.71}Te_{0.29}$) and if oxygen is provided, either from the substrate due to higher diffusion rate at higher temperature or from the air after preparing the TEM sample, Fe_3O_4 nano-clusters can be formed. This is in agreement with the high value of magnetic susceptibility measured for this sample (shown later) which might be an indication of the presence of magnetic impurity such as Fe_3O_4. Similar features have been observed in Fe(Se,Te) thin film on STO substrate and characterized as Fe_3O_4 particles by high-resolution TEM analysis [45]. Furthermore, there is no indication of

microcracks or holes in this film because at higher temperature, diffusion increases and strain can be relieved by more mobile boundaries leading to fewer defects in the microstructure, and a more continuous film with a smoother surface.

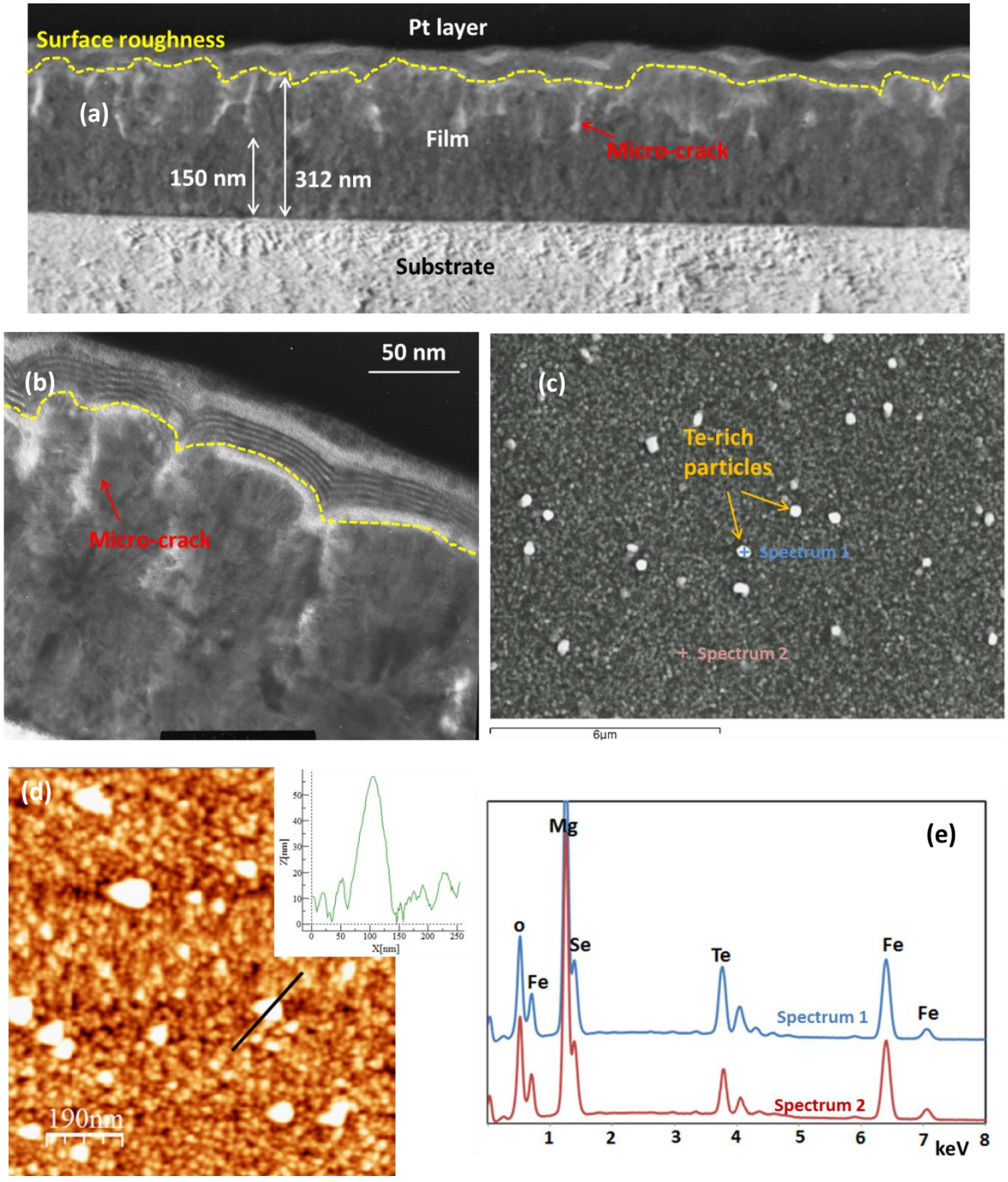

Figure 4.15: (a-b) Cross-sectional TEM micrographs of the film deposited on MgO at 310°C showing microcracks close to the surface, (c) plan-view SEM micrograph showing bright features distributed over the surface, (d) AFM image of the surface showing the height of the bright features, (e) EDX spectra of the indicated spots in the SEM image showing that the bright features are Te-rich regions.

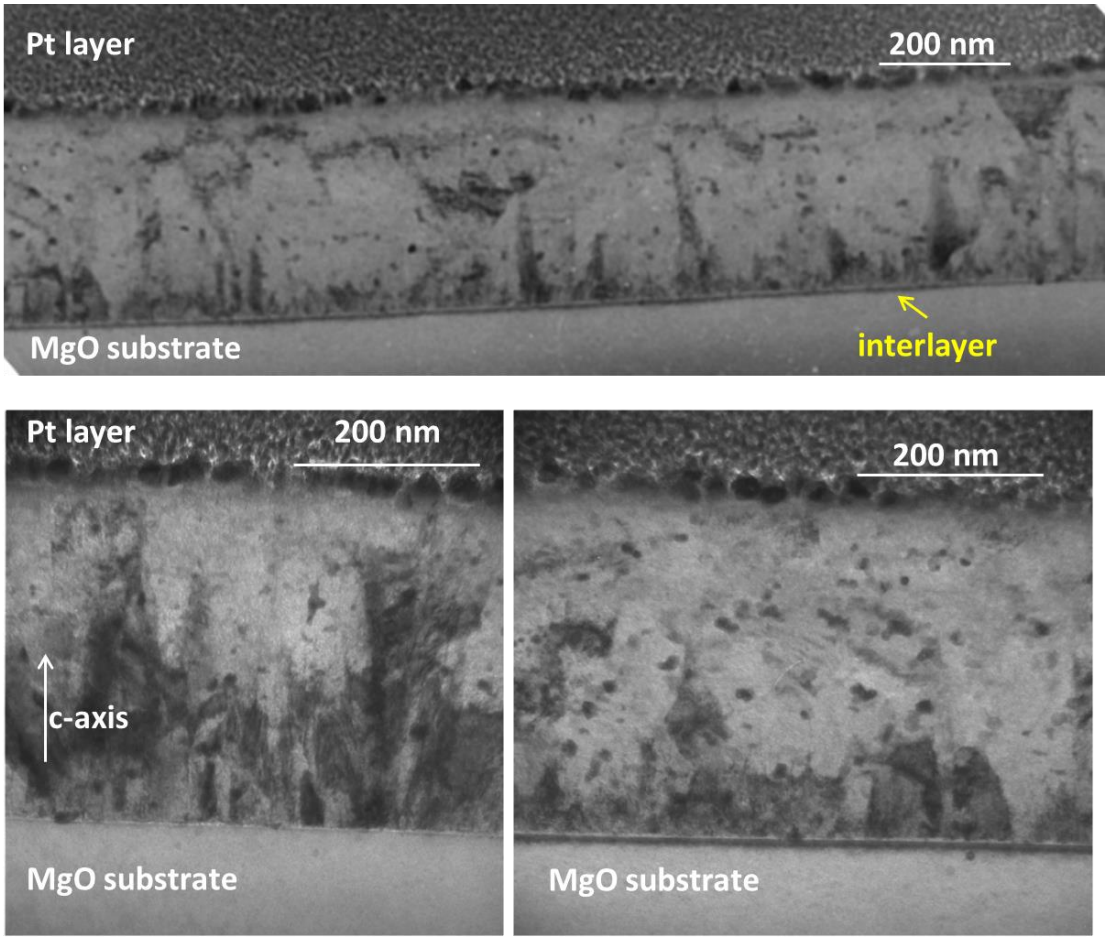

Figure 4.16: Cross-sectional TEM micrographs of the film deposited on MgO at 320°C showing that the film is not very homogenous. The darker regions might be due to variation in either chemical composition or crystallographic orientation.

4.6.2 Films on LAO

Cross-sectional TEM micrographs of the film deposited on a LAO substrate is shown in Figure 4.17. The film seems uniformly thick, and a thin gap is observed between the film and substrate which causes complete detachment of part of film from the substrate, as seen in Figure 4.17b. There are three possibilities for the presence of this gap; (1) bonding between the film and substrate is weak, (2) stress relief of the continuous film causes sliding of the film/substrate interface, (3) this gap has been formed during cooling due to the difference in thermal expansion between the film ($\alpha_{Fe(Se,Te)}$(along c-axis)= 37.5×10^{-6} K^{-1}) [46] and LAO substrate ($\alpha_{(LAO)}$= 10×10^{-6} K^{-1}). However the last possibility is less likely because no gap was observed

between films and other substrates which have even more different thermal expansion coefficients to that of the film. For example, the film was found to be properly stuck to the MgO substrate ($\alpha_{(MgO)}= 9\times10^{-6}\ K^{-1}$) which is expected to equilibrate at a higher temperature due to its higher thermal conductivity.

Furthermore, these TEM images show that the film consists of two regions, a thin layer with a thickness of 20 nm close to the interface, and the main part of the film which extends up to the surface of the film. Between these two regions, defects which are more similar to holes and grooves can be seen, and more columnar features are observed above these holes.

According to these observations, a hypothesis regarding growth morphology of this film can be suggested as follows. Due to the weak bonding between deposited atoms and the substrate atoms, growth of the film starts with a three-dimensional growth resulting in island formation. The islands grow until they impinge at the thickness of 20 nm and coalescence occurs. At this stage, a large amount of elastic distortion and strain will be generated in the film (known as coalescence strain [47]). According to XRD texture results (see Figure 4.13), there is strong in-plane alignment for the films grown on LAO substrates which means a high amount of strain is likely formed during coalescence. This coalescence strain can be partially relieved by the formation of defects such as holes, dislocations or nano-cracks where isolated islands meet (20 nm in this film). It is also likely that complete strain relief occurs by sliding of the film/substrate interface resulting in an obvious gap between the film and the substrate. After coalescence, continuous film thickening occurs on the pre-existing layer containing defects resulting in more columnar features distributed over the film as observed in Figure 4.17.

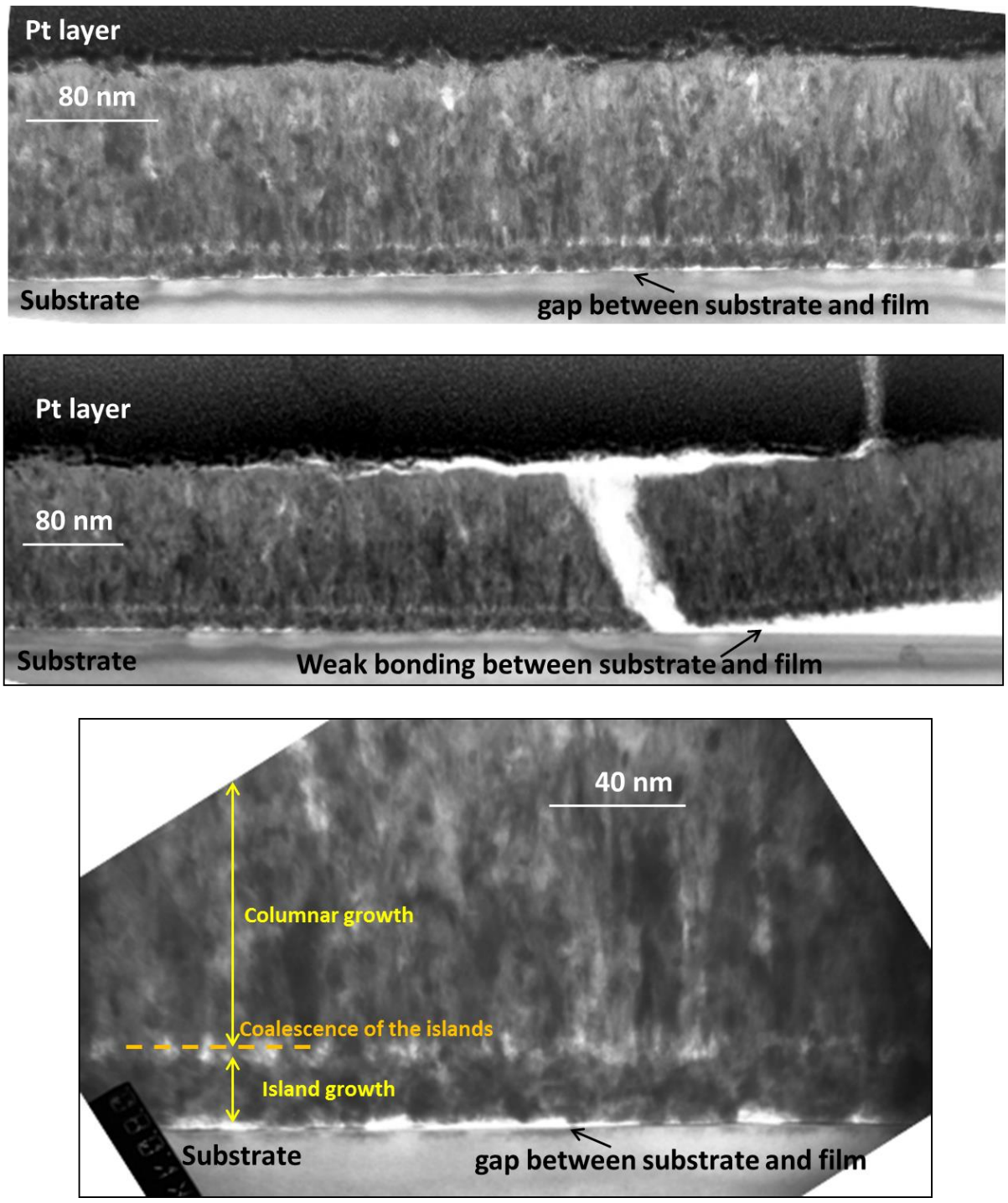

Figure 4.17: Cross-sectional TEM micrographs of Fe(Se,Te) thin film deposited on LAO at 315°C for 2hrs showing that the film/substrate bonding is not strong and there is a gap in the film/substrate interface. At a thickness of about 20nm, a row of defects (likely holes and nano-grooves) is seen possibly due to a particular growth mode in this film as a result of weak bonding between film and substrate.

4.6.3 Films on LSAT

The growth morphology of the film deposited on LSAT seems very different. As the cross-sectional TEM micrographs in Figure 4.18 show, there is no sharp interface between substrate and film indicating a strong bonding between deposit and the substrate or interaction between them. The film consists of two layers, one of which is close to the substrate with a thickness of about 65 nm, and the other layer with much brighter contrast and about the same thickness. In addition to these regions, columnar grains (about 10-50 nm thick) elongated from the substrate to the surface are seen in dark contrast compared to other two regions. Most of these grains are parallel to the c-axis, although in some parts of the film, they seem to deviate from the c-axis and are shown as off-axis grains in the image. All of these observations exhibit a poor-quality film, especially in crystallographic orientation, consistent with XRD-texture results where no indication of in-plane alignment was observed in the Phi-scan for the films deposited in LSAT. However, the surface of this film seems very smooth as can be seen in the TEM images. The root mean square (rms) surface roughness was estimated to be 4.56nm from AFM data. Compared to other deposited films, this film is one of the smoothest.

All of these observations, including the strong bonding in the interface and smoother surface, can be indications of layer-by-layer growth in this film. AFM images of the film deposited on the LSAT substrate for only 10 minutes confirm the layer-by-layer deposition for this film. As it is seen in Figure 4.19, after 10 minutes sputtering, the nuclei have grown laterally (in two dimensions) due to their strong bonding with the substrate, and they partially cover the surface of the substrate without obvious thick features. The film seems continuous with a fairly uniform thickness of 8-10 nm and faceted edges at some regions. This surface topography at the early stages of the growth is a typical characteristic of the layer-by-layer growth. Continuing growth will result in a relatively smooth surface.

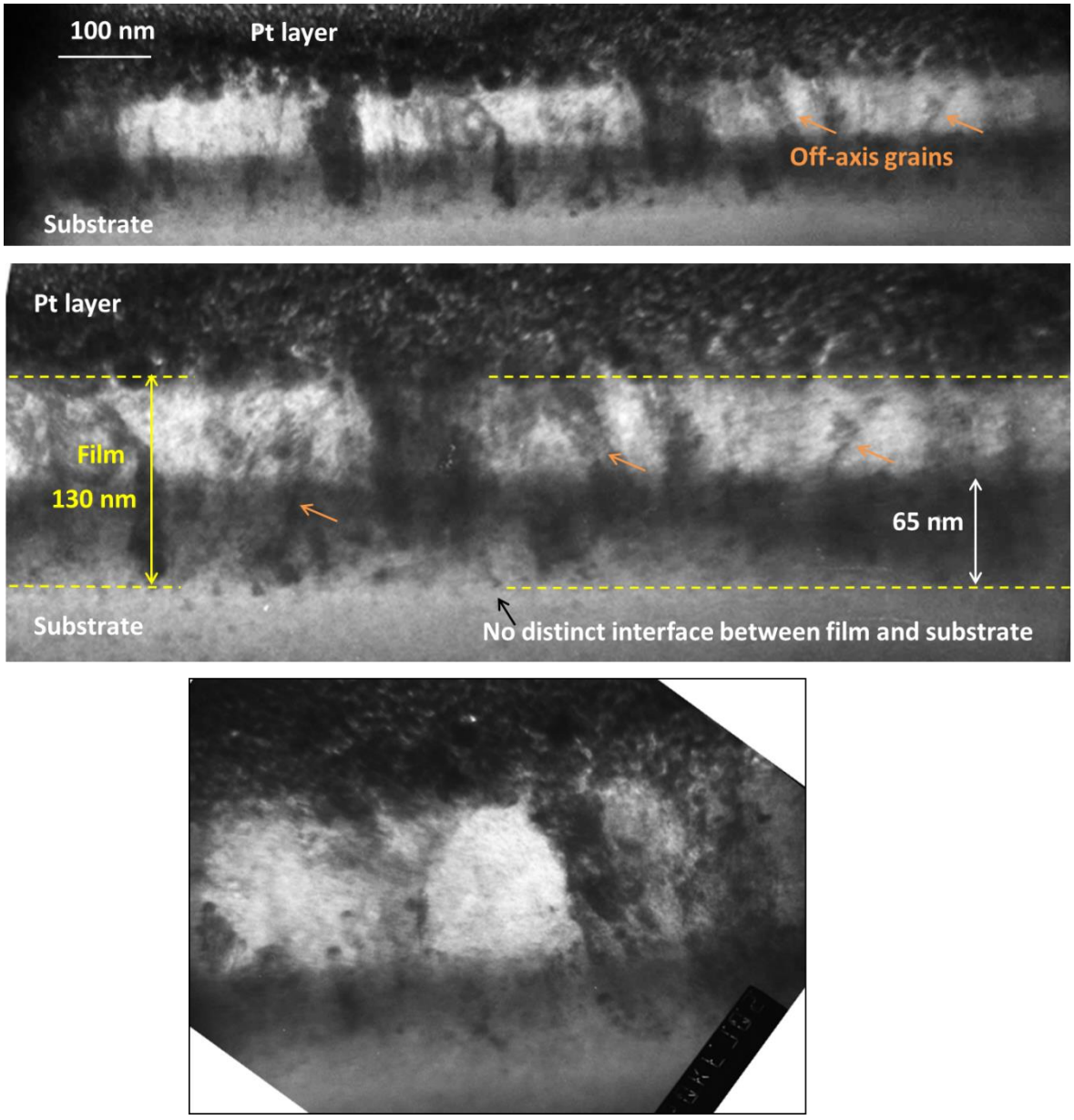

Figure 4.18: Cross-sectional TEM micrographs of Fe(Se,Te) thin film deposited on LSAT at 315°C for 2hrs showing that the film contains two layers, a dark layer close to the substrate with an unclear film/substrate interface and a bright layer close to the film surface. The orange arrows indicate regions which are not columnar and possibly they are off-axis grains growing on this substrate consistent with the texture XRD data indicating off-axis grains are present in this film.

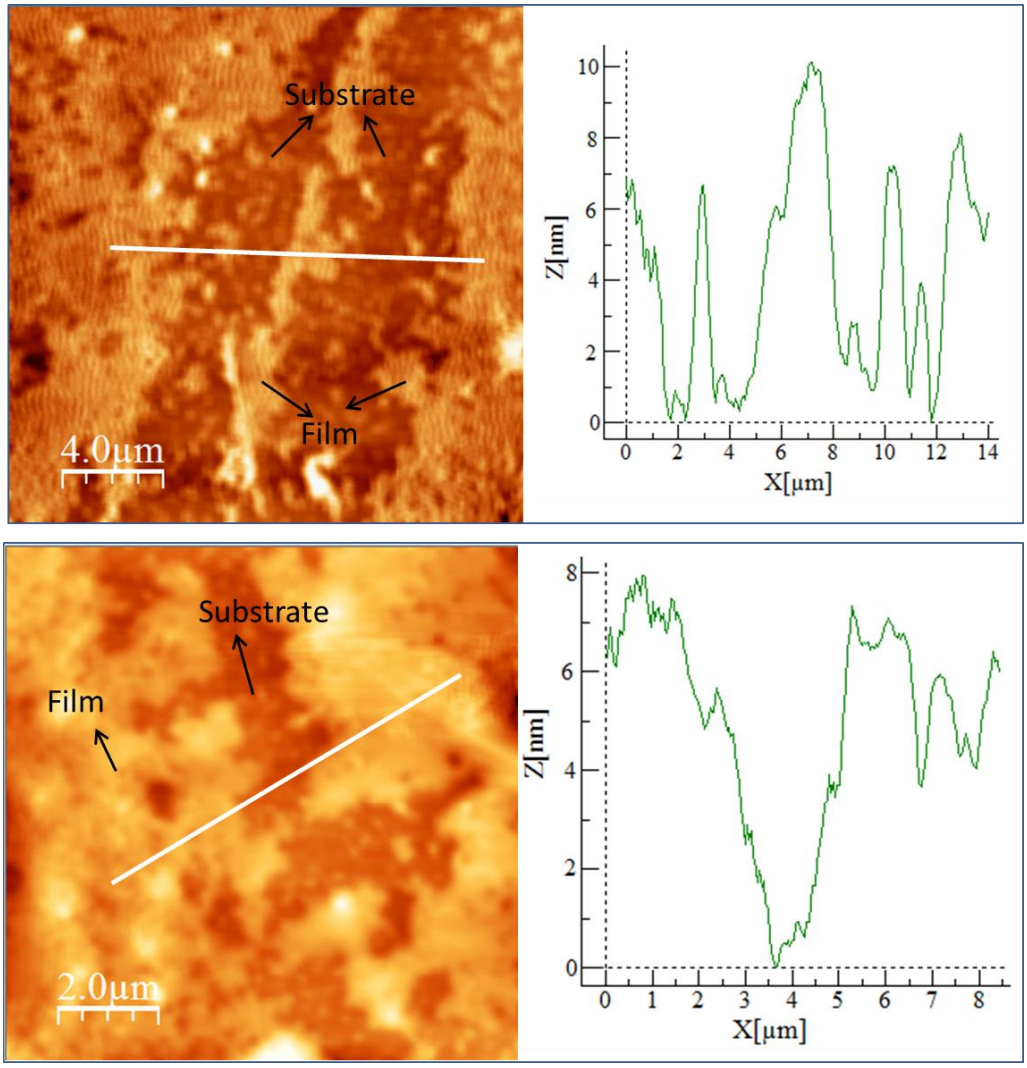

Figure 4.19: AFM image showing the surface topography of the film deposited on LSAT after 10 minutes sputtering.

4.6.4 Films on STO

The film grown on STO is continuous with a small number of holes close to the surface (see Figure 4.20). The film consists of a matrix with nano-scale precipitates uniformly distributed. Braccini et al have observed similar nano-scale features in the TEM micrographs of Fe(Se,Te) thin films grown on STO by PLD [48], and found that these columnar defects act as pinning sites and increase the critical current density of the film.

SEM micrographs of the film deposited on STO for 20 minutes and 30 minutes sputtering are shown in Figure 4.21. The film deposited for 20 minutes seems to be covered by connecting plate-shaped features forming a network structure on the surface. The remaining regions which are not yet covered by the deposit atoms, are faceted holes with a depth of about 46 nm (estimated by AFM image). Most of these faceted holes have edges along the [100] directions of the STO substrate, which shows high degree of alignment of the film consistent with the phi scan results. Deposition for a longer time (30 minutes) leads to more coverage of the surface by the film, resulting in smaller faceted holes with a depth of 17 nm. Some bright spots are also seen in both SEM and AFM images (6nm high). They might correspond to the columnar defects detected by TEM. The growth mechanism of this film might be a combination of both two-dimensional and three dimensional growth and the presence of a secondary phase might be due to non-uniform distribution of Te onto Se sites leading to nano-scale phase separation. High-resolution images of these regions as well as the nano-rods are strongly of interest for future work.

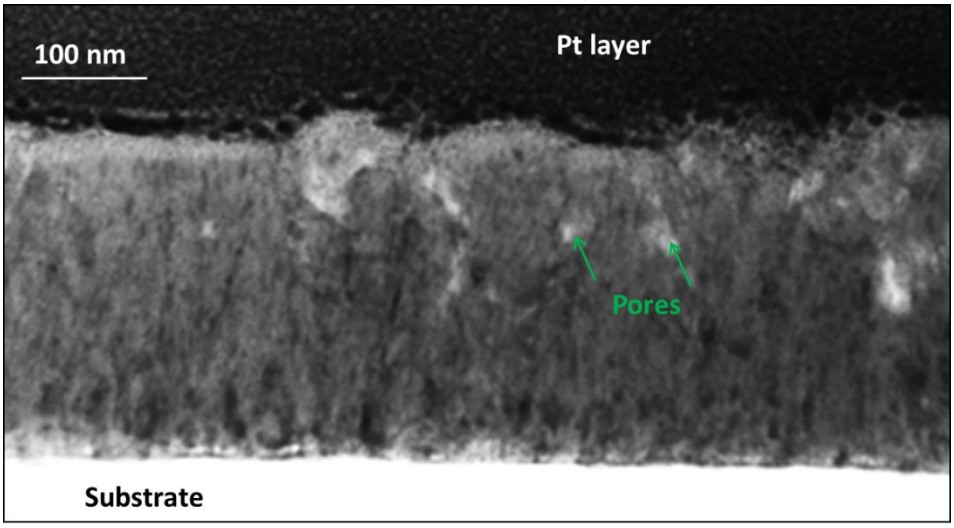

Figure 4.20: Cross-sectional TEM micrographs of Fe(Se,Te) film deposited on STO at 310°C showing the presence of pores close to the film surface and nano-scale inhomogeneities distributed across the film .

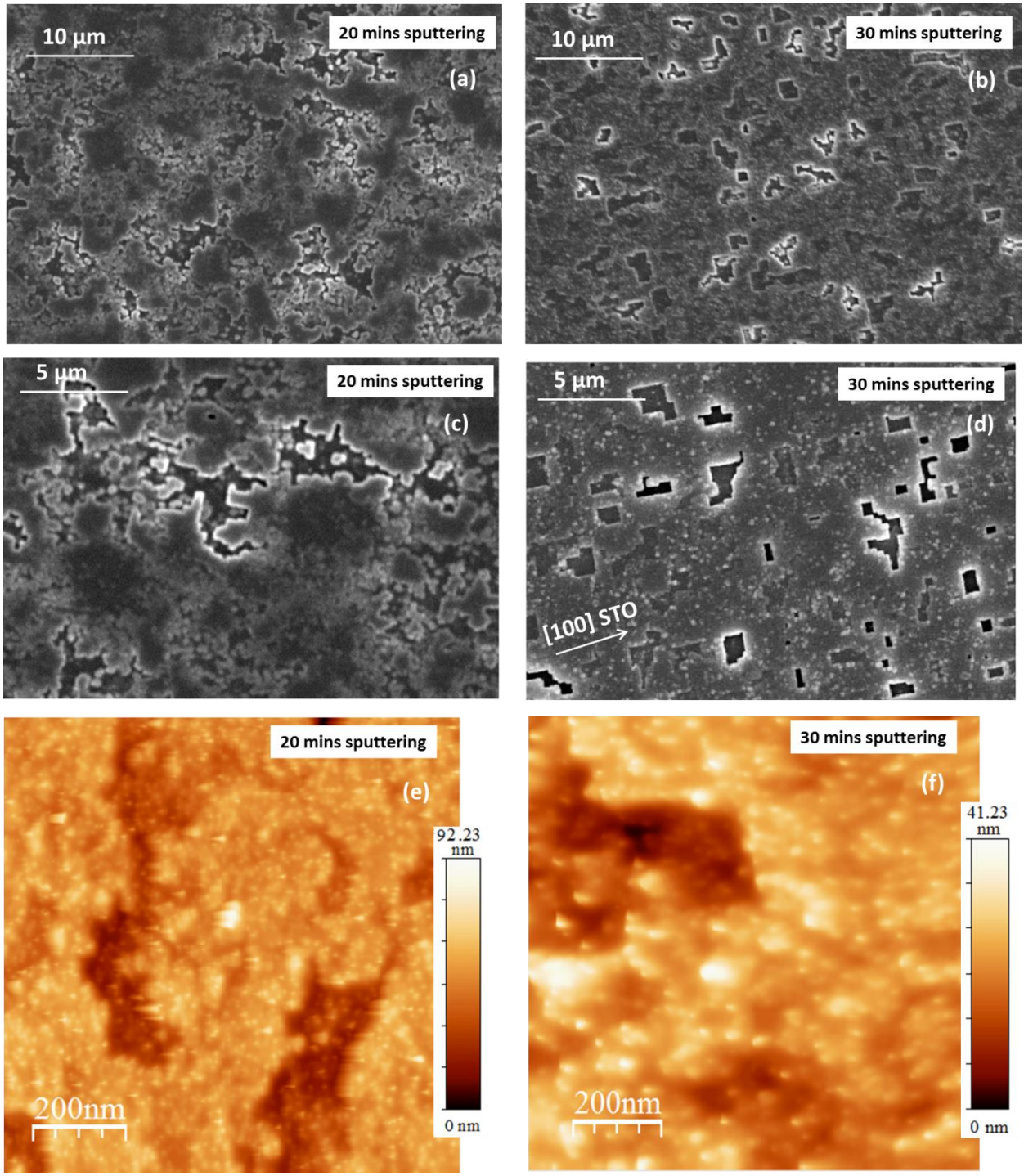

Figure 4.21: (a and c) SEM micrographs of the thin film deposited on STO for 20 minutes, (b and d) SEM micrographs of the thin film deposited on STO for 30 minutes showing regions with the edges along [100] direction of the STO substrate as a result of an epitaxial growth. AFM images of these films (e) 20 minutes and (f) 30 minutes.

4.6.5 Films on LiF

Deposited films on LiF substrate seem to be non-uniform with a large number of defects such as holes/micro-cracks and nano features in different shapes and sizes between 5-20nm (see Figure 4.22). The features are uniformly distributed in the film. This microstructure is in agreement with the XRD texture measurements which shows poor alignment in the films deposited on LiF. Moreover the surface is not very smooth with an rms value of about 210nm.In the literature, Fe(Se,Te) films on LiF have not been investigated, however there is a strong recommendation for using non-oxide substrates for growing Fe(Se,Te) films [49]. As a non-oxide substrate with a small lattice mismatch, LiF seems to be a good candidate. However, my results show that the film is of poor quality. Looking at the film/substrate in the TEM images, a number of steps can be seen. AFM experiments on the bare substrate shows that these steps are present on the surface of the LiF substrate. In fact, the as-received LiF substrates have non-flat surfaces with nano-scale steps which influence the growth morphology and quality of the deposited film. This might be the reason for the poor quality film on the LiF substrate in my work.

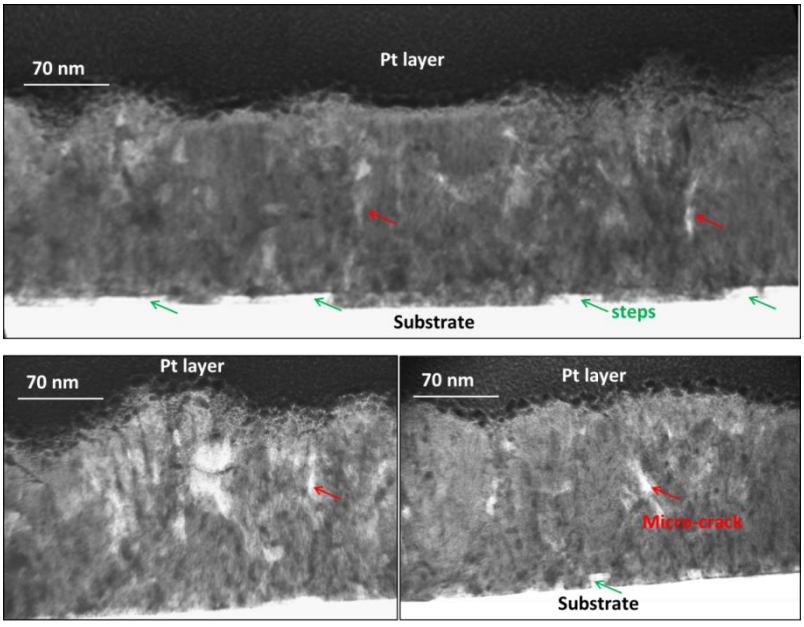

Figure 4.22: Cross-sectional TEM micrographs of Fe(Se,Te) film deposited on LiF (Red arrows indicate pores and micro-cracks and green arrows indicate the presence of steps on the substrate).

4.6.6 Oxygen penetration from the substrate to the film

In order to analyse compositional variations along the film, especially oxygen variation at the interface, EELS experiments with a spot size of 2 nm were carried out on two films deposited under the same processing conditions but different substrates; non-oxide substrate CaF_2 and oxide substrate MgO. The most significant difference appears in the oxygen content in the film close to the interface. The film deposited on MgO contains much higher oxygen especially at the interface. Both thin films have likely received a small amount of oxygen from the air despite care to limit exposure to air between FIB and TEM. This amount of oxygen is assumed to be the same across the TEM thin samples. However, in the film deposited on MgO, an oxygen gradient can be seen from the film/substrate to the film surface. For example, the film on MgO has 13.5% and 9.5% oxygen in atomic ratio at depths of 5 nm and 10 nm from the interface respectively. At these points in the film on CaF_2, the oxygen contents are 2.5% and 2.2 % respectively which likely comes from the air during sample handling. These values indicate that oxygen penetration occurs from the MgO substrate to the film. This might be related to the formation of the interface layer between MgO and films deposited at high temperatures because more oxygen penetration occurs at higher temperature. In sputtering, due to the bombardment of the substrate by high energy particles (an energy of 1-10 eV when they strike the substrates [5]), substrate surfaces might be even more damaged, encouraging oxygen penetration. The high concentration of oxygen in the film can possibly react with excess Fe which usually exists in the film due to the loss of volatile Se and Te, and appear as Fe_3O_4 precipitates. However, no XRD peak corresponding to Fe_3O_4 was found in the XRD patterns of deposited film which might be due to the low volume fraction and small size of Fe_3O_4.

Similar oxygen diffusion from substrate to Fe(Se,Te) films was previously reported [6, 45, 50] for oxide substrates such as MgO and $SrTiO_3$. In some cases, this has been detrimental for superconductivity in the films [31, 32], while in other cases it has been found to be a useful

way to extract excess Fe atoms out of the structure by forming Fe_3O_4 nanoparticles and improving superconducting properties by both adjusting composition (which improves T_C) and adding Fe_3O_4 particles which act as pinning sites and improve J_C [45].

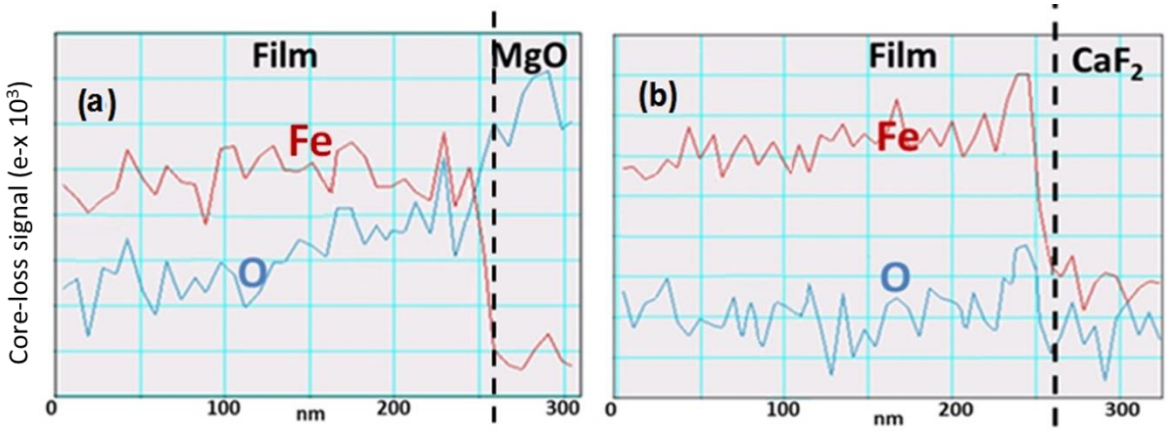

Figure 4.23: EELS data showing variation of Fe and O content at the film/substrate interface for (a) Fe(Se,Te) film on MgO and (b) Fe(Se,Te) film on CaF_2. This data shows that there is oxygen penetration from MgO substrate into the film at the interface.

4.7 Surface Morphology

From the visual appearance of the deposited films, almost all of them have a mirror-like shiny surface. Although nano-scale roughness was detected by both AFM and TEM, SEM investigation of the deposited films shows that most of the grown films have a smooth surface with no obvious defects, crack or holes. In fact, this is one of the advantages of sputtering which usually produces uniform, flat films. As can be seen in Figure 4.24, some bright circular features appear in these samples. The density of these features was found to be dependent on the substrate temperature. Increasing the growth temperature results in a higher number of these features per unit area. In the literature, columnar defects, acting as pinning sites and leading to higher current density, have been reported in a number of Fe(Se,Te) thin films grown by PLD [29, 48]. In order to figure out whether these features are columnar defects along the film or they are formed only on the surface, cross-sectional TEM analysis was carried out on these features.

Looking at the TEM images shown in Figure 4.25, a small gap can be seen between these features and the surface of the sample indicating that these features are not columnar features and possibly they are formed after the deposition. In some samples with relatively rough surfaces, these features tend to be accumulated around the surface defects as can be seen in Figure 4.26. The BE micrograph indicates that these features consist of heavier elements. The EDX mapping data reveal that Se and Fe are uniformly distributed across the film, but higher Te content is detected in the features. In these Te-rich regions, Mg is much lower compared to the matrix indicating that the features are Te-rich bumps on the surface. It can be explained that these features are formed by precipitation of Te atoms which are available in the sputtering chamber. As discussed, Te has a smaller sputtering yield compared to Fe and Se in addition to a higher vapour pressure, therefore many Te atoms are re-evaporated from the deposited film especially when the substrate temperature is high. Therefore, a high density of Te atoms will be present inside chamber especially above the deposited film. On the other hand, mean free path for Te atoms is much shorter than that of Fe and Se according to the following equation [2]:

$$M_1=\frac{1}{\pi(r_1+r_2)^2 n_2} \qquad \text{Equation 4.2}$$

where M_1 is the mean free path of sputtered atom 1, r_1 and r_2 are the atomic radius of sputtered atoms and discharge gas molecules (argon) respectively and n_2 is the density of discharge gas. According to this equation, the mean free path of Te is 0.61 that of Se. Therefore, Te atoms which are concentrated above the film will be likely precipitated back onto the film after sputtering when the sample is cooling down. Clearly, they choose preferential places on the surface such as surface defects, e.g. holes or cracks, for precipitation, resulting in a non-uniform distribution on a number of thin films.

To avoid precipitation of Te atoms on the surface, lower substrate temperatures cannot be suggested due to the poor crystallinity at low temperatures. However decreasing the Ar

pressure inside chamber immediately after deposition can be suggested since the mean free path of Te atoms will increase allowing them to find distant colder places on which to deposit. This was applied to a number of deposited films and no similar features were observed. Therefore, it can be suggested that it is essential to decrease Ar pressure inside the chamber immediately when deposition finishes in order to obtain high quality clear surfaces.

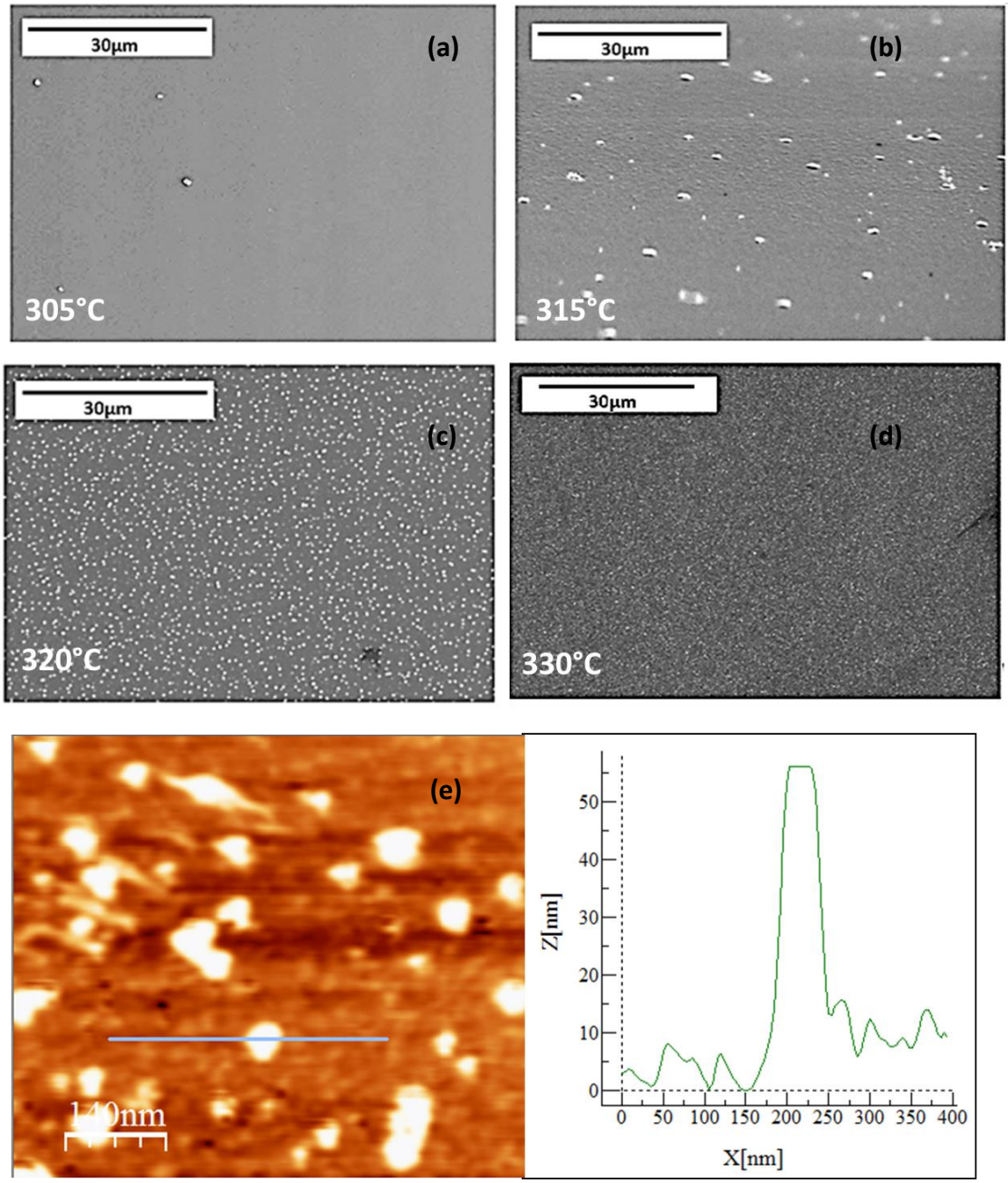

Figure 4.24: Surface morphology of the films grown on MgO substrate at different temperatures, (a) 305°C, (b) 3150°C, (c) 320°C, (d) 330°C showing the presence of bright features on the surface. The density of these bright features increases with temperature. (e) AFM image of the deposited film at 320°C showing the height of one of these features.

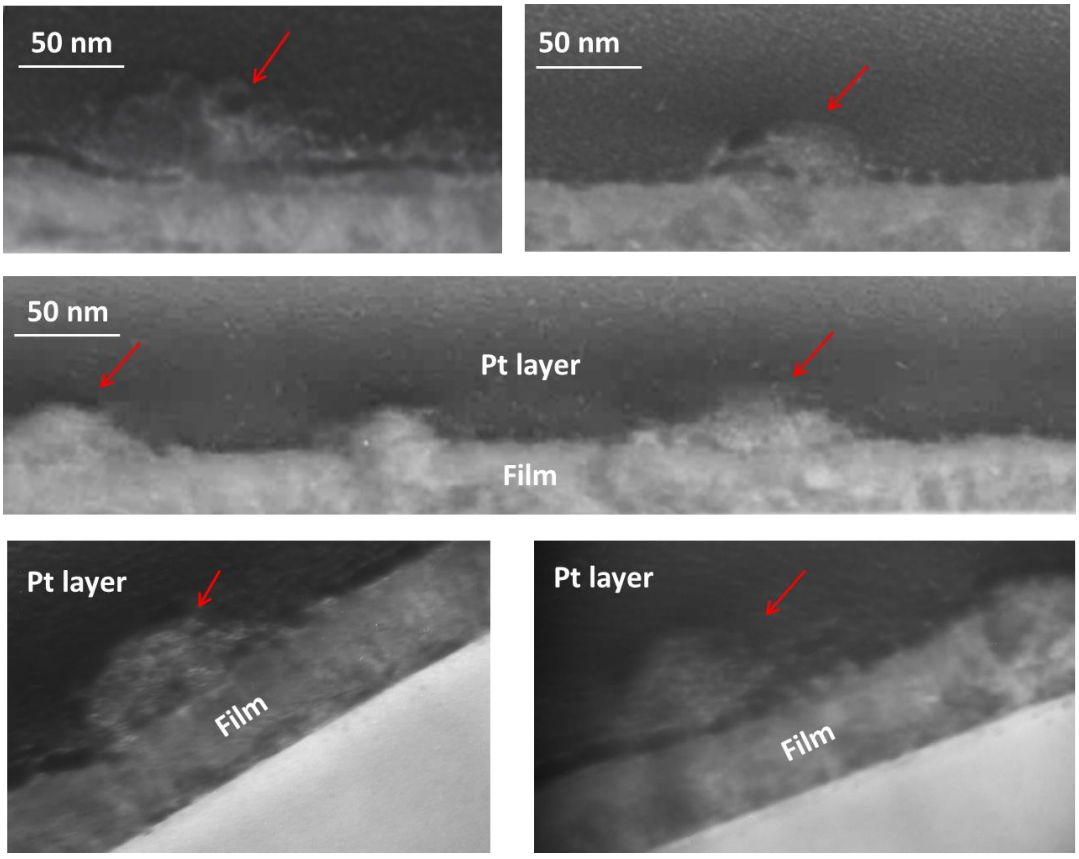

Figure 4.25: TEM micrographs of a typical Fe(Se,Te) thin film grown on MgO at 330°C showing the features on the film surface and a gap between these features and the film. Because of the presence of the gap, it is likely that these features are not part of the film and they are formed after the deposition of the film.

4.8 Ex-situ grown films with a post-deposition annealing

All the films presented so far were grown by the in-situ process, i.e. grown onto heated substrates. Another way of fabricating thin films by sputtering is deposition of the film on to a cold substrate followed by post a heat treatment (ex-situ process). In order to study how this processing method affects the overall quality of the grown films, a number of ex-situ processed films were deposited on MgO substrates. Two different post-annealing processes were carried out on the cold-deposited films; in Ar within the sputter chamber and in an evacuated quartz tube in a furnace.

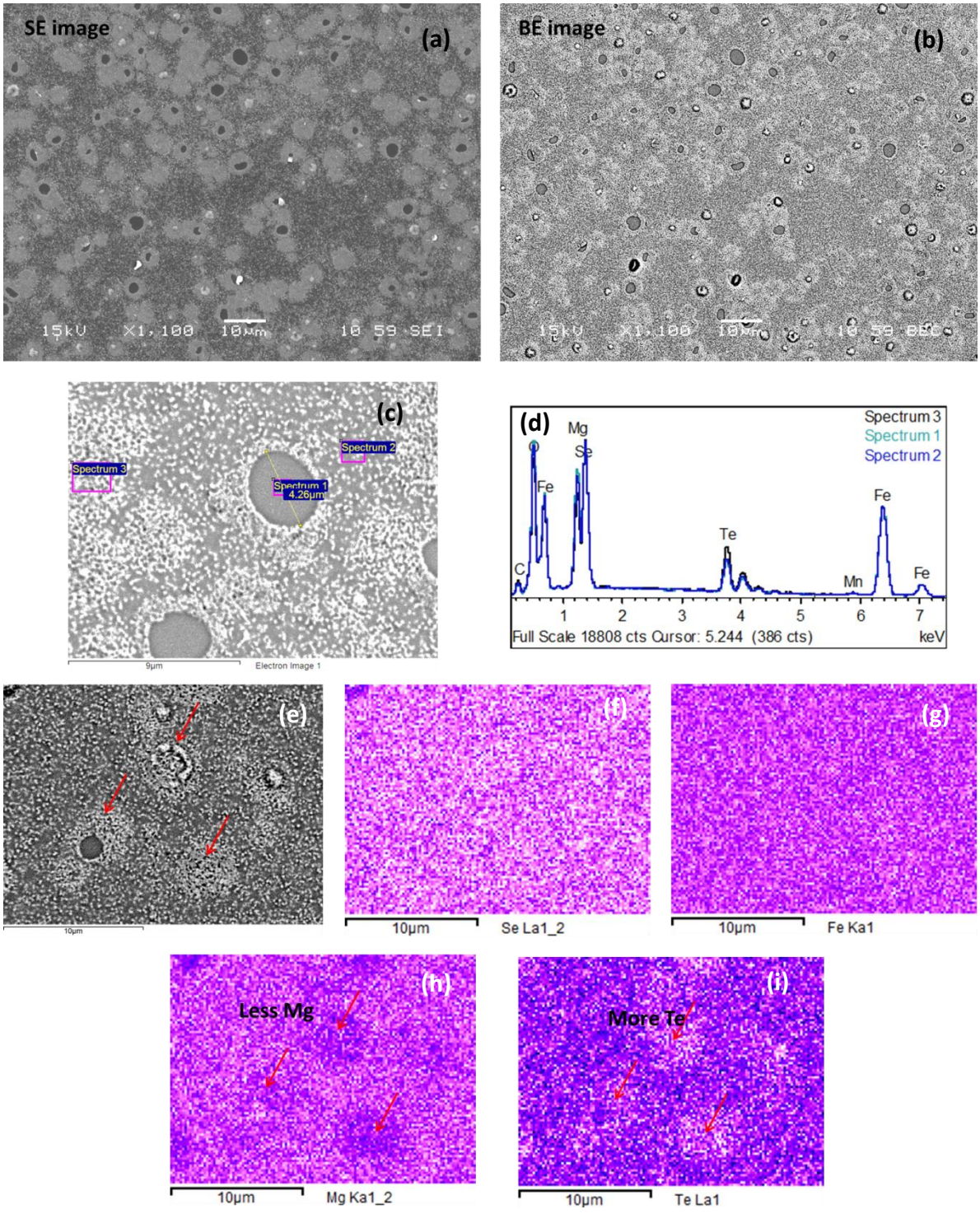

Figure 4.26: (a) Secondary and (b) backscattered electron images of a Fe(Se,Te) thin film deposited on MgO at 325°C, (c) high-magnification of a typical region, (d) EDX spectrum of the indicated regions, (e-i) EDX mapping of the selected region showing the presence of Te-rich regions on the surface.

4.8.1 Phase analysis

Figure 4.27 shows XRD patterns of deposited film before and after the annealing process. The cold-deposited film (before annealing) shows only MgO peaks with no trace of Fe(Se,Te) phase suggesting that the film is not crystalline as expected. The amorphous phase needs the annealing process to change from the amorphous to a crystalline phase. Annealing at 400°C for 2hrs leads to crystallization of the film and formation of the 11-phase as shown in Figure 4.27.

For the film annealed within the sputtering chamber, peaks corresponding to β-Fe(Se,Te) phase (tetragonal structure) appear in the XRD pattern. In addition to (*00l*) peaks, (101) peak can be also observed indicating that the sample is not perfectly c-axis aligned and there is mis-orientaiton. Moreover, all the peaks split into two sets implying coexistence of two structurally similar phases with a slightly difference in lattice parameters. These two phases possibly are possibly both 11 with different Se/Te ratios leading to two different sets of lattice spacings. This peak splitting has been also reported in other work [33, 37, 51], but only for the $FeSe_{0.75}Te_{0.25}$ stoichiometry. For example, Fang et al studied the phase evolution of $FeSe_{1-x}Te_x$ over the compositional range $0 \leq x \leq 1$, and found peak splitting only in $FeSe_{0.75}Te_{0.25}$ [33]. They reported that this phase separation happens because the structure of $FeTe_{0.75}$ is essentially different from that of $FeSe_{0.75}$ even though both of them can be described by a similar tetragonal lattice. One of these structure is stable for $0 \leq x \leq 0.15$, while the other one is stable for $0.3 \leq x \leq 1.0$ and both structural phases coexist in the range $0.15 \leq x \leq 0.3$ [33]. EDX data revealed $Fe_{1.18}Se_{0.83}Te_{0.17}$ to be the average composition of my annealed sample. Comparing this composition with what Feng et al reported, the ratio of Se/Te is within the coexistence region but the ratio of Fe/(Se+Te) is different. It can be suggested that phase separation (peak splitting) happens in the annealed sample as a result of local variations in Te/Se ratio, and possibly this phase separation is not highly sensitive to the Fe/Se ratio but the overall Se/Te ratio must lie in

the range identified above. This phase separation was only observed in this annealed sample, and none of in-situ grown films (the films grown onto heated substrates) on various substrates have shown similar peak splitting although a number of them are in the compositional range for phase separation. Perhaps 2-hrs annealing at 400°C provides enough time at a high enough temperature to encourage phase segregation. However, as was observed in the TEM images, there are traces of local nano-scale phase segregation in in-situ films as well (see Figure 4.20 and Figure 4.22) which shows that the kinetic restrictions for long diffusion of atoms can still allow local phase segregation.

For the films annealed under vacuum in a quartz tube within the furnace, no peak splitting is observed, but a number of weak peaks corresponding to the high-temperature δ-Fe(Se,Te) hexagonal structure appear in the XRD pattern in addition to the (*00l*) and (101) peaks of β-Fe(Se,Te). The reason why no hexagonal phase was detected in the sample annealed within the sputter chamber can be explained by the substrate being heated by a heating element beneath the substrate. The temperature of the top surface on which the film is growing depends on thermal conductivity of the MgO substrate which is not very high specially at higher temperatures. It is worth mentioning that the thermal conductivity of MgO single crystals hugely decreases with temperature. For example it is 38.1 $Wm^{-1}k^{-1}$ at 200°C, and 16.2 $Wm^{-1}k^{-1}$ at 400°C [52]. Therefore the temperature of the growing film may be lower than 400°C when it is annealed inside sputter chamber resulting in a sample free of high temperature phases such as the hexagonal phase.

The higher temperature of the specimen annealed in the furnace in addition to the vacuum atmosphere in the quartz tube may lead to evaporation of Se and Te and alteration of the composition of the sample. Therefore, the sample is no longer within the compositional range identified above resulting in no occurrence of phase separation of tetragonal β-Fe(Se,Te) in this sample. The difference in composition between these two samples can be also supported

by the peak shift towards larger angles (smaller c lattice parameter) for the sample annealed in the furnace.

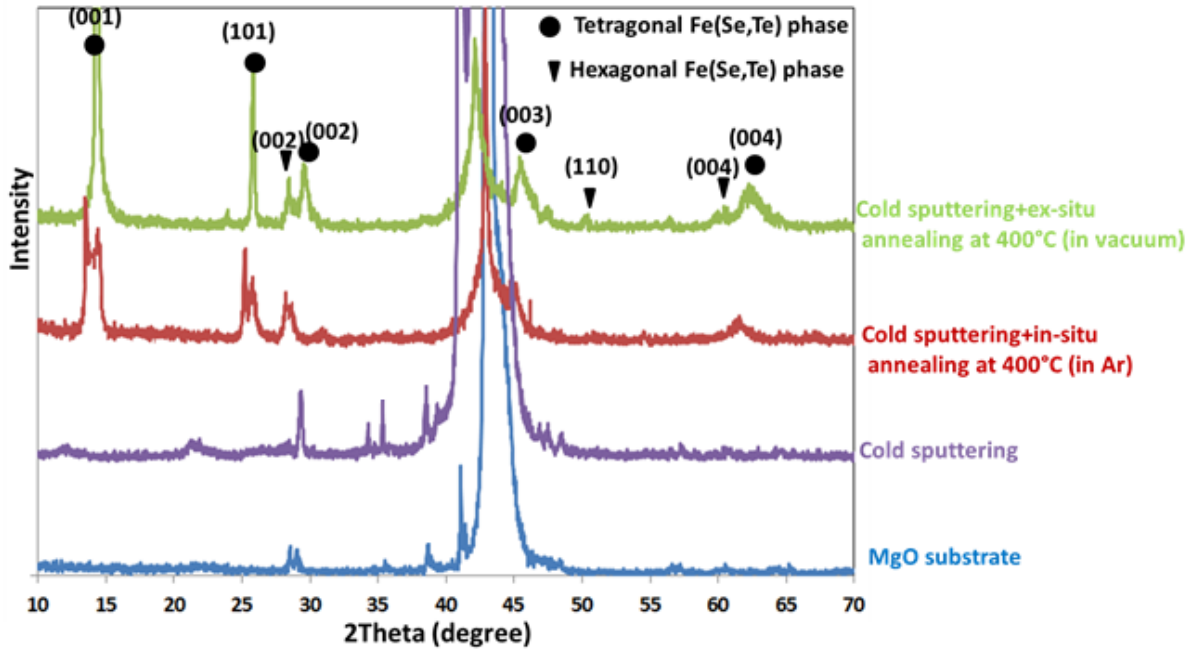

Figure 4.27: XRD patterns of Fe(Se,Te) thin films grown on MgO substrate for 2hrs at room temperature (cold sputtering) followed by in-situ and ex-situ annealing at 400°C for 2hrs showing that various annealing conditions result in different phases.

4.8.2 Surface morphology

SEM analysis of these samples (see Figure 4.28) shows that the as-deposited film has a relatively smooth surface, but the surface morphology of the annealed samples is not perfect and many defects such as holes and impurities can be seen on the surface, especially if they are compared with the surface morphology of the in-situ grown films.

Backscattered SEM images of the ex-situ annealed specimen consist of a large number of small regions in a brighter contrast compared to the matrix. High magnification imaging of these regions in Figure 4.29 shows that they contain some surface defects. The EDX maps of one of these regions (Figure 4.29) reveal that the distribution of Fe and Se is relatively uniform, but the Te content considerably increases around these circular features where the Mg content seems

low. It can be suggested that during annealing Te evaporates in the quartz tube, and when the sample is cooled down to room temperature Te is redeposited on the surface in preferential regions where defects exists.

These SEM results along with XRD data show that the overall quality of the ex-situ grown films is not as high as that of in-situ grown films because of the observation of phase impurities, in-plane mis-orientations and poor surface morphology in the ex-situ films. In particular, the texture develops more perfectly in in-situ films as the substrate is already heated when the sputtered atoms arrive to the surface and they can more easily form a unique crystalline structure. However, the post-annealing of an amorphous deposited film hardly leads to perfect out-of-plane and in-plane alignment. This fact has been also reported for some other thin films grown by sputtering [1, 53].

Annealing at higher temperature may lead to better texture alignment, but, as observed above, at higher temperatures there is the possibility of the formation of the hexagonal phase which destroys superconductivity in β-FeSe in addition to compositional variations and growth of Te-rich regions on the surface.

4.9 The effect of Mn substitution for Fe

As explained in the literature review chapter, it is interesting to study the effect of doping on the Fe site, which plays a significant role in the occurrence of superconductivity, with other elements especially transition metals with unpaired 3d electrons such as Mn because they offer the potential to study the interplay between magnetism and superconductivity. Gunther et al studied Mn-doped Fe(Se,Te) single crystals and found a higher onset temperature, a narrower width of the superconducting transition and a higher magnitude of the jump in the specific heat at T_C for Mn-doped samples in comparison to undoped samples [54].

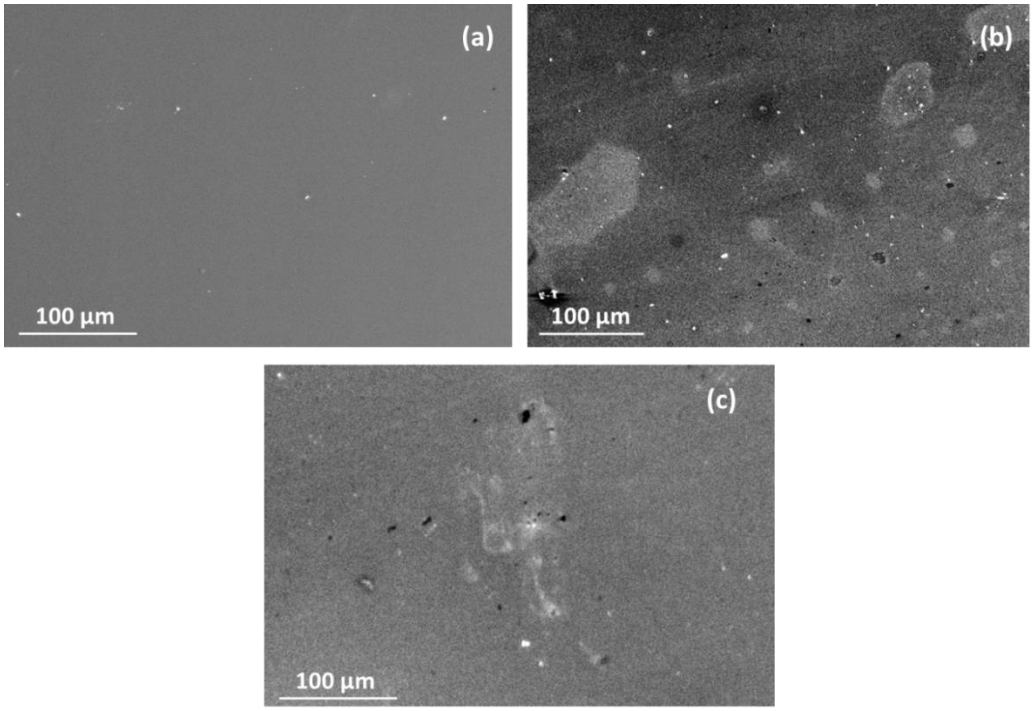

Figure 4.28: SEM micrographs of (a) cold-deposited film, (b) cold-deposited film annealed ex-situ in a furnace, (c) cold-deposited film annealed in-situ in sputter chamber showing more inhomogenities after annealing.

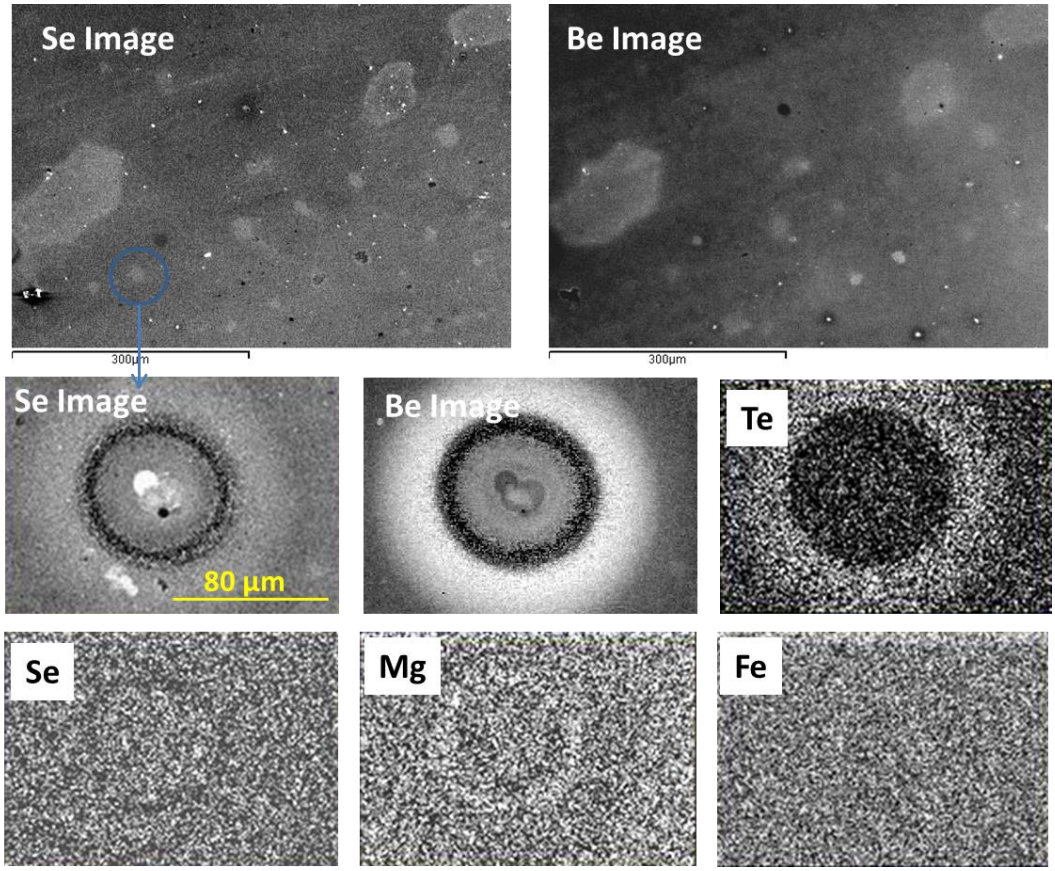

Figure 4.29: SEM micrographs and mapping data of the deposited film annealed in a furnace at 400°C for 2hrs showing Te-rich regions distributed over the sample especially around the surface defects.

However, in my thin films, the most significant effect of 2%Mn substitution for Fe was found to be improving epitaxy and stabilizing the β-Fe(Se,Te) tetragonal structure. Figure 4.30 shows Phi scans of the (101) plane for thin films of undoped Fe(Se,Te) and Mn-doped Fe(Se,Te) which have been grown under the same processing conditions. In the undoped sample, two sets of in-plane alignments (in 45°) are observed, whereas Mn-doped thin films are found to be single crystal with no mis-orientation. This is in agreement with the report in [54] where the widths of the XRD reflections for the Mn-doped sample was found to be narrower than those for the undoped sample.

Rather than stabilizing the tetragonal structure, no other obvious change, especially in superconducting properties, was found in the deposited films containing Mn. Similar results about the fact that Mn substitution has no effect on superconductivity in the Fe(Se,Te) phase have been reported in [55] where 5% Mn was substituted for Fe.

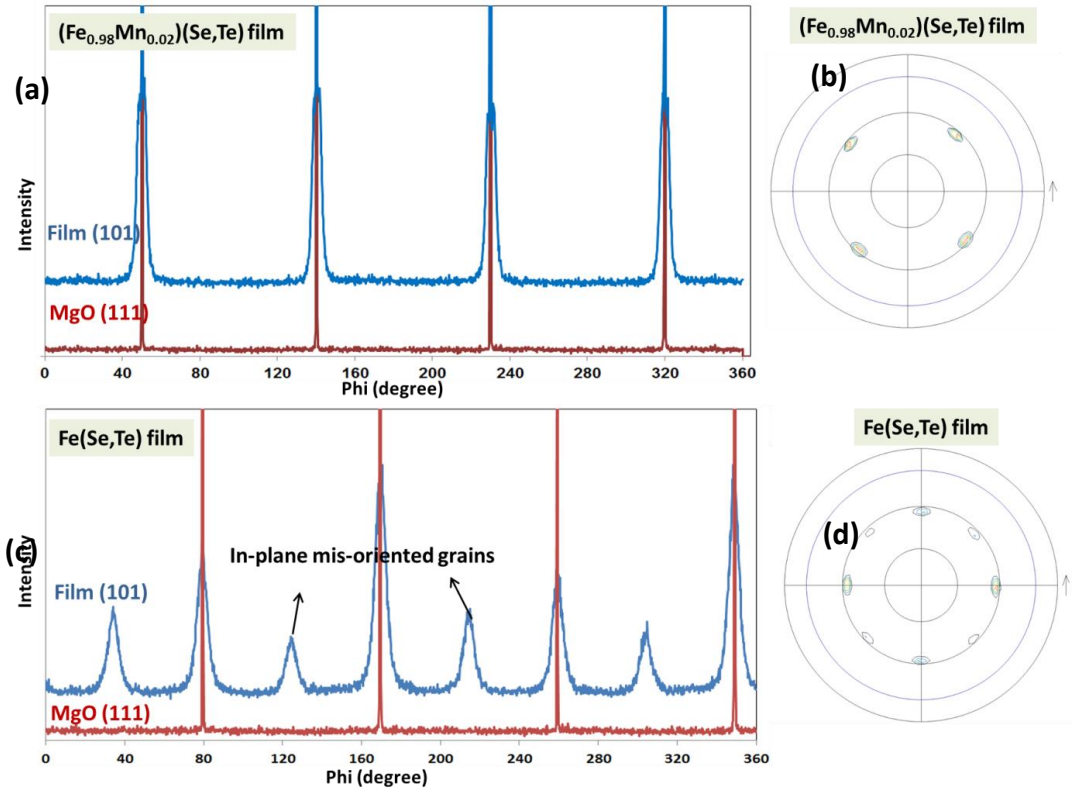

Figure 4.30: (a) Phi scan of MgO (111) and film (101) and (b) (101) pole figure of deposited film when 2% Mn is substituted for Fe in the Fe(Se,Te) structure, (c) Phi scan of MgO (111) and film (101) and (d) (101) pole figure of Fe(Se,Te) deposited film. The presence of Mn leads to better crystallographic alignment in the deposited film.

SEM/EDX data shows that the Mn concentration depends on Te content as seen in Figure 4.31. Increasing the Te content leads to a higher amount of Mn in the structure because of the large atomic size of Te compared to that of Se which leads to a considerable expansion in the unit cell. In an expanded unit cell, Mn atoms can diffuse more easily and settle in the structure substituting for smaller Fe atoms. However, plotting the variation of Mn concentration with Fe content (Figure 4.31) shows that the Mn concentration varies differently in Fe-deficient samples ($y<1$) and Fe-rich samples ($y>1$).

In Fe-deficient samples, the Mn concentration seems to be at the maximum level and almost independent of Fe content. However, in Fe-rich samples the Mn concentration shows a considerable reduction and decreases with Fe content. It can be suggested that in Fe-deficient samples, Fe vacancies exist in the structure allowing the maximum level of Mn incorporation into the structure. The independence of Mn and Fe contents in this region might be an indication of the fact that Mn atoms occupy the interstitial sites in the structure. As mentioned earlier and shown in Figure 4.31c, two different sites Fe1 (2a) and Fe2 (2c) are allowed in the Fe(Se,Te) structure [9, 56]. Fe atoms occupy Fe1 sites first, and if Fe content increases ($y>1$), the excess Fe occupy Fe2 sites [9]. Therefore, a constant maximum level of Mn concentration in Fe-deficient samples can be an indication that Mn atoms occupy the Fe2 sites, and when these sites are occupied by excess Fe (in $y>1$ samples) the Mn content decreases considerably. This explanation is in agreement with [54] where it is concluded that Mn atoms occupy interstitial sites in the Fe(Se,Te) structure. Although my explanation is consistent with the literature, it was concluded only from SEM/EDX data and more evidence (e.g. high-resolution TEM investigations) can be helpful to completely prove this conclusion.

4.10 Superconducting properties

Superconducting properties of the deposited films were investigated by two different methods, measuring magnetic moments as a function of temperature (SQUID system) and measuring electrical resistance as a function of temperature. The advantage of measuring magnetic moments rather than resistance is the possibility of detecting a discontinuous superconducting phase, but magnetic signals from substrate always interfere with the results.

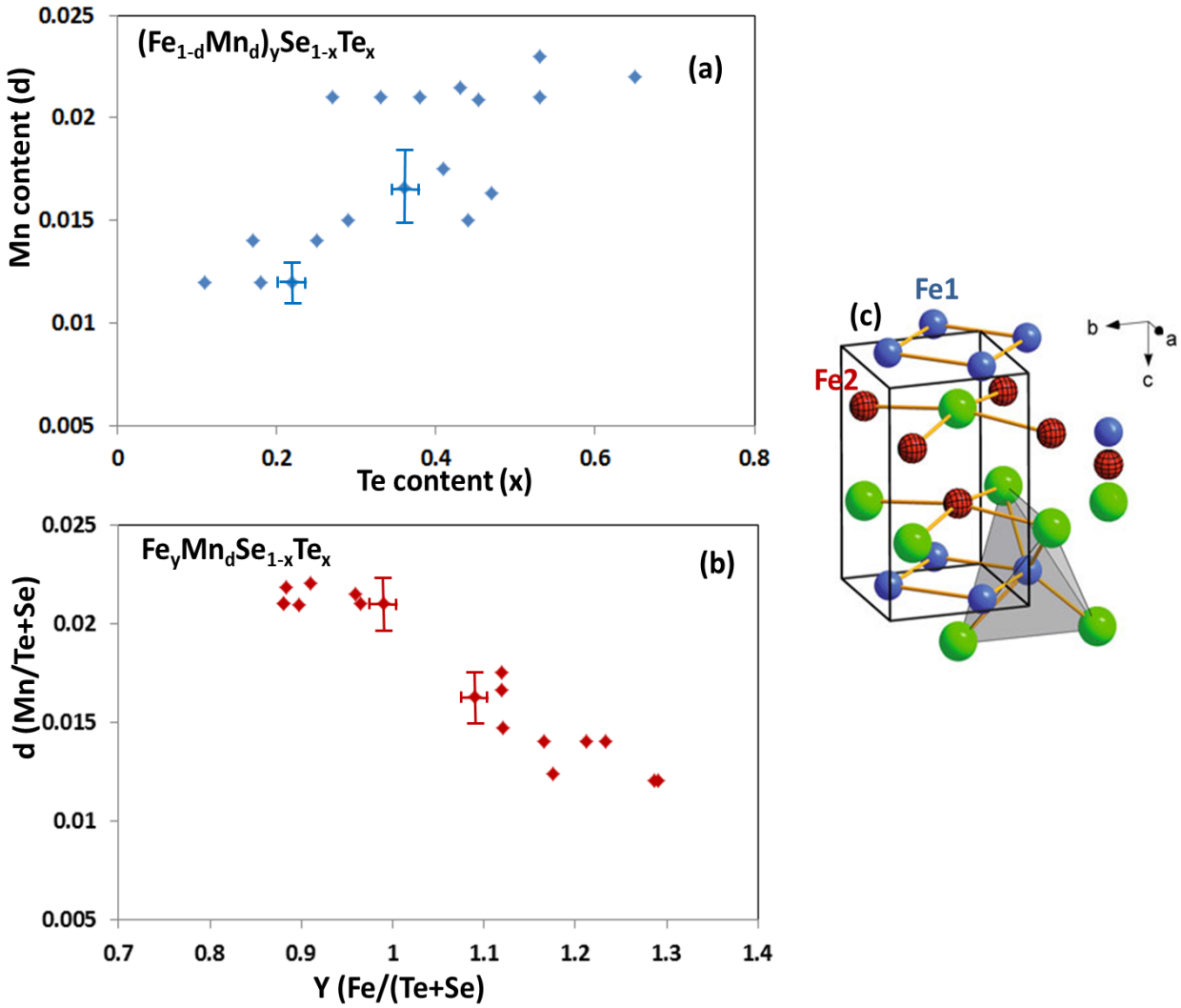

Figure 4.31: Variation of Mn content as a function of (a) Te content and (b) Fe content in the deposited films according to the formula written in each graph.

4.10.1 Transport measurements

Transport measurements were carried out on a large number of samples, but the temperature dependence of the resistivity for most of them show semiconducting behaviour, with higher resistivity for the samples containing more Te and more Fe similar to results reported in the literature [6, 20, 57].

Figure 4.32 shows resistivity as a function of temperature for a number of deposited films with different ρ(T) behaviours. As can be seen a sharp superconducting transition at $T_{C(onset)}$=10.2K occurs for the sample with $Fe_{1.01}Se_{0.56}Te_{0.44}$ composition. The width of the transition seems narrow indicating a high quality thin film with good crystallinity. Moreover, the p-T plot shows curved temperature dependence above the superconducting transition temperature ($T_{C(onset)}$=10.2K). This is one of the characteristics of the p-T plot for Te-doped FeSe [58]. Similar trends have been reported in the literature due to the effect of Te substitution, since the normal state resistivity of undoped FeSe usually shows a linear metallic behaviour from room temperature to the superconducting transition temperature [58].

The temperature dependence for the Mn-doped sample shows a higher resistivity at room temperature, and semiconducting behaviour on cooling. In general, substitution of the Fe sites leads to the suppression of superconductivity and higher resistivity at room temperature as it has been reported for $Fe_{1-x}Mn_xSe_{1-x}Te_x$ [57], $Fe_{1-x}Ni_xSe$ [51] and $Fe_{1-x}Co_xSe_{1-x}Te_x$ [59]. Moreover, in RT curve for the Mn-doped film, an anomaly around 100K can be seen. This is possibly an indication that a phase transition occurs at this temperature, consistent with XRD examination of $Mn_{0.1}Fe_{0.9}Se$ at low temperature by Wu et al which has shown that below 90-100K there is a structural transformation from tetragonal to monoclinic symmetry [57].

Another important point is the difference of electrical properties between two samples with almost the same composition but different thickness. From the SEM/EDX analysis, the Fe/Se/Te ratios are 1.01:0.55:0.45 for the superconducting (blue line in the graph) film and

1.02:0.41:0.59 for a film with semiconducting properties (green line in the graph). The Fe content, which is essential for the occurrence of the superconductivity, seems to be similar in both of these samples within measurement error. The properties of these two samples are summarized in Table 4.1. The film showing a superconducting transition is single crystalline with 68 nm thickness, while the film with semiconducting behaviour (green line in the graph) is 193 nm thick with no in-plane alignment and larger (001) FWHM. An obvious difference in lattice parameters is also observed. It can be suggested that in the thinner single crystal film, epitaxial strain leads to change of lattice parameter (e.g. smaller c-axis parameter due to the epitaxial compressive strain) and occurrence of superconductivity. In contrast, in the polycrystalline thicker film, in addition to the presence of grain boundaries, the lattice parameters are different leading to the destruction of superconductivity.

This result confirms that structural parameters and grain boundaries are as significant as chemical composition for achieving superconductivity in the Fe(Se,Te) compound, and compression along the c-axis, which can be controlled by the epitaxial strain, improves superconducting properties. Similar results have been previously reported for Fe(Se,Te) [25] [23, 27-32, 39-42].

In my thin films, a large number of the grown films did not show superconductivity mainly due to compositional deviations from the iedal $Fe_{1.01}$(Se,Te) stoichiometry, although other parameters such as strain, thickness, impurity and crystallinity of the films are also involved. As was shown in compositional analysis section, the deposited films have mostly an Fe-rich stoichiometry (i.e. y>1), and it was a big challenge to control composition of the deposited films. Since the occurrence of superconductivity strongly depends on stoichiometry, especially the Fe/(Se+Te) ratio, while the value of T_C depends on Se/Te ratio, it is believed that poor composition control is the main reason for the loss of superconductivity in my deposited films. The problems in controlling film stoichiometry have been described in section 4.2.

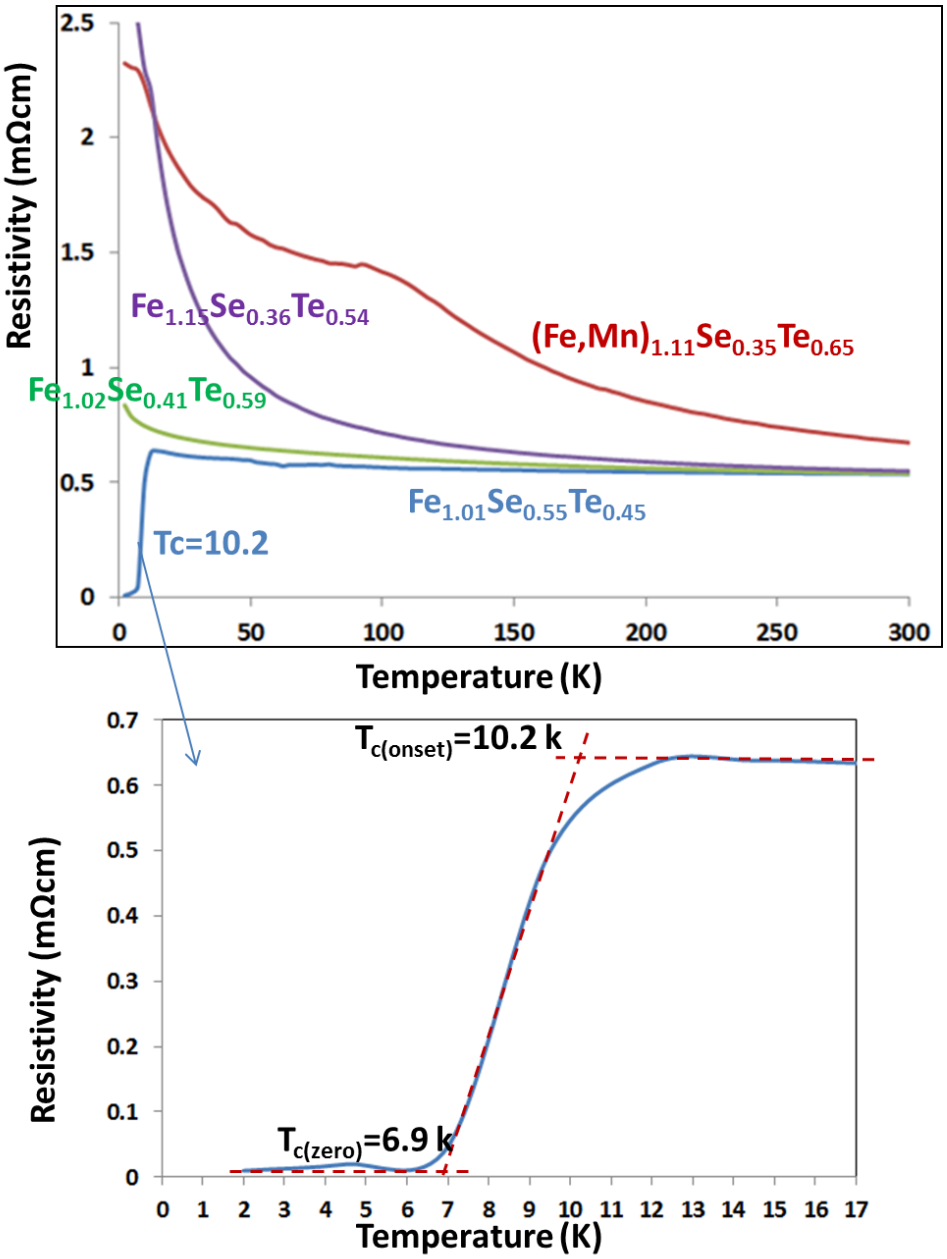

Figure 4.32: Temperature dependence of resistivity for a number of deposited thin films.

Table 4.1: A comparison of electrical and microstructural properties of two Fe(Se,Te) deposited films.

Processing conditions	Grown on MgO at 310°C for 45 min	Grown on MgO at 315°C for 120 min
Composition	$Fe_{1.01}(Se_{0.55}Te_{0.45})$	$Fe_{1.02}(Se_{0.41}Te_{0.59})$
Electrical properties	Tc=10.2 k	No Tc, semiconducting behaviour Higher normal resistivity
Out-plane mosaic	2.11	9.5
In-plane mosaic	4.54	-
Thickness	68 nm	193 nm
c-axis parameter	5.877	6.21
a-axis parameter	3.776	3.825
c/a ratio	1.556	1.623

4.10.2 SQUID measurements

The susceptibility (χ) of Fe(Se,Te) thin films was characterized by a SQUID magnetometer. First, the measurement was carried out on a piece of bare substrate, and magnetic moment was obtained for the substrate. The same measurement was done for the entire sample (both film and substrate) and magnetic moment of the film was obtained by subtracting these two values. Susceptibility of the film was then obtained by calculating magnetic moment per unit volume (scaled properly for shape) divided by the applied magnetic field (200 Oe). Due to anisotropic magnetism and strong 2D characteristics of the Fe(Se,Te) compound, magnetization is much more pronounced for the case where the applied field is parallel to the c-axis [60, 61].

Figure 4.33 shows the temperature dependence of the field-cooled (FC) susceptibility for a number of thin films chosen from a large number of measurements (more than 20 deposited films). As can be seen, the susceptibility for the most of these samples has a similar value, and below 20K it is temperature-independent. It has been reported in the literature that susceptibility decreases with increasing Te [62]. My data more or less shows a similar trend. However two samples (blue and orange lines) show much higher susceptibility and a paramagnetic tail at low temperature. Studying these two samples in detail shows both of them contain a large excess of Fe as well as an interlayer between the substrate and the film. It can

be suggested that the paramagnetic tail might be associated with localized iron ions at the interstitial sites similar to that reported in the literature [56]. The high value of susceptibility for these two samples might be an indication of the presence of magnetic impurities. Previous studies of Fe(Se,Te) have shown that iron oxide (magnetite Fe_3O_4) is the main magnetic impurity present in samples containing oxygen due to handling in air or preparing from impure elements [54, 56]. The susceptibility of the samples containing oxide impurities is significantly higher than that of oxygen-free samples. In these two samples, it can be suggested that the presence of Fe_3O_4 in the interface between film and substrate is likely because EDX has shown high Fe content in these samples and EELS experiments has proved the oxygen diffusion from the substrate to the film. Therefore, it is likely that the penetrated oxygen in the interface reacts with excess Fe forming magnetic Fe_3O_4 impurity in the interlayer consistent with TEM data showing nano-scale precipitations across the film especially close to the interface. However, XRD data did not show any evidence of Fe_3O_4 peaks which might be due to the small fraction and small size of Fe_3O_4 compared to the film and the MgO substrate which creates very high-intensity peaks in the diffraction pattern.

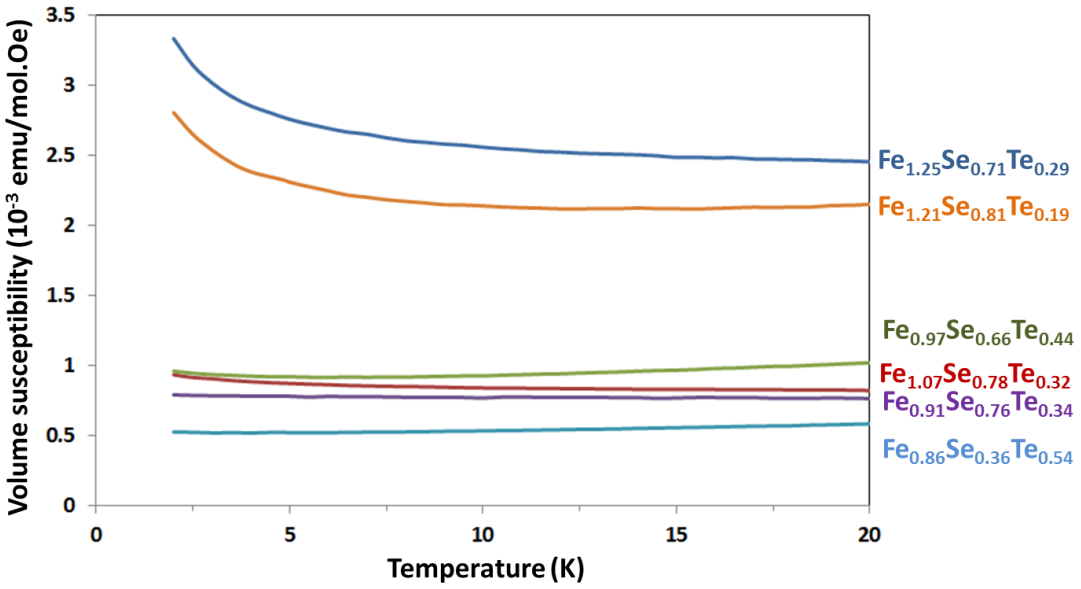

Figure 4.33: Volume magnetic susceptibility of Fe(Se,Te) thin films as a function of temperature with H ‖ c-axis in a field of 200Oe.

4.11 Conclusions

The feasibility of RF sputtering for the deposition of Fe(Se,Te) thin films was investigated. Compared to ex-situ sputtering, in-situ sputtering leads to higher quality films, e.g. smoother surface, pure phase, more uniform composition and better crystallographic alignment.

Phase evolution and texture development as a function of sputtering conditions were studied. Processing conditions for the in-situ epitaxial deposition of pure tetragonal β-$Fe_ySe_{1-x}Te_x$ films on MgO substrates were found to be a temperature window of 300-320°C and a thickness less than 50nm. Films deposited between 250-350°C develop a wide range of textures. The films are always c-axis aligned with different degrees of out-plane mis-alignments at different temperatures, but in-plane mis-orientations appear in the films depending on temperature. Out-of-plane alignment was found to be less temperature dependent compared to the in-plane alignment. The best alignment both in-plane and out-plane is obtained at 315°C, above which random in-plane alignments appear. The reason for this was found to be the formation of an interlayer between the MgO substrate presumably due to oxygen diffusion from substrate to the film.

Texture development was also found to be strongly dependent on the substrate. However, the relationship between texture and substrate is more related to the growth mechanism and microstructure rather than lattice misfit. Texture alignment for different substrate was found to be MgO>LAO>STO>CaF_2>LiF>LSAT, with the best texture on MgO and the worst texture on LSAT.

Chemical analysis of the films show that sputtering leads to a fairly uniform composition across the film although the films tend to enrich in Fe content. The stoichiometry of the films (especially Fe/(Se+Te) ratio) was found to be highly important for superconductivity. A sharp T_C of about 10.2K was obtained for a single crystal 58-nanometer thick film with a Fe/(Se+Te) ratio close to 1.

Surface morphology of the deposited films was shown to be flat and smooth with no obvious holes/cracks. However, Te-rich regions are formed on the surface after deposition, with higher densities at higher temperatures. Decreasing the Ar pressure inside the sputtering chamber was shown to be a useful way to prevent formation of these features on the surface.

As a conclusion, compared to other deposition techniques, e.g. pulsed laser deposition which has been widely used in the literature, sputtering offers a potential technique for the deposition of considerably high quality 11-phase in a wider range of temperature and more flexible conditions. However, with only one target made of all three elements (Fe, Se and Te), it is challenging to precisely control the composition of the deposited films due to large difference between the transferring rates of Fe and Se/Te resulted from their highly different vapour pressures. A sputtering system with multiple targets can be a strong potential to overcome this limitation.

A list of future work can be recommended as follows:

1- Deposition of Fe(Se,Te) films by multiple-target sputtering to avoid rapidly change in target composition, and accurately control the stoichiometry of the deposited films.

2- Deposition of the films in different sputtering conditions e.g. at higher Ar pressure which might be a solution for the Se and Te deficiency in the films.

3- High-resolution TEM investigation of the deposited film especially for the nano-scale phase segregation, Fe_3O_4 particles and substrate/film interface.

4.12 References

1. K. Wasa, M. Kitabatake, H. Adachi, *Thin film materials technology: sputtering of compound materials*, 2004, Norwich, NY, Heidelberg, William Andrew Pub, Springer.
2. K. Wasa, *Handbook of Sputter Deposition Technology Fundamentals and Applications for Functional Thin Films, Nanomaterials, and MEMS*, 2nd Edition Preface.
3. J. Sarkar, *Sputtering Materials for VLSI and Thin Film Devices*, 2013, William Andrew.
4. D. Depla, *Magnetrons, reactive gases and sputtering*, 1st ed, 2013, Diederik Depla.
5. B. Rainer, *Sputtering by Particle Bombardment*, 2007, Wolfgang.

6. T.M. McQueen, et al., *Extreme sensitivity of superconductivity to stoichiometry in FeSe*, Physical Review B, 2009, B79: p. 014522.
7. K.W. Yeh, Y. Huang, *Tellurium substitution effect on superconductivity of the alpha-phase iron selenide*, Europhysics Letters, 2008, 84(3): p. 14.
8. K.W. Yeh, T.W. Huang, P.M. Wu, Y.L. Huang, T.K. Chen, J.Y. Luo, M.K. Wu, *Se and Te Doping Study of the FeSe Superconductors*, J. Phys. Soc. Jpn., 2008(77): p. Supplement C 19-22.
9. T.J. Liu, X.K., B. Qian, J. Hu, D. Fobes, E. K. Vehstedt, H. Pham, J.H. Yang, M.H. Fang, L. Spinu, Y.L. Schiffer, and Z. Q. Mao, *Charge-carrier localization induced by excess Fe in the superconductor* $Fe_{1+y}Te_{1-x}Se_x$, Physical Review B, 2009, 80: p. 174509.
10. S.C. Speller, M. Saydam, H. Taylor, G. Burnell, A.T. Boothroyd, C.R.M. Grovener *Analysis of* $FeySe_{1-x}Te_x$ *thin films grown by radio frequency sputtering.* Supercond. Sci. Technol., 2011, 24: p. 075023.
11. K. Sugibuchi, Y. Kurogi, N. Endo, *Ferroelectric Field-Effect Memory Device Using* $Bi_4Ti_3O_{12}$ *Film*, Journal of Applied Physics, 1975, 46(7): p. 2877-2881.
12. B. Jae-Sang, Y.J. KIM, *Cooling effect enhancement in magnetron sputtering system*, Fifth International Conference on CFD in the Process Industries, 2006, Melbourne, Australia.
13. L.S. Brooks, *The Vapor Pressures of Tellurium and Selenium*, Journal of the American Chemical Society, 1952. 74(1): p. 227-229.
14. W.M. Haynes, D.R. Lide, *CRC handbook of chemistry and physics: a ready-reference book of chemical and physical data*, 91st ed, 2010, Boca Raton, Fla. CRC Press.
15. A. Billard, et al., *Influence of the target temperature on a reactive sputtering process*, Surface & Coatings Technology, 1999. 116: p. 721-726.
16. P.J. Kelly, R.D. Arnell, *Magnetron sputtering: a review of recent developments and applications*, Vacuum, 2000, 56(3): p. 159-172.
17. Z.L. Liau, et al., *Surface-Layer Composition Changes in Sputtered Alloys and Compounds*, Applied Physics Letters, 1977, 30(12): p. 626-628.
18. G. Hagg, A.L. Kindstrom, Z. Phys. Chem., 1933. 22: p. 455.
19. H. Hiramatsu, *Water-induced superconductivity in* $SrFe_2As_2$. Physical Review B, 2009, 80(5): p. 43.
20. Y. Han, L.X. Cao, S. Zhang, B. Xu, B.R. Zhao, *Preparation and superconductivity of iron selenide thin films.* J. Phys. Condens. Matter, 2009, 21(23): p. 5702.
21. F.C. Hsu, K.W. Yeh, *Superconductivity in the PbO-type structure β-FeSe*, Proceedings of the National Academy of Sciences, 2008. 105: p. 312.
22. A. Tsukada, et al., *Pulsed laser deposition conditions and superconductivity of FeSe thin films*, Applied Physics A, 2011, 104(1): p. 311-318.
23. T.G. Kumary, J. Janaki, A. Mani, A.T. Satya, R.M. Sarguna, P.K. Ajikumar, A.K. Tyagi, A. Bharathi, *Superconducting* $Fe_{1+\delta}Se_{1-x}Te_x$ *thin films: growth, characterization and properties*, Supercond. Sci. Technol., 2009, 22 (9): p. 5018.
24. A. Authier, *Early Days of X-ray Crystallography*, 2013, Oxford, Oxford University Press.
25. I. Tsukada, et al, *Epitaxial Growth of* $FeSe_{0.5}Te_{0.5}$ *Thin Films on* CaF_2 *Substrates with High Critical Current Density*, Applied Physics Express, 2011, 4: p. 053101.
26. I.Y. Imai, M. Hanawa, I. Tsukada, A. Ichinose, A. Maeda, T. Hikage, T. Kawaguchi, H. kuta, *Systematic Comparison of Eight Substrates in Growth of* $FeSe_{0.5}Te_{0.5}$ *Superconducting Thin Films*, applied physics express, 2010, 3: p. 043102.
27. S.X. Huang, V. Thampy, C. Broholm, *Control of tetrahedral coordination and superconductivity in* $FeSe_{0.5}Te_{0.5}$ *thin films*, Phys. Rev. Lett., 2010, 104: p. 217002.
28. E. Bellingeri, R. Buzio, A. Gerbi, D. Marre, M.R. Cimberle, M. Tropeano, M. Putti, A. Palenzona, C.Ferdeghini, T_C *=21K in epitaxial* $FeSe_{0.5}Te_{0.5}$ *thin films with biaxial compressive strain*, Appl. Phys. Lett., 2010, 96(10): p. 2512.
29. E. Bellingeri, A. Gerbi, D. Marre, S. Congiu, M. R. Cimberle, M. Tropeano, A.S. Siri, A. Palenzona, C. Ferdeghini, *High quality epitaxial* $FeSe_{0.5}Te_{0.5}$ *thin films grown on* $SrTiO_3$ *substrates by pulsed laser deposition*, Superconductor Science and Technology, 2009, 22 (10): p. 5007.

30. W. Si, Z.W.L., Q. Jie, W.G. Yin, A. Johnson, *Enhanced superconducting transition temperature in $FeSe_{0.5}Te_{0.5}$ thin films,* Appl. Phys. Lett., 2009, 95(5): p. 2504.
31. M. Hanawa, et al., *Empirical Selection Rule of Substrate Materials for Iron Chalcogenide Superconducting Thin Film,* Japanese Journal of Applied Physics, 2012, 51(1): p. 74.
32. M. Hanawa, S. Komiya, I. Tsukada, T. Akiike, Y. Imai, T. Hikage, T. Kawaguchi, H. Ikuta, A. Maeda, *Substrate Dependence of Structural and Transport Properties in $FeSe_{0.5}Te_{0.5}$ Thin Films,* Japanese Journal of Applied Physics, 2011, 50: p. 053101.
33. M.H. Fang, B. Qian, T.J. Liu, E.K. Vehstedt, Y. Liu, L. Spinu, *Superconductivity Close to Magnetic Instability in $Fe(Se_{1-x}Te_x)_{0.82}$,* Phys. Rev. B., 2008, 78: p. 224503.
34. C.H. Lee, et al., *Relationship between crystal structure and superconductivity in iron-based superconductors,* Solid State Communications, 2012, 152(8): p. 644.
35. A.R. Denton, N.W. Ashcroft, *Vegard's law,* Phys. Rev. A, 1991, 43(6): p. 3161.
36. H.L. Shi, et al., *Magnetic behavior of Fe(Se,Te) systems: First-principles calculations,* Journal of Applied Physics, 2011, 110(4): p. 942.
37. R.W. Gomez, et al., *Effects of Substituting Se with Te in the FeSe Compound: Structural, Magnetization and Mossbauer Studies,* Journal of Superconductivity and Novel Magnetism, 2010, 23(4): p. 551.
38. Y.C. Wen, et al., *Elastic stiffness of single-crystalline FeSe measured by picosecond ultrasonics.* Journal of Applied Physics, 2011, 110(7): p. 34672.
39. M. Jourdan, *Preparation, characterization, and upper critical field of epitaxial FeSe thin films,* J. Appl. Phys., 2010, 108: p. 023913.
40. G. Garbarino, P. Lejay, A. Sulpice, P. Toulemonde, W. Crichton, M. Mezouar, M. Nunez, A. Regueiro, *High temperature superconductivity (T_c onset at 34K) in the high pressure orthorhombic phase of FeSe* EPL, 2009, 86: p. 27001.
41. S. Medvedev, I.A. Troyan, T. Palasyuk, M.I. Eremets, R.J. Cava, S. Naghavi, F. Casper, V. Ksenofontov, G. Wortmann, C. Felser, *Electronic and magnetic phase diagram of β-$Fe_{1.01}Se$ with superconductivity at 36.7 K under pressure,* Nature Materials, 2009, 8: p. 630.
42. N.C. Gresty, A.Y. Ganin, T. McDonald, B. Claridge, D. Giap, Y. Mizuguchi, Y. Takano, T. Kagayama, Y. Ohishi, M. Takata, M.J. Rosseinsky, S. Margadonna, K. Prassides, *Structural Phase Transitions and Superconductivity in $Fe_{1+\delta}Se_{0.57}Te_{0.43}$ at Ambient and Elevated Pressures,* J. Am. Chem. Soc, 2009, 131: p. 16944.
43. S.C. Speller, et al., *Analysis of local chemical and structural inhomogeneities in $FeySe_{1-x}Te_x$ single crystals,* Appl. Phys. Lett, 2011, 99: p. 19.
44. M. Tegel, D. Johrendt, *The crystal structure of $FeSe_{0.44}Te_{0.56}$,* Solid State Commun., 2010, 150: p. 383.
45. L. Chen, Y. Zhu, Z. Bi, *Enhanced superconducting properties in epitaxial FeSe thin films with self-assembled Fe_3O_4 nanoparticles,* Physica C, 2011, 471: p. 515.
46. A. E. Bohmer, et al., *Lack of coupling between superconductivity and orthorhombic distortion in stoichiometric single-crystalline FeSe,* Phys. Rev. B, 2013, 87: p. 180505.
47. H.S. Nalwa, *Handbook of Thin Films, Deposition and processing of thin films,* 2002, Elsevier Inc.
48. V. Braccini, et al., *Highly effective and isotropic pinning in epitaxial Fe(Se,Te) thin films grown on CaF_2 substrates,* Applied Physics Letters, 2013, 103(17): p. 7982.
49. C.W. Schneider, et al., *The origin of oxygen in oxide thin films: Role of the substrate,* Applied Physics Letters, 2010, 97(19): p. 932.
50. J. Janaki, et al., *Synthesis, characterization and low temperature studies of iron chalcogenide superconductors,* Journal of Alloys and Compounds, 2009. 486(1-2): p. 37.
51. Y. Mizuguchi, Sh. Tsuda, T. Yamaguchi and Y. Takano, *Substitution Effects on FeSe Superconductor,*. J. Phys. Soc. Jpn., 2009, 78: p. 074712.
52. A.M. Hofmeister, *Thermal diffusivity and thermal conductivity of single-crystal MgO and Al_2O_3 and related compounds as a function of temperature.* Physics and Chemistry of Minerals, 2014, 41(5): p. 361.
53. N.J. Park, et al., *Effect of film thickness on the evolution of annealing texture in sputtered copper films,* Journal of Electronic Materials, 2005, 34(12): p. 1500.

54. A. Gunther, C. Kant, H.A. Krugvon Nidda, V. Tsurkan, A. Loidl, *Improvement of superconducting properties of $FeSe_{0.5}Te_{0.5}$ single crystals by Mn substitution,* Supercond. Sci. Technol., 2011, 24(4): p. 045009.
55. A.M. Zhang, et al., *Effects on superconductivity of transition-metal doping in $FeSe_{0.5}Te_{0.5}$.* Journal of Physics-Condensed Matter, 2010, 22(24): p. 3334.
56. V. Tsurkan, et al., *Physical properties of $FeSe_{0.5}Te_{0.5}$ single crystals grown under different conditions,* European Physical Journal B, 2011, 79(3): p. 289.
57. M.K. Wu, K.W. Yeh, T.W. Huang, J.Y. Luo, M.J. Wang, H.H. Chang, T.K. Chen, S.M. Rao, and C.L.C. B.H. Mok, Y.L. Huang, C.T. Ke, P.M. Wu, A.M. Chang, C.T. Wu, T.P. Perng, *The development of the superconducting PbO-type b-FeSe and related compounds,* Physica C, 2009, 469: p. 340.
58. R. Shipra, A. Sundaresan, *Effects of Ni and Co doping on the physical properties of tetragonal $FeSe_{0.5}Te_{0.5}$ superconductor,* Physica C,2010. 470: p. 528.
59. F. Nabeshima, et al., *Effect of Co Impurities on Superconductivity of $FeSe_{0.4}Te_{0.6}$ Single Crystals,* Japanese Journal of Applied Physics, 2012, 51(1): p. 843.
60. Y. Mizuguchi, *A review of Fe-chalcogenide superconductors: the simplest Fe-based superconductor,* J. Phys. Soc. Jpn., 2010, 79: p. 102001.
61. Q. Li, I.V. Dimitrov, *Films of iron chalcogenide superconductors,* Rep. Prog. Phys., 2011, 74: p. 124510.
62. K.W. Yeh, T.W. Huang, T.K. Chen, Y.L. Huang, P.M. Wu, M.K. Wu, *Superconducting $FeSe_{1-x}Te_x$ Single Crystals Grown by Optical Zone-Melting Technique,* Crystal Growth Design, 2009, 9: p. 4847.

Chapter 5: Microstructural analysis of Mn-doped Bi_2Te_3 single crystals

This chapter reports microstructural analysis of undoped Bi_2Te_3 single crystals and Mn-doped Bi_2Te_3 single crystals with nominal Mn concentrations of 0.09 and 0.15. All the samples were grown by collaborators in the Clarendon Laboratory of the University of Oxford. Following an introduction to Bi_2Te_3 and the reasons for doping the structure with Mn, this chapter will present sample preparation details and results, obtained by SEM and TEM, followed by conclusions and suggestions for future work.

5.1.Introduction

Bi_2Te_3 belongs to the class of V2VI3 binary chalcogenide semiconductors with a narrow band gap. Bi_2Te_3 is well known as one of the best thermoelectric materials near room temperature [1, 2] which means that it can reversibly convert heat into electrical energy, and can be used as a material in cooling or power generating systems [3]. It, therefore, has interesting applications in optoelectronic and electrochemical devices such as heat pumps, infrared sensors and high efficiency photovoltaic solar cells [4]. Due to these potential applications and excellent thermoelectric properties, the synthesis of high quality Bi_2Te_3 has attracted much interest. Recently, even more interest in Bi_2Te_3 and related materials has been revived with the discovery that the Bi_2Te_3 family of materials can be topological insulators [5].

Topological insulators (TIs) are a new group of materials which behave as an insulator in the bulk phase while permitting the movement of charges on the surface. In the bulk of a TI, (as shown in Figure 5.1) the electronic band structure resembles an ordinary band insulator, with the Fermi level falling between the conduction and valence bands. On the surface of a TI there are special states that fall within the bulk energy gap and allow surface metallic conduction [6-9]. This distinguishes TI from conventional insulators that do not feature such edge/surface states. In some materials of this family the Fermi level actually falls in either the conduction or valence bands due to naturally occurring defects, and must be pushed into the bulk gap by doping or gating [10]. For further details about physics of TI, the reader is referred to "Topological insulators and topological superconductors" by Bernevig [9].

Because of such new important fundamental properties, TI have attracted much attention from both theorists and experimentalists, and also shown great potential for new applications such as nanoelectronics, spintronics and, in particular, quantum computing [11, 12]. The first two-dimensional TI was discovered in HgTe in 2006 by Bernevig et. al [13]. Following this discovery, the first experimentally realized three dimensional TI state was discovered in bulk systems of bismuth antimony $Bi_{1-x}Sb_x$ [12]. Shortly thereafter, in 2009, three-dimensional TI

were also discovered in pure antimony, bismuth selenide (Bi_2Se_3) and bismuth telluride (Bi_2Te_3) [5]. Several other material systems are now believed to include topological insulator states.

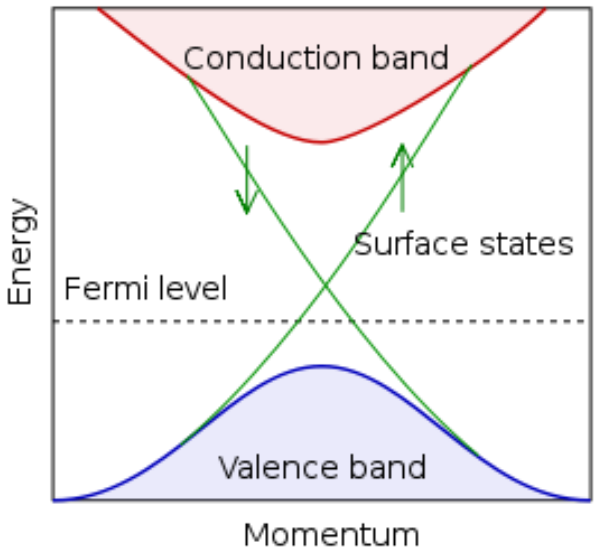

Figure 5.1. Schematic of surface states for a topological insulator. The Fermi level falls within the bulk band gap which is traversed by topologically-protected surface states.

Doping of topological insulators to decrease bulk carrier concentration [14] and induce superconductivity [15] has been performed in order to investigate various aspects of the surface states in these materials, including their potential applicability in novel electronic devices. Of particular interest are the effects of magnetic impurities and ferromagnetism on the topological surface states. For example, doping Bi_2Te_3 with transition metal ions such as Fe or Mn [16] can lead to the formation of ferromagnetic order, while undoped Bi_2Te_3 exhibits no magnetic ordering and single crystals are typically p-type semiconductors that can become superconducting under pressure [17]. The presence of magnetic ions can break the time reversal symmetry of a topological insulator, which is necessary for some applications. Moreover, transition metal doping of semiconductors is an active field of research, as magnetic semiconductors such as Mn-doped GaAs [18] are a prerequisite for spintronic applications in which both the spin and the charge of the electron are exploited for information processing

[19]. Therefore, doping Bi_2Te_3 with magnetic transition metal such as Mn is of interest from different aspects, and has been studied by a number of groups [16][14, 20]. One of the first studies to show the interplay between ferromagnetism and the breaking of time reversal symmetry in a topological insulator was reported by Hor et al [14] in Mn-doped Bi_2Te_3. They found that ferromagnetic order is established for Mn concentrations higher than x=0.04 in $Mn_xBi_{2-x}Te_3$, with a Curie temperature varying between 9 and 12 K.

However, in all of these studies, it has been found difficult to achieve ferromagnetism in homogeneous (i.e. segregation-free) versions of these materials, and the synthesis of doped-homogeneous single crystals is one of the challenges in the field [20]. So far, even nominally identically prepared samples show a diversity of magnetic transition temperatures, saturation magnetizations, and anisotropies. These properties can vary even over the extent of a small single crystal.

More importantly, the layered crystal structure of these materials allows the dopants not only to enter the host substitutionally, but also in the van der Waals gap between the layers (i.e. interstitial sites). For the realization of the topological properties in these materials, their bulk electronic properties have to be controlled by finding ways to reduce the defect densities, and by understanding the role of dopants and intercalated ions. Therefore, investigation of the microstructure and homogeneity of Mn-doped Bi_2Te_3 compounds, especially the distribution of Mn, is important since we expect it to considerably affect magnetic and electrical properties.

This chapter deals with microstructural analysis of Mn-doped Bi_2Te_3 single crystals. A wide variety of electrical and bulk/surface sensitive magnetic probes such as SQUID and torque magnetometry, muon spin rotation and x-ray magnetic circular dichroism have been used by collaborators to investigate electrical and magnetic properties of these samples [20]. In complementary work to study the doping of topological insulators and the link between the

structural details and the physical properties, I performed a microstructural study (mostly TEM) of these samples.

5.2. Crystal structure and properties of Bi_2Te_3

Bismuth telluride (Bi_2Te_3) crystallizes in a rhombohedral lattice ($R\bar{3}m$), and shows a layered structure with stacking of a five atomic layer block known as a "quintuple layer". As shown in Figure 5.2, the atomic arrangement in each quintuple layer occurs in the order Te(1)-Bi-Te(2)-Bi-Te(1) [21]. The quintuple layers are separated by a van der Waals gap across which the Te layers are only weakly bound. The presence of this weak Van der Waals bonding between quintuple layers is one of the important characteristics of the Bi_2Te_3 structure. This property has enabled mechanical and chemical exfoliation of this material and has raised prospects for manufacturing two-dimensional sample which can be used in a plethora of applications [22].

When Bi_2Te_3 is doped by mangenese, Mn atoms may enter the matrix in the van der Waals gap (i.e. interstitial site), or substitute onto Bi sites (substitutional sites), as shown in Figure 5.2.

5.3. Sample preparation

Mn-doped Bi_2Te_3 single crystals were grown by collaborators in the Clarendon Laboratory at Oxford University. Stoichiometric amounts of the high purity (>99.99%) Bi, Te and Mn, with stoichiometry $Mn_xBi_{2-y}Te_3$ with nominal Mn concentrations of x=0.09 and 0.15 were mixed, sealed in an evacuated quartz tube, and then heated to a temperature of 1003°C. The samples were cooled down to 855°C at the rate of 10°C/h and down to 529°C at the rate of 5°C/h. The

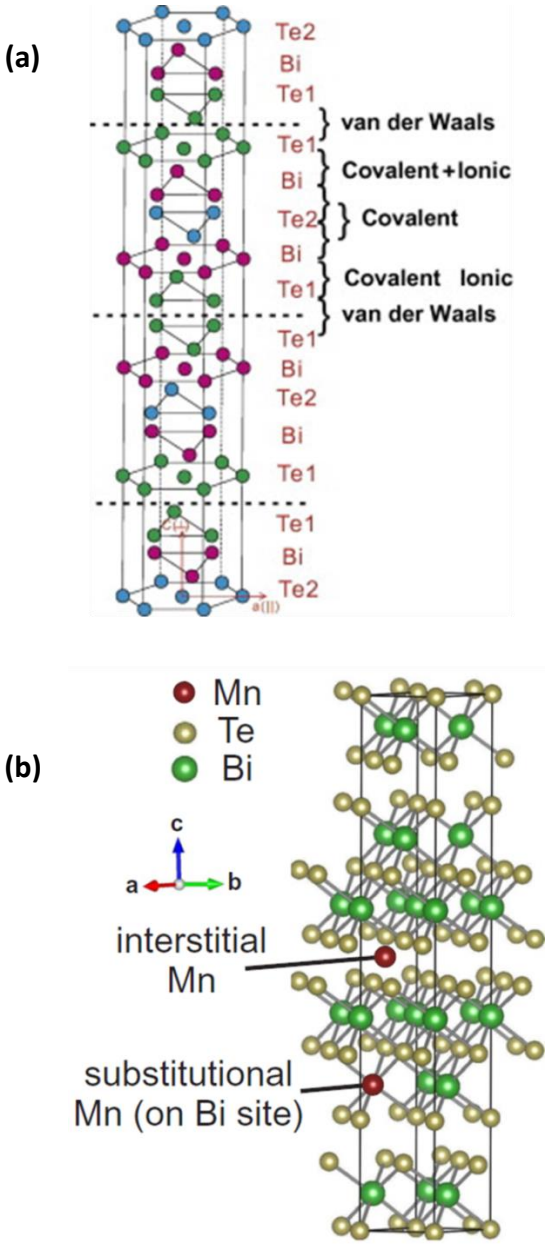

Figure 5.2: (a) Crystal structure of Bi_2Te_3, (b) Possible locations for Mn atoms as interstitial and substitutional sites in Mn-doped Bi_2Te_3 structure [20].

actual crystal growth occurred during the latter cooling process [20]. Finally, the crystals were annealed at 529°C (x=0.09) and 579°C (x=0.15). The annealing temperature is different because the melting point increases with Mn concentration. More details of this growth process can be found in [20]. Three samples studied in this chapter will be referred as Bi_2Te_3, 9%Mn and 15%Mn.

SEM and TEM techniques were used to characterise the microstructure of these samples. For TEM, two different types of TEM foils were prepared from these samples. Cross-sectional TEM samples were made by FIB lift out using the FIB 200 instrument. As these samples were exteremely soft, the voltage and beam current used for each step of FIB milling were chosen to be much lower than usual values to avoid introducing any damage or artifacts into the samples. Plan-view TEM samples were prepared by mechanical exfoliation from bulk single crystals. Figure 5.3 shows this procedure schematically. Using a sticky tape, a thin layer from the surface of the sample was exfoliated. This procedure was repeated for the newly exfoliated layer until only small flakes of the sample are left on the tape. Then the tape was dissolved in acetone, and flakes were scooped from the acetone by TEM grid under an optical microscope. TEM samples prepared by this method are about 2-9μm in size and cleaved along the ab-plane in Bi_2Te_3 structure due to weak Van der Waals bonding. Therefore the normal direction of these TEM samples is the rhombohedral c-axis.

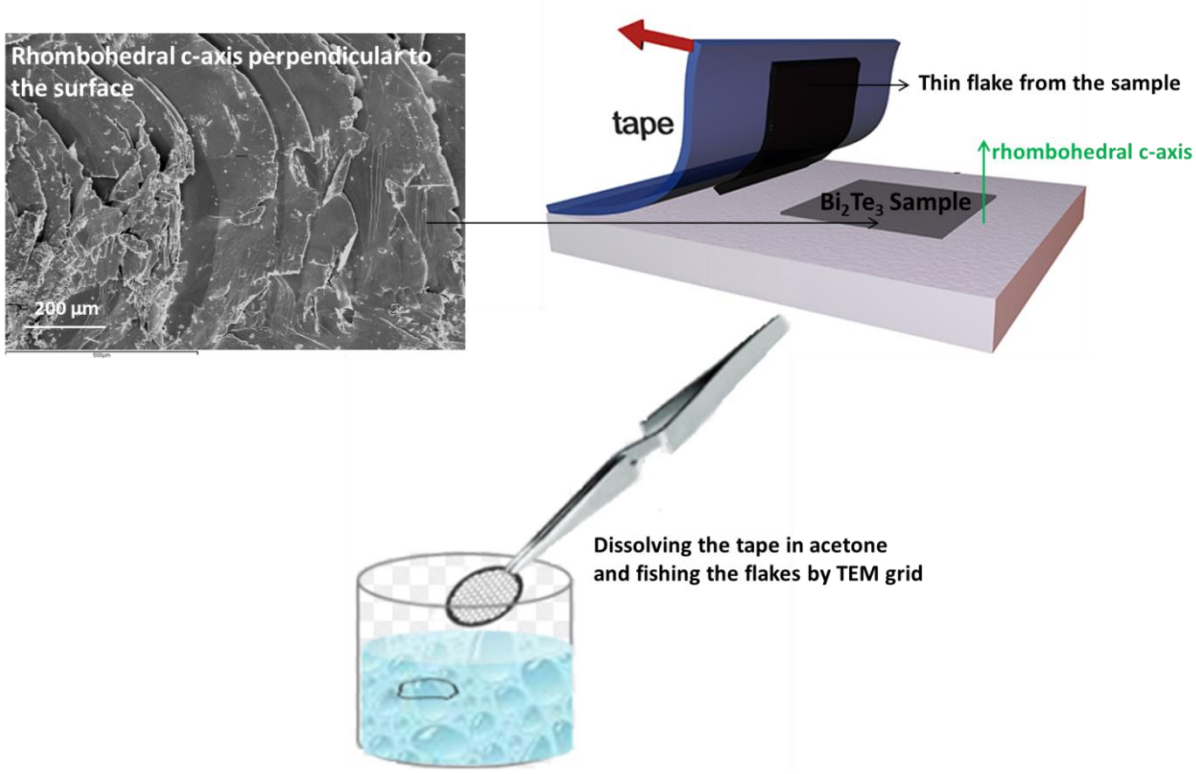

Figure 5.3: TEM sample preparation by exfoliation method.

5.4.Results

5.4.1. SEM observations

SEM micrographs of the undoped Bi_2Te_3 and Mn-doped Bi_2Te_3 samples with different doping values are shown in Figure 5.4. Many steps can be seen on the surface of these samples. Before doing these SEM experiments, a layer from the top surface of the sample was cleaved using sticky tape in order to provide a fresh unaffected region for SEM analysis. Therefore due to the layered structure of the Bi_2Te_3, these surface steps can be easily formed during cleavage. Moreover, no trace of secondary phases or precipitates can be seen in these images at this scale indicating that all of these samples, even the sample with high concentration of Mn doping, are uniform at least within SEM resolution. In Figure 5.4e-f, both secondary and backscattered electron micrographs of a typical region of the highly Mn-doped sample are shown. In the backscattered electron micrograph no contrast is observed revealing that there is no serious compositional inhomogeneity across the sample and at this scale these crystals are chemically homogeneous.

5.4.2. Compositional analysis

In order to determine the composition of these three samples and find out how Mn is distributed microscopically over the sample, both TEM/EDX and SEM/EDX were performed. In SEM/EDX experiments, 10 large regions (100μm×100μm) from each sample were analysed to get an average of the composition, in addition to many EDX points inside each region as shown in Figure 5.5 to see whether there is compositional variation from point to point within SEM resolution. All of these experiments were carried out, along with other TEM and SEM imaging, to find out how the addition of Mn affects the microstructure of the Bi_2Te_3 single crystals. There are three possibilities for Mn atoms:

1- Formation of secondary phases or precipitations.

2- Substitution onto Bi sites.

3- Insertion into the van der Waals gap (i.e. intercalation).

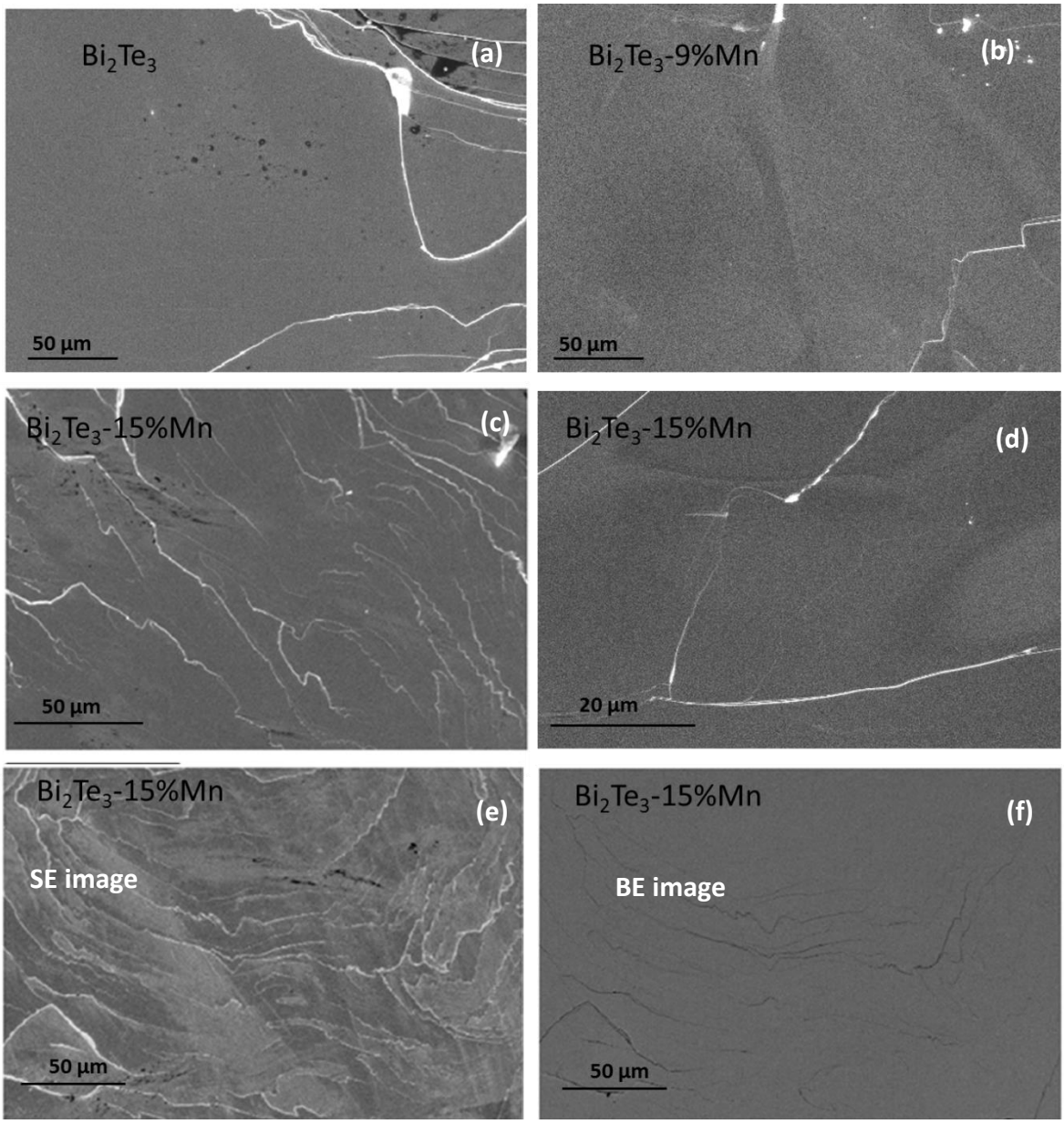

Figure 5.4: SEM micrographs of (a) Bi_2Te_3, (b) 9%Mn, (c-f) 15%Mn, (f) Backscattered electron image of the region showed in (e) showing there is no indication of chemical segregation at this scale.

The SEM images show that at the micron scale, the samples are free of any precipitates. EDX data obtained by SEM are presented in Figure 5.6. If Mn is substituted onto the Bi site, the formula of the structure will be $Mn_xBi_{2-x}Te_3$, shown by the green dashed line in Figure 5.6, and if the Mn atoms are located in van der Waals gap as an intercalant, then the formula $Mn_xBi_2Te_3$ will represent the structure, shown by the black dashed line in the graph. For both cases,

whether $Mn_xBi_{2-x}Te_3$ or $Mn_xBi_2Te_3$, there should be a fixed stoichiometry of 3 for Te, and the only difference is the variation of Bi relative to Mn. Therefore, in the first graph in Figure 5.6, the Bi content is plotted versus Mn content relative to a fixed Te content of 3. The EDX data for the sample with higher doping concentration (15%Mn) shows tendency towards the $Mn_xBi_2Te_3$ line (intercalant line), while the data from the 9%Mn sample is more dispersed and closer to the substitution line. Moreover, both of the 9%Mn and 15%Mn samples have almost the same average Mn doping concentrations. More EDX/SEM analysis in addition to EPMA (electron probe micro-analysis which gives more accurate quantitative compositional information), have been also carried out in our group and fairly similar results were obtained. A hypothesis for this observation can be that the maximum solubility of Mn in the growing Bi_2Te_3 single crystals is about 0.12. When the Mn doping is low, all of the Mn atoms go into the Bi site, and at higher doping concentration they tend to go in van der Waals gap. However, from only these data, the position of the Mn atoms cannot be confidently concluded, and this hypothesis needs to be confirmed.

In Figure 5.6b the Bi:Te ratio obtained from several large scanned regions is presented for these three samples. It is worth mentioning that there is a wide possible range of Bi:Te ratio according to the Bi-Te phase diagram [23]. Therefore, it is expected to measure a variation in Bi:Te ratio even in undoped-Bi_2Te_3. However, the 9%Mn sample once again shows a larger scatter of the data and lower Bi:Te ratio compared to other two samples indicating that the 9%Mn sample is less chemically uniform. The data deviation between the scanned area, as an average, and the EDX/spots within these areas (Figure 5.5a) revealed that the 15%Mn sample is chemically more uniform. For example, standard variations for Bi in the 9%Mn and 15%Mn are 11.5% and 3.3% respectively. If at lower Mn concentrations the substitution onto Bi sites is happening, then it is reasonable to detect larger variations in Bi content and subsequently in Bi:Te ratio. In

contrast, in the intercalation situation, both Bi and Te atoms are in their normal atomic positions retaining the Bi:Te ratio unchanged at its stoichiometric value.

For a comparison, TEM/EDX experiments were performed to analyse point to point compositional variations but with a much smaller beam spot. However, it was difficult to detect the Mn peak in these TEM samples even in the sample with high Mn concentration. The reason for this can be the presence of a strong Cu peak (from the Cu-grid and the TEM column) in the TEM spectrum which makes the weak Mn peaks invisible because the Mn peak is much weaker than Bi and Te peaks as it is seen in the spectrum in Figure 5.5. It was even more difficult to detect the Mn peak in cross-sectional TEM samples compared to plan-view ones probably due to the damage from the FIB sample preparation method as explained in the next section.

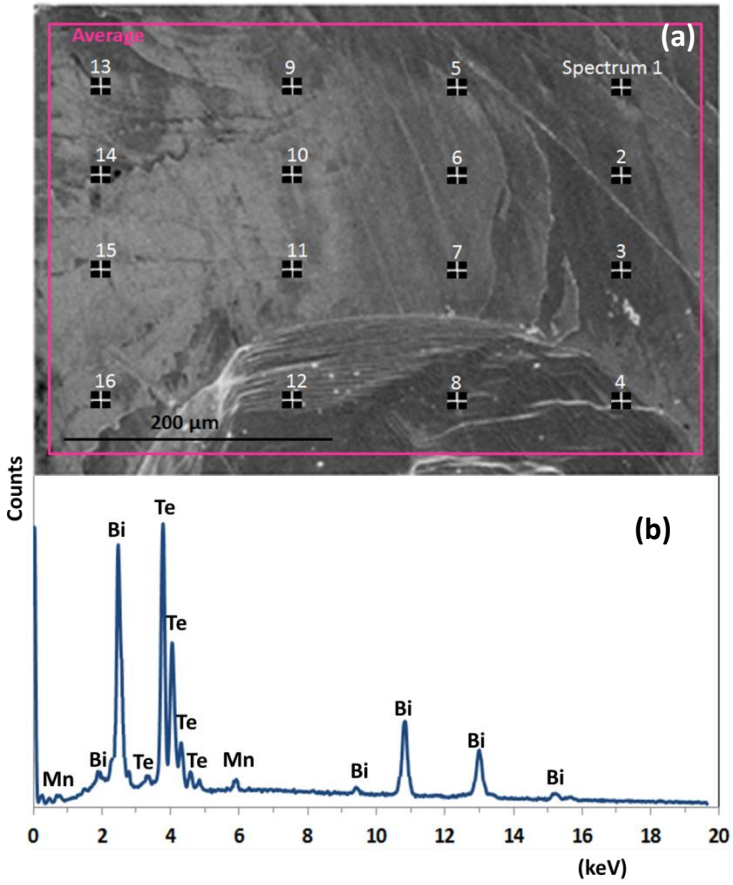

Figure 5.5: (a) A typical SEM micrograph of 15%Mn showing the regions analysed by EDX in order to obtain average compositions and to study chemical variations inside each region, (b) EDX spectrum of the selected region showing Bi, Te and Mn peaks with no overlap.

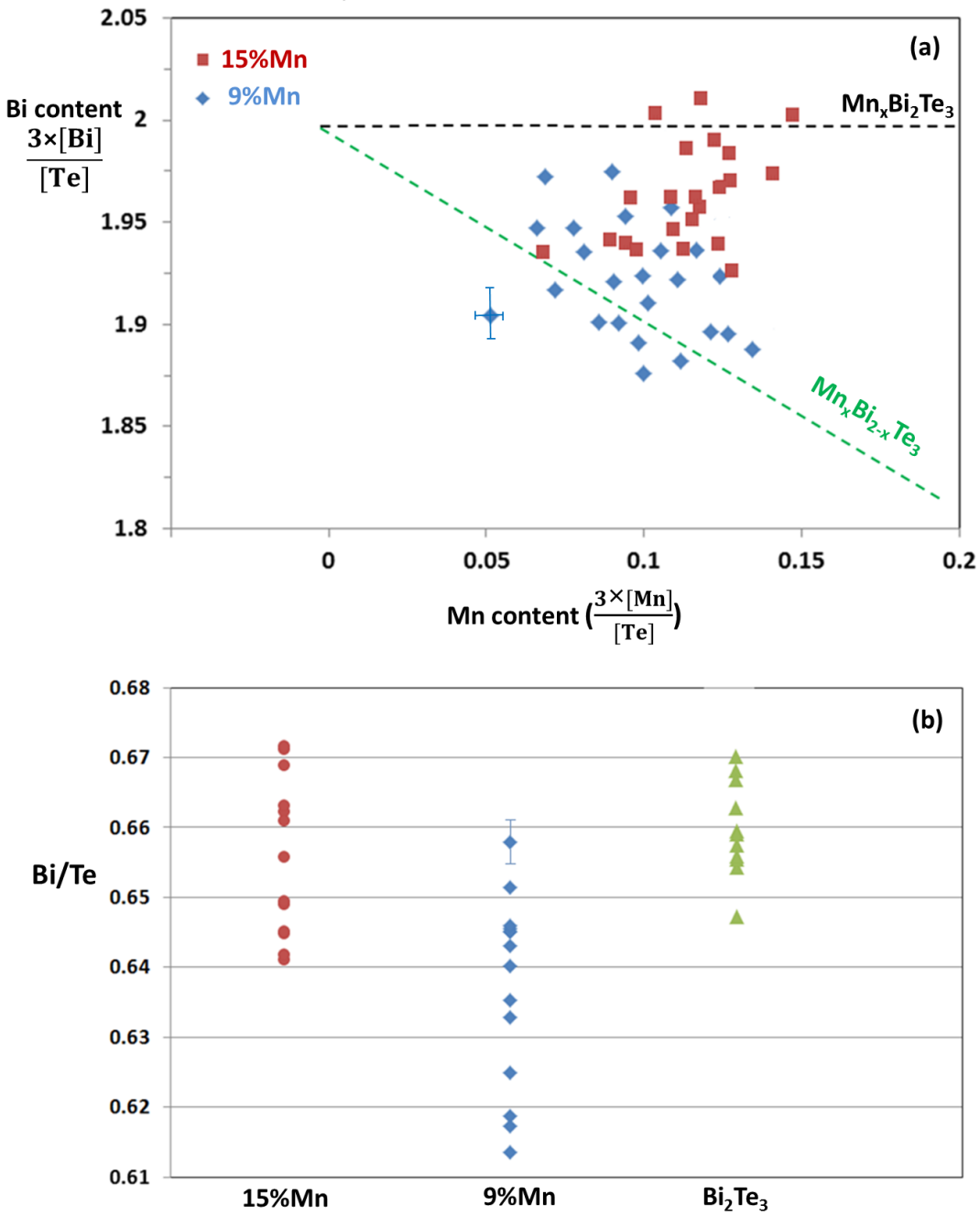

Figure 5.6: SEM/EDX data of Bi_2Te_3, 9%Mn and 15%Mn crystals (a) Bi content versus Mn content for Mn-doped crystals. In this graph the black dashed line corresponds $Mn_xBi_2Te_3$ formula representative of the structure with intercalated Mn and the green dashed line corresponds $Mn_xBi_{2-x}Te_3$ formula representative of the structure with Mn substituted for Bi. (b) Bi:Te ratio for these three crystals (the typical error bar is shown for one point in each graph).

5.4.3. Beam sensitivity of the TEM foils

For TEM analysis, as mentioned in the sample preparation section, two different TEM samples, cross-section and plan view, were prepared. Cross-sectional TEM foils prepared by FIB milling showed a high sensitivity to the electron beam in microscopes working at accelerating voltages of 300kV and 200kV. As can be seen in Figure 5.7, holes in the ab plane start to expand in a direction perpendicular to the c-axis when the sample is exposed to the electron beam. The degree and the rate of damage highly depend on the thickness of the TEM foil. For very thin foils, this damage was so severe that even taking TEM images was impossible and the sample was completely deformed after about 10 minutes of exposure. For thicker foils, like the sample shown in Figure 5.7, the sample survived longer, but damage occurred by focusing the beam or going to higher magnifications. As is seen, the damage occurs in the ab planes where the weak van der Waals bonds exist between Te layers. To avoid this problem, microscopes operating at lower voltages (e.g. 80kV) were used, but the resolution became lower at this voltage and even thinner TEM foils were needed to get enough transparency at this lower accelerating voltage. This issue restricted TEM observations of these cross-sectional samples. However, plan-view TEM foils prepared by mechanical exfoliation were stable enough in microscopes operating even at 200kV because in this direction the beam does not directly interact with the weakly bonded layers. Similar effects have been observed by other workers when a high degree of disorder was found in the (h0l) and (0kl) planes, whereas the (hk0) plane was always cleaner with fewer defects and disorder [20],[24]. Therefore most of the TEM images reported in this chapter are plan-view, and the remaining ones are cross-sectional TEM images taken at 80kV.

This beam sensitivity and vulnerability of the samples also suggests that the samples can receive a considerable amount of damage, including compositional changes, during milling by the Ga beam inside the FIB, and that this can be another reason for compositional difference obtained in the TEM and SEM data.

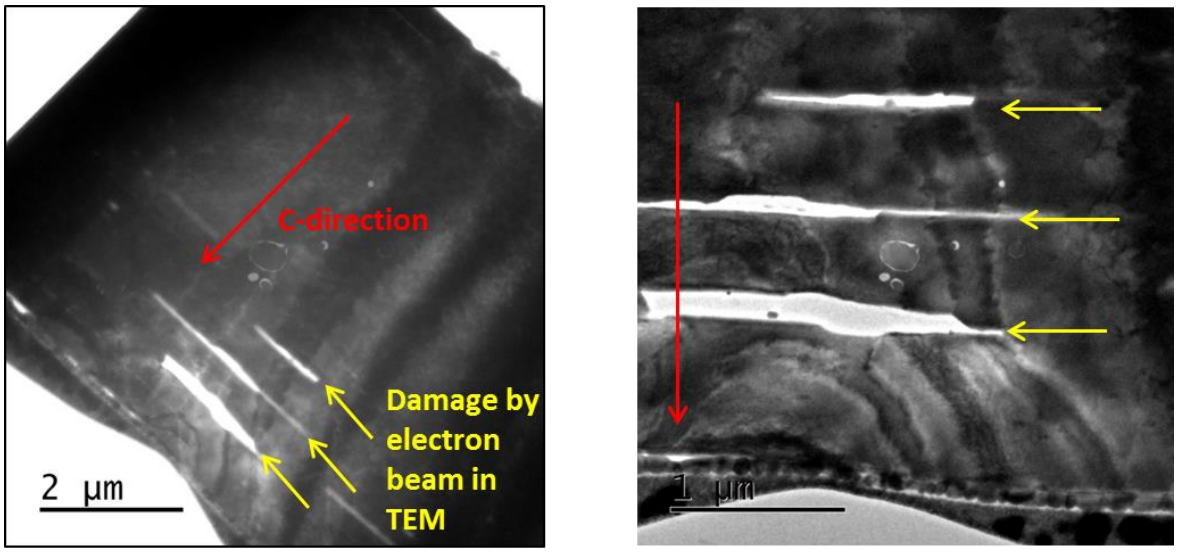

Figure 5.7: Cross-sectional TEM micrographs of the Bi_2Te_3 crystal showing damage produced by the electron beam of TEM in the ab plane.

5.4.4. TEM analysis of undoped Bi_2Te_3

Plan-view TEM micrographs of Bi_2Te_3 single crystal are shown in Figure 5.8. As indicated by the arrows, bend contours, arrays of dislocations and cleavage steps can be seen. The dislocation arrays are likely to have been generated during the cleavage process. In mechanical exfoliation, a cleavage force is applied to the TEM foil and, depending on the mechanical properties of the material and the cleavage process, this produces a huge density of dislocations [25]. These dislocations usually form a dense tangle rather than individual dislocations, and are formed along specific orientations depending on the mechanical properties of the material and the direction of the applied force. Such dislocation networks have been observed in similar exfoliated samples with a weakly-bonded layered structure such as graphite [26, 27]. Cleavage steps are also formed in the layered material and usually in the same direction during mechanical exfoliation.

The electron diffraction pattern taken from the circled region shown in Figure 5.9 exhibits only a pattern consistent with the [001] zone-axis of the Bi_2Te_3 compound. The absence of additional reflections in the diffraction pattern indicates that the sample is uniformly single crystalline with no detectable secondary phases or lattice disorder.

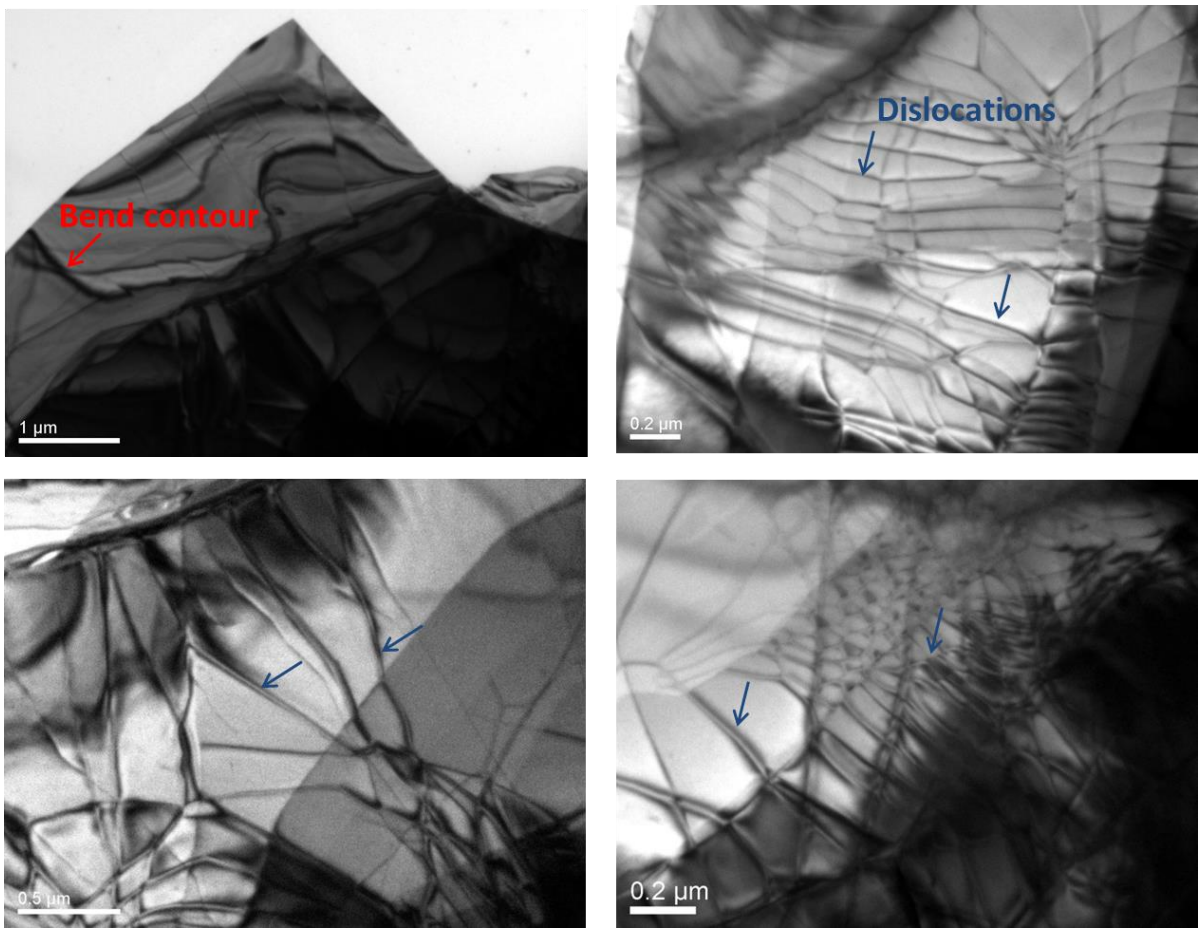

Figure 5.8: Plan-view bright-field TEM micrographs from the Bi_2Te_3 single crystal showing high density of dislocatios. Red arrows indicate bend contours and blue arrows indicate dislocations.

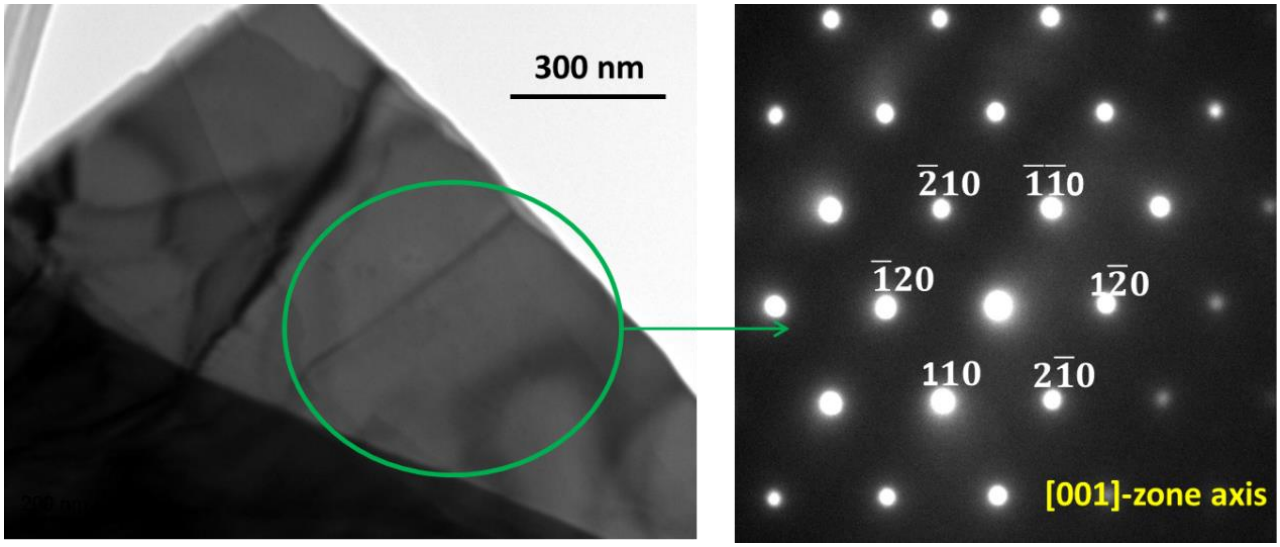

Figure 5.9: A typical c-axis hexagonal diffraction pattern of the Bi_2Te_3 crystal taken from the indicated region.

5.4.5. TEM analysis of Mn doped Bi_2Te_3 (9%Mn)

Plan-view bright-field TEM micrographs of the 9%Mn crystal (see Figure 5.10) are very similar to those of undoped sample. A high density of dislocation arrays covers almost the whole sample in addition to thickness contrast which is another characteristic of exfoliated foils. Except for these dislocation bands, an even contrast with no obvious features is seen inside each domain indicating that the sample has no apparent precipitation.

Typical diffraction patterns of this sample taken along the c-axis direction using two SAD apertures with different sizes are shown in Figure 5.11. The diffraction patterns taken from both large and small regions show only a pattern consistent with the [001] zone-axis of the Bi_2Te_3 compound. The lack of indication of extra reflections proves that the sample is single phase with no large secondary precipitates or lattice disorder. In fact adding 9% Mn to Bi_2Te_3 makes no obvious change either to the diffraction pattern or the TEM images. High-resolution TEM micrographs of this sample along with their FFT patterns (see Figure 5.12), also indicate that the sample is a single crystal with no nanoscale inhomogeneity.

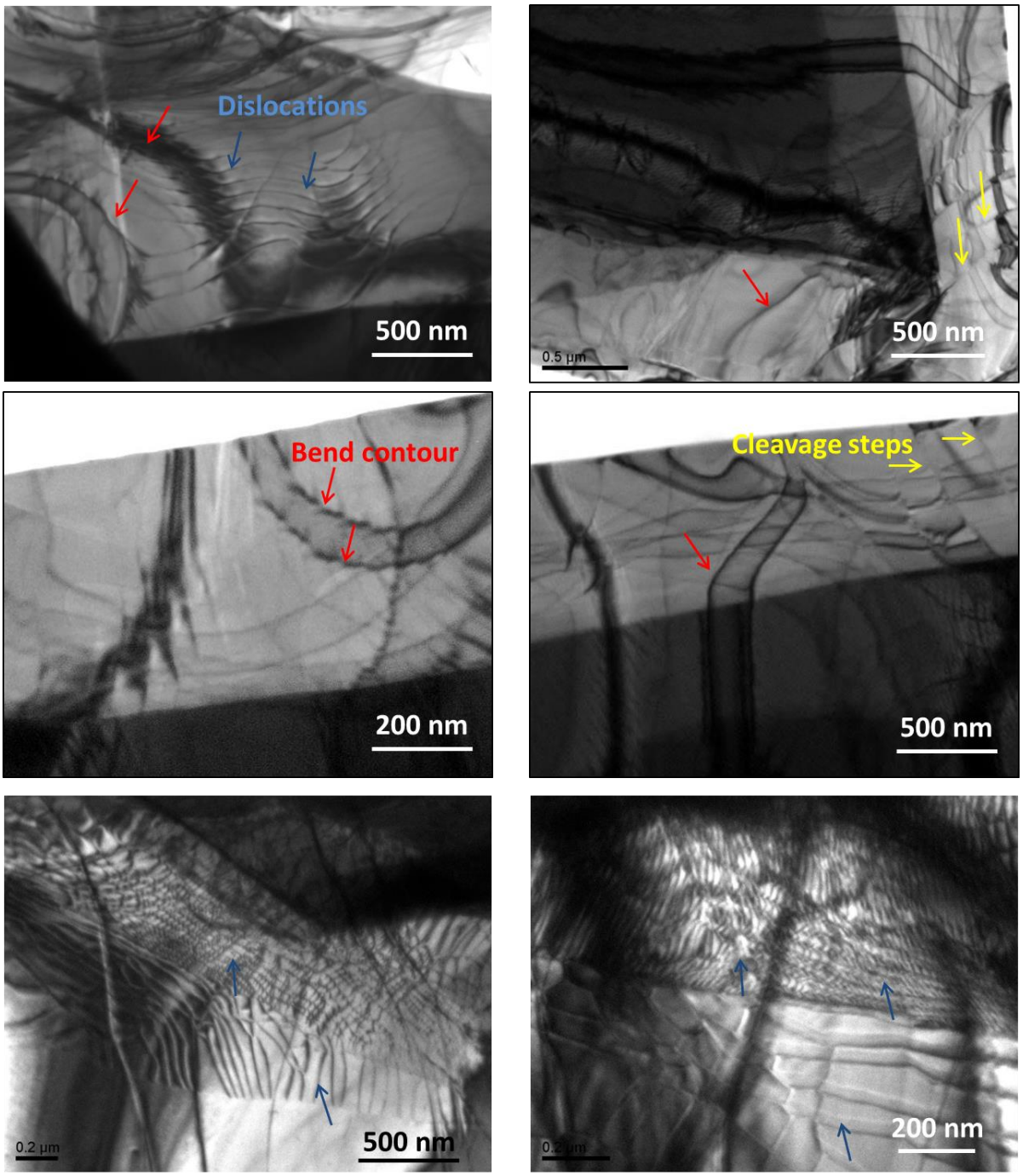

Figure 5.10: Plan-view bright-field TEM micrographs of the 9%Mn single crystal showing high density of dislocations (red arrows: bend contour, yellow arrows: cleavage steps, blue arrows: dislocations).

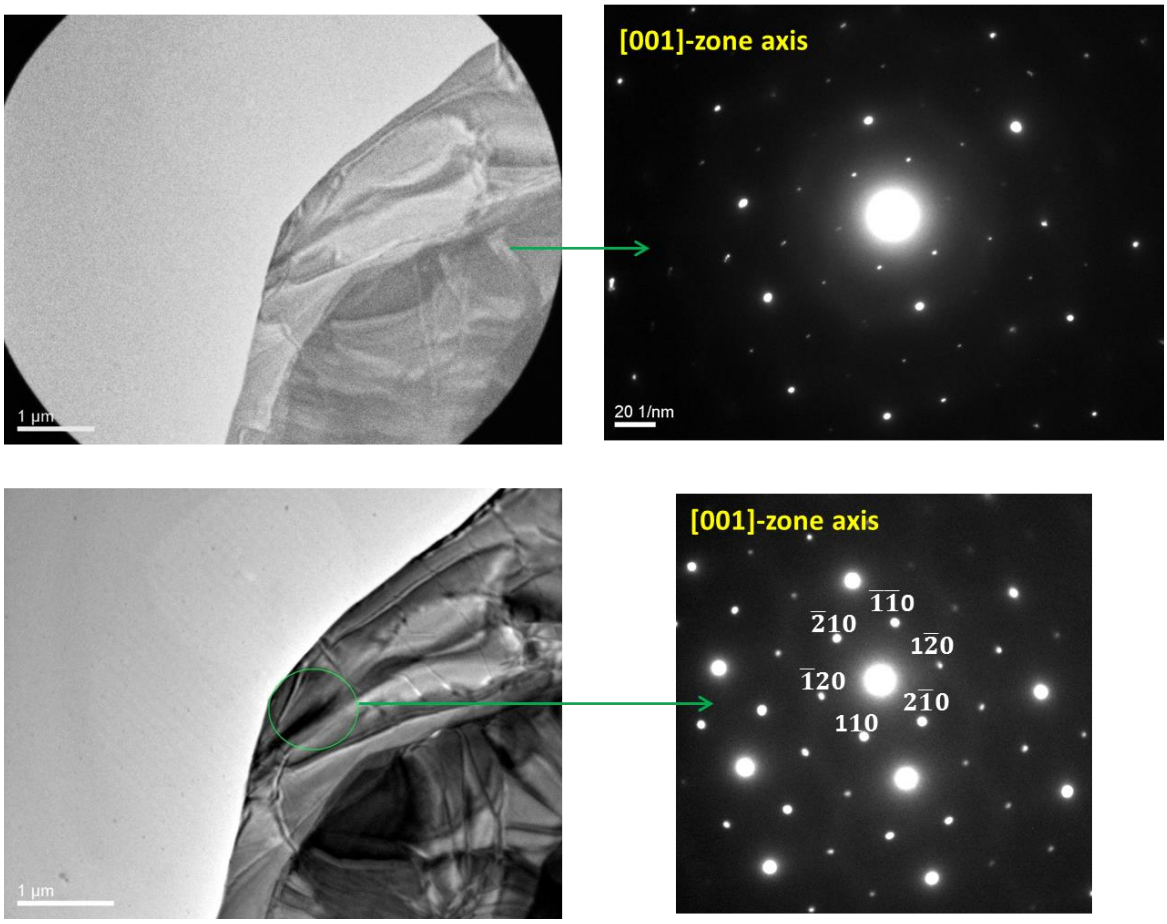

Figure 5.11: Diffraction patterns taken along the c-axis direction from the indicated large and small regions of the 9%Mn single crystal.

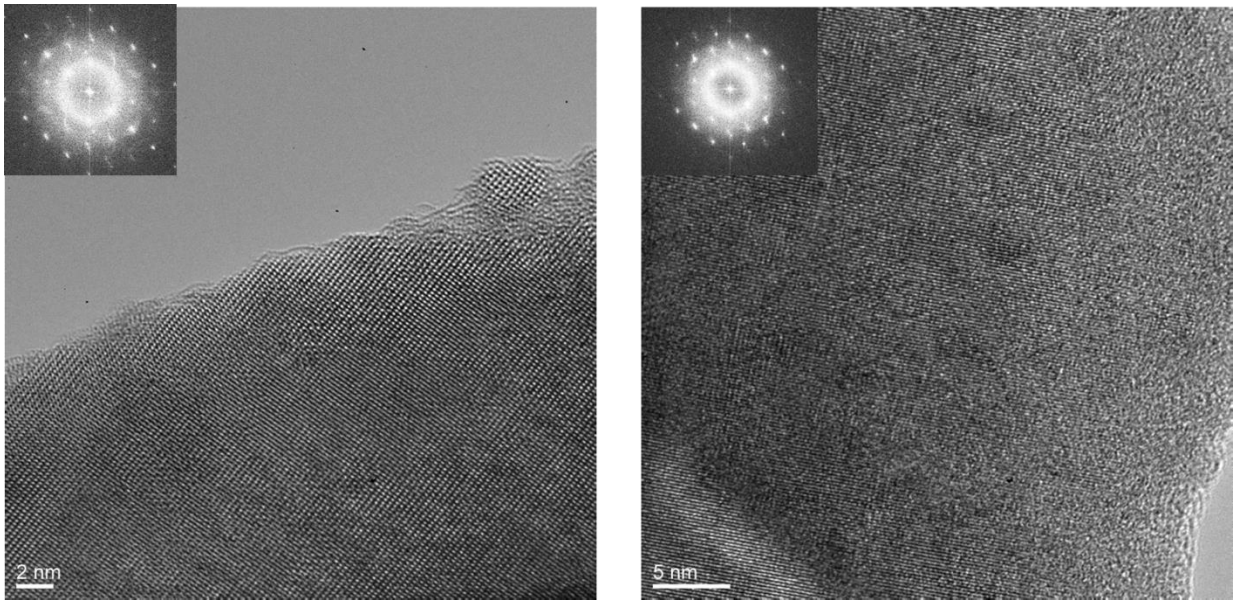

Figure 5.12: High-resolution TEM images of the 9%Mn single crystal with inset FFTs showing that the sample is free of secondary phase and precipitates.

5.4.6. TEM analysis of Mn doped Bi_2Te_3 (15%Mn)

Bright-field TEM images of the 15%Mn sample (see Figure 5.13) show similar features including dislocations and cleavage steps formed by mechanical exfoliation with no indication of a secondary phase. Looking at the sample at higher magnifications, nanoscale secondary phase can be seen in a different contrast from the matrix. For a comparison, high-resolution TEM images of these three samples, undoped Bi_2Te_3, 9%Mn and 15%Mn crystals, are shown in Figure 5.14. By increasing the Mn content, more contrast appears in the images indicating that the uniformity of the sample decreases. In 15%Mn, irregular nanoscale precipitates (about 5-30 nm) are clearly observed, whereas 9%Mn is free of these features. This suggests that Mn is incorporated in solid solution in the lower-doped sample but as the concentration of Mn is increased, supersaturation occurs in the crystal and nano-scale Mn-rich precipitates are formed during cooling. These precipitates might be pure Mn or intermetallic phases such as MnBi or MnTe, and this identification would be a good target for future research on these materials.

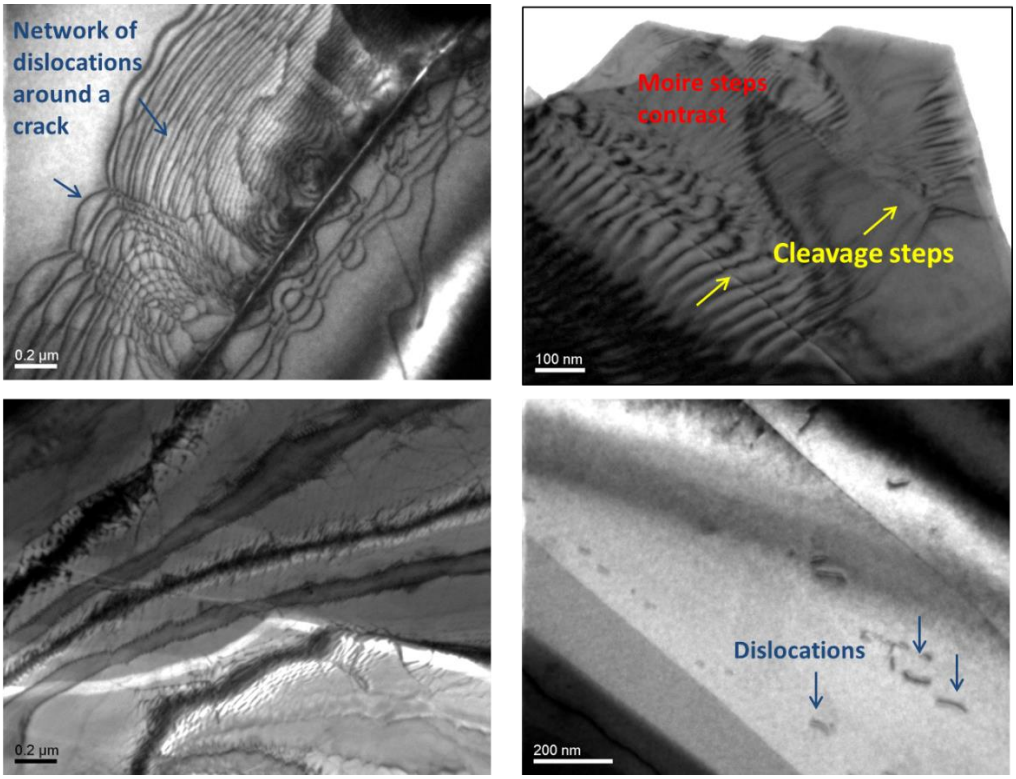

Figure 5.13: Plan-view bright-field TEM micrographs of the 15%Mn single crystal showing high density of dislocations (yellow arrows: cleavage steps, blue arrows: dislocations).

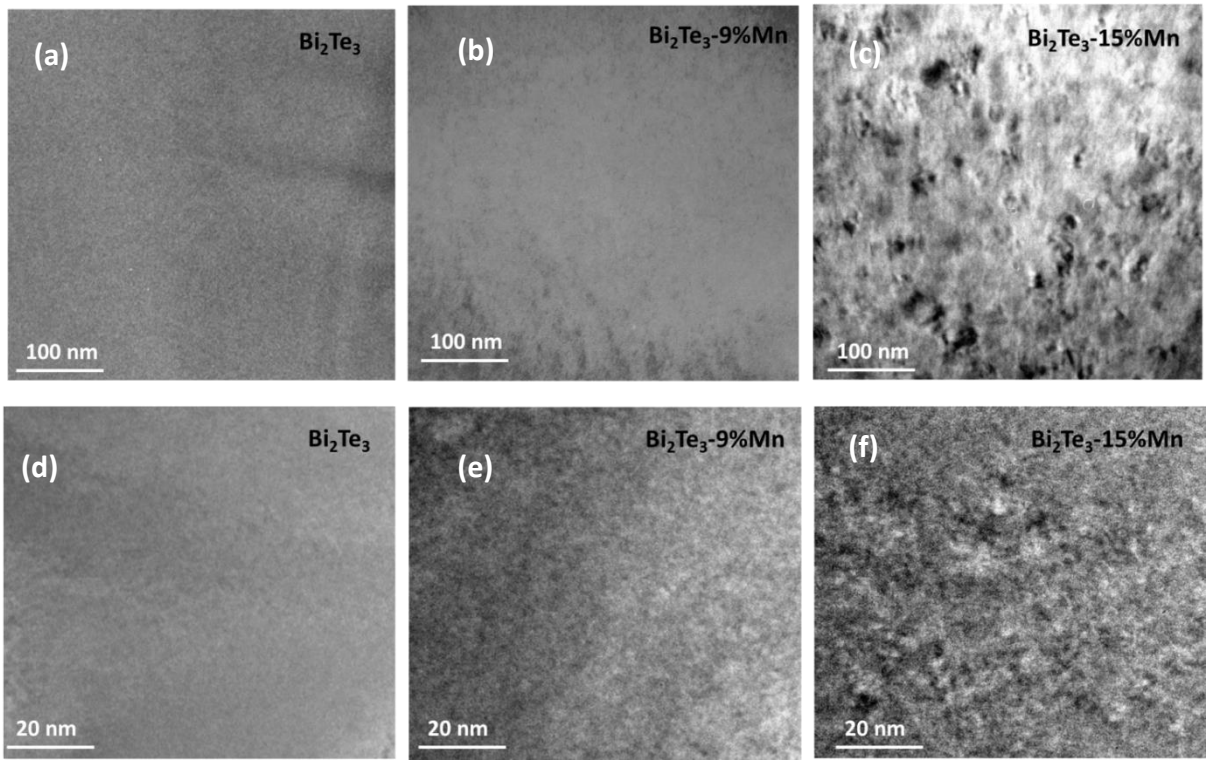

Figure 5.14: Bright-field TEM micrographs at higher magnification of (a,d) undoped Bi_2Te_3, (b,e) 9%Mn, (c,f) 15%Mn showing nano-scale precipitates/secondary phases are formed when the doping content increases.

Diffraction patterns from the 15%Mn sample are found to be different from that of undoped Bi_2Te_3 and low-Mn doped samples (see Figure 5.15). New weak diffraction spots appear between the main strong spots which were observed for the previous two samples. To explore if this superlattice pattern is associated with a secondary phase or to modifications to the main crystal structure, dark-field TEM images were taken using these extra weak spots. It can be seen in Figure 5.15 that the whole sample becomes bright in these dark-field images. This suggests that no secondary phase or precipitates create these weak spots, and that they originate from the crystal structure of the sample.

Moreover, I never detected superlattice patterns in the pure Bi_2Te_3 verifying that the superlattices are associated with the addition of Mn atoms. By calculating the d-spacing corresponding to these spots, I can index them as (-100), (0-10), (1-10), (-110), (010) and (100). This set of planes, which are in the category of $h+2k=3n\pm1$ and l is even, is forbidden in the

fcc-like ABC stacking in the Bi_2Te_3 lattice. That is why they did not appear in two previous samples. But the presence of these spots in this sample implies a breaking of the symmetry whereby the A, B, and C atomic columns no longer have the same scattering amplitudes. In other words, the ABCABC stacking order no longer exists in the structure. A likely interpretation is that the extra Mn atoms are mostly placed in the interstitial sites in the van der Waals gap and have sufficient ordering to break the symmetry in the c-direction and create the weak extra spots. To verify this statement, the diffraction pattern was simulated for a Bi_2Te_3 structure with the Mn atoms located between Te layers (i.e. on the interstitial site). As can be seen in Figure 5.16, the presence of the Mn atoms in interstitial sites leads to the appearance of weak spots similar to those obtained from the 15%Mn specimen.

Similar diffraction patterns have been obtained by Koski et al in the Bi_2Se_3 structure, which has the same structure as Bi_2Te_3, after adding Sn and Ni as an intercalant [28, 29]. They have reported the same interpretation for the appearance of these weak spots, and stated that the critical concentration of the intercalant should be above 10 atomic percent before the superlattice pattern appears. In fact, above 10 atomic percent, there would be enough atoms to become ordered and form superlattice spots in the electron diffraction pattern [28]. According to this model, in my 9%Mn sample, the absence of these weak reflections can be due to either the low concentration of Mn or the Mn taking substitutional sites. However, the latter is more likely because other evidence such as composition and lattice parameter measurement still confirm that the 9%Mn sample has substituted Mn not intercalated Mn.

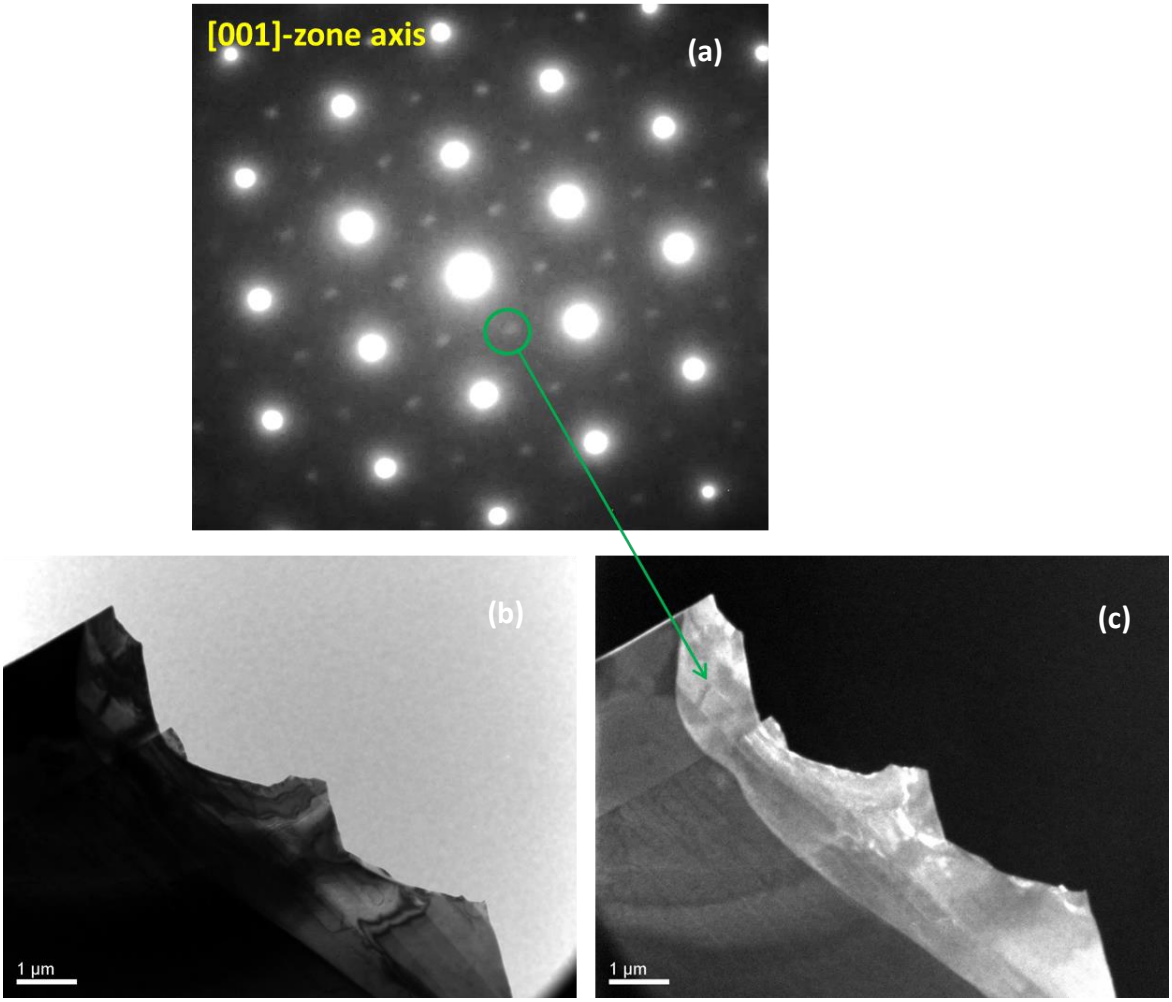

Figure 5.15: (a) [001]-zone axis diffraction pattern of 15%Mn showing strong and weak reflections, (b and C) Bright-field and dark-field TEM micrographs using the indicated weak spot in the diffraction pattern showing that the weak spots are generated from the whole sample and no precipitate or secondary phase is responsible for the creation of the weak spots.

5.4.7. Lattice parameter evaluation

Some of the strongest experimental evidence for intercalation in layered compounds has been reported to be a considerable change in in the unit cell volume, especially through an increase in the c-axis parameter [28, 30, 31]. Substitution can also change the lattice parameters of the parent phase, and depending on the difference in the size of host and guest atom this change might be an increase or decrease the unit cell parameters. However, in intercalation, there is always an increase in c-axis parameter whether the intercalated atom is smaller or larger than the parent atoms since the intercalated atoms lie between the weekly bonded atomic layers [29].

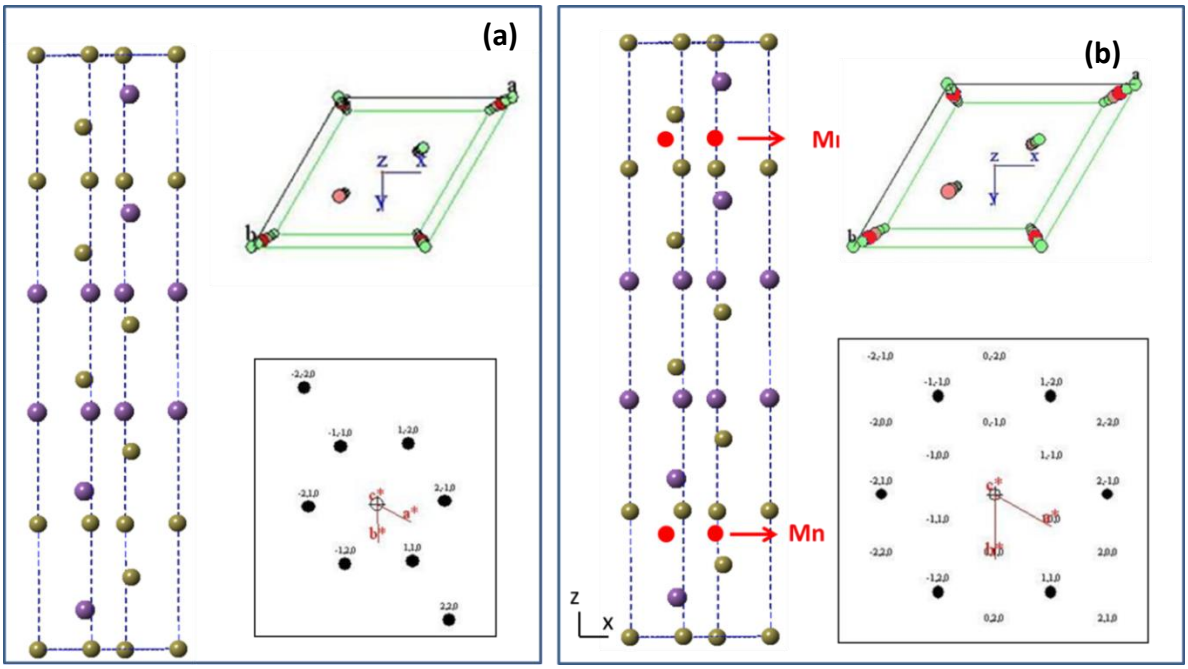

Figure 5.16: Simulated diffraction patterns for (a) a perfect Bi_2Te_3 structure, (b) Bi_2Te_3 structure with Mn atoms located in interstitial sites. When Mn atoms are added to the structure, the simulated diffraction pattern shows ordered weak spots.

In order to investigate the variation of the unit cells in these three samples, lattice parameters were calculated from diffraction patterns. In the 9%Mn sample, the calculated c-axis parameter is c=30.012Å which is lower than obtained for the undoped sample (c=30.435 Å). This suggests that in the 9%Mn sample, Mn atoms are substituted for Bi atoms and since the atomic radius is much smaller than that of Bi atoms (r_{Mn}=1.27 Å vs r_{Bi}=1.56 Å), this substitution decreases the c-axis lattice parameter. The 15%Mn sample shows a larger c-axis parameter (c=30.575Å) compared to the undoped Bi_2Te_3, however, the increment is not as large as what usually happens in intercalation structures. This may suggest that in this sample both substitution and intercalation of the Mn occur. We might speculate that up to a critical Mn concentration, substitution is the dominant phenomenon, but if the doping concentration increases above this value extra Mn atoms go between the layers and expand the unit cell. Therefore in this sample, a combination of both substitution and intercalation exist in addition to the small nano-scale precipitates observed in the TEM images.

5.5.Discussion and conclusion

The aim of this chapter was to study the effects of Mn addition on the microstructure of Bi_2Te_3 single crystals and how Mn atoms incorporate with the Bi_2Te_3 structure. Understanding these issues is of great significance because the position and homogeneity of the Mn atoms strongly affects the overall magnetic properties of Mn-doped Bi_2Te_3 single crystals, and subsequently their potential application as topological insulators.

Bringing all the results together, it can be concluded that of a low doping concentration (9%Mn), Mn atoms are randomly substituted onto Bi sites. This substitution does not change the symmetry of the structure and, as a result, the same diffraction pattern as the undoped Bi_2Te_3 is obtained. However, as Mn atoms are smaller than Bi atoms, the unit cell shrinks leading to smaller lattice parameters. According to my EDX data, the distribution of the Mn atoms onto Bi sites is not very uniform. However, all the Mn atoms go into solution in the crystal since no evidence of nano/micro clusters was detected.

When the doping concentration increases to 15%Mn, the extra Mn atoms form Mn-rich nanoclusters and some of the Mn atoms also occupy the interstitial sites in such an ordered pattern that superlattice spots, additional weak reflections, appear in the diffraction pattern. The Mn intercalation was further confirmed by an increase in the lattice spacing along the c-axis. Lattice expansion and superlattice patterns are considered to be strong evidence of intercalation [28, 30, 31]. Another important requirement for intercalation is the zero valency of the intercalant [28]. When Mn atoms are between layers as intercalants, no charge transfers between Mn atoms and the parent Bi_2Te_3 and Mn would retain zerovalent. In contrast, substitution is usually accompanied by changing the oxidation state of the substituent. To evaluate the oxidation state of the Mn in these samples, EELS technique was used as it is a powerful technique to identify the oxidation states of a transition metal from the near-edge fine

structure, such as L_3/L_2 ratio [32]. However, it was again challenging to detect Mn peak probably due to the background noise which was higher than the small Mn peak as well as the damage of TEM specimens during sample preparation.

Compositional analysis also supported these conclusions about the way that Mn is incorporated in the Bi_2Te_3 by the data showing a tendency towards $Mn_xBi_{2-x}Te_3$ line (substitution) for low Mn concentration and towards the $Mn_xBi_2Te_3$ line (intercalation) for high Mn concentration. The compositional variations for the 15%Mn sample were smaller than in the 9%Mn sample, consisting of the ordering of the Mn intercalant concluded from the diffraction pattern. In contrast, in the substitutional case, Mn atoms are more randomly distributed in Bi sites making larger variation in the composition.

All of these results are also in agreement with the EBSD data obtained on the same samples by other workers in our group [20] where a large variation in c/a ratio was obtained for 9%Mn, whereas the high Mn doped sample was found to be more homogenous due to more uniform chemical composition and less internal stress (see Figure 5.17). In fact in intercalation, as the atoms are between layers, the structure is less stressed compared to the situation where the atoms go into solution in the Bi_2Te_3 structure [30].

This conclusion is consistent with the work done by Hor et al where they used scanning tunnelling microscopy to study the position of the Mn atoms in the structure [14]. They only studied $Mn_xBi_{2-x}Te_3$ samples with the x value less than 0.09. However, in this range they found that Mn randomly substitutes on the Bi sites with no indication of secondary phase [14]. In other work by Choi et al, once again low Mn concentrations (x=0.01 and 0.02) are studied and the material was found to be the substituted $Mn_xBi_{2-x}Te_3$ compound [16]. In none of these other studies have compounds with higher Mn concentrations been studied, but for low Mn concentrations my results are very similar to what they have reported.

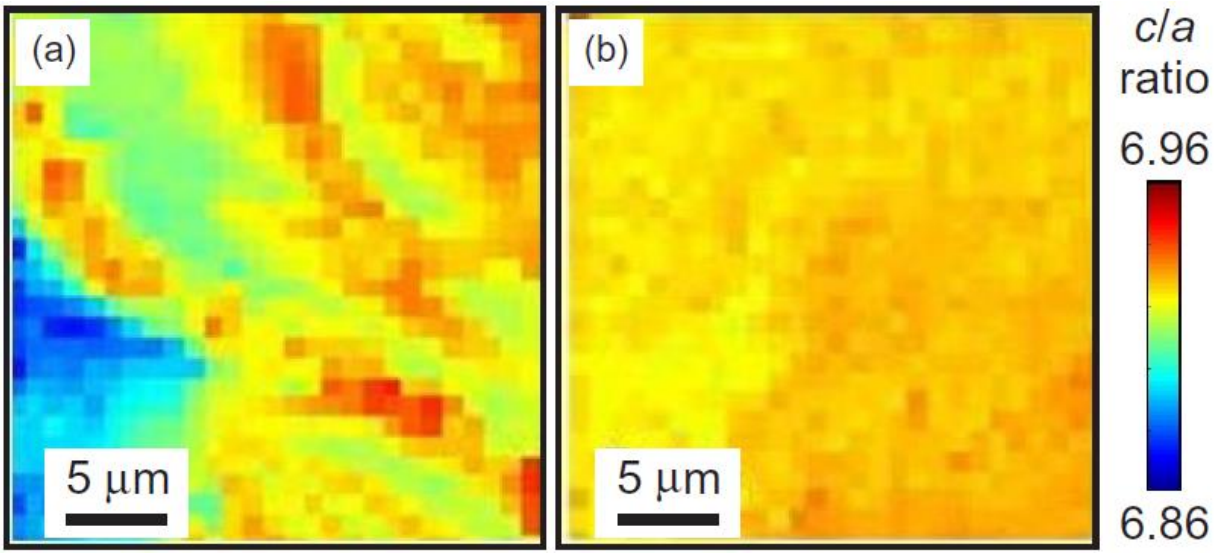

Figure 5.17: High-resolution electron-back-scatter diffraction maps showing spatial variation in c/a ratio in (a) 9%Mn and (b) 15%Mn [20]. c/a ratio is more uniform for the 15%Mn sample.

Therefore, there seems to be a limit for solubility of the Mn into Bi_2Te_3 single crystals. Below 0.09, Mn atoms substitute onto the Bi sites in the structure, whereas by increasing the Mn concentration, supersaturation occurs and the extra Mn atoms go to the van der Waals gap in interstitial sites as well as forming nanoscale Mn-rich precipitates. The intercalation in 15%Mn was confirmed by lattice expansion, EDX data and superlattice spots in electron diffraction patterns.

Another conclusion from this chapter is that there is an extreme sensitivity to the electron beam when it hits the samples in a direction perpendicular to the c-axis. Therefore using microscopes operating at the voltages lower than 100kV is necessary for cross-sectional TEM specimens. However, plan-view TEM study of these samples does not have this restriction.

For future work, Mn-doped Bi_2Te_3 crystals with different Mn concentrations could be studied to investigate how Mn incorporates with the structure at various doping levels. High-resolution aberration-corrected TEM can be also used, especially for the ordered intercalated sample, to understand how Mn atoms are arranged in intercalation sites to provide a preferred long range ordered structure and also the nature of the precipitates.

5.6. References

1. W.S. Liu, et al., *Studies on the Bi_2Te_3-Bi_2Se_3-Bi_2S_3 system for mid-temperature thermoelectric energy conversion*, Energy & Environmental Science, 2013, 6(2): p. 552.
2. H.J. Goldsmid, *Recent Studies of Bismuth Telluride and Its Alloys*, Journal of Applied Physics, 1961, 32: p. 2198.
3. O.J. Kwon, et al., *The effect of microstructure on the thermoelectric properties of Bi_2Te_3-PbTe alloy*, Current Applied Physics, 2011, 11(1): p. S242.
4. S. Golia, et al., *Electrochemically deposited bismuth telluride thin films*, Current Applied Physics, 2003, 3(2-3): p. 195.
5. Y. Xia, et al., *Observation of a large-gap topological-insulator class with a single Dirac cone on the surface*, Nature Physics, 2009, 5(6): p. 398.
6. J.E. Moore, *The birth of topological insulators*, Nature, 2010, 464(7286): p. 194.
7. X.L. Qi, S.C. Zhang, *Topological insulators and superconductors*, Reviews of Modern Physics, 2011, 83(4): p. 984.
8. D. Bradley, *When topological insulators met superconductors*, Materials Today, 2013, 16(11): p. 415.
9. B.A. Bernevig, T.L. Hughes, *Topological insulators and topological superconductors*, 2nd ed, Princeton Press.
10. G.D. Mahan, *Condensed matter in a nutshell*, 2011, Princeton University Press.
11. M. Konig, et al., *Quantum spin hall insulator state in HgTe quantum wells*, Science, 2007, 318(5851): p. 766.
12. D. Hsieh, et al., *A topological Dirac insulator in a quantum spin Hall phase*. Nature, 2008, 452(7190): p. 970.
13. B.A. Bernevig, T.L. Hughes, S.C. Zhang, *Quantum spin Hall effect and topological phase transition in HgTe quantum wells*, Science, 2006, 314(5806): p. 1757.
14. Y.S. Hor, et al., *Development of ferromagnetism in the doped topological insulator $Bi_{2-x}Mn_xTe_3$*. Physical Review B, 2010, 81(19): p. 0543.
15. Y.S. Hor, et al., *Superconductivity in $Cu_xBi_2Se_3$ and its Implications for Pairing in the Undoped Topological Insulator*, Physical Review Letters, 2010, 104(5): p. 0313.
16. J. Choi, et al., *Magnetic properties of Mn-doped Bi_2Te_3 and Sb_2Te_3*. physica status solidi (b), 2004, 241(7): p. 1541.
17. J.L. Zhang, et al., *Pressure-induced superconductivity in topological parent compound Bi_2Te_3*, Proceedings of the National Academy of Sciences of the United States of America, 2011, 108(1): p. 24.
18. T. Jungwirth, et al., *Prospects for high temperature ferromagnetism in (Ga,Mn)As semiconductors*, Physical Review B, 2005, 72(16): p. 9632.
19. S.A. Wolf, et al., *Spintronics: A spin-based electronics vision for the future*, Science, 2001, 294(5546): p. 1488.
20. M.D. Watson, et al., *Study of the structural, electric and magnetic properties of Mn-doped Bi_2Te_3 single crystals*, New Journal of Physics, 2013, 15: p. 5612.
21. J.R. Drabble, C.H.L. Goodman, *Chemical Bonding in Bismuth Telluride*, Journal of Physics and Chemistry of Solids, 1958, 5(1-2): p. 142.
22. R. Mas-Balleste, et al., *2D materials: to graphene and beyond*, Nanoscale, 2011, 3(1): p. 20.
23. H. Okamoto, L.E. Tanner, T.B. Massalski, *Binary Alloy Phase Diagrams*, 2nd ed, 1990, ASM International.
24. B. Jariwala, D.V. Shah, *Stacking fault in Bi_2Te_3 and Sb_2Te_3 single crystals*, Journal of Crystal Growth, 2011, 318(1): p. 1179.
25. H.P. Chang, A.J. Bard, *Observation and Characterization by Scanning Tunneling Microscopy of Structures Generated by Cleaving Highly Oriented Pyrolytic-Graphite*, Langmuir, 1991, 7(6): p. 1143.
26. P.J. Ouseph, *Graphite dislocations induced by collision of neutral mercury droplets*, Applied Surface Science, 2009, 256(1): p. 96.
27. W.T. Pong, J. Bendall, C. Durkan, *Observation and investigation of graphite superlattice boundaries by scanning tunneling microscopy*, Surface Science, 2007, 601(2): p. 498.

28. K.J. Koski, et al., *Chemical intercalation of zerovalent metals into 2D layered Bi_2Se_3 nanoribbons.* Journal of the American Chemical Society, 2012. 134(33): p. 13773.
29. Koski, K.J., et al., *High-density chemical intercalation of zero-valent copper into Bi_2Se_3 nanoribbons.* Journal of the American Chemical Society, 2012, 134(18): p. 7584.
30. W. Muller-Warmuth, *Progress in intercalation research, Physics and chemistry of materials with low-dimensional structures*,1994, Dordrecht; London, Kluwer Academic.
31. F. Louvy, *Intercalated layered materials*, Physics and chemistry of materials with layered structures, 1979, Boston, D. Reidel Pub.
32. S.B. Leapman, et al., *Cyclosporin A prevents the appearance of cell surface "activation" antigens,* Transplantation, 1982, 34(2): p. 94.

Chapter 6: TEM investigation of $CaFe_2As_2$ single crystals

In this chapter transmission electron microscopy (TEM) has been used to investigate the microstructure of $CaFe_2As_2$ single crystals prepared using the FeAs flux method and different annealing processes by collaborators at the Ames Laboratory in Iowa State University. Following an introduction and a review of microstructural studies of $CaFe_2As_2$ in the literature, sample preparation details and my results will be presented in three subsections.

6.1.Introduction

Soon after the discovery of the RFeAsO family (the 1111-phase) as the first Fe-based superconductors [1], it was understood that the FeAs layers are critical for superconductivity in these materials. This led to the discovery of the related AFe_2As_2 phase (A: Ca, Sr, Ba and Eu), the 122-phase. These AFe_2As_2 compounds can be superconductors under certain conditions e.g. partial substitution on the A site and application of hydrostatic pressure [2-4]. The highest superconducting T_C in this family is found to be about 49 K in $CaFe_2As_2$ via electron-doping by partial replacement of Ca by rare-earth elements at ambient pressure [5]. AFe_2As_2 compounds are also more interesting than the complex RFeAsO family because of their lack of oxygen, their well-known $ThCr_2Si_2$ structure and the ability to grow substantial single crystals.

$CaFe_2As_2$, in particular, has attracted considerable attention because it is an extreme example of the combined magnetic-structural phase transition which can be used to understand the physics of the undoped parents of FeAs-based superconductors [6, 7]. The first-order structural transition takes place near 170 K in single crystals at ambient pressure from a high-temperature tetragonal (I4/mmm) phase to a low-temperature orthorhombic (Fmmm) phase [8]. This structural transition has been confirmed by observation of the splitting of the (220) reflection of the tetragonal structure into the (400) and (040) reflections of the orthorhombic structure [9]. The low temperature orthorhombic structure has four formula units per cell (tetragonal $CaFe_2As_2$ has two formula units per cell), and Ca atoms occupy the 4a sites (000) while iron and arsenic atoms are present at the 8f (1/4 1/4 1/4) and 8i sites (0 0 0.3538) respectively [10]. This structural transition is accompanied by magnetic ordering of the Fe atoms. In other words, co-incident with the structural change, the compound also exhibits a first order magnetic phase transition and/or spin density wave (SDW) magnetic phase transition from a paramagnetic phase to an antiferromagnetic phase. This magnetic-structural phase transition is extremely pressure-dependent, and $CaFe_2As_2$ is the most pressure sensitive of the AFe_2As_2 and 1111

compounds, with its structural-magnetic phase transition being suppressed by over 100 K per GPa applied [11].

The occurrence of this structural-magnetic phase transition in $CaFe_2As_2$ also depends on the synthesis method used to prepare the compound. Single crystals of $CaFe_2As_2$ were initially grown using a Sn-flux to give well-formed faceted plates, but they were very small (0.1-0.5 mm thick) [12, 13]. Using a FeAs-flux, the crystals are large enough for more detailed characterization. However, they needed post annealing at 500°C, which is similar to the decanting temperature of the Sn-flux samples, to exhibit a structural-magnetic phase transition similar to that observed in the smaller Sn-grown crystals [14]. Without annealing, the transition temperature is dramatically suppressed in FeAs-flux grown samples. This large suppression can be systematically changed from 170K to below 100K, with the lowest transition temperature for the samples having a transition to the nonmagnetic phase with a collapsed tetragonal state [14]. This decrease in transition temperature is only observed in FeAs-flux grown $CaFe_2As_2$ in the AFe_2As_2 series and can be prevented by annealing.

Interestingly, for annealing temperatures above 400°C, the relation between transition temperature and annealing temperature has been found to be remarkably similar to the relation between transition temperature and pressure for Sn-grown samples (see Figure 6.1). This similarity raises the question of how the effect of annealing can be similar to that of pressure. In order to investigate the effects of annealing temperature, which would help to understand the nature of this magnetic-structural phase transition, different annealing temperatures were studied by Ran et al [14]. They performed a wide variety of measurements including transport, thermodynamic, microscopic and magnetic. In collaboration with them, I have performed TEM analysis of their samples to investigate the microstructural differences, especially the presence of nanoscale precipitates and defects, in the samples annealed under various conditions.

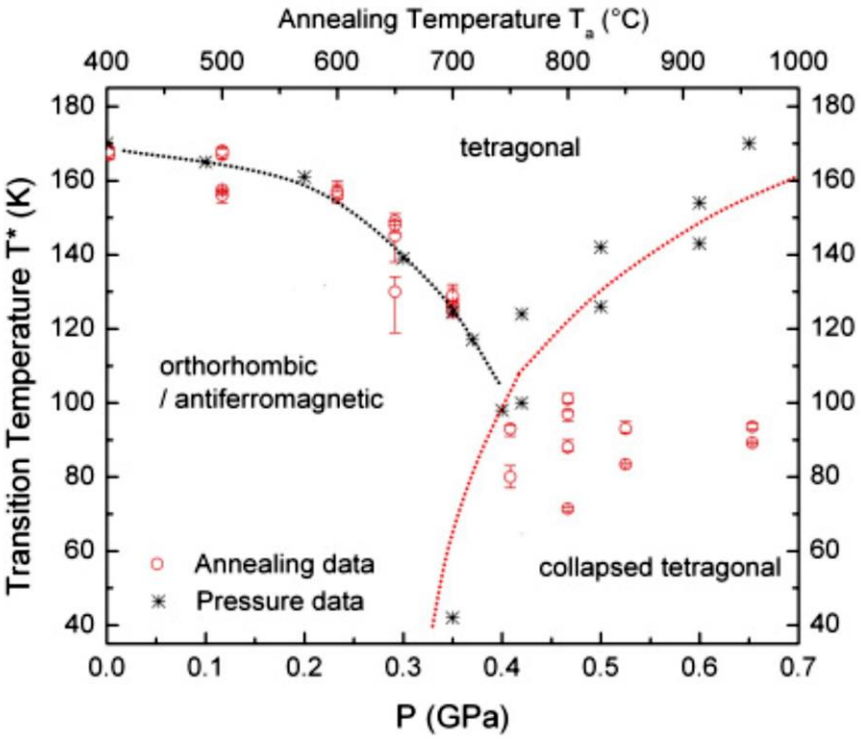

Figure 6.1: Structural-magnetic phase transition temperature (inferred from resistivity and susceptibility data) as a function of pressure for Sn-flux grown $CaFe_2As_2$ and annealing temperature for FeAs-grown $CaFe_2As_2$ [14].

6.2. Crystal structure and properties of $CaFe_2As_2$

The crystal structure of $CaFe_2As_2$ at room temperature is shown in Figure 6.2. It has the $ThCr_2Si_2$ tetragonal structure with an I4=*mmm* space group, consisting of FeAs planes separated by Ca layers. The layers of Ca are capped by Fe–As tetrahedra along the *c*-axis. These Fe–As tetrahedra are the common structural units of the Fe-based RFeAsO and AFe_2As_2 superconductors. There is only one FeAs-unit per unit cell of LaOFeAs, whereas in AFe_2As_2 there are two. Fe and Ca atoms occupy the 2a and 4d crystallographic sites respectively, which are fixed, while the As atoms occupy the 4e site (0, 0, *z*). According to [6] the lattice parameters in this compounds are a = 3.887Å and c = 11.7582 Å.

Another characteristic of $CaFe_2As_2$ single crystals is their high deformability e.g. single crystalline $CaFe_2As_2$ plates can be easily bent or rolled even by a tweezers. $CaFe_2As_2$ is one of the rare examples of a malleable intermetallic compound [14].

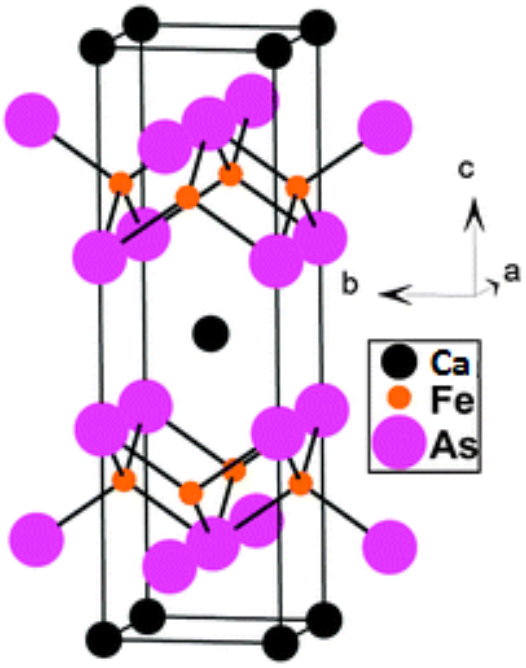

Figure 6.2: Crystal structure of $CaFe_2As_2$ [6].

6.3.Microstructural analysis of $CaFe_2As_2$ in the literature

The microstructure of $CaFe_2As_2$ has not been extensively studied, and there are only a few papers in the literature. Shi et al prepared $CaFe_2As_2$ samples by Sn-flux, FeAs-flux and solid-state reactions and studied their microstructure and properties. They observed various microstructures as well as different behaviours in both phase transition temperature and transport properties in these samples [7]. As shown in Figure 6.3a the resistivity behaviour, especially the resistivity anomaly which is associated with the phase transition or SDW instability, is very different in these samples. A variety of microstructures can also be seen in the plan-view TEM analysis of these samples. In the self-flux (FeAs-flux) sample, a tweed-like pattern parallel to $[-110]_{tetra}$ and $[110]_{tetra}$ directions is observed with a separation of about 40 nm between the linear features (Figure 6.3b). They interpret these structural features as local fluctuations in the Ca^{2+} concentration. The presence of this tweed-like pattern breaks the symmetry of the structure and, as a result, weak diffraction spots appear at the extinction positions for the space group I4/mmm in the diffraction pattern as seen in the inset to Figure

6.3b [7]. TEM micrographs of $CaFe_2As_2$ single crystals made by the Sn-flux method (Figure 6.3c) reveal a large quantity of dislocations and complex dislocation networks mostly in the [1-10] and [110] directions. In the sample fabricated by solid state reaction, a periodic structural modulation, which has been interpreted as local structural distortion in the [110] direction, is observed (Figure 6.3d). These results indicate the significant role of processing method on both the microstructure and transport properties of $CaFe_2As_2$.

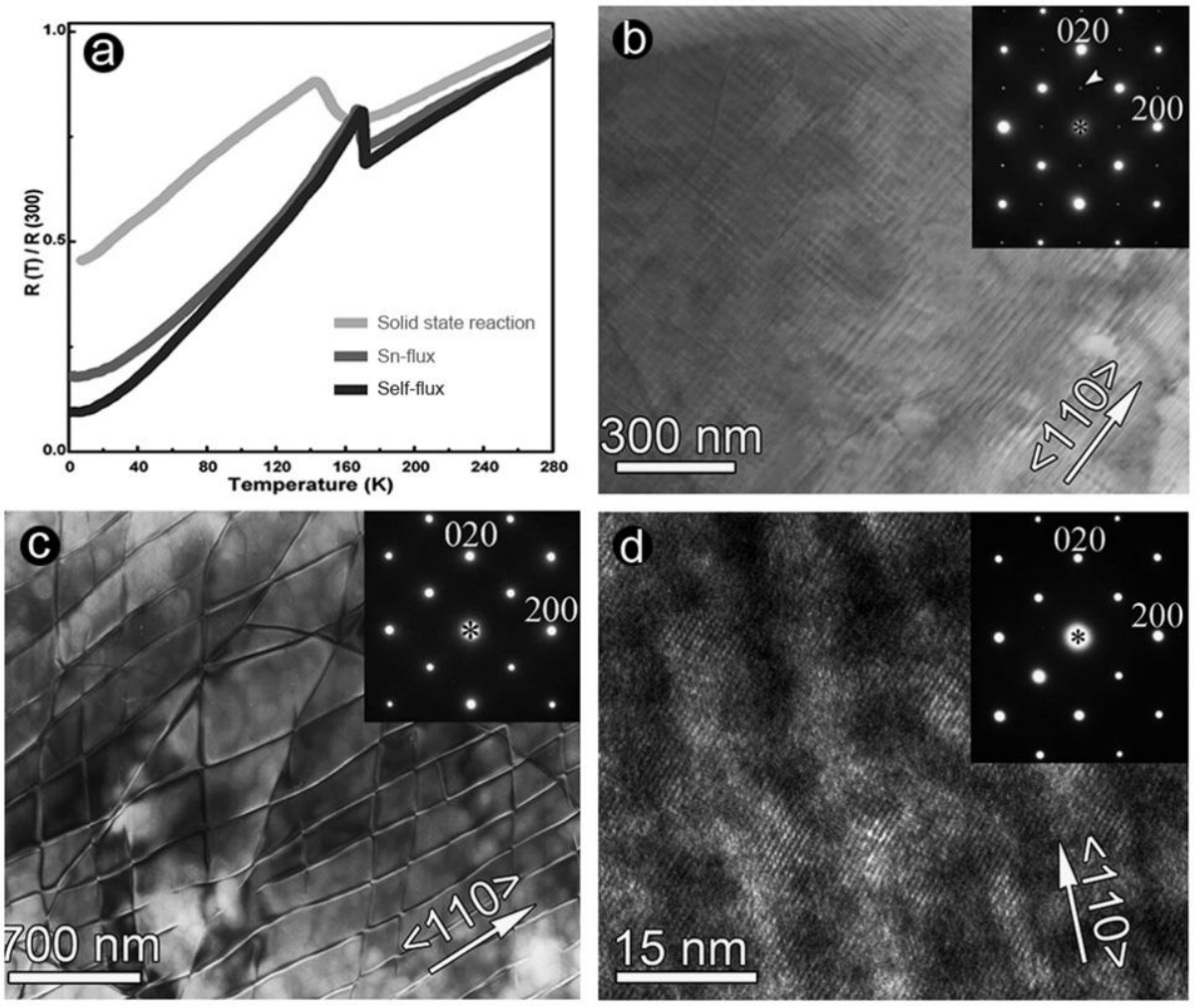

Figure 6.3: (a) Resistivity as a function of temperature for $CaFe_2As_2$ samples synthesized by different methods, TEM images and diffraction patterns (inset) of $CaFe_2As_2$ sample made by (b) FeAs-flux, (c) Sn-flux and (d) solid state reaction [7].

In other work by the same group, a series of in situ TEM studies, from room temperature to 20K, were carried out on the $CaFe_2As_2$ sample grown by the FeAs-flux method to observe the structural changes associated with the low temperature phase transition [8]. As shown in Figure

6.4b, at low temperature, a transition from tetragonal to orthorhombic symmetry is characterized by splitting the spots along [110] and forming twin domains which are 50-100nm in width. As the tweed-like structure is still observed in low temperature, the authors suggested that the twinning and tweed structure are independent and occur in different atomic layers i.e. Fe layers for twinning and the Ca layers for the tweed pattern.

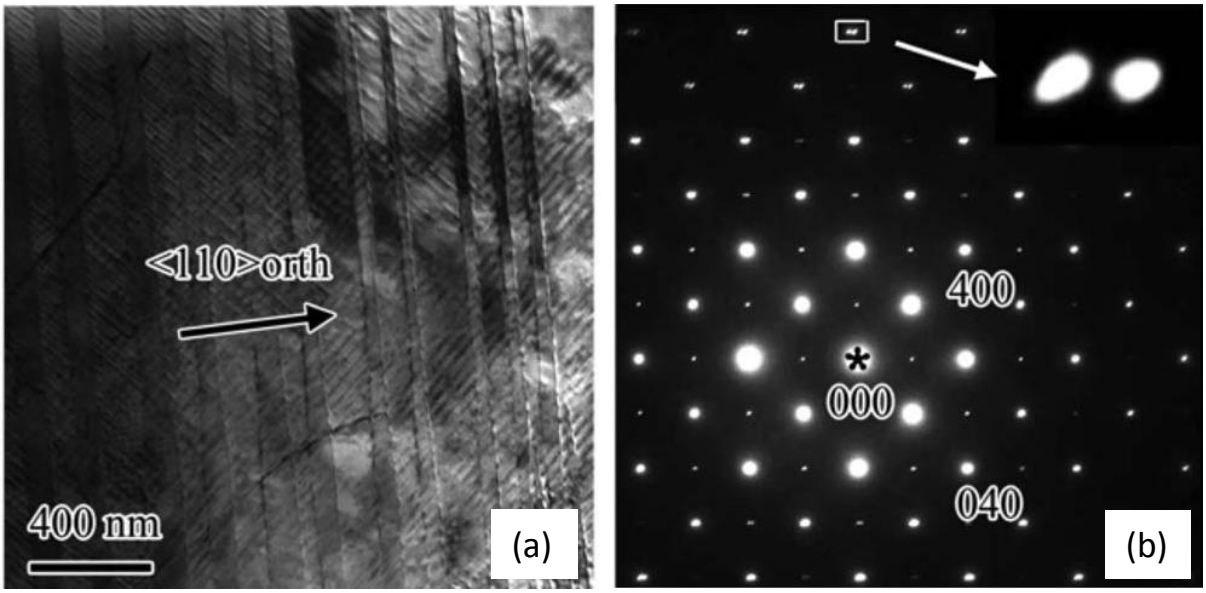

Figure 6.4: (a) Low temperature bright-field plane view TEM image of $CaFe_2As_2$ grown from FeAs-flux and its (b) diffraction pattern at low temperature [8].

Other TEM measurements were carried out by Ran et al. on $CaFe_2As_2$ samples grown from FeAs-flux before and after annealing at 500°C[14]. Similar to the results obtained by Shi et al, a tweed-like pattern with 40 nm separation of features is observed in the as grown sample (Figure 6.5a). However, these linear features are found to be parallel to the (h00) planes contrary to the tweed pattern in the sample grown by Shi et al where the features are along [110] directions (see Figure 6.3b). The sample annealed at 500°C appears completely different and shows uniformly distributed small precipitates about 25 to 100 nm in width and with a length to width aspect ratio of about 5:1 (Figure 6.5b). These precipitates are also fairly uniformly

separated, by ~500 to 1000 nm, and have their long axis parallel to (h00), as was observed in the tweed pattern of the as-grown sample. The coherency of the two lattices was suggested by the authors from the fact that the diffraction pattern including both matrix and precipitate does not show any extra spots or splitting of spots [14]. In order to precisely understand the formation of these precipitates, e.g. their chemistry and structure, as well as the similarity of the effect of annealing and pressure on this material, more TEM analysis are needed, especially for the samples which are annealed at different temperatures. Moreover, cross-sectional TEM analysis of these samples can provide new information of the nature of this compound. This chapter deals with the TEM investigation of these samples (grown by Ran et al by the FeAs-flux method) before and after different annealing processes.

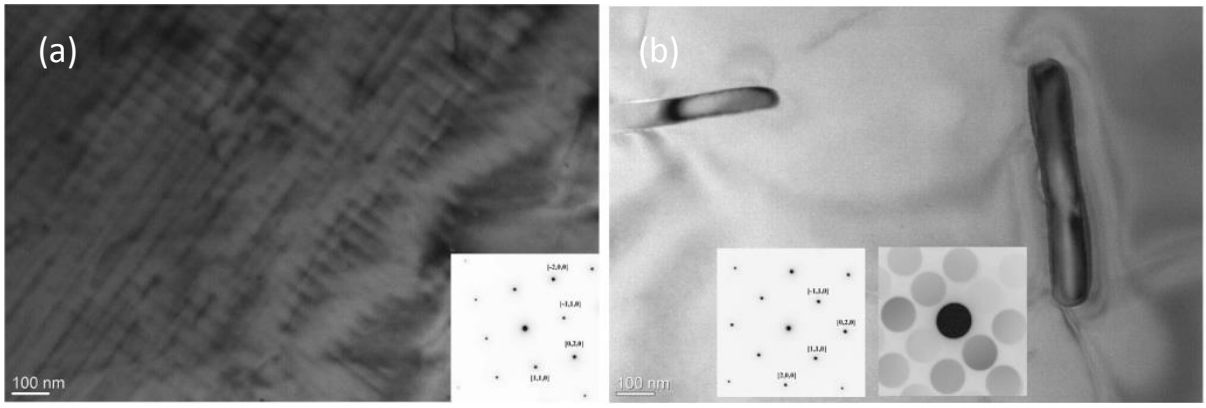

Figure 6.5: Plan-view TEM micrographs of (a) $CaFe_2As_2$ single crystal grown by FeAs-flux with an inset diffraction pattern, and (b) $CaFe_2As_2$ single crystal grown by FeAs-flux after annealing at 500°C for a week, the left inset is a diffraction pattern of the matrix and precipitate and the right inset is a CBED of only the precipitate phase [14].

It is worth noting that the tweed structure, observed in as-grown samples, appears only in $CaFe_2As_2$, not in either $BaFe_2As_2$ or $SrFe_2As_2$. As the Ca^{2+} (0.99 Å) ion is smaller than Sr^{2+} (1.12 Å) and Ba^{2+} (1.34 Å) ions, Ma et al suggested that this tweed structure arises from local structural distortions within the Ca atomic layers, which results in a stripe pattern along the [110] direction of the tetragonal structure (the diagonal of the Ca squares) [8]. They also reported the presence of this kind of structure only in $CaFe_2As_2$ as a reason to explain the very

different physical properties and structural instabilities observed in the $CaFe_2As_2$ compared to $SrFe_2As_2$ and $BaFe_2As_2$, because the anomalies in $CaFe_2As_2$ associated with the SDW instability in both electrical resistivity and magnetic susceptibility show obvious dissimilarities with those in $SrFe_2As_2$ and $BaFe_2As_2$ [8]. These results all emphasise on the importance of the precise study of $CaFe_2As_2$ system to understand the effect of Ca on the structure and properties of this compound.

6.4.Sample preparation

Single crystalline $CaFe_2As_2$ was prepared by our collaborators using the FeAs flux method and different annealing processes. A molten mixture of $CaFe_4As_4$ is rapidly cooled down from 1180°C to 1020°C in 3hrs followed by slow cooling from 1020°C to 960°C in 35hrs. Then the excess FeAs liquid was decanted off and the remaining crystals were quenched from 960°C to room temperature, to create the "as grown" samples. For post annealing, the as-grown samples were sealed into evacuated silica tubes and were placed into a furnace stabilized at 400°C or 700°C for 24 hrs and then quenched to room temperature. More details on sample preparation can be found in [14] and [15]. In this chapter, the three different samples listed in Table 6.1 were studied by TEM in cross-section. TEM samples were made by FIB (lift out using the FIB 200 instrument) as explained in the experimental methods chapter.

Table 6.1: Different samples studied in this chapter.

Sample	Growth conditions
AG	rapidly cooling a melt of $CaFe_4As_4$ from 1180°C to 1020°C over 3h + slowly cooling from 1020°C to 960°C over 35 h+Quench to room temperature
AG400	AG+ Annealed at 400°C for 24 hrs and quenched.
AG700	AG+ Annealed at 700°C for 24 hrs and quenched.

6.5.Results

6.5.1. As grown samples (AG)

Figure 6.6 shows the optical images and the FIB micrographs of the as-grown (AG) sample. At the surface of the sample elongated holes can be seen most of which are perpendicular to each other. These holes might be due to the presence of a second phase with a higher volatility in these directions. It is also possible that different properties in these directions lead to the presence of defects in this kind of pattern. As discussed earlier, plan-view TEM micrographs of this sample by Ran et al [14] show the tweed-like pattern in (h00) directions confirming the presence of preferential directions for the defects in these samples. The c-axis is perpendicular to the sample surface and all TEM samples are made by FIB in cross-section from the regions without any features.

Low magnification TEM micrographs (Figure 6.7) show that the sample seems uniform without any obvious secondary phases. Bend contours can be seen over the sample, and in some places, delamination of the ab plane (perpendicular to c-axis) is observed. These delamination regions are surrounded by dense arrays of dislocations and, as expected, are the places for the intersection of the bend contours. The delamination might be due either to a high amount of strain accumulated in the ab plane or the presence of a weak bonding in this direction. A long linear crack can be also seen exactly parallel to the surface which again indicates different properties in the ab planes. It has been observed in other references that the $CaFe_2As_2$ single crystals can be easily cleaved and/or separated into individual sheets on the ab plane because they are layered with a weak bonding in the c direction [8, 12, 14].

The electron diffraction pattern taken using a large selected area aperture (SAD) which almost covers the whole sample shows only a pattern consistent with the [100] zone-axis of the

$CaFe_2As_2$ compound. The absence of additional reflections in the diffraction pattern indicates that the sample is single crystalline with no large secondary phases or lattice disorder. However, some spots, especially those which are furthest away from the direct beam, appear to be split. This might be due to local changes in crystal orientation from bending and crystal defects, which is more obvious in the higher index diffraction spots.

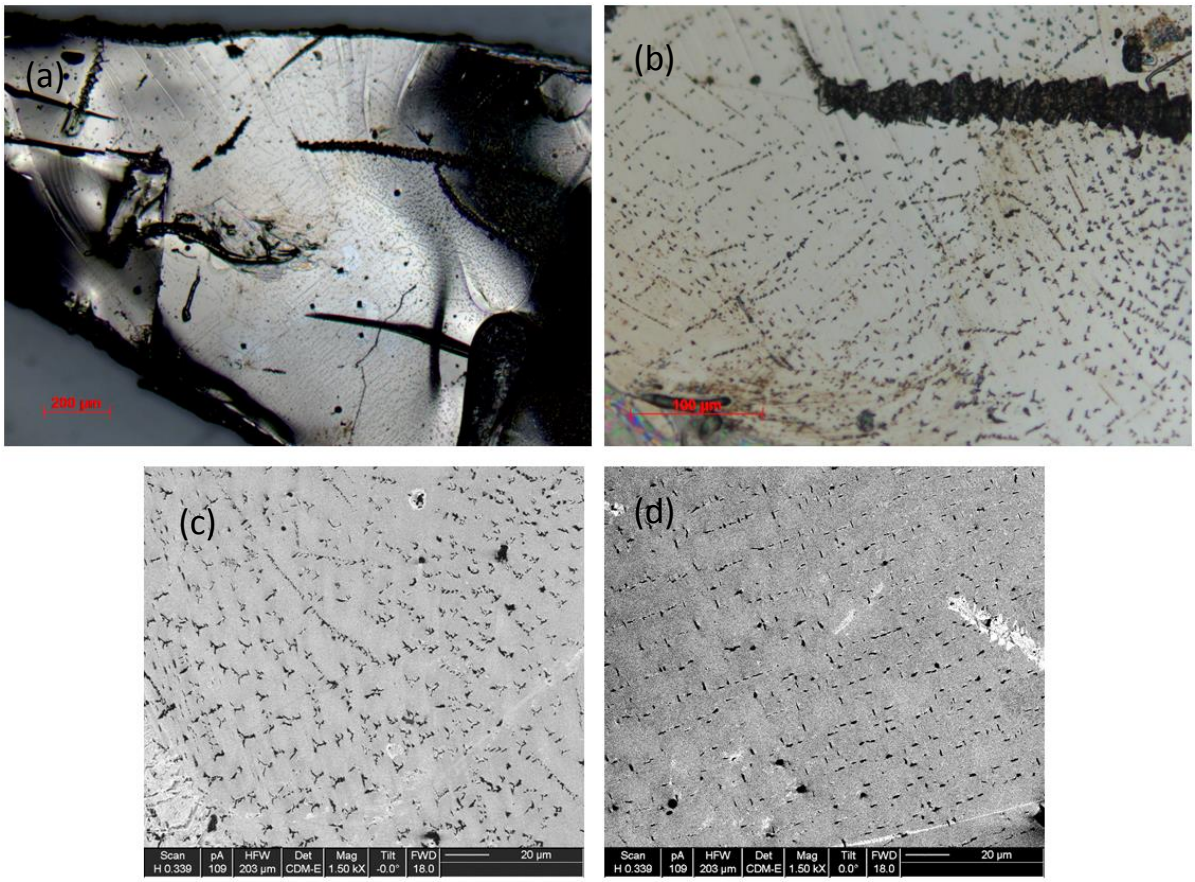

Figure 6.6: (a) and (b) Optical images of the AG sample, (c) and (d) FIB micrographs of the AG sample showing elongated holes in two perpendicular directions.

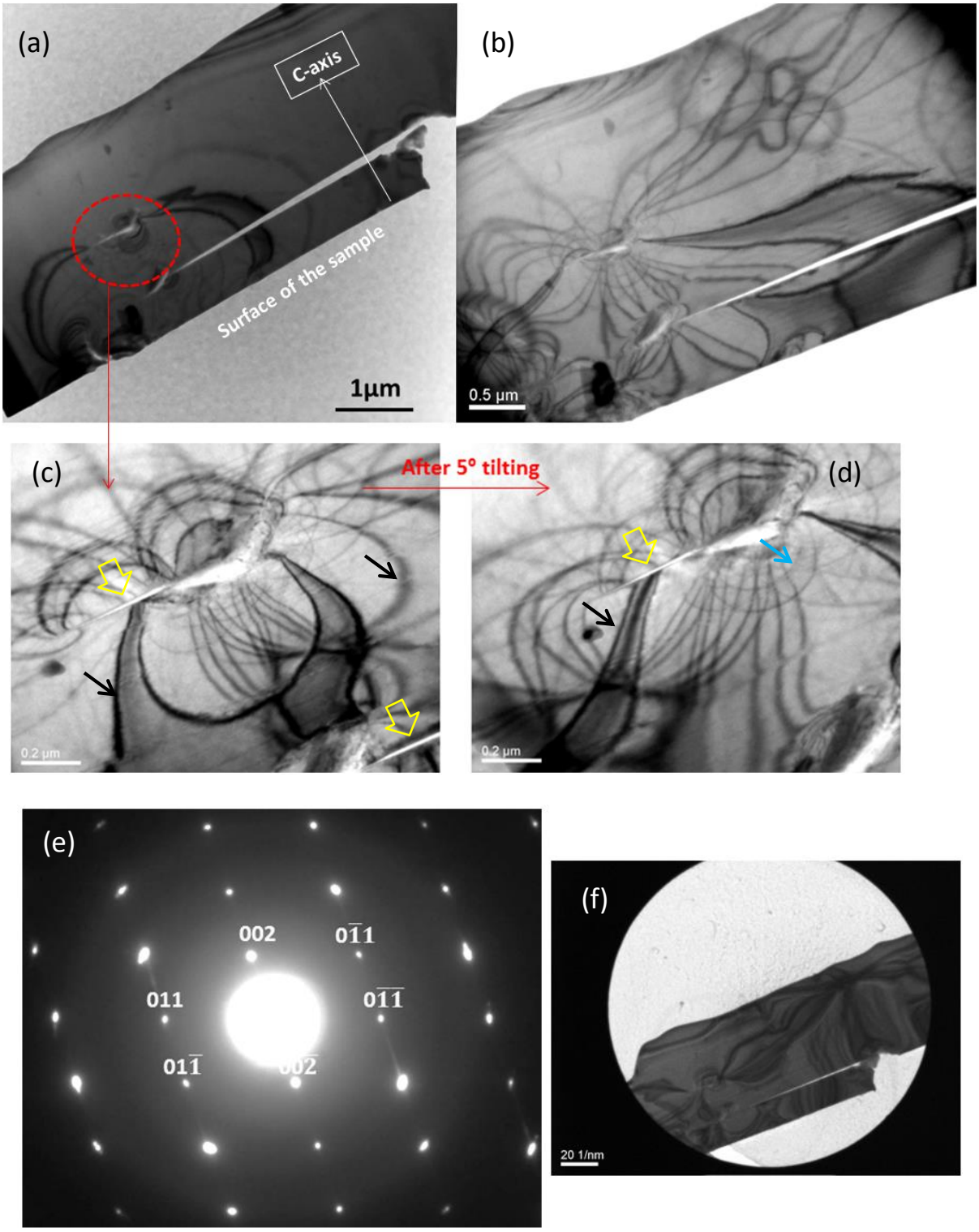

Figure 6.7: (a) and (b) Low magnification cross-sectional bright-field TEM micrographs of the AG sample, (c) and (d) delamination (yellow arrows) in the ab plane, bend contours (black arrows) and arrays of dislocations (blue arrows) around the delaminations, (e) and (f) [100] zone-axis diffraction pattern (at camera length of 250 cm) from the shown area.

TEM images of the AG sample at higher magnifications (Figure 6.8) again show no trace of obvious secondary phases or impurities, but very long thin linear features parallel to the surface of the sample (perpendicular to the c-axis) can be seen almost all over the sample. Tilting experiments revealed that these features are two-dimentional. These linear features are stacking faults in the ab plane, and are not uniformly distributed with seperations varying from 10nm to 75nm. Due to the weak van der Waals bonding between the Ca and Fe-As layers in the $CaFe_2As_2$ structure [12] (see the delamination exactly on one of these planes in Figure 6.8c), it is likely that stacking faults are easily formed on this plane. The liquid phase growth process used to fabricate the sample can be another reason encouraging the formation of stacking faults since it is likely that excess FeAs layers are incorporated during growth and trapped in the ab plane making stacking faults.

When a large number of stacking faults is present in the sample, streaking will occur in the diffraction pattern in a direction perpendicular to the stacking fault plane [16]. In this sample, there are not enough stacking faults to give noticeble streaks in the diffraction pattern.

The lattice parameters of the $CaFe_2As_2$ tetragonal structure were calculated from diffraction patterns after camera length calibration. Using the diffraction patterns obtained from the whole sample (large SAD aperture), the calculated lattice parameters were a=3.91 Å and c=11.595 Å. In order to investigate if these parameters are similar everywhere in the sample, a small SAD aperture was used to obtain diffraction patterns from different regions in the sample (see Figure 6.9). Lattice parameters calculated from those regions are listed in the table in Figure 6.9. As can be seen, the lattice parameters are almost homogenous over the sample, and no significant differences were observed. However, the measured variation in the c parameter is slightly larger than the variation in the a parameter which can be due to the larger concentration of defects and mechanical strain in the c direction. As the camera length calibration was done exactly before this experiment, and all the measurements (distance between spots) were done

using Digital Micrograph software, even if there is any error in the calculation, it would be the same for all regions. Therefore, the comparison of the lattice parameters values can be safely considered to be significant.

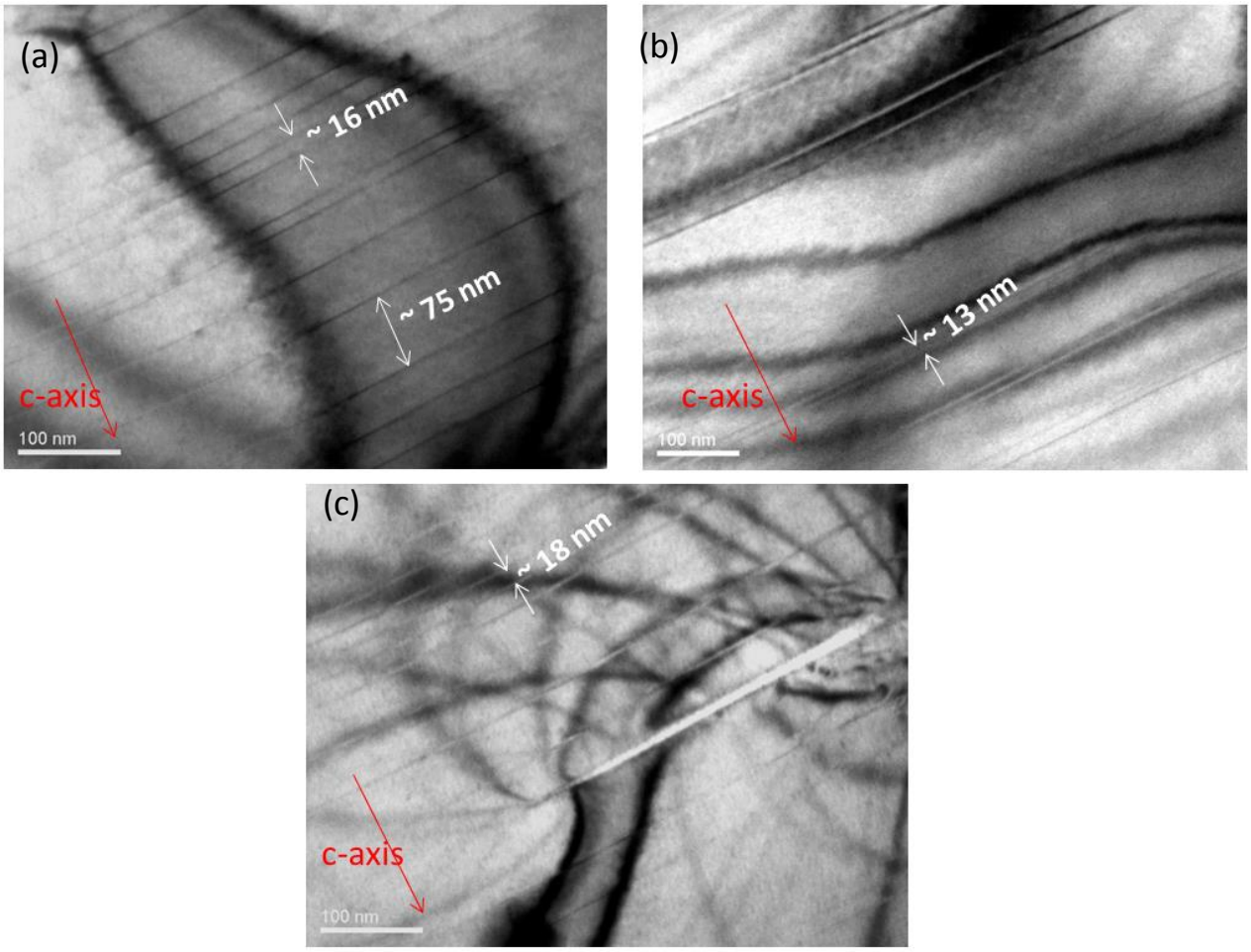

Figure 6.8: Cross-sectional bright-field TEM micrographs of the AG sample showing stacking faults parallel to the surface of the sample (perpendicular to the c-axis).

TEM-EDX analysis was carried out in different regions of the sample in order to investigate whether we can detect any compositional variation. Figure 6.10a shows a typical TEM-EDX spectrum of the AG sample. No impurity elements are observed in the sample (the Cu peak is from the copper grid and the TEM column). EDX Point analyses were carried out in different spots over the sample with a separation of about 1μm.

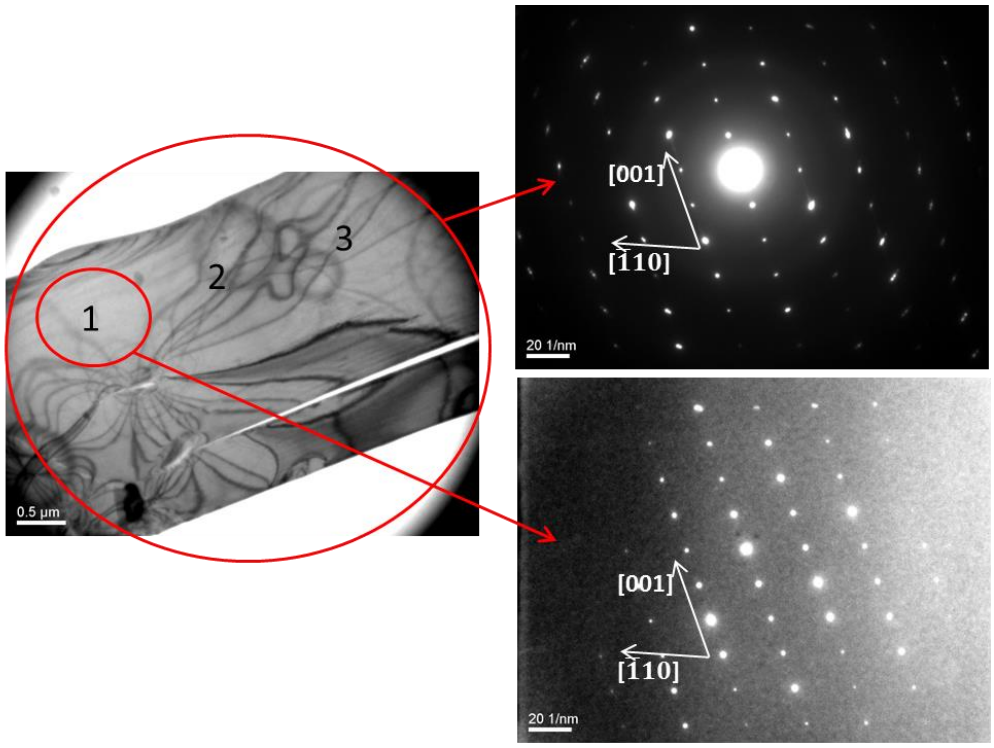

	Region 1	Region 2	Region 3	Region 4	Region 5	Whole sample
a-axis parameter(Å)	3.91	3.91	3.91	3.9	3.91	3.91
c-axis parameter(Å)	11.61	11.59	11.61	11.59	11.59	11.6
c/a ratio	2.97	2.97	2.97	2.97	2.97	2.97

Figure 6.9: Diffraction patterns using different SAD apertures from various regions of the AG sample and the lattice parameters calculated in different regions (the error bar is ~0.004Å) showing the variation of lattice parameters in different regions in the sample.

In Figure 6.10b the Fe content is plotted versus Ca content according to the stoichiometry of $Ca_xFe_yAs_2$, relative to a fixed As content of 2. The sample seems homogenous in Fe content, but the Ca content varies significantly in different regions. The variation of x (Ca content) is between ~0.91-1.07 (16%) which is larger than the variation of y (Fe content) ~1.95-2.08 (6%). Looking at the unit cell in Figure 6.2, the fluctuation in Ca content would change the c-axis parameter in the structure rather than the a-axis. This might be a convincing reason for the larger variation observed in the c-axis parameter compared to the a-axis parameter in Figure 6.9. Considering all the results, it can be suggested that the AG sample is a saturated $CaFe_2As_2$

sample having extra FeAs in the ab planes and, consequently, a high degree of stress, especially in these planes, leading to delamination and cracks in a perpendicular direction to the c-axis. However, the sample is essentially a single crystal with no macroscopic secondary or impurity phases, but variation in the local Ca content and c-axis lattice parameter.

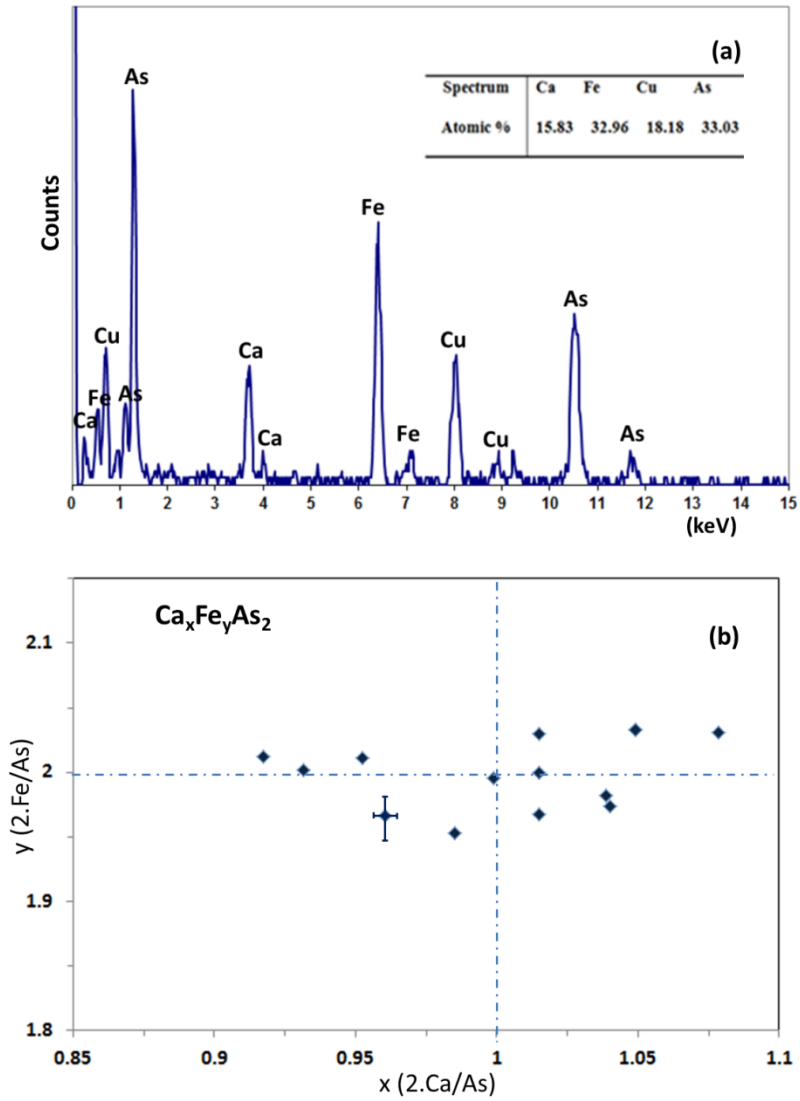

Figure 6.10: (a) Typical TEM-EDX spectrum from the AG sample, (b) Compositional distribution obtained from TEM-EDX point analysis in different regions of the AG sample, the dashed lines indicate perfect stoichiometry. (x and y are Ca content and Fe content respectively according to a stoichiometry of $Ca_xFe_yAs_2$).

6.5.2. As grown sample annealed at 700°C (AG700)

Figure 6.11 shows optical images of the sample annealed at 700°C (AG700). The elongated holes which were observed in the AG sample are not seen in this sample. The c-axis is

perpendicular to the sample surface. Low magnification cross-sectional TEM images, as shown in Figure 6.12, are very different to those seen from the AG. Pairs of long lines can be seen. These lines move together when the imaging conditions (brightness/tilting) are changed. Stacking faults have completely disappeared in this sample, and no trace of them is observed even at high magnification.

Diffraction patterns using both large SAD and small apertures in different regions show only the diffraction spots corresponding to the [100]-zone axis of the $CaFe_2As_2$ single crystal (see Figure 6.13). The lattice parameters of the AG700 sample were calculated from these diffraction patterns and a and c were measured to be 3.91Å and 11.65Å respectively. Both the c/a ratio and the c parameter in the table are larger than those measured in the AG sample, but the variation of lattice parameters over the sample is similar to those measured in the AG sample (more alteration in the c-axis parameter compared to the a-axis).

At higher magnifications (Figure 6.14), dislocations can be seen running through the sample. Some of these dislocations appear as pairs which might be either dipoles (where the dislocations have Burger vectors of opposite sign) or superdislocations (where both dislocations have Burger vectors with the same sign). The way of distinguishing dipoles from superdislocation is by tilting experiment. When a tilt of either the incident beam or the specimen happens, the image positions for a superdislocation pair move in unison, whereas the two dipole images move in opposite directions. As a result, the separation between superdislocations remains constant when the sample is tilted, whereas the dipole width decreases. By applying this method for this sample, the dislocation pairs were found to be dipoles.

Moreover, in this sample, as shown in Figure 6.15, very thin and long features perpendicular to the c-axis are observed. As can be seen this feature has a length of about 2.15 μm and is about 60-70 nm in width. TEM-EDX point analysis was carried out inside and outside the feature

using a small condenser lens and a large volume of spot size providing a beam of 30nm for precise measurement. Although the beam spreads to the larger area thorough the thickness of the sample, but the comparison of the results from different areas can be considered for the investigation of the compositional variations. It can be seen in Figure 6.15b that the Ca content is systematically lower in this feature compared to the matrix, suggesting that precipitation of a FeAs-based compound takes place during annealing at 700°C. The precipitate did not make any change to the diffraction pattern, and no extra spots were detected when the SAD aperture included both the feature and the matrix. The disappearance of stacking faults and the presence of this type of low-Ca precipitates (linear shape with the long dimension parallel to the ab plane, i.e., the same direction as the stacking faults in the AG sample) suggests that the segregation of extra FeAs takes place during annealing. Consequently, the matrix exhibits no stacking faults but some dislocations which can be formed when the stacking faults disappear. Regarding the pairs of long lines observed in Figure 6.12, it is not clear how they are formed and why, in some images, they are in pairs of black/white lines.

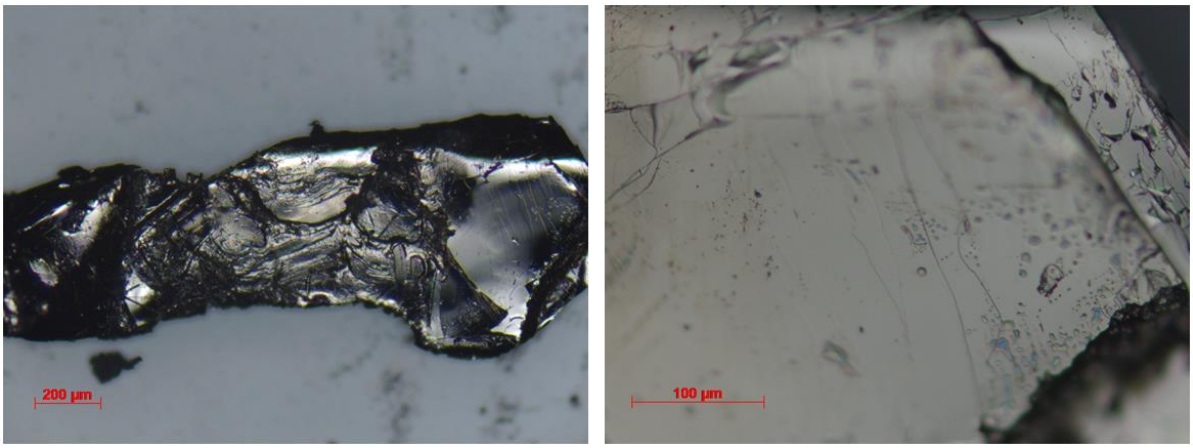

Figure 6.11: Optical images of the AG700 sample.

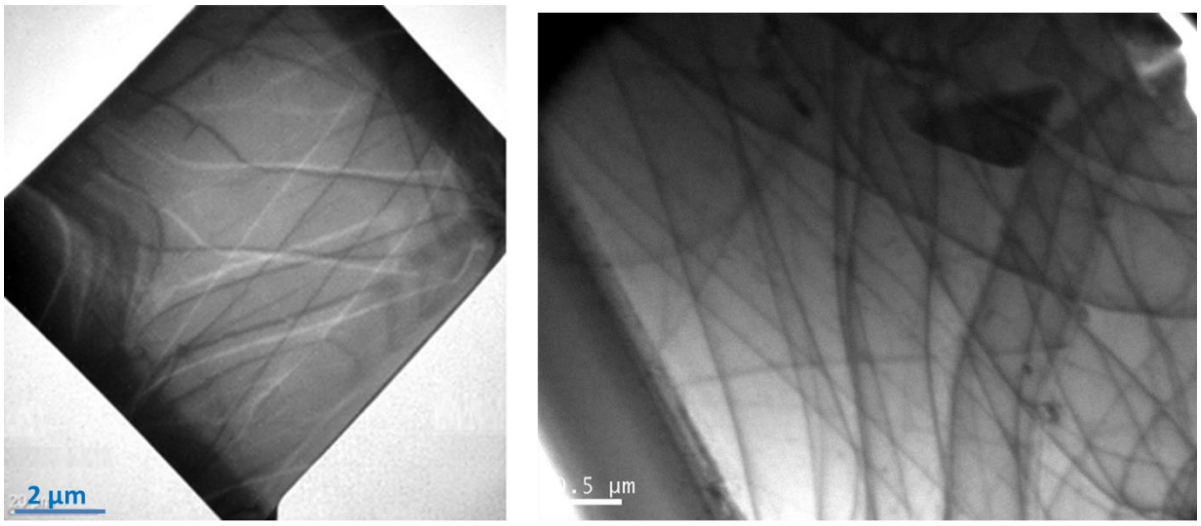

Figure 6.12: Low-magnification bright-field TEM images of the AG700 sample showing the pairs of long line.

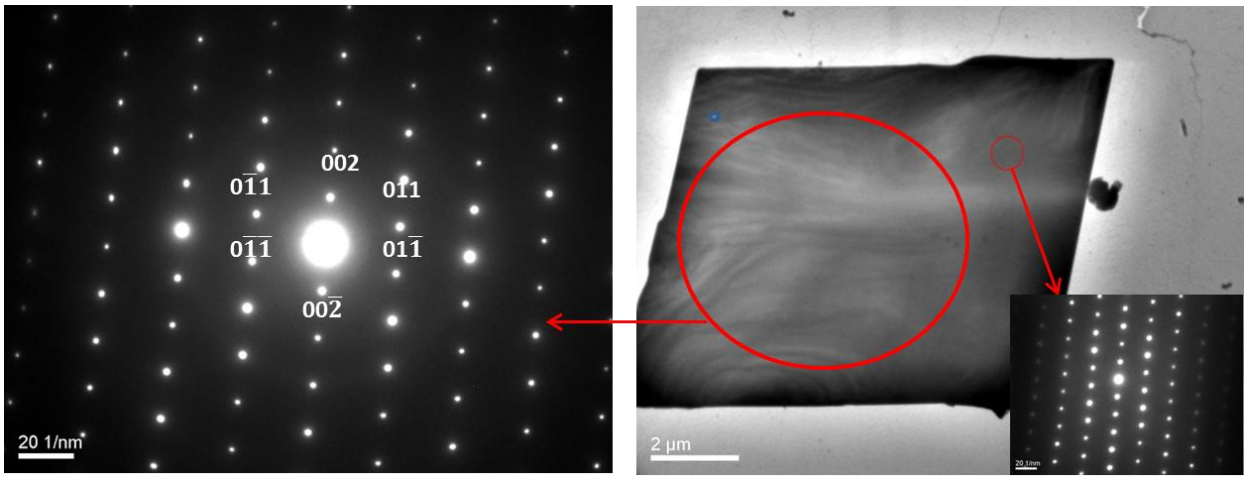

	Region 1	Region 2	Region 3	Region 4	Region 5	Whole sample
a-axis parameter(Å)	3.91	3.91	3.92	3.91	3.92	3.91
c-axis parameter(Å)	11.66	11.64	11.65	11.66	11.64	11.65
c/a ratio	2.97	2.98	2.97	2.98	2.97	2.98

Figure 6.13: Diffraction patterns of the AG700 sample using a large area aperture covering the whole sample and a small SAD aperture at camera length 250cm. The table includes the lattice parameters calculated from small SADs in different regions of the sample and shows how lattice parameters vary over the sample.

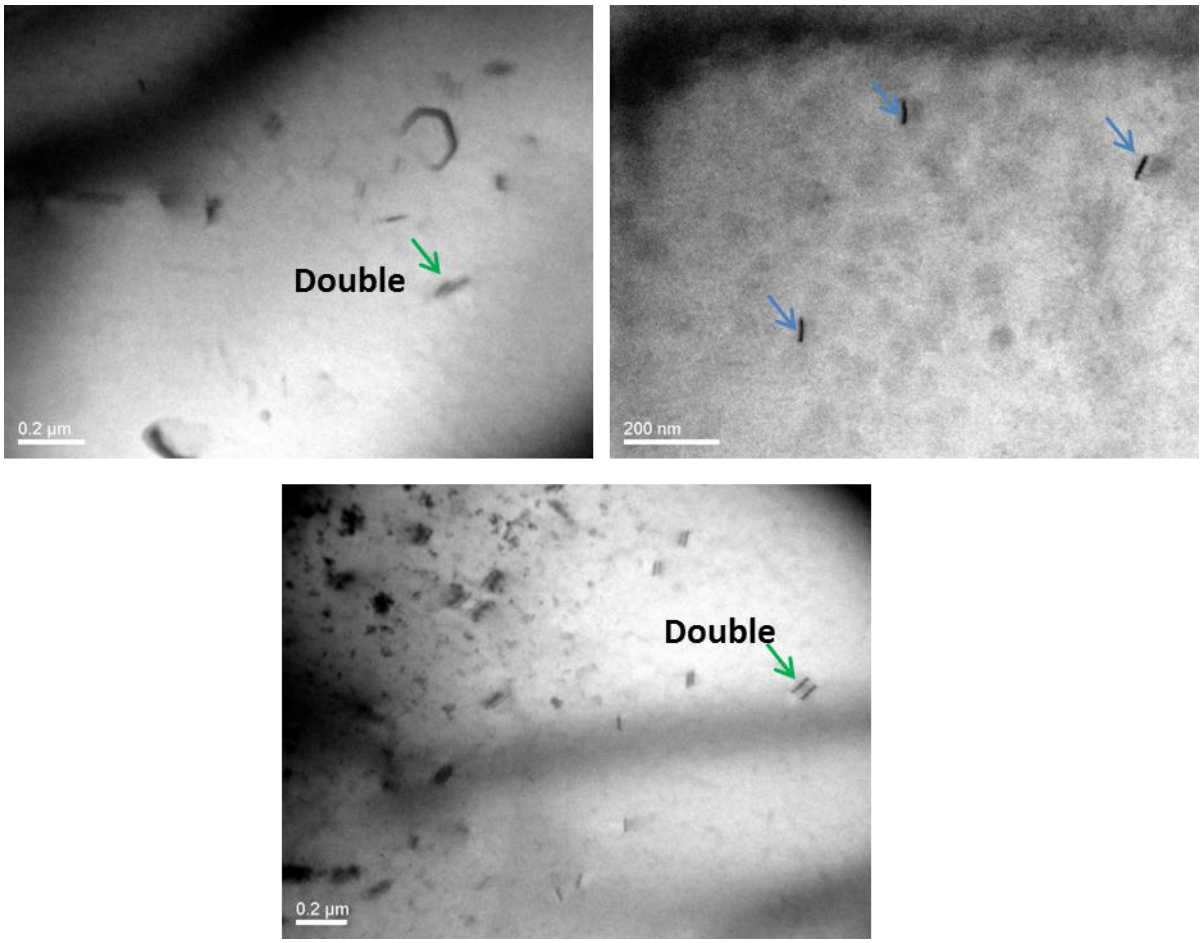

Figure 6.14: Bright-field TEM images of AG700 showing dislocations and dipoles.

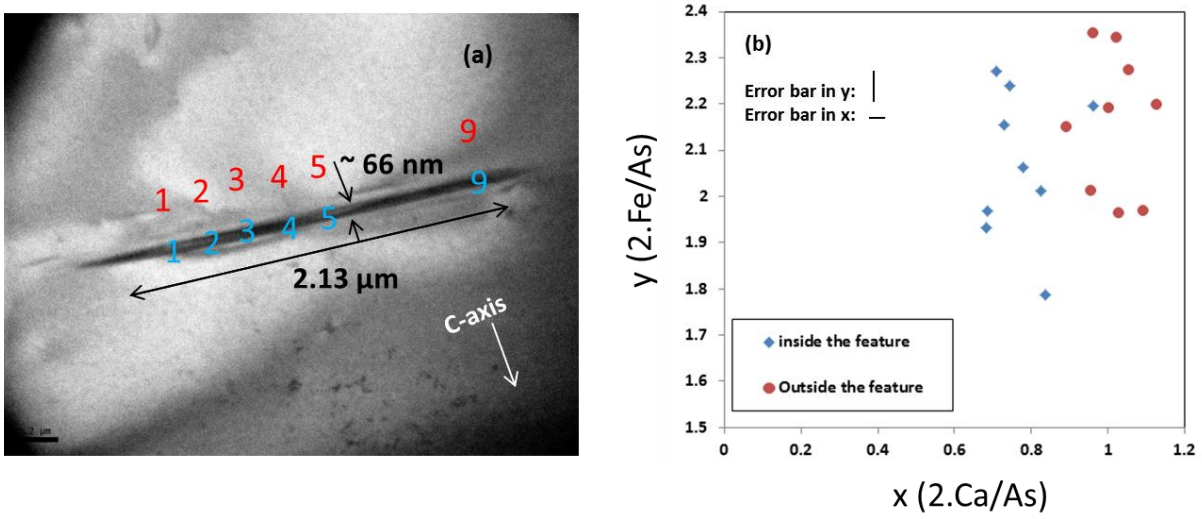

Figure 6.15: (a) Bright-field TEM image showing a needle-shape precipitate in the AG700 sample and (b) the composition of the precipitate and the matrix obtained by point TEM-EDX using a beam spot of about 30 nm. The precipitate contains less Ca compared to the matrix.

6.5.3. As grown sample annealed at 400°C (AG400)

The low magnification TEM micrograph of the AG400 sample (Figure 6.16a) shows bend contours, delamination at few regions and a long crack running along the ab plane. As can be seen, the sample is not uniform in thickness. In the thicker part (Figure 6.16c), a high density of stacking faults is observed, while the thinner part (Figure 6.16b) does not exhibit these features and is so thin that the features of carbon layer from beneath the sample can be seen. The density of stacking faults in this sample is much higher than observed in the AG sample. This result in comparison with the AG and AG700 samples suggests that the stacking faults in AG400 are stabilized after annealing at low temperature most likely due to the segregation of extra FeAs in the ab plane from the supersaturated quenched sample.

The reason for the absence of these stacking faults in the thin part of sample can be the damage from ion milling (sample preparation) in thinner regions. In fact, milling above 5 keV can make milling artifacts, including an amorphous layer, which form a more significant fraction of the total sample thickness in the thinner samples.

The diffraction pattern taken using a large SAD aperture (Figure 6.16d) shows the sample is still single crystal with no extra reflections. However, the diffraction pattern using smaller SAD aperture covering the region including stacking faults shows extra reflections which can originate from the high structural distortion in this region or from a secondary phase precipitated in the ab plane. In this sample, a few very long needle-shaped features are also observed, as shown in Figure 6.17a. Similar features have been observed in cross-sectional SEM images taken by our collaborators (Figure 6.17b).

It can be seen from SEM image that the most of these features are perpendicular to the ab plane; however, a few of them lie at 45° relative to the c-axis similar to those observed by TEM. TEM-EDX point analysis inside and outside the features using a spot of 30nm (Figure 6.18) shows these features contains much less Ca compared to the matrix. Allowing for the inevitable

beam spreading in the sample, this data suggests that the needle-shape features are very low in Ca, and may be pure FeAs as suggested by [14]. Diffraction patterns from a region including both a needle-shape feature and the matrix does not show any extra spots or splitting of spots and it is very similar to the diffraction pattern when only the feature is included. These characteristics are similar to the precipitates in the AG700 sample. However, the Ca content in the precipitates in the AG400 sample is lower compared to these precipitates in the AG700 material.

The presence of these precipitates in $CaFe_2As_2$ after annealing has been also observed by Ran et al in plan-view (as discussed in section 3 and Figure 6.5). Comparing my results with theirs and the different directions of observation, it can be suggested that the precipitates that we observed are cross-sections of the precipitates observed by Ran et al [14]. As the width of these needle-shape features varies along the feature, the apparent size of the precipitates in plane-view would depend on the section in which the TEM sample is made. Therefore, the observed difference in width of precipitates in cross-section view and plan-view can be explained.

6.6. Discussion and conclusion

Considering all of the results obtained both by this work and by our collaborators, we can summarize that the growth process from a FeAs-flux and quenching from 960°C results in an unstable FeAs-supersaturated sample containing a high amount of strain. The extra FeAs is trapped in both the ab plane, resulting in the stacking faults visible in my cross-sectional TEM images, and the a/b directions, resulting in the tweed-like patterns visible in the plan-view TEM images. In fact these places are thermodynamically favourable due to the layered structure of $CaFe_2As_2$ and the weak van der Waals bonding between the layers.

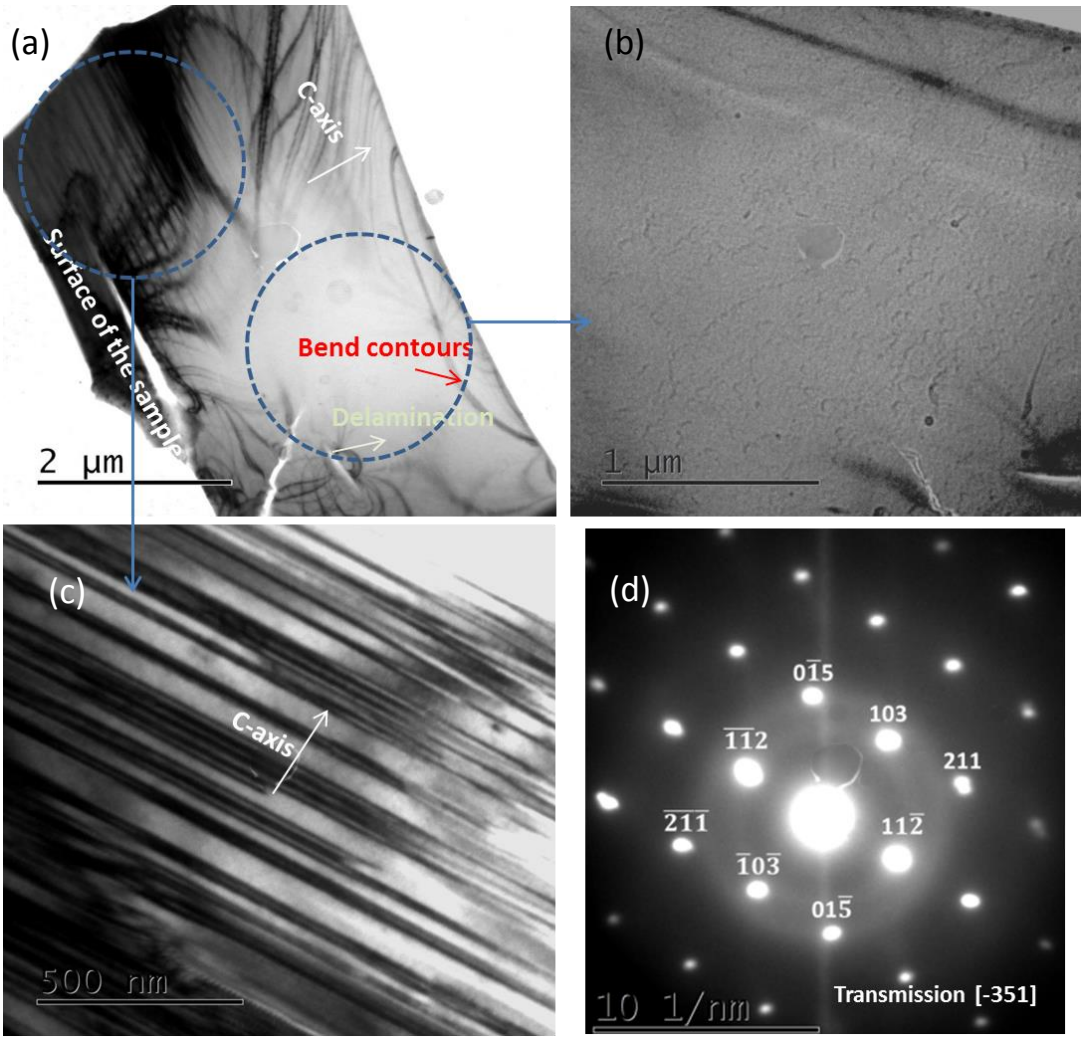

Figure 6.16: (a) Low magnification TEM-cross sectional images of the AG400 sample showing that stacking faults are only in some regions, (b) and (c) Higher magnification of indicated regions, (d) Diffraction pattern using a large SAD aperture showing that the sample is single crystalline.

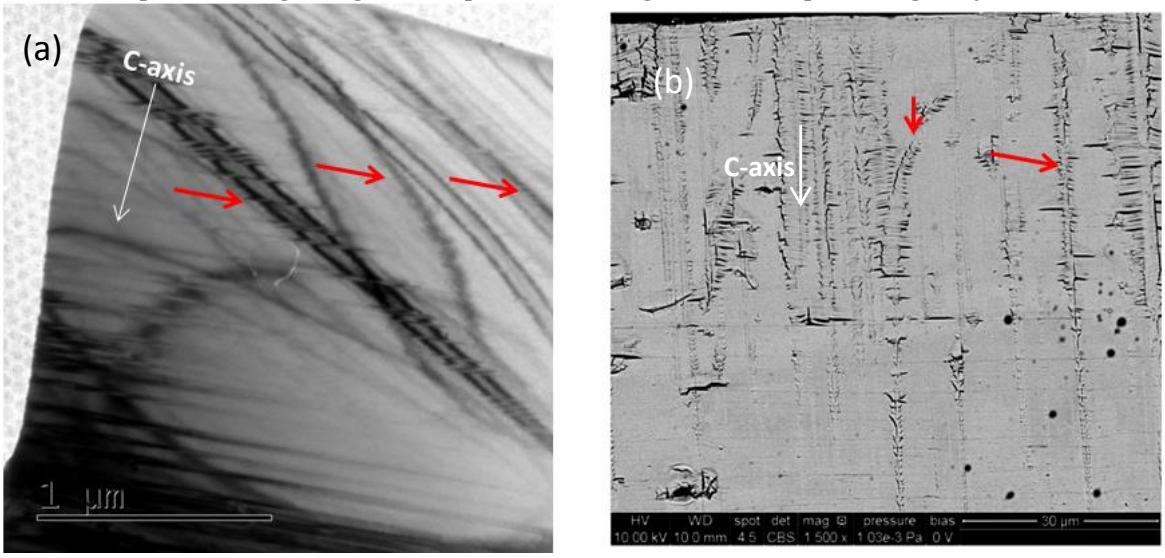

Figure 6.17: (a) Bright-field cross-sectional TEM micrographs of AG400 showing long needle-shaped features as indicated by red arrows, (b) Cross-sectional SEM image of the same sample taken by the collaborators showing similar features.

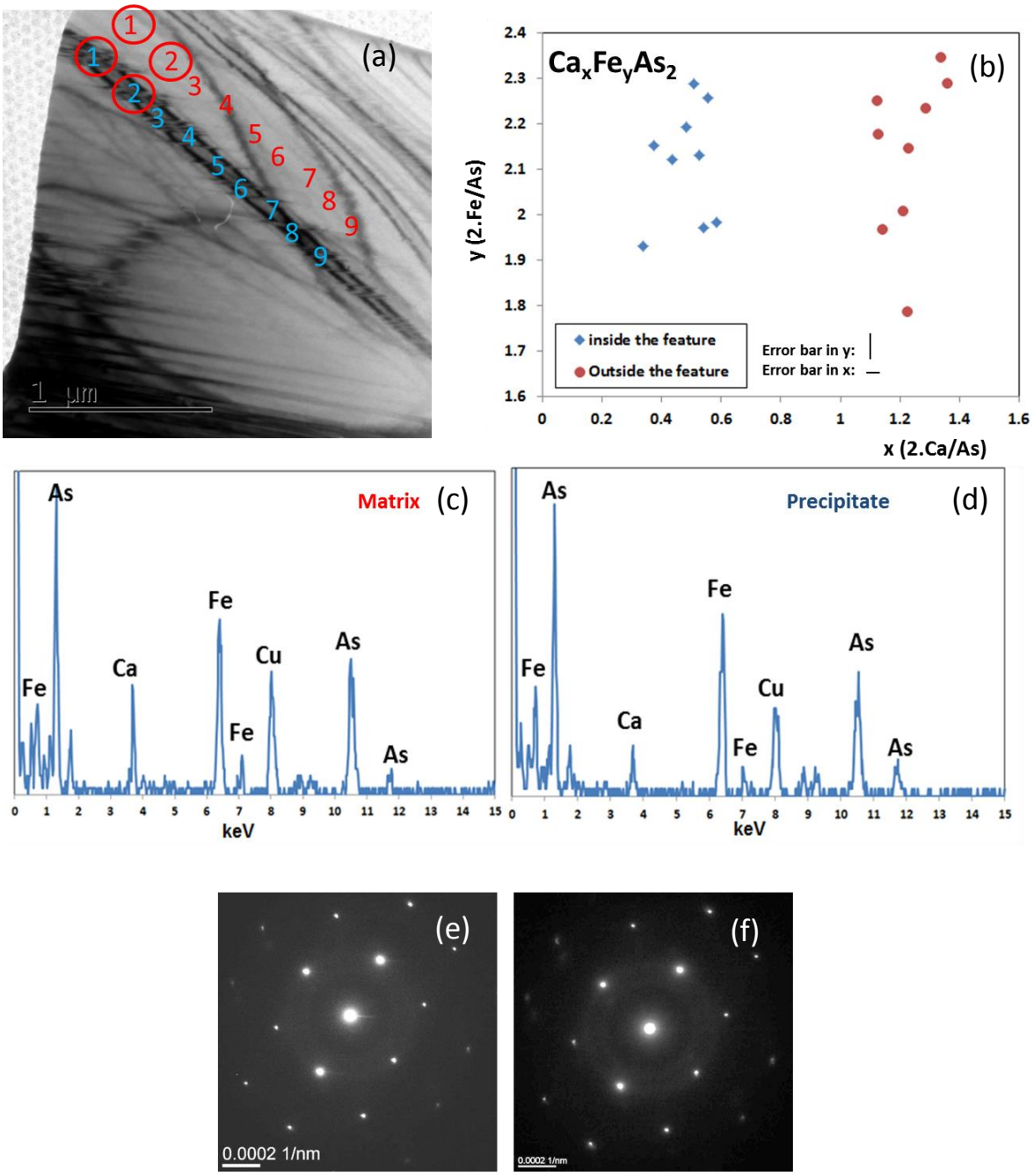

Figure 6.18: (a) Bright-field TEM image showing a needle-shaped precipitate in the AG400 sample (b) corresponding composition of the precipitate and the matrix obtained by point TEM-EDX using a spot of about 30 nm of the points indicated in (a) showing that the precipitate contains less Ca compared to the matrix, typical EDX spectrum of (c) the matrix, (d) the precipitate, Diffraction pattern of the region including (e) both precipitate and matrix, (f) only precipitate indicating similar structure of the precipitate and matrix.

After annealing at high temperature (AG700), the extra FeAs starts to precipitate by the diffusion of the Ca atoms, which are smaller than Fe and As atoms, and the matrix exhibits dislocations instead of stacking faults. Long precipitates of an FeAs-based compound are

formed with their long dimension perpendicular to the c-axis. In fact, it seems possible that the presence of extra FeAs layers in the ab plane (the stacking faults) leads to the formation of the precipitates of this particular shape. Therefore, the AG sample has less Ca in the matrix as it is supersaturated in Fe-As. Although there are stacking faults of excess Fe-As, the quantity of Fe-As is still higher in this phase. This explains the lower c axis in this sample. If the c-axis is lower, it replicates high applied pressure as applied pressure will squash the c-axis. Moreover, there might be mechanical compressive strain produced by the stacking faults in this sample.

Annealing at lower temperature results in local density of stacking faults compared to the AG sample and higher density of smaller linear precipitates compared to the AG700. Moreover, the precipitates have lower Ca content relative to the precipitates in the AG700. Indeed, after low temperature annealing, the supersaturated single crystal is less thermodynamically stable and a significant amount of segregation takes place resulting in lower Ca content precipitates. The TEM-EDX results of these three samples (Figure 6.19) also confirms this fact by showing a large variation in Ca content for the AG400 sample and a small compositional variation for AG.

On the other hand, during low temperature annealing the diffusion of the atoms cannot be as fast as in the AG700 sample in spite of the larger driving force for segregation, therefore the accumulation of FeAs happens at the closest possible places, which are the ab planes, leading to a local higher density of local stacking faults and smaller precipitates.

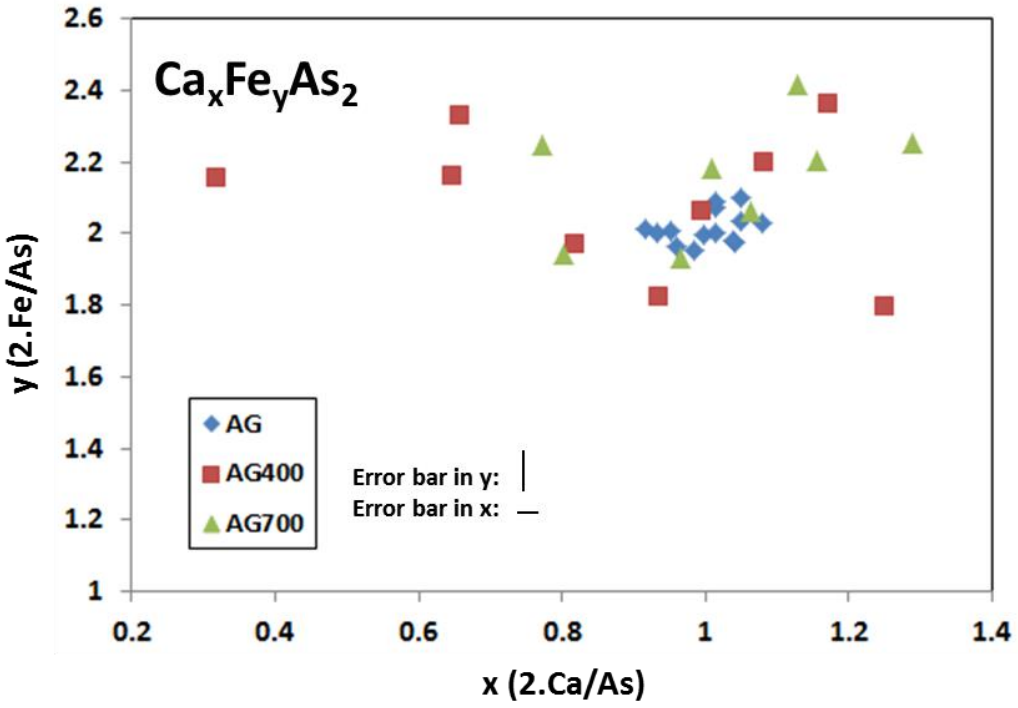

Figure 6.19: Compositional distribution (obtained by TEM-EDX point analysis) in AG, AG400 and AG700 samples (x and y are Ca content and Fe content respectively according to a stoichiometry of $Ca_xFe_yAs_2$). The AG sample shows less data scatter and annealing leads to more chemical segregation.

The ternary phase diagram of Ca-Fe-As is unknown, but according to the binary phase diagram of Fe-As, shown in Figure 6.20, there are several possible compounds for the FeAs-based precipitates; $FeAs_2$ with an orthorhombic structure (e.g. FeS_2), FeAs with a MnP-type orthorhombic structure, high-temperature Fe_3As_2 with unknown structure and Fe_2As with a Cu_2Sb-type tetragonal structure. There is another phase, $Fe_{12}As_5$, which is stable only under high pressures [17]. According to the diffraction data, the lattice structure of the precipitate is most likely to be very similar to the matrix ($CaFe_2As_2$ with tetragonal structure), and among all these phases, the Fe_2As compound has similar crystal structure to the $CaFe_2As_2$, but TEM-EDX data do not show an As:Fe ratio of 2:1 for the precipitates. To precisely identify the chemistry and structure of this second phase more microscopy experiments, especially, high-resolution lattice images are needed.

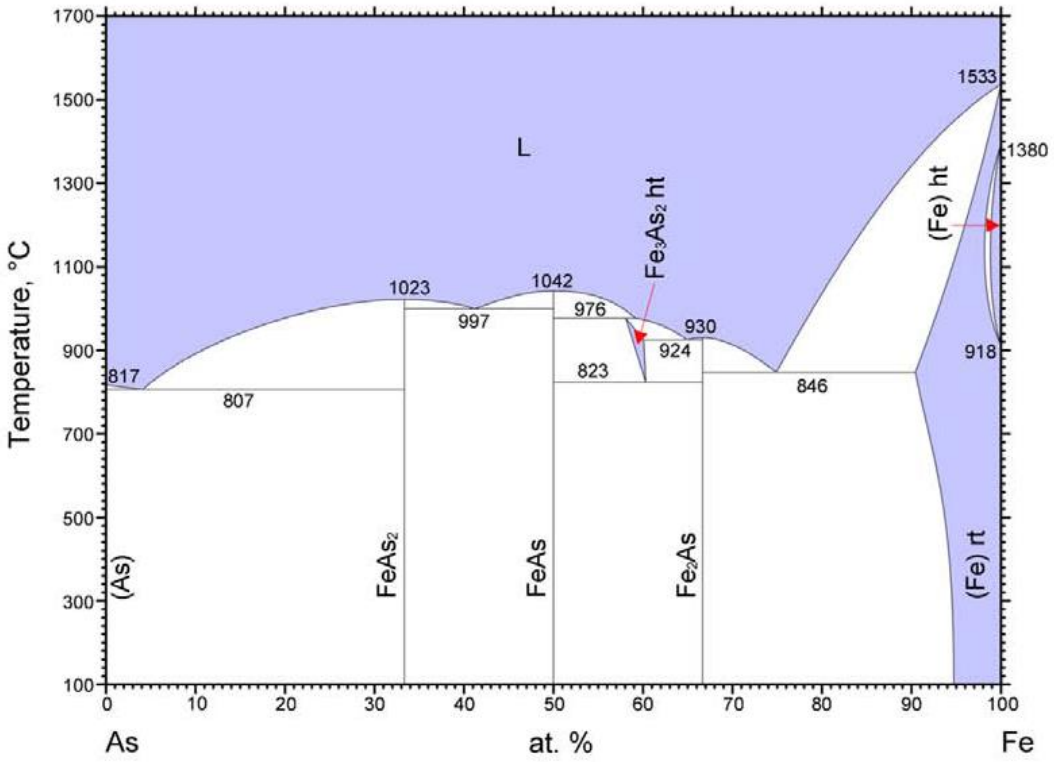

Figure 6.20: Binary phase diagram of Fe-As [17].

It can be concluded that the microstructure of the $CaFe_2As_2$ single crystals, e.g. the density of stacking faults, the amount of strain, the density of precipitates, size and shape of precipitates, can be controlled by selecting the annealing temperature. This might be the answer for the main question discussed in the beginning of this chapter, i.e., why are the effects of annealing temperature (for FeAs-flux grown sample) similar to the effects of external pressure (for Sn-flux grown sample) on the low-temperature phase-transition. In fact, different annealing temperatures create different amount of Ca and different amount of strain in the sample leading to various c-axis parameters as can be seen in Table 6.2. The sample with smaller c-axis parameter is similar to the situation when the material sustains external pressure.

Table 6.2: The experimental average values of lattice parameters for AG, AG700 and AG400 single crystals.

	c-axis parameter (Å)	a-axis parameter (Å)
AG	11.59	3.91
AG700	11.65	3.91
AG400	11.69	3.93

To more precisely study this, further structural studies using high-resolution TEM could be helpful to understand the structure of the precipitates, the interface between precipitates and the matrix and the crystalline defects e.g. stacking faults and dislocations which are all important in the overall strain created in the system. Especially $Fe_{12}As_5$ is a compound which is stable at high pressure in this system and it is possible that this compound precipitates under a high degree of internal strain.

In-situ TEM analysis could also be part of future work to investigate the low-temperature phase transition in these three samples and to investigate the effects of annealed microstructure on this low temperature structural transition.

6.7.References

1. Y. Kamihara, et al., *Iron-based layered superconductor $La(O_{1-x}F_x)FeAs$ (x=0.05-0.12) with T_c=26 K*, Journal of the American Chemical Society, 2008, 130(11): p. 3296.
2. M.S. Torikachvili, et al., *Pressure induced superconductivity in $CaFe_2As_2$*, Physical Review Letters, 2008, 101(5): p. 876.
3. Y. Zheng, et al., *Thermodynamic evidence for pressure-induced bulk superconductivity in the Fe-As pnictide superconductor $CaFe_2As_2$*, New Journal of Physics, 2012, 14: p. 241.
4. K. Sasmal, et al., *Superconducting Fe-based compounds $(A_{1-x}Sr_x)Fe_2As_2$ with A=K and cs with transition temperatures up to 37 k*, Physical Review Letters, 2008, 101(10): p. 951.
5. B. Lv, et al., *Unusual superconducting state at 49 K in electron-doped $CaFe_2As_2$ at ambient pressure*, Proceedings of the National Academy of Sciences of the United States of America, 2011, 108(38): p. 15705.
6. F. Ronning, et al., *Synthesis and properties of $CaFe_2As_2$ single crystals*, Journal of Physics-Condensed Matter, 2008, 20(32) p. 854.
7. H.L. Shi, et al., *Structural and physical properties of $CaFe_2As_2$*, Journal of Physics and Chemistry of Solids, 2011, 72(5): p. 420.
8. C. Ma, et al., *Microstructure and tetragonal-to-orthorhombic phase transition of AFe_2As_2 (A=Sr,Ca) as seen via transmission electron microscopy*, Physical Review B, 2009, 79(6): p. 060506.
9. Q. Huang, et al., *Neutron-Diffraction Measurements of Magnetic Order and a Structural Transition in the Parent $BaFe_2As_2$ Compound of FeAs-Based High-Temperature Superconductors*, Physical Review Letters, 2008, 101(25), p. 01236.

10. Y.A. Izyumov, et al., *High-T_c superconductors based on FeAs compounds*, 2010, Springer.
11. M.S. Torikachvili, et al., *Hydrostatic pressure study of the structural phase transitions and superconductivity in single crystals of $(Ba_{1-x}K_x)Fe_2As_2$ (x=0 and 0.45) and $CaFe_2As_2$*, Physica B-Condensed Matter, 2009, 404(19): p. 3223.
12. N. Ni, et al., *First-order structural phase transition in $CaFe_2As_2$*, Physical Review B, 2008, 78(1): p. 3865.
13. P.C. Canfield, et al., *Structural, magnetic and superconducting phase transitions in $CaFe_2As_2$ under ambient and applied pressure*, Physica C-Superconductivity and Its Applications, 2009, 469(9-12): p. 404.
14. S. Ran, et al., *Stabilization of an ambient-pressure collapsed tetragonal phase in $CaFe_2As_2$ and tuning of the orthorhombic-antiferromagnetic transition temperature by over 70 K via control of nanoscale precipitates*, Physical Review B, 2011, 83(14): p. 0835.
15. P.C. Canfield, et al., *Growth of single crystals from metallic fluxes*, Philosophical Magazine, 1992, 65(6): p. 1117.
16. A. Fitzgera, et al., *Electron Diffraction from Crystal Defects-Fraunhofer Effects from Plane Faults*, Proceedings of the Royal Society of London Series a-Mathematical and Physical Sciences, 1966, 293(1433): p. 169.
17. H. Okamoto, *The As-Fe (arsenic-iron) system*, Journal of Phase Equilibria, 1991, 12(4): p. 457.

Chapter 7: Conclusions and suggestions for future work

7.1 $Fe_ySe_{1-x}Te_x$ thin films

The feasibility of RF sputtering method for the deposition of superconducting $Fe_y(Se_xTe_{1-x})$ (Fe-11) thin films was studied, and it was found that sputtering can offer a strong potential for deposition of superconducting Fe(Se,Te) thin films.

The quality of the films highly improves when the films are deposited onto heated substrates. In-situ sputtering leads to high quality films, while ex-situ sputtering (deposition onto an unheated substrates and subsequent annealing) causes less uniformity, rough surface and poor texture. For in-situ sputtering, phase evolution and texture development as a function of processing conditions are studied (see Figure 7.1), and the optimum conditions for the best quality film in terms of purity, crystallinity and uniformity were found. The crystallization and epitaxial growth of the pure β-Fe(Se,Te) phase occur at 250°C and 300-320°C respectively. The c-axis alignment is obtained in most of the processing conditions, while in-plane alignment is shown to be strongly dependent on the substrate temperature and the film thickness. When the substrate temperature exceeds 325°C, an interlayer is formed between films and MgO which precludes epitaxial growth.

It has been shown that substrate choice plays a significant role in growth mechanism, microstructure of the films and texture development. The relationship between texture and substrate is more related to the growth mechanism rather than lattice misfit. The degree of texture alignment decreases on different substrate in this order MgO>LAO>STO>CaF_2>LiF>LSAT, i.e. the best texture is obtained on MgO. However, it

was shown that oxygen penetration can happen from substrate to the film. Therefore, non-oxide substrates are more recommended.

Surface roughness was found to be highly dependent on the growth mechanism and thickness rather than substrate temperature. Depending on processing conditions, Te-rich regions are formed on the surface after deposition with higher density at higher temperatures due to condensation of Te atoms. Decreasing the Ar pressure inside sputtering chamber was shown to be a useful way to prevent formation of these features on the surface.

Deposited $Fe_ySe_{1-x}Te_x$ films show a large data scatter in composition and most of them are Fe-rich ($y>1$) due to different transferring rate for Fe, Se and Te from the target to the substrate. As a result, using sputtering with only one target made of three elements, the deposited films tend to enrich in Fe content. Superconductivity was found to be highly dependent on Fe/(Se+Te), and the excess Fe suppresses superconductivity of the films. A sharp transition at 10.2 K is found for the films with an Fe/Se+Te ratio of about 1.

Compared to other deposition techniques, e.g. pulsed laser deposition which has been widely used in the literature for deposition of Fe(Se,Te) films, sputtering offers a potential technique for the deposition of considerably high quality 11-phase in a wider range of temperature and more flexible conditions. However, with only one target made of all three elements (Fe, Se and Te), it is challenging to precisely control the composition of the deposited films due to high difference between the transferring rates of Fe and Se/Te resulted from their highly different vapour pressures. A sputtering system with multiple targets can be a strong potential to overcome this limitation.

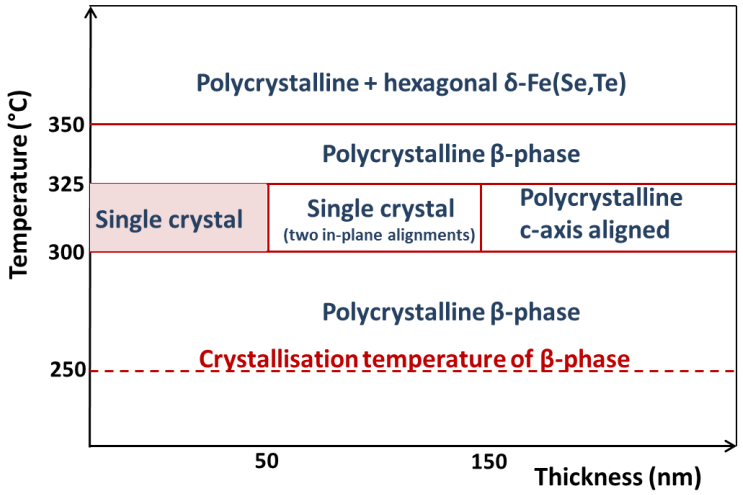

Figure 7.1: Crystallinity and texture development of the Fe(Se,Te) films as a function of temperature and thickness.

7.2 Mn doped Bi_2Te_3 single crystals

Mn doping incorporates with the Bi_2Te_3 structure differently depending on the Mn concentration. In the low doping concentration (9%Mn), Mn atoms are randomly substituted onto Bi sites leading to smaller lattice parameters. No evidence of nano/micro clusters was observed indicating that 9% is below solubility limit and all of the Mn atoms go into the structure. Due to non-uniform internal stress originated from the random distribution of Mn, lattice parameters vary in different regions. This substitution does not change the symmetry of the structure and, as a result, the same diffraction pattern as the undoped Bi_2Te_3 is obtained.

When the doping concentration increases to 15%Mn, supersaturation occurs and, in addition to the substitution on Bi sites, the extra Mn atoms go to the van der Waals gap in interstitial sites (i.e. Mn intercalation occurs) as well as the formation of nanoscale Mn-rich precipitates. The intercalation is ordered enough to create superlattice reflections in the diffraction pattern. Due to more ordered distribution of Mn, variations in both composition and lattice parameter are less than that in the low-deped single crystal. As a result of this intercalation, the lattice spacing along the c axis increases.

7.3 $CaFe_2As_2$ single crystals

$CaFe_2As_2$ single crystals grown by the FeAs-flux method and quenching from 960°C have been shown to be unstable FeAs-supersaturated crystals containing a high amount of strain but almost uniform composition. Due to the layered structure of $CaFe_2As_2$ and the weak van der Waals bonding in this direction, the extra FeAs is mostly trapped in the ab plane resulting in stacking faults and creating mechanical compressive strain.

Annealing at high temperature (700°C) causes the extra FeAs to precipitate by the diffusion of the Ca atoms, which are smaller than Fe and As atoms, and the matrix exhibits dislocations instead of stacking faults. Long precipitates of an FeAs-based compound are formed with their long dimension perpendicular to the c-axis possibly due to the presence of extra FeAs layers in the ab plane. To precisely identify the chemistry and structure of the precipitates, more microscopy experiments, especially high-resolution lattice images are recommended for future work.

Annealing at lower temperature (400°C) also results in a number of stacking faults and similar precipitates with lower Ca. Since Ca diffusion at 400°C is not as fast as that in 700°C, the accumulation of FeAs happens at the closest possible places leading to a local higher density of local stacking faults and smaller precipitates.

Annealing of this unstable supersaturated compound leads to phase segregation (low-Ca precipitates) and point-to-point compositional variation. Depending on annealing temperature, precipitates with different Ca contents are formed and strain will be partially relived leading to various degrees of stress in the sample and various c-axis parameters. This replicates different values of external pressure on the single crystal. Therefore, the microstructure of the $CaFe_2As_2$ single crystals, e.g. the density of stacking faults, the amount of strain, the density of precipitates, size and shape of precipitates, can be controlled by selecting the annealing temperature.

Future work

My results showed that sputtering can be a strong potential for making superconducting Fe(Se,Te) thin films, however, in order to accurately control the stoichiometry of the deposited film, multiple sputtering sources are required. Using sputtering with multiple targets can be considered as future work. Moreover, deposition at higher Ar pressure can be a solution for the Se and Te deficiency in the films and can be suggested for future work.

My results showed that Fe(Se,Te) thin films grown on MgO substrate has high quality compared to the films grown on the other substrates. However, oxygen penetration has to be avoided and buffer layer can be considered in future work.

TEM investigation of the deposited films in my work shows nano-scale inhomogenities. More TEM analysis can be carried out to understand the origin of these inhomogenities in this material, especially superconductivity of Fe(Se,Te) compound is very sensitive to composition and if there is nano-scale compositional variation, it may affect superconducting properties.